# Wire Array Photovoltaics

Thesis by
Dan Turner-Evans

In Partial Fulfillment of the Requirements
for the Degree of
Doctor of Philosophy


California Institute of Technology
Pasadena, California

2013

(Defended May 23, 2013)

To all of my teachers,

both in school and in life.

I am but the product of those who have invested time in me.

## Acknowledgements

The last five years have been a time of tremendous personal and professional growth. I have been blessed to have been surrounded by so many learned people, both in the ways of the world and in the ways of the lab. They have taught me how to approach an experiment with an open mind rather than an anticipated answer, how to work through challenges with patience and reason, and how to be critical but respectful. They are also wonderful and inspiring people who have given me their friendship and for all these things I am eternally grateful.

First and foremost, I have to thank Prof. Harry Atwater. When I first saw him speak at MIT in 2006, I was drawn to him for his infectious enthusiasm and creativity. To this day, I am impressed by his boundless knowledge and his bottomless well of ideas. He has also been an invaluable presence in GSC soccer and basketball, and I have been glad to have had him on my side. As I have grown, I have found father figures in all areas of my life, and Harry is among them.

I would also like to thank the other members of my committee: Prof. Keith Schwab, Prof. Nate Lewis, and Prof. Oskar Painter. I was fortunate enough to TA for Keith, an experience which launched a great friendship. Keith and I have explored the mountains of California together and somehow have yet to run out of things to talk about. He has incredible insight into both the physical workings of the world and the behavior of mankind. I look forward to our outdoor adventures in the years to come. I have also benefited tremendously from Nate and Oskar's Labs. The Lewis group has been a second home base during my time in grad school, the source of countless engaging and inspiring scientists, and a perennial softball rival. Oskar's lab has been the source of an excellent roommate and of constant inspiration.

I have also drawn inspiration from my greatest mentor and role model during graduate school, Dr. Mike Kelzenberg. From my days as a SURF student to the present, I have looked to Mike as a guide and have constantly been in awe of his patience, his unending curiosity, and his ability to visualize and create even the most fantastic machines. I firmly believe that no challenge is beyond Mike's abilities. On top of it all, he is also a lovely person: hilarious, caring, and thoughtful. I will forever aspire to "be like Mike."

I would also be remiss if I didn't acknowledge Dr. Morgan Putnam, Prof. Shannon Boettcher, Prof. Nick Standwitz, Prof. Shane Ardo, and Prof. Adele Tamboli for their sage counsel. Morgan contributed to much of the work in the first half of this thesis and contributed even more in perspective and support over the years. Successively over my graduate career, first Shannon, then Adele, then Nick, and finally Shane served as excellent sources of scientific insight and as role models. I owe them all many more words of praise then the above paltry sentence, but suffice it to say that they have served as consummate examples of the professional scientist, and their leadership was, and still is, inspiring.

Moving to the younger generation, none of the work in the latter half of this thesis would have been possible without Chris Chen and Hal Emmer. They have been excellent colleagues and great friends, and I look forward to following their successes in the years to come. I am also indebted to Max Bryk, Julie Jester, and Ben Lieber, SURF students who were more than willing to while away their summers working with me and who taught me much about mentoring.

In general, the Atwater Group is composed of an amazing group of people, and I have benefited from the knowledge and the camaraderie of every single student, postdoc, and

staff member who has passed through during my tenure. Tiffany Kimoto and Jennifer Blankenship have been a pleasure to get to know and the source of good advice over the years. I owe them many times over for all of the logistical drudgeries that they have helped me through. I also have to thank Lyra Hass and April Neidholdt for their help in the same vein early on. In terms of friendship and support, I was lucky enough to be placed in an office with Ana Brown, Carissa Eisler, and Emily Warmann, the best group of coconspirators around. I will miss our rapport. Dr. Anna Beck, Dr. Matt Bierman, Dr. Ryan Briggs, Dr. Mike Deceglie, Dr. Vivian Ferry, Prof. Mike Filler, Dr. Ron Grimm, Dr. Brendan Kayes, Emily Kosten, Dr. Liz Santori, Dr. Matt Sheldon, and Dr. Emily Warren all provided excellent advice over the years. Also, if you ever need to make music or play volleyball or soccer, you can find no better folk than Jeff Bosco, Dr. Victor Brar, Dennis Callahan, Dr. Matt Escarra, Jim Fakonas, Chris Flowers, Amanda Shing, and Sam Wilson (along with many of the people mentioned previously).

Furthermore, the facilities at Caltech are unparalleled and their greatness is due in large part to the people who oversee them. Reginalda Montaya has been a sunny and welcoming presence every morning in Watson. Christy Jenstad and Michelle Aldecua have kept Applied Physics running flawlessly. Melissa Melendes, Bophan Chhim, Nils Asplund, Dr. Guy Derose, and Mary Sikora have been a pleasure to work with in the KNI as has Alireza Ghaffari with the Applied Physics Cleanroom. Rick Gerhart, Mike Roy, and Steve Olson of the Chem/ChemE shops have also provided invaluable support as have Caltech Shipping and Receiving, particularly Rick Germond.

Finally, I have to thank all of my friends and family who have kept me grounded and happy during my time at Caltech. On campus, Jason Rabinovitch and Nick Parziale have always helped me get out of lab and into life. Off campus, Mark Cotter has given my some much need humanistic coloring of the world, and I will always thank him for teaching me how to hug. I am also indebted to his family, who have taken me in and welcomed me as one of their own. I will forever look back fondly on our Easters and Thanksgivings. And, last but not least, I have to thank my moms and my sister for their encouragement and support during my California adventure.

Financial support for my studies and for the work in this thesis was provided by the National Science Foundation, the Department of Energy, DARPA, and BP. I particularly owe my gratitude to the NSF for fellowship support.

*Daniel B. Turner-Evans*
*May 2013*
*Pasadena, CA*

## Abstract

Over the past five years, the cost of solar panels has dropped drastically and, in concert, the number of installed modules has risen exponentially. However, solar electricity is still more than twice as expensive as electricity from a natural gas plant. Fortunately, wire array solar cells have emerged as a promising technology for further lowering the cost of solar.

Si wire array solar cells are formed with a unique, low cost growth method and use 100 times less material than conventional Si cells. The wires can be embedded in a transparent, flexible polymer to create a free-standing array that can be rolled up for easy installation in a variety of form factors. Furthermore, by incorporating multijunctions into the wire morphology, higher efficiencies can be achieved while taking advantage of the unique defect relaxation pathways afforded by the 3D wire geometry.

The work in this thesis shepherded Si wires from undoped arrays to flexible, functional large area devices and laid the groundwork for multijunction wire array cells. Fabrication techniques were developed to turn intrinsic Si wires into full p-n junctions and the wires were passivated with a-Si:H and a-SiNx:H. Single wire devices yielded open circuit voltages of ∼600 mV and efficiencies of 9%. The arrays were then embedded in a polymer and contacted with a transparent, flexible, Ni nanoparticle and Ag nanowire top contact. The contact connected >99% of the wires in parallel and yielded flexible, substrate free solar cells featuring hundreds of thousands of wires.

Building on the success of the Si wire arrays, GaP was epitaxially grown on the material to create heterostructures for photoelectrochemistry. These cells were limited by low absorption in the GaP due to its indirect bandgap, and poor current collection due to a diffusion length of only ∼80 nm. However, $GaAs_xP_{1-x}$ on $Si_{1-x}Ge_x$ offers a superior combination of materials, and wire architectures based on these semiconductors were investigated for multijunction arrays. These devices offer potential efficiencies of 34%, as demonstrated through an analytical model and optoelectronic simulations. $Si_{1-x}Ge_x$ and Ge wires were fabricated via chemical-vapor deposition and reactive ion etching. GaAs was then grown on these substrates at the National Renewable Energy Lab and yielded ns lifetime components, as required for achieving high efficiency devices.

## Contents

**List of Figures** **xi**

**List of Tables** **xv**

**List of Publications** **xvi**

**1 Introduction** **1**

1.1 The State of Solar . . . . . 1

1.1.1 Energy Use and The Availability of Renewables . . . . . 1

1.1.2 The Cost of Solar . . . . . 2

1.1.3 Developing Solar Technologies . . . . . 3

1.2 The Solid State Physics of Photovoltaics . . . . . 6

1.3 Theoretical Maximum Efficiencies . . . . . 9

1.4 Wire Array Cells - Previous Work . . . . . 11

1.5 Heterostructure Multijunction Cells - Previous Work . . . . . 12

**2 Si Wire Array Growth and p-n Junction Formation** **14**

2.1 Introduction . . . . . 14

2.2 Vapor-Liquid-Solid Wire Growth . . . . . 15

2.3 Improving Array Fidelity . . . . . 17

2.3.1 The Importance of Catalyst Size and Patterning . . . . . 17

2.3.2 The Effects of Oxygen and Water Vapor . . . . . 19

2.4 *In Situ* Doping . . . . . 21

2.5 Emitter Formation . . . . . 22

2.6 Surface Passivation with a-Si:H and a-$SiN_x$:H . . . . . 25

2.7 Device Properties . . . . . 26

2.7.1 Diffusion Length . . . 26
2.7.2 Current-Voltage Curves . . . 29
2.8 Summary and Outlook . . . 31

**3 Flexible Arrays** **33**
3.1 Polymer Infill . . . 34
3.2 Ni Nanoparticle Direct Contact . . . 35
3.3 Ag Nanowires . . . 37
3.4 On Substrate Performance . . . 40
3.4.1 Comparison to Indium Tin Oxide Contacts . . . 41
3.4.2 Thermal Imaging of Shunts . . . 43
3.5 Peeled Off Cells . . . 43
3.6 Summary and Outlook . . . 45

**4 GaP on Si** **46**
4.1 Motivation . . . 46
4.2 Device Overview . . . 47
4.3 Optoelectronic Modeling . . . 48
4.3.1 GaP/Si Full Field Optical Modeling . . . 48
4.3.2 GaAs/Si Optical Modeling . . . 52
4.3.3 GaP/Si Device Physics Modeling . . . 55
4.3.4 AlP Window Layers . . . 56
4.4 Structure Growth and Characterization . . . 57
4.4.1 GaP Growth . . . 58
4.4.2 Modeling the Optical Effects of Surface Roughness . . . 60
4.4.3 Single Wire Measurements . . . 63
4.5 Summary and Outlook . . . 64

**5 $GaAs_xP_{1-x}$ on $Si_{1-x}Ge_x$: Modeling** **65**
5.1 Motivation . . . 65
5.2 Material Choice . . . 66
5.3 Device Architectures . . . 66
5.4 Analytical Model . . . 67

5.5 Optical Modeling . . . . . 74
5.6 Electronic Modeling . . . . . 80
5.7 Summary and Outlook . . . . . 86

**6 $Si_{1-x}Ge_x$ Wire Growth 88**
6.1 Previous Work and Overview . . . . . 88
6.2 Discussion of Ge Chemistry and Catalysts . . . . . 89
6.3 Au Catalyzed Ge Growth . . . . . 90
6.4 Influence of HCl, $BCl_3$, or $SiCl_4$ on Growth . . . . . 91
6.5 Ni, In, and Cu Catalyzed Ge Growth . . . . . 92
6.6 Cu Catalyzed $Si_{1-x}Ge_x$ Wire Growth . . . . . 95
6.7 Reactive Ion Etched Ge . . . . . 96
6.8 Masking Wires . . . . . 97
6.9 Summary and Outlook . . . . . 98

**7 GaAs Growth on Ge 100**
7.1 Previous Work and Overview . . . . . 100
7.2 Structure Overview . . . . . 101
7.3 Material Characterization . . . . . 101
7.3.1 Patterned, Planar Substrates . . . . . 102
7.3.2 X-Ray Diffraction . . . . . 103
7.3.3 Photoluminescence . . . . . 103
7.4 Parameter Optimization for Device Design . . . . . 106
7.5 Summary and Outlook . . . . . 109

**8 Conclusion 111**
8.1 Si Wire Array Solar Cells . . . . . 111
8.1.1 State of the Art . . . . . 111
8.1.2 Future Work . . . . . 112
8.2 Multijunction Wire Array Cells . . . . . 113
8.2.1 State of the Art . . . . . 113
8.2.2 Future Work . . . . . 114
8.3 The Wide World of Wire Arrays . . . . . 115

**A Si Wire Array Processing Steps** **116**

A.1 Fabricating Arrays with p-n Junctions . . . . . 116

A.2 Creating Flexible, Contacted Large Area Arrays . . . . . 119

**B Code for Making Rough GaP for FDTD Simulations** **121**

**C Code for the Analytical Tandem Model** **123**

C.1 Code to Plot the Mie Optical Generation Profile . . . . . 123

C.2 Code to Generate Plots at Each Wavelength . . . . . 125

C.3 Code to Calculate the Internal Fields of a Particle Given Mie Theory . . . . 126

C.4 Code to Plot the Beer-Lambert Optical Generation Profile . . . . . 128

C.5 Code to Generate Subcell, Tandem J-V Curves . . . . . 129

C.6 Code for the Hemispherical Subcell . . . . . 133

C.7 Code for the Wire Subcell . . . . . 137

**D Transmission Matrix Method Code** **140**

**E Sentaurus Code** **142**

E.1 Code from the Tandem Simulations . . . . . 142

E.2 Comparison between Lumerical and Sentaurus FDTD . . . . . 196

**Bibliography** **196**

## List of Figures


1.1 The cost of crystalline Si modules over time . . . . . 3
1.2 A Si wire array . . . . . 5
1.3 Overview of semiconductor bands . . . . . 7
1.4 Ideal Si cell IV curve and AM 1.5G spectrum . . . . . 8
1.5 Predicted Si wire efficiency as a function of wire radius and diffusion length 12

2.1 Overview of the wire growth process and a Cu/Si phase diagram . . . . . 16
2.2 High fidelity wire arrays in (a) square and (b) hexagonal patterns . . . . . 16
2.3 Comparison of catalyst size and growth fidelity as a function of the Cu thickness ($t_{Cu}$) and hole area . . . . . 17
2.4 45° view of a Si wire array showing typical height variation . . . . . 18
2.5 Morphologies of the wire tops for different cooling conditions . . . . . 18
2.6 Localized and large area wire array defects . . . . . 19
2.7 Varying wire cross sections for different growth conditions . . . . . 20
2.8 The growth reactor . . . . . 20
2.9 $BCl_3$ doping density measurement . . . . . 21
2.10 "Booting" the Si wires . . . . . 23
2.11 Experimental doping profiles and theoretical junction dependent dark current 24
2.12 Microwave reflectivity measured lifetimes of a-Si:H and a-$SiN_x$:H passivated wafers . . . . . 26
2.13 Cross-sectioned $SiN_x$ coated wire revealing the coating thickness variation along the wire length . . . . . 27
2.14 EQE maps of a-Si:H and a-$SiN_x$:H coated wires . . . . . 28
2.15 Light I-V curves of single wire solar cells . . . . . 30

3.1 Overview of a transparent, flexible contact for Si wire arrays . . . . . 34
3.2 Overview of an infilled wire array . . . . . 35
3.3 Measuring the Si/Ni resistance with a nanoprobe . . . . . 36
3.4 Examining the Ni/Si interface . . . . . 38
3.5 Optical properties of flexible, transparent top contact components . . . . . 39
3.6 Electronic properties of an on substrate Ni np/Ag nw embedded Si wire array solar cell . . . . . 41
3.7 Electronic properties of an on-substrate ITO/Ag nw embedded Si wire array solar cell . . . . . 42
3.8 Thermal images of a large area Si wire array . . . . . 43
3.9 Performance of a peeled off wire array . . . . . 44

4.1 GaP/Si device overview and band diagram . . . . . 48
4.2 Isoefficiency contour plot as a function of core and shell bandgaps . . . . . 49
4.3 Simulations of GaP on a Si grating . . . . . 50
4.4 Normal incidence GaP/Si and GaAs/Si wire array absorption . . . . . 51
4.5 Comparison of Beer-Lambert and full field radial optical absorption for GaP/Si wire cross sections . . . . . 52
4.6 Comparison of Beer-Lambert (B-L) and full field optical absorption (TE and TM) as a function of wavelength and GaP thickness for a radial cross section of a GaP on Si wire . . . . . 53
4.7 Properties of GaNPAs . . . . . 54
4.8 Simulated GaP/Si wire array light I-V characteristics . . . . . 55
4.9 Influence of an AlP window layer on GaP on Si cell performance . . . . . 57
4.10 SEMs of GaP on a Si wire array . . . . . 58
4.11 XRD plots of Si wires, planar GaP on Si, and GaP on Si wires . . . . . 59
4.12 Optical absorption of (a) a peeled off Si wire array and (b) a peeled off GaP/Si wire array . . . . . 60
4.13 Simulation of Rough GaP coated Si wire arrays . . . . . 61
4.14 Finding the GaP diffusion length . . . . . 62
4.15 Process diagram for single wire measurements of GaP coated Si wires . . . 63

5.1 Lattice matched material combinations overlaid on an isoefficiency contour plot for series connected, two junction cells . . . . . 67
5.2 Overview of the multijunction wire array geometries and electronic structure 68
5.3 Polar coordinate plots comparing Mie Theory and Beer-Lambert absorption for the upper $GaAs_{0.9}P_{0.1}$ cell . . . . . 70
5.4 Efficiency, short circuit current density, and open circuit voltage of hemispherical $GaAs_{0.9}P_{0.1}$ solar cell structures as a function of device radius and diffusion length . . . . . 73
5.5 Light IV curve of the shell as the outer ($r = d_1 + d_2$) and inner ($r = 0$) surface recombination velocities are varied . . . . . 74
5.6 Light IV curves for the subcells and tandem device . . . . . 75
5.7 The effect of series resistance ($R_s$) on the performance of the second tandem cell in Table 5.1 . . . . . 76
5.8 2D vs. 3D optical simulation comparison . . . . . 77
5.9 Comparison of the absorption profiles for FDTD optical simulations run at 25 nm wavelength steps vs. 50 nm wavelength steps . . . . . 78
5.10 Optical properties of multijunction wire arrays . . . . . 79
5.11 Plot of the relative absorption in the core and shell for all three structures for varying pitch . . . . . 81
5.12 Cartoon depicting the loss and absorption mechanisms in a wire array tandem cell . . . . . 82
5.13 Efficiency, short circuit current density, and open circuit voltage of the tandem wire array solar cell structures as a function of the $GaAs_{0.9}P_{0.1}$ lifetime 83
5.14 Shockley-Reed-Hall recombination for $\tau_n = 500$ or 5 ps in the $GaAs_{0.9}P_{0.1}$ cell for an array with a 7 $\mu$m pitch . . . . . 84
5.15 The influence of a "defective layer on device performance . . . . . 87

6.1 Phase diagrams for Ge and Au or Cu . . . . . 89
6.2 Ge on Si growth morphology as a function of growth temperature and $GeCl_4/H_2$ flow rates . . . . . 91
6.3 XRD and EDAX of Ge wires grown on Si . . . . . 92

6.4 The effects of small amounts of $BCl_3$, HCl, or $SiCl_4$ on the Ge growth morphology . . . 93
6.5 Growth attempts with Au, Cu, Ni, and In catalysts . . . 94
6.6 The influence of temperature and flow rate on Ge wires grown from Cu . . . 94
6.7 Suggested mechanism describing the evolution of the Ge wire morphology . . . 95
6.8 XRD plot of Cu catalyzed Ge wires grown on Si . . . 95
6.9 $Si_{1-x}Ge_x$ wire growth . . . 96
6.10 Reactive ion etched Ge pillars on (111) and (100) substrates . . . 97
6.11 A Ge wire masked with PECVD $SiO_x$ . . . 98

7.1 GaAs Growth on (311) Ge . . . 102
7.2 SEMs of structured Ge before and after GaAs growth . . . 103
7.3 GaAs growth on planar, oxide masked Ge . . . 104
7.4 XRD of GaAs on structured Ge . . . 105
7.5 PL of GaAs grown on structured Ge . . . 105
7.6 TRPL of GaAs grown on structured Ge . . . 106
7.7 Overview of the simulated structure for optimizing the doping levels for a GaAs device grown on Ge . . . 107
7.8 Device values for a GaAs hemispherical cell as a function of emitter and base doping . . . 108
7.9 Device values for a GaAs hemispherical cell as a function of window and defect doping . . . 109

D.1 TMM calculations . . . 141

E.1 Layout of Sentaurus simulations for finding the optical generation in tandem wire arrays . . . 142
E.2 Comparison of FDTD simulations from Sentaurus and Lumerical . . . 197

## List of Tables


1.1 U.S. average levelized costs (2011 $/MWhr) for plants entering service in 2018. 2

1.2 Current and anticipated total installed module costs from DOE's $1/W challenge . . . . . 4

1.3 Limiting theoretical solar conversion efficiencies . . . . . 10

2.1 Device properties of single wire solar cells with different surface coatings . . 29

3.1 AM 1.5G electrical characteristics of an on-substrate Ni np/Ag nw contacted Si wire array solar cell . . . . . 40

3.2 AM 1.5G electrical characteristics of an on-substrate ITO/Ag nw contacted Si wire array solar cell . . . . . 42

5.1 Light IV characteristics for subcells and tandem cell as the geometry of the shell and wire are varied . . . . . 75

5.2 Calculated ideal (IQE=1) $J_{SC}$ of layers under course (50 nm wavelength step) and fine (25 nm step) simulations . . . . . 80

5.3 Light IV characteristics for a representative hemispherical tandem . . . . . 85

5.4 Device performance as a function of surface recombination velocity . . . . . 86

7.1 Overview of GaAs on Ge growth run . . . . . 101

## List of Publications

The work in this thesis has primarily been drawn from the following publications:

- M. D. Kelzenberg,* D. B. Turner-Evans,* M. C. Putnam, S. W. Boettcher, R. M. Briggs, J. Y. Baek, N. S. Lewis, and H. A. Atwater. High-performance Si microwire photovoltaics. *Energy & Environmental Science*, 4, 866-871, 2011.

- D. B. Turner-Evans, H. Emmer, C. T. Chen, and H. A. Atwater. Flexible, transparent contacts for inorganic nanostructures and thin films. *Advanced Materials*, Accepted, 2013.

- A. C. Tamboli,* D. B. Turner-Evans,* M. Malhotra, M. D. Kelzenberg, and H. A. Atwater. GaP/Si wire array solar cells. *35th IEEE Photovoltaic Specialists Conference*, 2010.

- D. B. Turner-Evans, M. D. Kelzenberg, C. T. Chen, E. C. Warmann, A. C. Tamboli, and H. A. Atwater. Optoelectronic design of multijunction wire-array solar cells. *36th IEEE Photovoltaic Specialists Conference*, 2011.

- D. B. Turner-Evans, C. T. Chen, H. Emmer, and H. A. Atwater. Optoelectronic analysis of multijunction wire array solar cells. *Journal of Applied Physics*, Accepted, 2013

Small pieces from the following publications have also been included where appropriate:

- N. C. Strandwitz, D. B. Turner-Evans, A. C. Tamboli, C. T. Chen, H. A. Atwater, and N. S. Lewis. Photoelectrochemical behavior of planar and microwire-array Si/GaP electrodes. *Advanced Energy Materials*, 2, 1109-1116, 2012.

- A. C. Tamboli, C. T. Chen, E. L. Warren, D. B. Turner-Evans, M. D. Kelzenberg, N. S. Lewis, and H. A. Atwater. Wafer scale growth of silicon microwire arrays for photovoltaics and solar fuel generation. *IEEE Journal of Photovoltaics*, 2, 294-297, 2012.

- S. W. Boettcher, E. L. Warren, M. C. Putnam, E. L. Santori, D. B. Turner-Evans, M. D. Kelzenberg, M. G. Walter, J. R. McKone, B. S. Brunschwig, H. A. Atwater, and N. S. Lewis. Photoelectrochemical hydrogen evolution using Si microwire arrays. *Journal of the American Chemical Society* 133(5), 1216-1219, 2011.

- A. C. Tamboli, M. Malhotra, G. M. Kimball, D. B. Turner-Evans, and H. A. Atwater. Conformal GaP layers on Si wire arrays for solar energy applications. *Applied Physics Letters* 97(22), 221914-221913, 2010.

- M. C. Putnam, S. W. Boettcher, M. D. Kelzenberg, D. B. Turner-Evans, J. M Spurgeon, E. L. Warren, R. M. Briggs, N. S. Lewis, and H. A. Atwater. Si microwire-array solar cells. *Energy & Environmental Science* 3(8), 1037-1041, 2010.

- M. D. Kelzenberg, S. W. Boettcher, J. A. Petykiewicz, D. B. Turner-Evans, M. C. Putnam, E. L. Warren, J. M Spurgeon, R. M. Briggs, N. S. Lewis, and H. A. Atwater. Enhanced absorption and carrier collection in Si wire arrays for photovoltaic applications. *Nature Materials* 9(3), 239-244, 2010.

- S. W. Boettcher, J. M. Spurgeon, M. C. Putnam, E. L. Warren, D. B. Turner-Evans, M. D. Kelzenberg, J. R. Maiolo, H. A. Atwater, and N. S. Lewis. Energy-conversion properties of vapor-liquid-solid grown silicon wire-array photocathodes. *Science* 327(5962), 185-187, 2010.

- M. C. Putnam, D. B. Turner-Evans, M. D. Kelzenberg, S. W. Boettcher, N. S. Lewis, and H. A. Atwater. 10 $\mu$m minority-carrier diffusion lengths in Si wires synthesized by Cu-catalyzed vapor-liquid-solid growth. *Applied Physics Letters* 95(16), 163116-163113, 2009.

- M. D. Kelzenberg, M. C. Putnam, D. B. Turner-Evans, N. S. Lewis, and H. A. Atwater. Predicted efficiency of Si wire array solar cells. *34th IEEE Photovoltaic Specialists Conference*, 2009.

- M. D. Kelzenberg, D. B. Turner-Evans, B. M. Kayes, M. A. Filler, M. C. Putnam, N. S. Lewis, and H. A. Atwater. Photovoltaic measurements in single-nanowire silicon solar cells. *Nano Letters* 8(2), 710-714, 2008.

- M. D. Kelzenberg, D. B. Turner-Evans, B. M. Kayes, M. A. Filler, M. C. Putnam, N. S. Lewis, and H. A. Atwater Single-nanowire Si solar cells. *33rd IEEE Photovoltaic Specialists Conference*, 2008.

# Chapter 1

# Introduction

## 1.1 The State of Solar

### 1.1.1 Energy Use and The Availability of Renewables

In 2009, the world generated 20 petawatt-hours of electricity.(1) While this ever-growing consumption of energy has allowed for vast improvements in quality of life, it has come at a cost. Humanity's accelerated combustion of fossil fuels has led to ever-increasing carbon dioxide emissions. The US alone emitted 5,444.6 Tg of $CO_2$ in 2011.(2) These $CO_2$ emissions are affecting the world's climate such that a 2°C global increase in temperature now seems inevitable,(3) and an increasing number of major weather events are linked to the effects of climate change. However, despite dire warnings from climate scientists, world governments seem unable to agree on how to tackle the problem; developing countries feel entitled to use as much electricity as more prosperous countries, and wealthy nations are unwilling to lower their energy use at the risk of hurting their GDP.

One obvious solution is to switch to a form of electricity generation that emits much less $CO_2$ than conventional fossil fuel power plants. Hydro and nuclear power have been used for decades, but hydro cannot be expanded much beyond current levels and nuclear seems forever stigmatized by safety concerns. Wind energy has seen tremendous growth and is cost competitive with coal, but has an overall limited glocal capacity of $\sim$2 TW.(4)

Solar energy, on the other hand, has a huge potential. If all of the sun's energy that falls on the earth were captured for one hour, it would provide 14 TW of continuous power for a year, close to the 15+ TW of power that the world uses. Practically, more than 600 TW of power is available from the sun.(4) Thus, solar is an attractive energy solution for

lowering $CO_2$ emissions.

### 1.1.2 The Cost of Solar

While the cost of solar generated electricity is currently more expensive than power from coal or natural gas over much of the U.S. (see **Table 1.1**), the cost of photovoltaic modules has dropped drastically over the last decade (see **Figure 1.1**) and is projected to continue falling.(5) This drop has been due in large part to the rapid growth of module manufacturing, particularly in China (financed by very low interest loans from the state), leading to benefits from economies of scale.

Table 1.1: U.S. average levelized costs (2011 $/megawatthour) for plants entering service in 2018.(6)

| Plant Type | Capacity Factor (%) | Levelized Capital Cost | Fixed O&M | Variable O&M (+Fuel) | Transmission Investment | Total System Levelized Cost |
|---|---|---|---|---|---|---|
| Coal (*Conventional*) | 85 | 65.7 | 4.1 | 29.2 | 1.2 | 100.1 |
| Coal (*Advanced*) | 85 | 84.4 | 6.8 | 30.7 | 1.1 | 123 |
| Natural Gas (*Combined Cycle*) | 87 | 15.8 | 1.7 | 48.4 | 1.2 | 67.1 |
| Natural Gas (*Adv. Combined Cycle*) | 87 | 17.4 | 2 | 45 | 1.2 | 65.6 |
| Advanced Nuclear | 90 | 83.4 | 11.6 | 12.3 | 1.1 | 108.4 |
| Geothermal | 92 | 76.2 | 12 | 0 | 1.4 | 89.6 |
| Biomass | 83 | 53.2 | 14.3 | 42.3 | 1.2 | 111 |
| Wind | 34 | 70.3 | 13.1 | 0 | 3.2 | 86.6 |
| Wind (*Offshore*) | 37 | 193.4 | 22.4 | 0 | 5.7 | 221.5 |
| **Solar Photovoltaic** | 25 | 130.4 | 9.9 | 0 | 4 | 144.3 |
| Solar Thermal | 20 | 214.2 | 41.4 | 0 | 5.9 | 261.5 |
| Hydro | 52 | 78.1 | 4.1 | 6.1 | 2 | 90.3 |

In the Southwest US (which gets more sun than the rest of the nation), in parts of Southern Europe, and in many developing nations with limited electrical grids, solar electricity is already competitive with peak electricity costs.(5) These areas have seen rapid growth in the number of solar installations in the last decade, and the overall installed generation capacity should only continue to rise as the module price falls. As of February 2013, 100 GW of solar was installed on the global grid,(8) and a recent McKinsey report predicted a 50 fold increase in solar installations by 2050.(5)

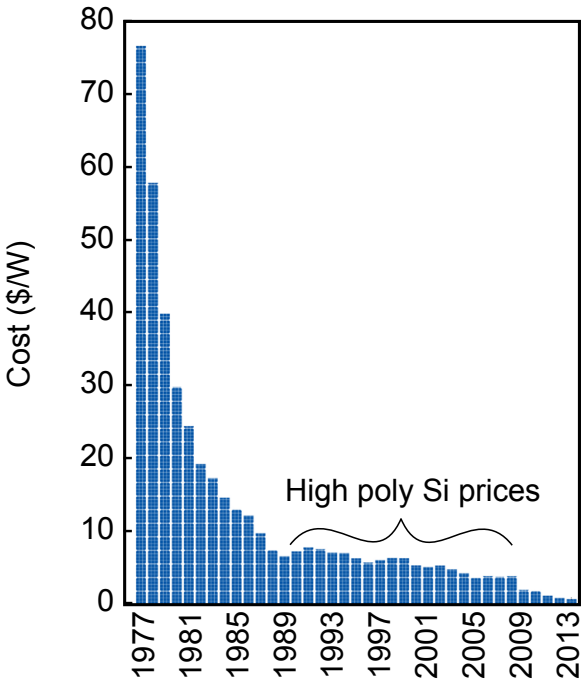


Figure 1.1: The cost of crystalline Si modules over time. The plateau in the mid 2000s is due to a shortage of polycrystalline Si.(7)

### 1.1.3 Developing Solar Technologies

Further economies of scale will certainly continue to lower the cost of PV modules. However, in order to gain significant market penetration, new technologies must be developed to make the cost of solar electricity competitive with that of natural gas at $\sim \$1/W$. **Table 1.2** outlines the component cost of modules as of 2010 and the anticipated relative costs in 2017 for achieving a $\$1/W$ installed module.

The high cost of 2010 modules, \$1.70, is due in large part to the conventional Si cell fabrication process. In this process, large mono or polycrystalline ingots are manufactured in the energy intensive, time consuming Czochralski process. This process, in which large single crystalline Si boules are slowly pulled from a melt, requires 214 MWh/ton of energy.(10) After growth, the boules must then be cut into the desired shape and size. The cutting process both limits the potential thickness of the cells to $\sim 150\mu$m and causes significant waste due to the thickness, or "kerf," of the saw. The wafer must then undergo a number of expensive processing steps, including high temperature emitter formation and contact firing and plasma-enhanced chemical-vapor deposition of passivation and anti-reflective coatings, in order to become a fully functional solar cell.

Table 1.2: Current and anticipated total installed module costs from DOE's \$1/W challenge.(9)

| Component | 2010 Cost (\$/W) | 2017 Goal (\$/W) |
|---|---|---|
| PV Module - Total | **1.70** | **0.50** |
| PV Module - Semiconductor | 0.54 | |
| PV Module - Cell Fab | 0.45 | |
| PV Module - Module Packaging | 0.70 | |
| Inverter | **0.22** | **0.10** |
| BOS/Installation | **1.48** | **0.40** |

In contrast, "thin film" solar cells seek to lower module costs by both using far less material for the cell and by using *in situ* processing techniques. CdTe, $CuIn_xGa_{1-x}Se_2$, and a-Si can all be formed in ∼100s of nm films on metal, glass, or plastic substrates, and have all exceeded 10% efficiencies.(11) They are deposited directly through chemical vapor deposition and the junctions are deposited *in situ* by modulating the material doping during growth. By utilizing these techniques, First Solar has successfully commercialized CdTe films and has captured a significant share of the market.

However, Si is still the dominant commercial technology ($> 80\%$ of commercial cells are made with crystalline Si),(9) Si modules have been made with $> 20\%$ efficiencies (Sunpower), and Si costs have room to drop significantly if the material used to make cells can be thinned and fabricated in an inexpensive process.

Along these lines, a few companies, notably 1366 and Solexeil, have developed innovative kerf-free processes for making thin Si cells. 1366 pulls 200 $\mu$m wafers directly from the melt. Solexeil creates 35 $\mu$m thick wafer by growing epitaxial Si on porous Si and then lifting the wafers off by etching away the porous layer. Both companies have demonstrated that their products can be incorporated directly into conventional cell fabrication lines and produce cells of comparable efficiencies to those from standard wafers.

Si wire array solar cells offer another (potentially) low cost approach (**Figure 1.2**). They are formed with a unique vapor-liquid-solid growth method and use the planar equivalent of $\sim 3\mu$m of material. While the wires are grown on a Si wafer, they can be embedded in a flexible polymer and peeled off, allowing the substrate to be reused for growth.(12; 13) Additionally, both p and n-type doping can be done during wire growth, lowering the cell

fabrication costs. Due to the extremely small amount of material needed and the ability to draw upon decades of knowledge about Si, Si wire arrays offer an exciting avenue for getting closer to the $\$1/W$ goal.

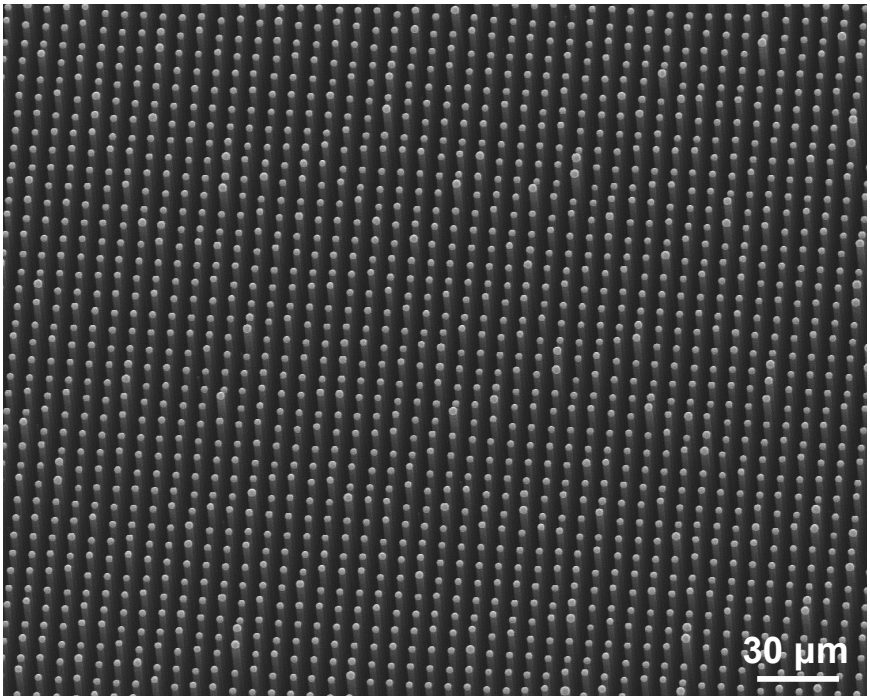


Figure 1.2: A Si wire array.

However, reducing the module cost alone is not enough to reach a $\$1/W$ total cost. The balance of systems (BOS) and installation costs of solar modules also need to be lowered. Here as well, Si wire arrays offer an advantage. They can be embedded in a transparent, flexible polymer to create a freestanding array that can be rolled up for easy installation in a variety of form factors, unlike the current rigid modules.(12) The combination of reduced fabrication costs *and* reduced installation costs are necessary, and Si wire array solar cells offer solutions on both fronts.

Furthermore, the wire array concept is not limited to Si. By incorporating multijunctions into the wire array morphology (e.g. by growing a $GaAs_xP_{1-x}$ cell on $Si_{1-x}Ge_x$ wire cells), higher efficiencies can be achieved. High efficiency ($> 20\%$) solar modules benefit from a relatively low BOS/installation cost, assuming that additional components are not needed for tracking or concentration. Fewer modules need to be installed in order to generate a given amount of power as compared to conventional systems.

While high efficiency modules are currently much more expensive than single junction systems, the unique geometry of wire arrays may help to mitigate the cost. Conventional multijunction cells are grown on expensive substrates such as Ge or GaAs, and they require a significant amount of material to be deposited through metal-organic-chemical-vapor-deposition (MOCVD), a costly growth step. Thick layers must be deposited in order to mitigate defects that arise from growing dissimilar materials on top of one another. In contrast, wire arrays use much less material than planar wafers, circumventing the substrate cost. Furthermore, the outer cell layers would only be deposited on the wire tips and, due to the wire geometry, defects due to lattice mismatch could relax radially, allowing high quality films to grow axially and requiring less overall MOCVD deposition.

Thus, single junction Si and multijunction wire array cells have the potential to reach the $1/W goal.

## 1.2 The Solid State Physics of Photovoltaics

In order to understand the development of wire array solar cells, knowledge of solid state physics is essential. I offer a brief overview here and encourage the reader to look at Ashcroft and Mermin (14); Ibach and Luth (15); Kittel (16); Sze and Ng. (17) for further understanding.

Just as atoms have discrete electronic energy levels, corresponding to the periodic orbit of electrons around the nucleus, crystals have allowed and forbidden energies, corresponding to the movement of electrons through the periodic arrangement of atoms that make up the crystal lattice. However, rather than having discrete levels, crystals have a density of electronic states over the range of energies. The electrons populate these states up to a certain level, the Fermi energy. If excited, by light for example, the electrons may move to occupy higher energy states.

In semiconductors, the density of states is zero for a range of energies above the Fermi energy (see **Figure 1.3**); electrons are forbidden from having an energy at these values. The distance between the Fermi energy and the next allowable state is called the semiconductor's bandgap. The continuum of energies below the Fermi energy is called the valence band while the range of allowed energies above the bandgap is called the conduction band. Light with energy greater than the bandgap energy can excite an electron into the conduction band from the valence band. The excited electron leaves behind an empty state. This empty

state behaves as a particle all of its own, with opposite charge of and motion to an electron. Thus, it is treated as a quasiparticle and dubbed a "hole."

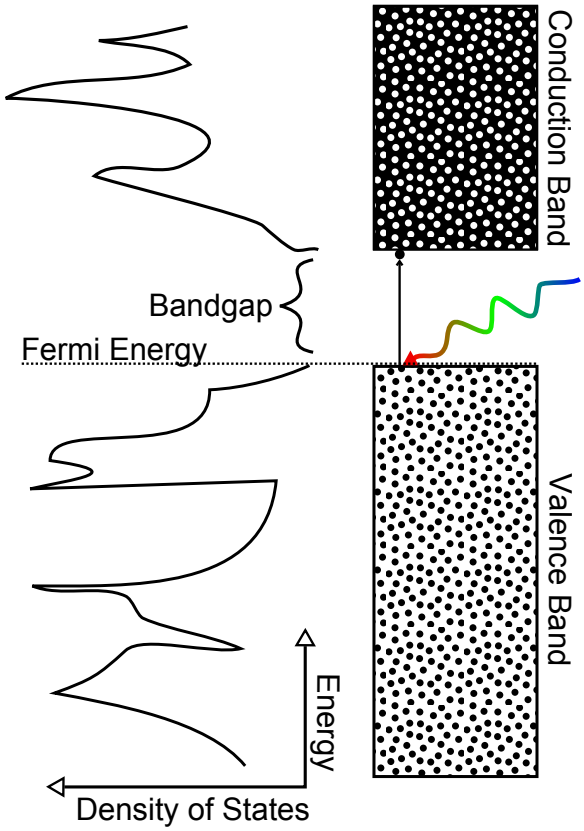


Figure 1.3: Overview of semiconductor bands.

Solar photovoltaics use the excited electron and hole to generate power. Light of all energies above the bandgap is absorbed in the material, creating a large population of energetic carriers (electrons and holes). The carriers diffuse throughout the material according to the transport equations:

$$\vec{J_n} = q\mu_n n\vec{E} + qD_n\vec{\nabla}n$$

$$\vec{J_p} = q\mu_p p\vec{E} - qD_p\vec{\nabla}p$$

where $n$ refers to the electron density, $p$ refers to the hole density, $\vec{J}$ refers to the current, $q$ is the fundamental electronic charge, $\mu$ is the mobility, $\vec{E}$ is the electric field, and $D$ is the diffusion coefficient.

While there is no innate $\vec{E}$ in the material, one can be built in to give directionality to the photocarrier movement. By replacing the base atoms of the semiconductor crystal

with elements that have more (less) electronic charge, the material's chemical energy can be increased (decreased). Material with an excess of negative charge is called n-type and material with an excess of positive charge is called p-type. Placing p-type and n-type material together in series creates a built-in electric field. The flow of photoexcited carriers across the field creates a current and the chemical potential difference between the n-type and p-type material creates a voltage, allowing power to be extracted. The electric field can be found from Poisson's equation.

An ideal current-voltage curve for a Si solar cell under AM1.5G conditions is shown in **Figure 1.4**. AM1.5G is the spectrum from the sun after it has passed through 1.5 atmospheres (i.e. at an angle as for latitudes away from the equator and/or times of day other than noon) and includes both direct and diffuse components. The figure also includes a power curve, which can be found by multiplying the current times the voltage.

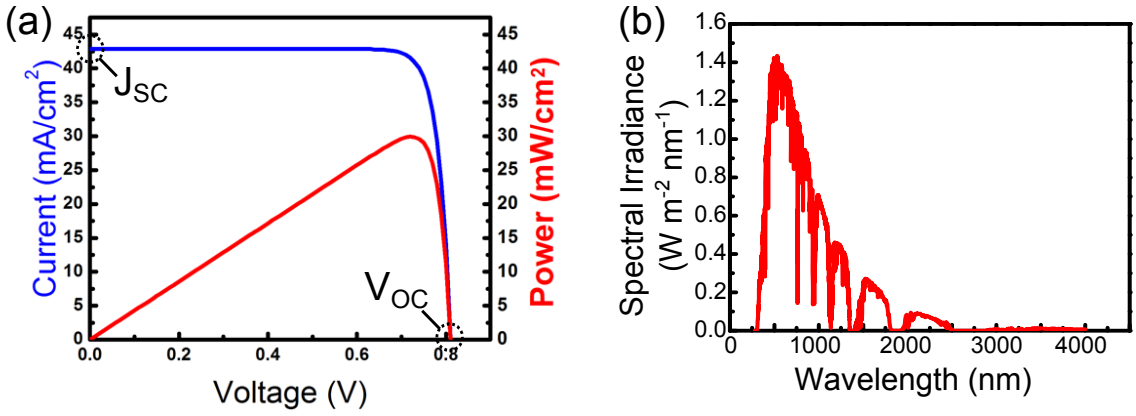


Figure 1.4: (a) Current-voltage and power curves for an ideal Si cell under AM1.5G illumination. (b) AM 1.5G spectrum.

A number of points on the current-voltage curve are of particular interest for understanding the cell performance. The current at zero bias is referred to as the short-circuit current ($J_{SC}$) and depends on the number of photons that are absorbed and the number of generated carriers that are then collected. The voltage at zero current is called the open-circuit voltage ($V_{OC}$). The open-circuit voltage will ideally be close to the bandgap energy, though it will be roughly 400 mV lower due to thermodynamic losses.* It represents

*Just as semiconductors can absorb light and create charge carriers, the opposite process can happen, with electrons and holes recombining to form a photon. This process is inevitable and leads to the voltage loss.

the maximum electrochemical potential of the excited carriers. The ratio of the maximum power to the product of $J_{SC}$ and $V_{OC}$ is called the fill factor ($FF$). Each of these metrics is essential to achieving a high efficiency cell and can reveal a great deal about problems and limitations of the device performance as follows:

1. $J_{SC}$ can be lower than ideal if not all of the incident light is absorbed or if the generated carriers run into defects and recombine, creating heat, before they can be collected by the external circuit.

2. $V_{OC}$ is a good indicator of cell quality. Defects within the material lead to recombination which in turn lowers the electrochemical potential and thus the $V_{OC}$.

3. $FF$ often gives some insight into resistive losses within the cell. Resistance in the cell is considered either in series, leading to a reduced slope around $V_{OC}$, or as a shunt, leading to a noticeable slope around $J_{OC}$

In general, a great deal of materials science and solid state physics goes in to making a cell with a high $J_{SC}$, $V_{OC}$, and $FF$. Specifics along these lines will be mentioned throughout the thesis.

## 1.3 Theoretical Maximum Efficiencies

Before attempting to fabricate a device, a researcher must understand the theoretical performance limits in order to define realistic goals. To understand the limiting efficiencies of solar energy converters, we will start with the Carnot cycle and describe further losses from that point onward, generally following the treatment of Henry (18).

A Carnot engine converts heat to work through isothermal and isentropic expansion and compression. For the sun, at a temperature of roughly 5800K and assuming the surrounding temperature is 300K, the Carnot efficiency is:

$$1 - T_{surrounding}/T_{sun} = 95\%.$$

However, as mentioned, the Carnot cycle is isentropic. In reality, some entropy will be gained in the photon absorption and radiative emission processes. This leads to additional losses and the so called Landsberg limit of 93%.(19)

Furthermore, the above processes assume that the hot and cold reservoirs freely exchange energy. However, while the converter will readily emit photons as a black body, they will likely be scattered by the atmosphere or absorbed by the surroundings, preventing them from reaching the sun. This loss of energy leads to an additional drop in performance, resulting in an $\sim$ 86% possible conversion efficiency. This is the upper limit for a solar energy converter.

Additional efficiency losses can come from the entropy difference between the incident photons, which come in only around the solid angle subtended by the sun, and the emitted photons, which can take all angles. This loss leads to $\sim$ 7% further drop in efficiency. By using concentration, and thus increasing the angles of the incident photons, or by limiting the range of emission angles from the cell, this loss can be avoided.

Next, if using a variety of semiconductors for energy conversion, the finite number of bandgaps will lead to thermal losses. Absorbed photons with energies above the bandgap of a cell will generate hot carriers (carriers occupying energy levels above the conduction band edge) which will then relax back down to the edge. The excess energy will be lost as heat. **Table 1.3** lists the maximum efficiencies for three, two, and one bandgap cells.

Table 1.3: Limiting theoretical solar conversion efficiencies

| Number of Cells | Spectrum | Efficiency |
|---|---|---|
| 3 | Black Body/AM 1.5D | 47% (20) |
| 2 | Black Body/AM 1.5D | 41% (20) |
| 1 | AM 1.5G | 31% (21) |

Finally, the efficiency of an ideal silicon cell is 29%, with additional losses due to Auger recombination and a bandgap that is slightly off of the ideal value for the solar spectrum.(22) In Auger recombination, an excited electron recombines and gives its excess energy to another exciting electron (turning it into a hot electron). The doubly excited electron then relaxes back to the band edge.

Thus, Si wire array cells will have a limiting efficiency of 29 % and multijunction wire cells will be limited to 41 % for two materials and 47 % for three materials (assuming that the wires do not benefit from concentration effects, which could raise the limits).

## 1.4 Wire Array Cells - Previous Work

Now that the limiting efficiencies have been defined, it is worthwhile to explore the state of the art for wire array cells. The work of many excellent scientists has opened up the possibility of even considering making photovoltaic wire arrays. Herein lies a *brief* survey of a few of the important players in the history of the technology, but many more great researchers are left unmentioned.

The growth of undoped Si and Ge wires alone has a rich history. Si "whiskers" were first reported by Wagner and Ellis (23) in 1964. Wagner and Ellis, then at Bell Labs, grew Si wires from a Au catalyst using a high temperature cholorosilane growth mechanism and proposed the vapor-liquid-solid (VLS) growth process that is still accepted today. Givargizov also made important contributions to the area over the next decade, and demonstrated the first growth of Ge wires.(24) In the modern era, Prof. Charles Lieber of Harvard popularized the growth of nanowires, beginning in the late 1990s, and Dr. Francis Ross at IBM has done some excellent work in advancing understanding of the physics of wire growth.(25; 26)

In 2005, Kayes suggested the idea of using Si wires in photovoltaics.(27) He posited that wire arrays would allow the optical absorption and carrier collection directions to be decoupled, allowing for high efficiencies despite potential low lifetimes in the wires. He further predicted efficiencies of over 10% for diffusion lengths greater than 10$\mu$m, as shown in **Figure 1.5**. At the time of writing, Kayes's paper has well over 600 citations and has led to an explosion of research into the field of wire array photovoltaics.

The Atwater and Lewis groups have since made impressive gains in creating high efficiency Si wire array cells,(28–36) along with many other groups in the area. To briefly mention a few, Prof. Joan Redwing's group at Penn State has helped to advance the understanding of high temperature chlorosilane wire growth.(37; 38) Dr. Loucas Tsakalakos at GE fabricated some of the earliest Si wire array cells.(39) Dr. Eric Garnett, formerly at Berkeley and Stanford, now at AMOLF, has done some nice work in furthering the experimental understanding of light trapping in wire array cells.(40) Finally, Leiber's group demonstrated high performance single wire cells.(41)

III-V wires have also been grown and demonstrated promising performance in both single wire and large area devices.(42; 43) To pick a few recent examples, they have been used to make lasers on Si,(44) thresholdless coaxial lasers,(45) and GaN LEDs on amorphous

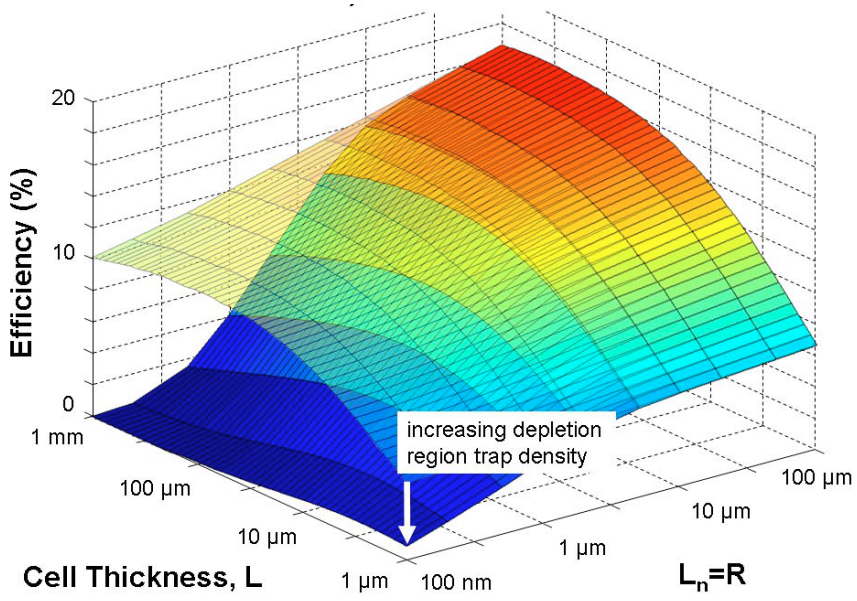


Figure 1.5: Predicted Si wire efficiency as a function of wire radius (cell thickness) and diffusion length. Reprinted with permission from (27). Copyright 2005, American Institute of Physics.

substrates.(46) For photovoltaics, Dr. Bernd Witzigmann at ETH outlined many important considerations for both optical emission and absorption in wire arrays. (47) Prof. Lieber, Prof. Ali Javey at Berkeley, Profs. Fan, McIntyre, Cui, and Harris at Stanford, Prof. Anna Fontcuberta i Morral at EPFL, Prof. Dan Dapkus at USC, and Prof. Diana Huffaker at UCLA have all demonstrated high performance III-V wire array cells.(48–56) Finally, a group at Lund recently demonstrated 13.8% efficient InP cells by leveraging many of the important design principles outlined in literature.(57; 58)

## 1.5 Heterostructure Multijunction Cells - Previous Work

Finally, the field of heterostructure solar cells has a long and full history, though the extension to wire morphologies is recent. A number of people at NREL, particularly Dr. John Geisz and Dr. Dan Freidman have contributed to the growth of high efficiency triple junction cells on Ge and once held the record for the highest efficiency tandem for a dual metamorphic structure grown on GaAs.(59) Dr. Richard King at Spectrolab has traded record efficiencies with the NREL group and has further contributed to growth on Ge.(60) Solar Junction holds the current record cell with a 44% efficient triple junction stack.(11)

Moving to wires, a number of axial and radial III-V heterostructures have been fabricated, but the use of wires to seed low defect density, lattice-mismatched materials is far more recent; in 2012, a group at ETH demonstrated that high quality Ge could be seeded on RIE etched Si micropillars.(61) However, the use of masked structures to grow low defect density III-V material does have more of a precedent, with epitaxial lateral overgrown employed in order to grow high quality GaN LEDs.(62) The lessons learned from these experiments have been brought to bear on multijunction wire array growth and design.

# Chapter 2

## Si Wire Array Growth and p-n Junction Formation

### 2.1 Introduction

While Si wires have been grown since 1964,(23) the ability to grow highly uniform, oriented arrays of wires is relatively recent, stemming from the work of Kayes et al. (63) in 2007. Furthermore, while wires were traditionally grown from Au catalyst particles, Kayes et al. (63) found that they could still achieve high fidelity wire growth by replacing the Au catalyst with Cu despite the potential for creating Cu silicides. Au is known to have a deep level trap in Si,(17) causing high levels of nonradiative recombination and limiting the effective diffusion length to $\sim 2\mu$m in the wires.(30) Cu is much more electronically benign, though it has a high solubility level in Si.(64; 65) Additionally, the Au, or impurities in the Au, led to unintentional n-type doping in the wires. The use of Cu, on the other hand, resulted in both longer lifetimes and low intrinsic doping densities, as reported in Putnam et al. (33). However, Cu is not as catalytically favorable as Au for initiating oriented wire growth.

Thus, the transition to Cu catalyst from Au spurred the need to more carefully control the wire growth chemistry in order to consistently achieve high fidelity arrays and opened up the possibility to add controlled *in situ* doping to the crystal growth. To that end, the use of a larger volume of catalyst and the elimination of water vapor and $O_2$ due to air leaks allowed for consistent growth of high fidelity arrays. Furthermore, by adding dilute $BCl_3$ to the reactor, the wires could reliably be doped p-type. These arrays achieved 3% energy-conversion efficiencies when used as photocathodes in contact with an aqueous methyl viologen$^{2+}$ electrolyte (28) and demonstrated near unity internal quantum efficiencies across the solar spectrum.(31) Additionally, the technology was demonstrated to be scalable; high fidelity arrays were successfully grown across an entire 6 inch wafer.(36)

The ability to repeatedly grow controllably doped, high fidelity arrays then allowed for the rapid development of solid state, Si wire array solar cells. *In situ* doped arrays were cleaned and oxidized, and a three dimensional patterning technique was developed to selectively expose the upper region of the wire for doping. A thin, highly doped, n-type emitter was diffused into the exposed region to create a p-n junction. Arrays fabricated in this manner yielded $> 5\%$ energy-conversion efficiencies under 1 sun illumination when used as photocathodes for $H_2$ evolution from $H_2O$.(29)

To further improve the performance of wire array solar cells, a-Si:H and a-$SiN_x$:H surface passivation layers were deposited on the arrays. The wires have very large surface area to volume ratios and thus effective surface passivation is essential to making high efficiency devices. Passivated arrays with areas of $\sim$0.1 $mm^2$ demonstrated efficiencies of up to 7.9%,(34) and single wire devices revealed $V_{OC}$s approaching 600 mV and the potential for achieving up to 17% efficient devices.(32)

This chapter explores the above solid state advances in more detail, demonstrating the advances that transformed undoped wire arrays into passivated, p-n junction solar cells.

## 2.2 Vapor-Liquid-Solid Wire Growth

Silicon microwire arrays were grown through the vapor-liquid-solid process using chemical vapor deposition, as detailed in **Figure 2.1 (a)**. A degenerately doped, p-type, $< 111 >$ Si wafer with a 500 nm oxide layer was used as the growth substrate. Photoresist was drop-cast on the oxide coated wafer and photolithographically patterned to create a series of holes. For the bulk of the work in this thesis, the holes were 3 $\mu$m in diameter and were arrayed in either square or hexagonal patterns with a 7 $\mu$m center-to-center spacing. After patterning, the oxide was selectively etched at the holes with buffered hydrofluoric acid (BHF). Finally, the substrates were coated with $\sim$400 nm of Cu to form an array of catalyst particles, and the resist and excess metal were lifted off.

The wafers were then loaded into a custom built growth reactor (**Figure 2.8**) under a $N_2$ ambient. The temperature was raised to 1000°C under $H_2$ at atmospheric pressure, and the substrate was annealed for 20 min. During the anneal, the Cu catalyst particle forms a liquid alloy with the Si substrate, as outlined in Figure 2.1 (b). $SiCl_4$ was then introduced to the process flow. During growth, Si diffuses into the catalyst particle, and the particle becomes supersaturated (the dotted line in Figure 2.1 (b)), and thus begins

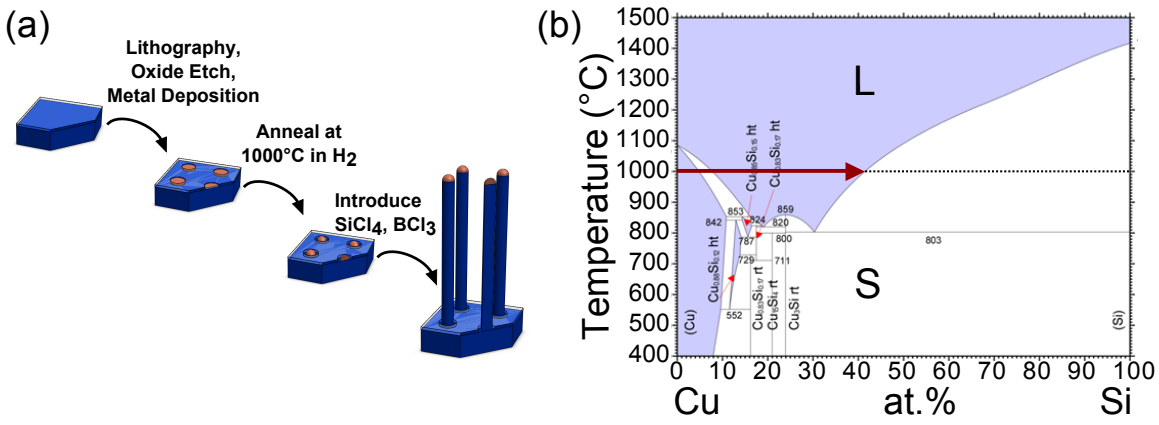


Figure 2.1: (a) Overview of the wire growth process. (b) Phase diagram for Cu and Si, overlaid with the growth process flow. The catalyst particle is supersaturated with Si (dotted line), forcing crystalline Si to be deposited at the substrate. Reprinted with permission of ASM International. All rights reserved. www.asminternational.org (66)

to deposit crystalline Si at the substrate interface, forming a single crystal Si wire that is registered to the substrate and allowing the liquid alloy to return to a more energetically favorable mixture. Under these conditions, growth in the $< 111 >$ direction is favored, and thus the wires grow vertically on the substrate, at roughly 5 $\mu$m per minute. When the desired height/time was reached, the $H_2$ and $SiCl_4$ flow were cut off and replaced by $N_2$. The growth chamber was purged for the next 20 min, and the furnace was allowed to cool to 650°C. The chamber was then evacuated and refilled with $N_2$ for unloading. High quality growths of square and hexagonal arrays are shown in **Figure 2.2**.

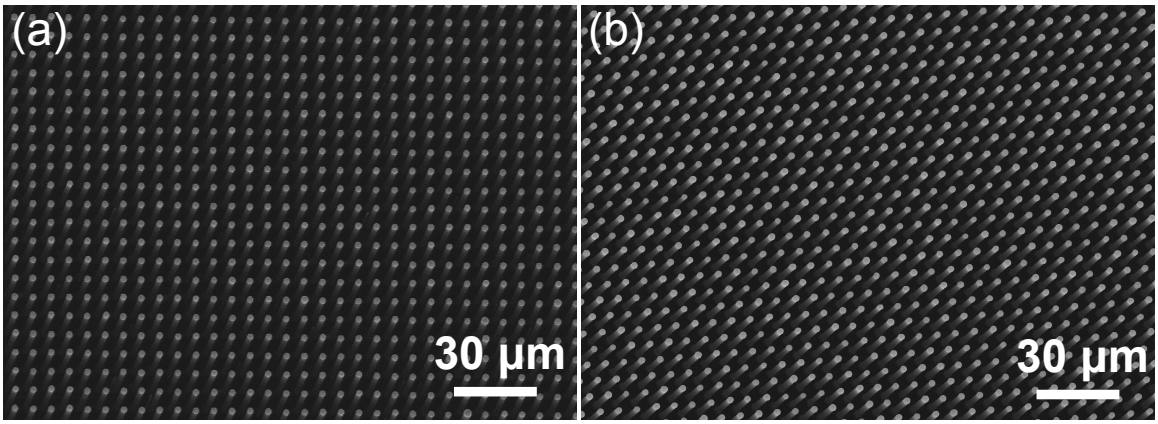


Figure 2.2: High fidelity wire arrays in (a) square and (b) hexagonal patterns.

## 2.3 Improving Array Fidelity

### 2.3.1 The Importance of Catalyst Size and Patterning

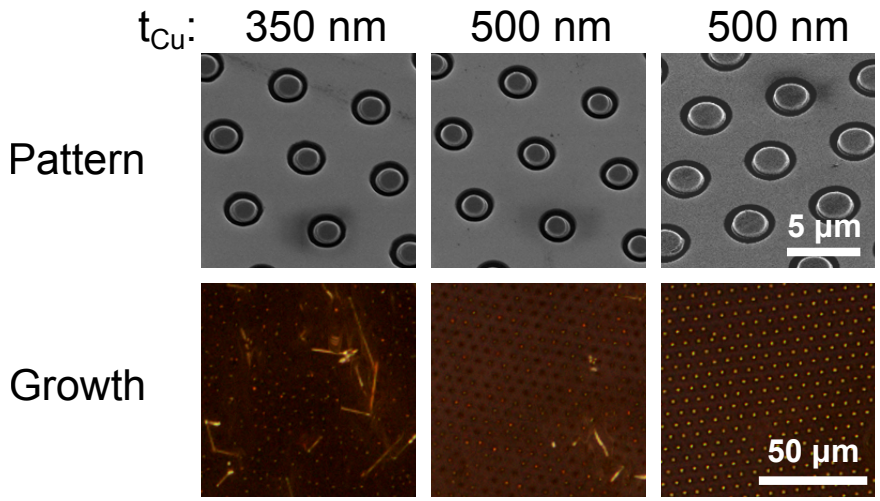


Figure 2.3: Comparison of catalyst size and growth fidelity as a function of the Cu thickness ($t_{Cu}$) and hole area.

While growing wire arrays from Au was relatively straightforward, Cu proved to be more susceptible to the perils of processing variability. Small changes in growth conditions or in the reactor setup led to widely varying array appearance and properties. The growth substrate also affected wire growth. As shown in **Figure 2.3**, the volume of catalyst metal had a significant effect on array fidelity, with more Cu translating to a higher probability of seeding an oriented wire. The larger contact area between the catalyst and the wire likely stabilizes the interface by inhibiting modifications to the surface energy by contaminants and then promoted the growth of wires oriented to the substrate.

Larger catalyst particles also led to faster wire growth, as demonstrated in **Figure 2.4**. The height distribution of Figure 2.4 is typical and is a result of catalyst size variation from the substrate preparation. Kendrick and Redwing (67) observed this phenomenon as well as variations in growth height with wire packing density. Additionally, wires could be made to grow faster/taller by moving the sample farther forward in the tube (closer to the gas source).

As a final note, the cooling rate of the reactor was found to drastically effect wire electronic quality. Experiments by Dr. Shannon Boettcher suggested that the reactor

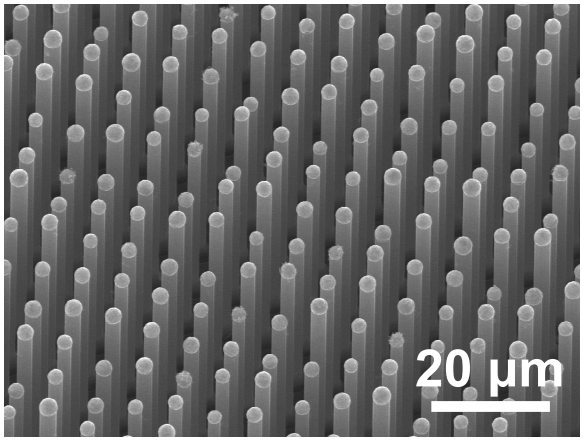


Figure 2.4: 45° view of a Si wire array showing typical height variation.

should be cooled to at least 750°C in order to obtain high $V_{OC}$s from the wires. This process takes around 20 min and likely results in Cu (and other metals that are incorporated within the wire during growth) diffusing to the surface rather than being quenched in the bulk. Additionally, the morphology of the top of the wire varied depending on whether the substrate was immediately cooled (Figure 2.5 (a)) or whether the wire was annealed at temperature (**Figure 2.5 (b)**) after the growth.

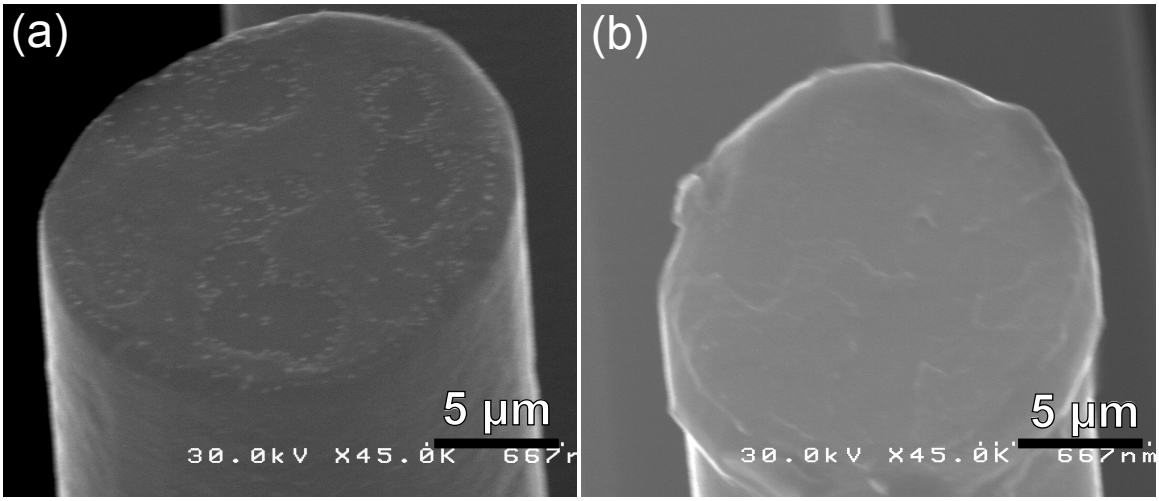


Figure 2.5: Morphologies of the wire tops for different cooling conditions. (a) An abrupt top. (b) A top with rough epitaxial growth.

### 2.3.2 The Effects of Oxygen and Water Vapor

Oxygen and water vapor, unintentionally introduced through leaks, had the biggest impact on array fidelity. Their presence caused areas of non-ideal growth either over the entire substrate or in localized regions (**Figure 2.6**). A leak in the reactor led to the growth shown in Figure 2.6 (a), with nonoriented wire growth distributed amongst oriented wires. Nonoriented growth occurs more rapidly than oriented growth. Localized growth, as in Figure 2.6 (b), often occurred even if leaks were eliminated, but seemed to be mitigated by cleaning the boat or by purging the tube with $N_2$ for 20 min before initiating growth, suggesting that water vapor trapped on the sample or in the boat initiated selective nonoriented growth.

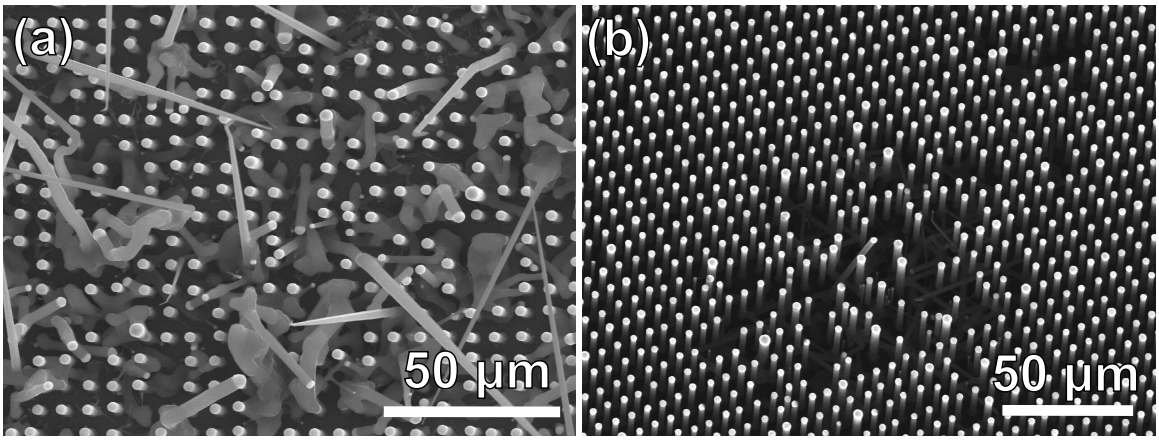


Figure 2.6: Localized and large area wire array defects. (a) A low fidelity array. (b) A"spotting" defect.

Water vapor or oxygen likely change the surface energetics, favoring defect formation. Hydrogen, on the other hand, passivates the surface. Hexagonal or dodecagonal cross-sections result from passivated surfaces, while unpassivated surfaces lead to round wire profiles (**Figure 2.7**).(68; 69)

In order to combat leaks, the growth reactor was rebuilt according to the schematics in **Figure 2.8**. Outside of regular operation, the valve to the turbo pump was opened and the system was allowed to pump down overnight. If the chamber pressure did not fall below $\approx$1 x $10^{-5}$, the system had an unacceptable leak rate and the fidelity would likely be poor. During normal operation, the system was pumped on with the roughing pump and booster pump or vented through the KOH scrubber to purge the effluent process gas. Leaks most

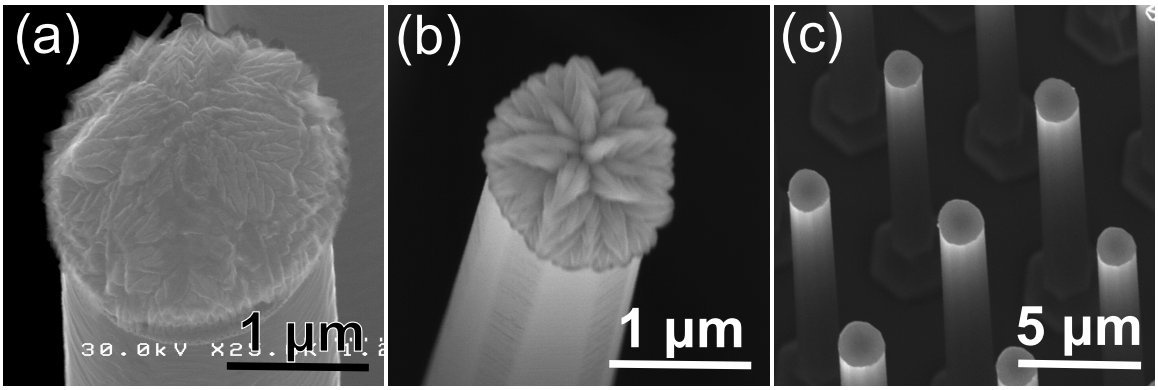


Figure 2.7: Varying wire cross sections for different growth conditions. (a) Round wires. (b) Dodecagonal wires. (c) Dodecagonal wires with hexagonal bases.

often originated from the Ultra-Torr seals at either end of growth tube and could be fixed by replacing the o-rings and/or retightening the connections. Occasionally, the sources (the bubbler of $SiCl_4$, the $BCl_3$, or the $H_2$) were contaminated and had to be replaced. Filters were added to the $BCl_3$ and $H_2$ lines in order to remove $O_2$ and $H_2O$ and seemed to help. All in all, every effort was made to keep the reactor leak tight.

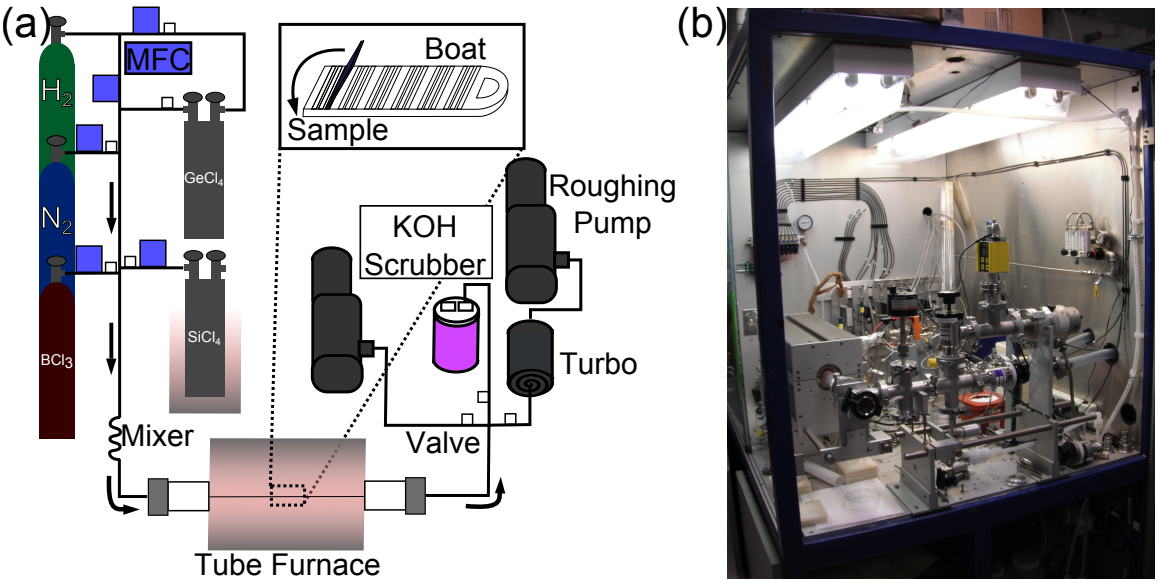


Figure 2.8: The growth reactor. (a) Schematic of the growth reactor. (b) Picture of the growth reactor. The tube furnace is on the left.

## 2.4 *In Situ* Doping

While Cu catalyzed wires proved more difficult to grow with high fidelity than Au catalyzed wires, the transition to Cu led to intrinsic material and the possibility of controllably doping the arrays. Trimethylboron and diborane have been used to grow p-type wires from silane or disilane,(70–75), but $BCl_3$ is favored for $SiCl_4$ wire growth (76) and hence was selected for its demonstrated compatibility with the array growth process. Thus, a tank of 0.02% $BCl_3$ in $H_2$ was added to the reactor.

Wire array growths were then performed at a variety of $BCl_3$ flow rates. The $BCl_3$ improved the growth fidelity, likely through the additional Cl that it adds to the growth process. This added Cl will change the partial pressures of the Si-H-Cl species that result from the $SiCl_4$ decomposition.(37) Some of these species etch Si and will thus "clean" the wire surfaces, inhibiting defect formation. However, if the $BCl_3$ flow was too great, the wires grew as cones rather than as cylinders. The Cu catalyst was etched by the Cl, leading to a decreasing catalyst size, and thus wire diameter, as the wire grew.

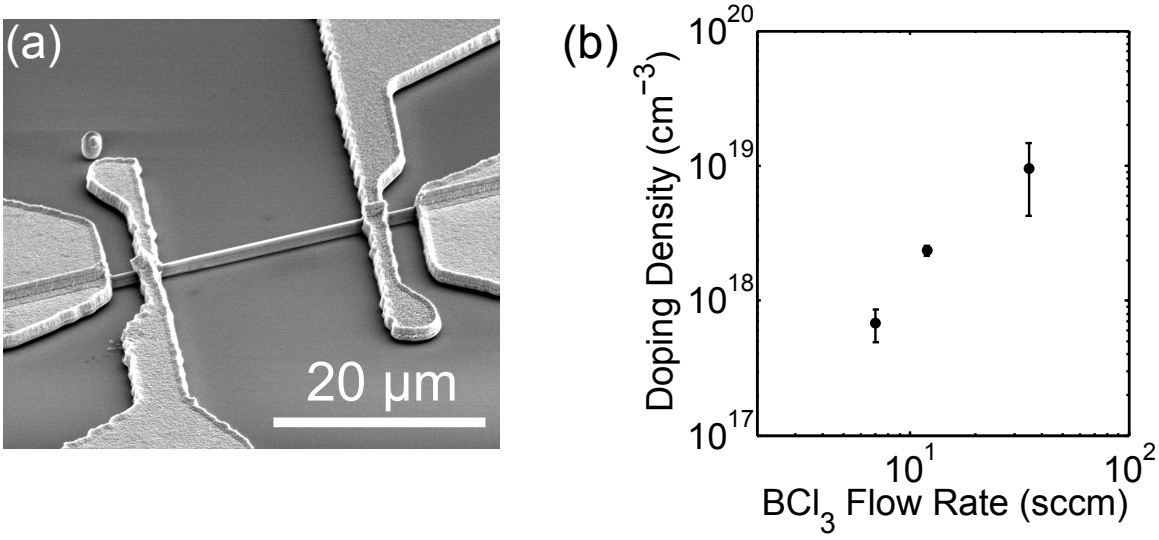


Figure 2.9: $BCl_3$ doping density measurement. (a) Four point contacted Si wire. (b) $BCl_3$ flow rate vs. wire doping density.

After growth, $\sim$1 mm$^2$ of wires was removed from the growth substrate for single wire contacting. The substrate was wet with a solvent (IPA or $H_2O$), a razor blade was scraped over the surface of the substrate to remove small areas of wires, and the solvent/wire solution

stuck to the razor was deposited in a vial along with further solvent. The solution was then placed on a $SiN_x$ coated Si substrate and allowed to dry. LOR 10A lift off resist and S1813 were spun on the substrate and four point contacts were photolithographically defined over 6-10 wires. 1 $\mu$m of Al and Ag was evaporated on the samples and the resist lifted off to leave the 4 point contacts shown in **Figure 2.9 (a)**.

Next, the four point resistance of the wires, $R$, was then measured and the resistivity calculated from $\rho = \frac{R \cdot A}{l}$, where $l$ is the wire length and $A$ is the wire area. The wire dimensions were found in the SEM. The wires were assumed to be cylinders for the purpose of calculating the area. Finally, the wire doping was estimated from standard Si doping vs. resistivity curves.(77) Figure 2.9 (b) displays the doping as a function of $BCl_3$ flow. Gating of the wires by applying a potential to the Si wafer confirmed that the wires were p-type (applying a positive bias to the substrate led to a decrease in wire conductivity). Additionally, some of the B from the degenerately doped growth substrate likely diffuses up into the wires to create a highly doped back surface field at the wire base.

## 2.5 Emitter Formation

Once repeatable, high fidelity, p-type arrays became a reality, fully solid state cells could be envisioned. While a one step, n-type diffusion would lead to fully radial p-n junctions, the base would be difficult to contact if the arrays were removed from the growth substrate, and shunting to the highly doped substrate or to the back surface field would be likely. Thus, the three-dimensional patterning process of **Figure 2.10** was developed to control the extent of the junction. The processing proceeded as follows:

1. The wire arrays were cleaned by immersing them in the following chemicals: buffered hydrofluoric acid (BHF, Transene, Inc) for 30 sec, RCA-2 (metals clean) (1:1:6 HCl:$H_2O_2$:$H_2O$) at 75°C for 10 min, BHF for 10 sec, and 60 wt% KOH at 40°C for 30 sec.

2. A ~200 nm barrier oxide was grown on the wire arrays by placing them in a 1100°C tube furnace with $O_2$ flowing at 3 lpm for 1 hr and 40 min.

3. The arrays were infilled with a dilute solution of polydimethylsiloxane (PDMS) (1 g of PDMS base, 0.1 g of PDMS curing agent, 5 g of toluene) by twice spin coating at 3000 rpm for 30 sec. They were then baked at 60°C for at least 30 min to crosslink the polymer. Roughly 5 $\mu$m of the base was protected with the polymer.

4. The oxide from the exposed tips was removed by immersing the embedded arrays in BHF for 5 min.

5. The PDMS was removed by placing the array in a 1:1 solution of dimethylformamide:tetra-n-butylammonium fluoride in tetrahydofuran for 45 min.

6. The arrays were cleaned with a piranha solution (1:3 $H_2O_2$:$H_2SO_4$) for 10 min, dipped in BHF for 10 sec, cleaned with RCA-2, and finally dipped in BHF again for 10 sec.

7. The arrays were doped by placing them in a solid source, phosphorous doping furnace at 850°C for 10 min.

The oxide layer, referred to as the "boot," served as a barrier, protecting the underlying Si from the P doping. The oxide thickness was selected by doubling the values suggested in Hamilton and Howard (78).

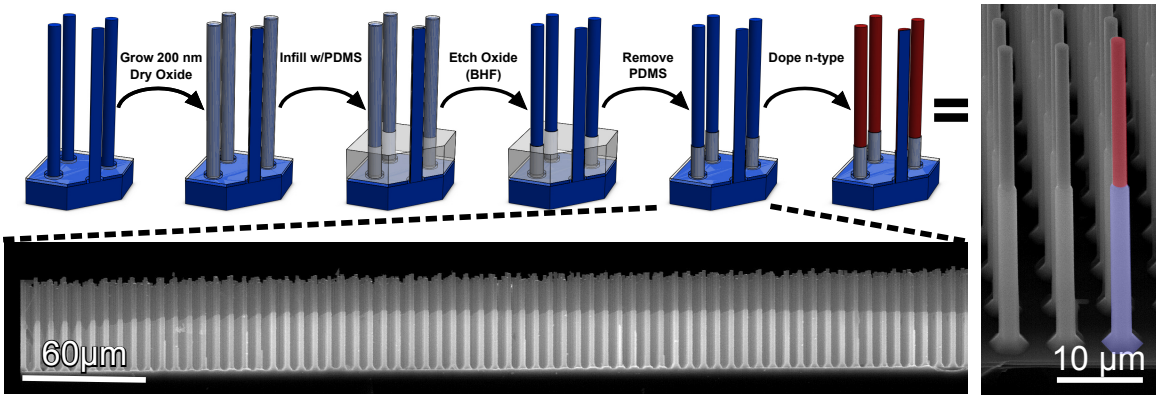


Figure 2.10: "Booting" the Si wires. (top) Schematic of the processing steps required to create a radial pn junction wire array. (bottom) SEM demonstrating the uniformity of the oxide "boot" across the array. (right) SEM image giving a close up of the "booted" wires. The false coloring corresponds to the n and p-type regions indicated in the cartoon.

The emitter profile proved to have a significant impact on device performance, and thus the doping density and layer thickness were calibrated on planar Si chips. $CeP_5O_{14}$ solid source wafers (PH 900 from Saint Gobain) were used to form the n-type layer. The chips were placed into a tube furnace loaded with the solid source P wafers at 750, 800, and 850°C for 2, 5, 10, and 15 min. They were then sent to Solecon Labs where lap angle measurements were performed to assess the junction profile. Three such profiles are seen

in **Figure 2.11 (a)**. They do not exactly follow the Gaussian model found in introductory textbooks, but they are in line with more rigurous models.(79)

In light of the given profiles and considering the dark current model of King et al. (80), 10 min and 850°C were chosen as the doping time and temperature, respectively. The chosen profile was selected to reach the optimal tradeoff between doping induced degradation and quasi Fermi level splitting. The higher the doping, the higher the splitting between quasi Fermi levels and thus the higher potential open circuit voltage. However, the lifetime and mobility of Si tend to fall off drastically as the doping is increased beyond $\sim 10^{19}$ cm$^{-3}$. Thus, the dark current is minimized at $\sim 10^{18}$ cm$^{-3}$ and for as shallow an emitter as possible, as shown in Figure 2.11 (b). In order to avoid shunting, slightly higher doping values and a 100 nm emitter were targeted. Due to depletion of the doping wafers over time, the emitter formation process was calibrated regularly.

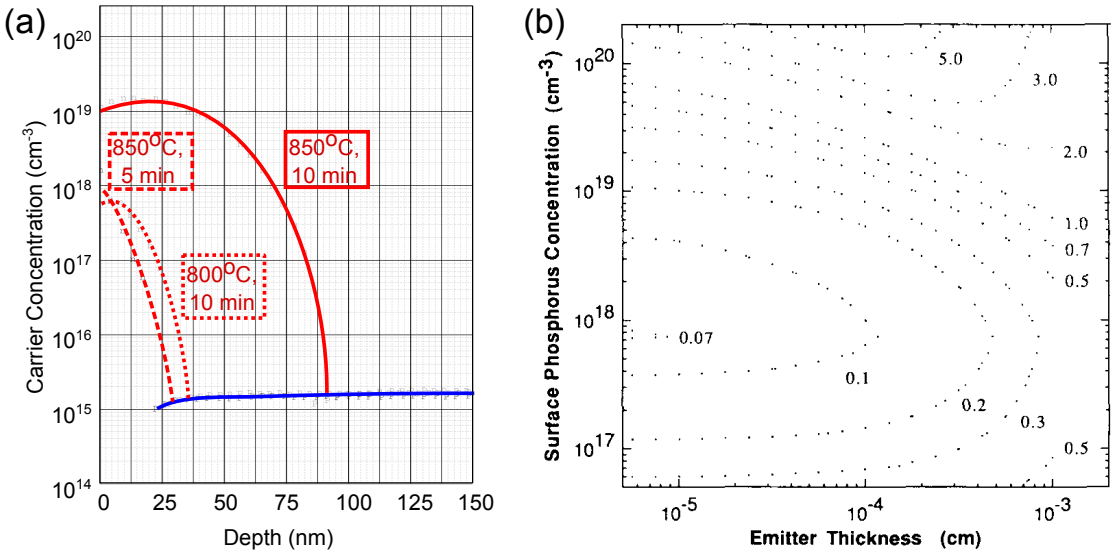


Figure 2.11: (a) Planar doping profiles for a variety of temperatures and times as a function of depth. (b) Dark current as a function of emitter thickness and surface concentration. ©1990 IEEE. (80)

Doping through the use of spin-on dopants and a rapid thermal annealer was also attempted,(81) but was abandoned due to the difficulty of uniformly coating the arrays with the dopant glass.

## 2.6 Surface Passivation with a-Si:H and a-SiN$_x$:H

Due to the high surface area to volume ratio of the wires, the development of an effective surface passivation technique was deemed essential to achieving high performance devices. Along these lines, a-Si:H and a-SiN$_x$:H have seen extensive use over the years in the Si processing community as surface passivation layers. a-Si:H passivation can lower the silicon SRV to 3 cm/s,(82) and a-SiN$_x$:H has achieved SRVs as low as 1 cm/s. However, the exact value is heavily dependent on the substrate doping and on the injection conditions.(83; 84) a-SiN$_x$:H can also act as an effective antireflective coating for Si.(85) These coatings passivate the Si surface in three ways:

1. They neutralize dangling bonds by attaching a H or a Si atom to each site.

2. They have a larger bandgap than the Si and a type I offset and thus reflect minority carriers.

3. They retain ionic H, and thus a positive charge, creating a surface field that proves effective for passivating the surface of n-type material.

The surface passivation abilities of the two materials was first tested on planar Si pieces by depositing material on both sides of a high lifetime ($\sim$1 ms), 400 $\mu$m thick, double side polished, float zone wafer. The a-Si:H was deposited with plasma enhanced chemical vapor deposition (PECVD) at 240°C and 500 mTorr, using 5% $SiH_4$ in Ar at a total flow rate of 100 sccm, and a 13.56 MHz plasma at 3 W forward power. 10 nm of material was deposited on each side. The a-SiNx:H was deposited at 350 C and 1 Torr in a parallel-plate reactor (Plasmalab System100, Oxford Instruments), using a $SiH_4/NH_3$ gas chemistry whose ratio was chosen to produce films that had a refractive index of $\sim$ 2.0 (400 sccm 5% $SiH_4$ in $N_2$, 30 sccm $NH_3$). *In situ* stress control was performed by alternating between a 3.56-MHz and 50-kHz plasma frequency, both with 20 W of forward power (65% RF duty cycle). $\sim$80 nm of material was deposited on each side.

Microwave reflectivity measurements, seen in **Figure 2.12 (a)** were used to assess the surface passivation quality of the two materials. In this technique, a pulsed laser diode is used to excite carriers within a Si wafer. The carriers then diffuse throughout the wafer, recombining at the surface or at any internal defect sites. Throughout the process, microwaves are reflected off of the underside of the wafer. The microwave reflectivity of the

wafer is directly proportional to the excess carrier concentration, and thus the reflected microwave power will be directly proportional to the number of excited carriers. Thus, by monitoring the transient of the reflected microwave power, as seen in Figure 2.12 (b), the carrier lifetime may be found. If the sole source of recombination is the wafer surface, then the SRV will equal $\frac{t/2}{\tau}$ where $t$ is the wafer thickness and $\tau$ is the measured lifetime. The a-Si:H passivated wafer was found to have a lifetime of 0.975 ms and thus a bounded SRV of 20 cm/sec. The a-SiN$_x$:H wafer had a lifetime of 1.07 ms and thus a bounded SRV of 19 cm/sec.

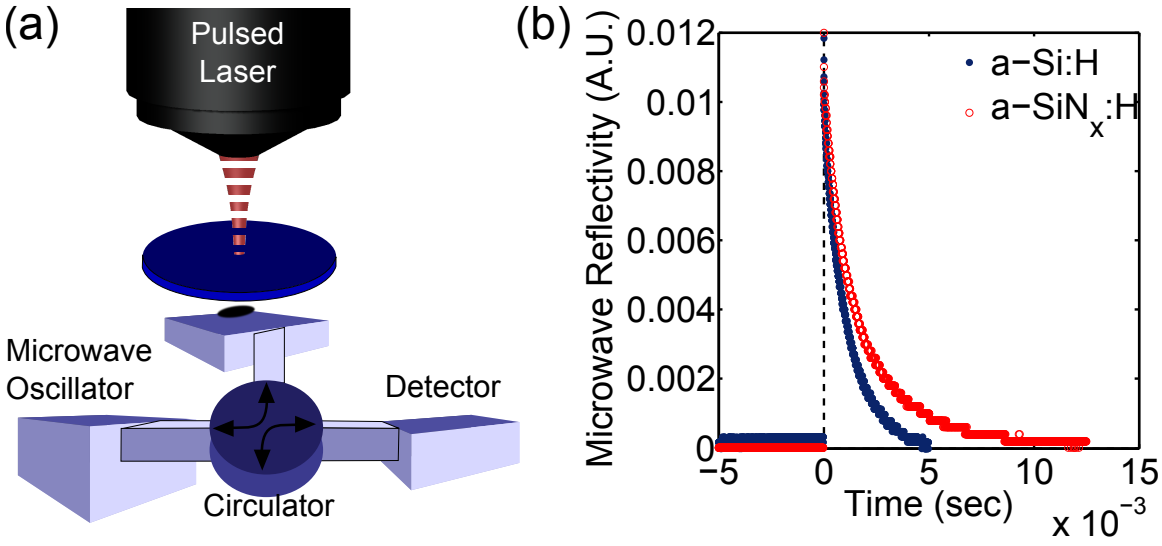


Figure 2.12: (left) Schematic of the microwave reflectivity setup. (right) Microwave reflectivity as a function of time for a-Si:H and a-SiN$_x$:H passivated planar, float zone Si wafers.

## 2.7 Device Properties

### 2.7.1 Diffusion Length

Given the effectiveness of the surface passivation layers on planar Si, they were next applied to fully cleaned, p-n junction wire arrays. A 30 min deposition time of a-Si:H was chosen to produce a ∼10 nm thick layer of nominally intrinsic material on the wire sidewalls. For the a-SiN$_x$:H, deposition was performed for 25 min, producing a coating that varied from ∼30 nm thick at the wire base to ∼130 nm thick at the wire tip, as observed by milling

out wire cross-sections with a focused ion beam and imaging the cuts with SEM (**Figure 2.13**). Two point contacts were then made to single wire devices as described in the *In Situ* Doping section. After metallization, the a-Si:H-coated single-wire devices required a 30 min anneal at 275°C in forming gas (5% $H_2$ in $N_2$) to produce ohmic contacts through the a-Si:H layer. For the a-Si$N_x$:H, prior to removing wires from the growth substrate, the arrays were partially infilled with wax (Quickstick 135, South Bay Tech.) and then etched for 10 s in 49% BHF to remove the a-Si$N_x$:H from the uppermost ∼10 $\mu$m of each wire, enabling the formation of single-wire contacts.

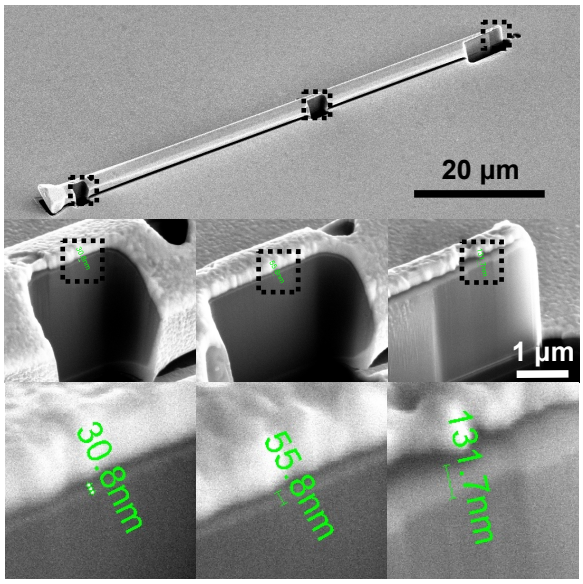


Figure 2.13: Cross-sectioned Si$N_x$ coated wire revealing the coating thickness variation along the wire length.

After verifying that the single wires behaved as photodiodes by taking a light biased current-voltage sweep with a Keithley 246 Source Measure Unit, scanning photocurrent microscopy (SPCM) was performed to extract the effective wire diffusion lengths, $L_{eff}$. In SPCM, a 650 nm laser is swept over the wire while any generated photocurrent is collected through the wire contacts and passed through a transimpedance amplifier. The output voltage is then compared to the voltage output from a calibrated photodiode with known external quantum efficiency (EQE).* This produces a spatially resolved map of minority-carrier collection within the single-wire solar cell.

*EQE is the number of cariers collected as photocurrent per single incident photon.

For unpassivated wires, relatively uniform carrier collection was observed throughout the radial portion of the wires, but no carrier collection was observed from the axial portion. In fact, the abrupt spatial transition between the two collection regimes could not be resolved by the ∼0.5 $\mu$m diameter beam spot of the illumination source, indicating that $L_{eff}$ was <0.5 $\mu$m for the as-fabricated Si wires. In comparison, the SPCM profile of a typical a-Si:H-coated single-wire solar cell indicated axial-region carrier collection with a characteristic decay length of ∼10 $\mu$m, as shown in **Figure 2.14 (a)**, indicating a surface recombination velocity <450 cm $s^{-1}$, as calculated by following the treatment in the supplementary info of Allen et al. (86).

The SPCM profile of a typical a-$SiN_x$:H-coated single-wire solar cell (Figure 2.14 (b)) exhibited high carrier collection efficiency throughout the entire axial portion of the wire, with no apparent decay length. Furthermore, the EQE of the a-$SiN_x$:H-coated devices was markedly higher than that of the noncoated devices, due to the anti-reflective nature of the nitride coating. In fact, the EQE was usually greatest within the axial portion of these wires, because the tapering thickness of the a-$SiN_x$:H in this region yielded a nearly optimal antireflective coating at the excitation wavelength. While the long $L_{eff}$ of the a-$SiN_x$ wire was originally interpreted as stemming from the combination of very low surface recombination velocities and diffusion lengths significantly greater than 30 $\mu$m, further experiments have suggested that the nitride is instead inverting the p-type region, leading to an effective radial junction along the length of the wire. If given a negative charge with a charge gun, the collection in the nitride coated p-type region drops to zero. This inversion could be exploited in devices; wire arrays could be made with minimal diffused junctions, instead relying on an inverting layer to separate carriers throughout most of the length.

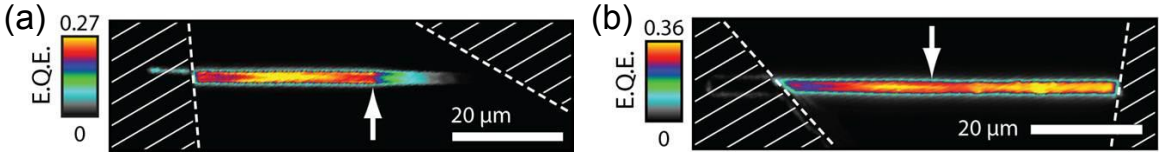


Figure 2.14: EQE maps of (a) a-Si:H and (b) a-$SiN_x$:H coated wires. The emitter lies to the left of the white arrow.

Overall, the effective diffusion length in the a-Si:H sample is still presumed to be an accurate reflection of the carrier decay, and may be due to the internal diffusion length, to

Table 2.1: Device properties of single wire solar cells with different surface coatings. The champion cells are listed in bold.

| Wire coating | $L_{eff}$ ($\mu$m) | $S$ (cm s$^{-1}$) | $\eta$ (%) | $V_{OC}$ (mV) | $J_{SC}$ (mA cm$^{-2}$) | $FF$ (%) |
|---|---|---|---|---|---|---|
| Original | $< 0.5$ | $> 4\text{x}10^5$ | **4.6** | **451** | **13** | **77** |
| ($N = 12$) | | | 1.5-4.6 | 390-496 | 6.9-16 | 58-81 |
| a-Si:H | 5-10 | 450-600 | **7.4** | **564** | **16** | **81** |
| ($N = 20$) | | | 3.6-7.4 | 561-595 | 7.8-17 | 77-82 |
| a-SiN$_x$:H | * | * | **9.0** | **535** | **23** | **75** |
| ($N = 13$) | | | 4.8-9.0 | 462-543 | 17-26 | 56-78 |

the quality of the surface passivation, or to the a-Si:H layer getting thinner down the length of the wire. As $L_{eff}$ was also measured as $\sim$10 $\mu$m in Putnam et al. (33) and lifetimes of tens of nanoseconds have been measured in bulk suspensions of Si wires, the Si diffusion length is assumed to be 10 $\mu$m.

### 2.7.2 Current-Voltage Curves

The solar power generating capacity of single wire cells was also measured, allowing us to report the highest open circuit voltages ($V_{OC}$), fill factors (FF), and apparent photovoltaic efficiencies ($\eta$) to date for VLS-grown Si wire solar cells, as summarized in **Table 2.1**. To improve the absorption of incident sunlight, all devices were fabricated on reflective substrates consisting of Si wafers that had been coated with 100 nm of evaporated Ag (to provide high reflectivity) and $\sim$300 nm of PECVD SiN$_x$ (to prevent the contacts from shorting). Full field, finite difference optical simulations suggest that using reflective Ag substrates enabled $17-22\%$ greater $J_{SC}$s than would be possible using the SiN$_x$-coated Si substrates of prior studies.(32) **Figure 2.15** plots the current density vs. voltage behavior of the most efficient device of each surface coating type.

Following the convention of prior single-wire solar cell studies,(30; 41; 87) current density was determined by normalizing the device current by the total non-shaded physical area of each wire (including both the axial and radial regions and the surface coating thickness). Note, however, that the wave nature of light and the photonic dimensions of micro- and nanowires enable them to interact with (and potentially absorb) more sunlight than

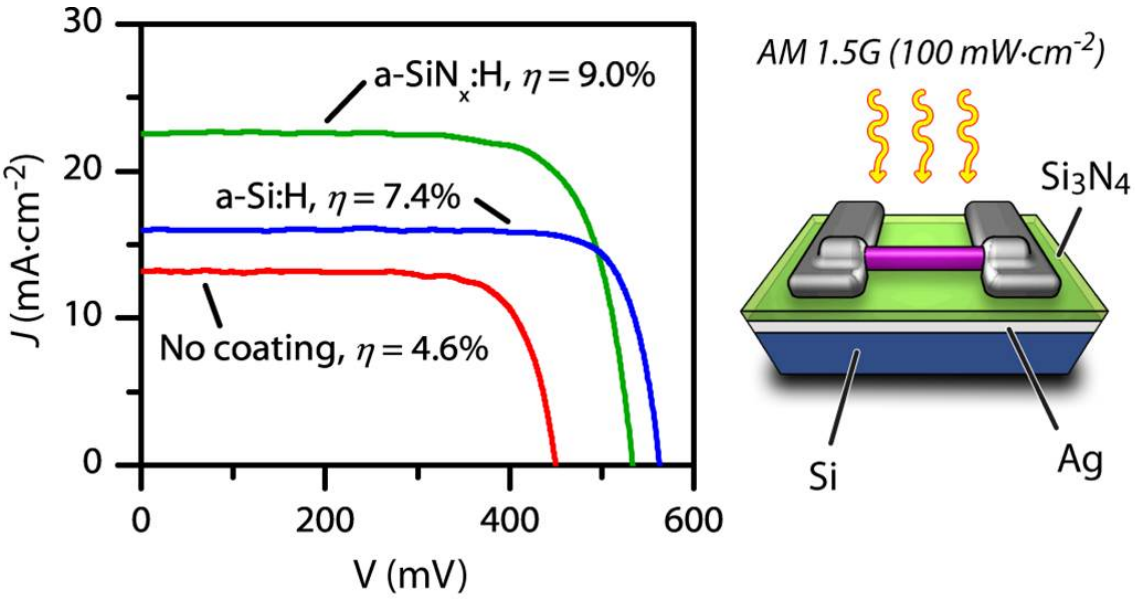


Figure 2.15: (left) AM 1.5G I-V curves for as fabricated, a-Si:H, and a-$SiN_x$:H coated single wire solar cells. (right) Schematic of the measurement setup.

predicted by their physical area, from a classical ray-optics perspective. This ill-defined absorption area prevents a true definition of photovoltaic efficiency for single-wire devices, and results in an apparent EQE exceeding 100% at certain wavelengths for some of the devices. Nonetheless, for microwires of the diameter range studied herein ($1.2 - 1.8\mu$m), numerical simulations suggest that minimal systematic error ($< 4\%$ relative overstatement of $J_{SC}$) is introduced by normalizing the photovoltaic performance of the champion devices to their physical area.

Comparing the PECVD coatings, the reduced reflectivity of the a-$SiN_x$:H-coated devices consistently yielded the highest short-circuit current densities (up to 26 mA $cm^2$), and resulted in the device with the greatest apparent photovoltaic efficiency ($\eta = 9.0\%$) due to the full collection across the wire length from the inversion layer. The a-Si:H had the highest $V_{OC}$ as it effectively passivated the surface while the a-$SiN_x$:H simply inverted it.

Finally, the absorption properties of wire arrays from Kelzenberg et al. (31) were used to calculate the photocurrent that would be expected to pass through a single wire in an entire, upright array. The illumination on a single, a-Si:H passivated, two point contacted wire was then increased until the photocurrent reached this expected value. The measured current-voltage curve suggested that an upright efficiency of 17% would have been achieved

for an array made of these wires.

## 2.8 Summary and Outlook

In summary, the realization of repeatable, high fidelity growth from Cu catalyst opened the door for the development of high quality p-n junctions within the wires. The addition of surface passivation layers allowed us to fabricate the highest efficiency Si wire solar cells to date, with 9% single wire efficiencies and projected 17% array efficiencies. Due in part to these promising results, Caelux Inc. sought to leverage the technology from 2010 onward in order to make $> 10\%$ efficient, low cost solar modules.

Additionally, the electrical measurements, in particular the diffusion length data, suggest many ripe areas for further investigation. The lifetimes of the VLS grown Si are currently low, likely stemming from impurities incorporated during the growth process or stacking faults and dislocations. TEMs of wire cross sections have suggested that the substrate/wire interface is particularly prone to defective regions and additional defects may reside throughout the wire. Varying the growth temperature to slow the wire growth rate and annealing the wires for extended periods of time at higher temperatures may help to mitigate these defects. Gettering the Si, through slow cools or the growth of oxides, doped or otherwise, may also help, leeching impurities out of the bulk so that they can be removed at the surface.(88) Mass spectroscopy of wires to determine the primary contaminants would also be invaluable. Finally, placing Schottky contacts at various points along a cleaned, passivated wire could allow position dependent diffusion lengths to be measured to see if different regions of the wire are more or less recombination active.(89)

The emitter profile could also be further optimized. If the diffusion lengths can be increased to $\sim$100 $\mu$m, then axial junctions should increase the $V_{OC}$ by limiting dark current due to junction area. In this case, the junction should be located at the bottom of the cell, in order to limit absorption in the highly doped emitter. Also, the junction doping density and depth have not been fully optimized, leaving further room for device improvement. Shallower, less highly doped junctions with well passivated surfaces should enhance performance. Finally, while the arrays are believed to have an innate back surface field due to diffusion of dopants from the wafer, this aspect of the devices has not been well characterized.

As for the surface passivation layers, the a-Si:H and a-$SiN_x$:H could be combined to

create a layer that effectively passivates the surface as well as providing an anti-reflective coating. Atomic layer deposition of passivation layers should also be explored. Finally, the inverting properties of the nitride could be used to minimize the p-n junction, streamlining the fabrication process.

Overall, the potential of Si wire solar cells was demonstrated, but room exists for further improvements.

# Chapter 3

## Flexible Arrays

After demonstrating the potential for 17% array efficiencies in single wire devices,(32) the remaining hurdle to making an efficient, large area device was to fabricate a flexible, transparent top contact. While Spurgeon et al. (35) fabricated substrate-free, flexible, PDMS embedded wire array photoelectrodes with metal back contacts, these electrodes relied on the liquid to make a top contact to the devices. In contrast, thin films and nanostructures often use conductive oxide contacts. However, these materials are brittle and fracture if bent to a radius beyond 1 cm.(90) Thus, a new contacting scheme was needed for polymer embedded wire arrays.

Silver nanowire (Ag nw) contacts have attracted the attention of the material science community for their high transmission and low resistivity ($\sim$ 80% across the visible spectrum with a sheet resistance of $\sim$ 20 $\Omega/\square$), flexibility, and ease of processing.(91–93) While a number of organic solar cells and organic light emitting diodes have incorporated Ag nw contacts,(94; 94–97) their application to inorganic devices has been far more limited;(92; 98; 99) depositing Ag nws directly on inorganic semiconductors does not lead to low barriers contacts.

However, by depositing metal nanoparticles on the semiconductor surface to create localized contacts and then incorporating Ag nws to bridge the devices, a flexible, transparent top contacting scheme for polymer embedded Si wires was formed. In particular, combining electroless nickel deposition with dropcast Ag nws, as in **Figure 3.1**, led to the creation of flexible, robust, transparent contacts and the demonstration of a monolithic array of 100,000s of single wire solar cells connected in parallel with an overall series resistance of 14.0 $\Omega$ cm$^2$, a fill factor of 55.5%, and a Si wire contact yield of $>$ 99%.

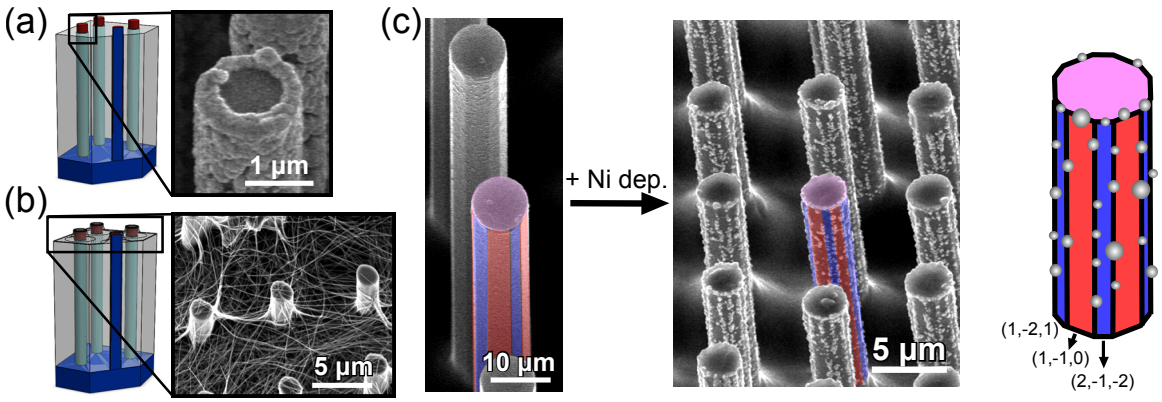


Figure 3.1: Overview of the two stage top contacting scheme. (a) Ni nanoparticles are deposited on the Si wires through electroless deposition. (b) Ag nanowires are drop cast on the array to create a continuous top contact. (c) By varying the deposition time and temperature, the Ni nps can be limited to coat the wire edges alone. (left) SEM of the array before and after Ni np deposition. (right) Schematic of the wire crystal morphology and Ni np sites.

## 3.1 Polymer Infill

The first step in creating a flexible wire array solar cell was to develop a reliable polymer infilling process. The polymer preserves the wire array fidelity and offers mechanical robustness and flexibility after the wires are removed from the substrate. To this end, the method of Plass et al. (12) was modified to embed the wire array in silicone polymer (Dow Corning 93-500 Space Grade Encapsulant), leaving $\sim$5 $\mu$m of the wire tips exposed for contacting. While Plass et al. (12) used poly(dimethlysiloxane) (PDMS) to infill the wires, PDMS was found to repel the electroless Ni solution and hence the use of 93-500, which tolerated the Ni solution and was otherwise functionally equivalent to the PDMS.

When embedding the wires, a 10:1:15 w/w/w ratio of Dow Corning 93-500 Space Grade Encapsulant base, 93-500 Space Grade Encapsulant curing agent, and toluene was mixed to create a dilute film that was drop cast on the wires at 3000 rpm for 30 sec multiple times until the wires were completely covered with polymer. The infilled polymer surface was then covered with toluene which was rapidly spun off at 3000 rpm to leave $\sim$5 $\mu$m of the tips exposed. The film was cured at 60°C for 10 hours.

While the average height of individual wire arrays varied from 40-80 $\mu$m, depending on growth time, and the individual wires showed $\sim$5 $\mu$m height variation due to slight

differences in catalyst size, the polymer infill was still reliably uniform over the bulk of the sample. **Figure 3.2** shows a large area overview of an infilled wire array. However, as is typical for a drop cast solution, the corners and edges of the array experienced a polymer buildup and hence led to small inactive areas.

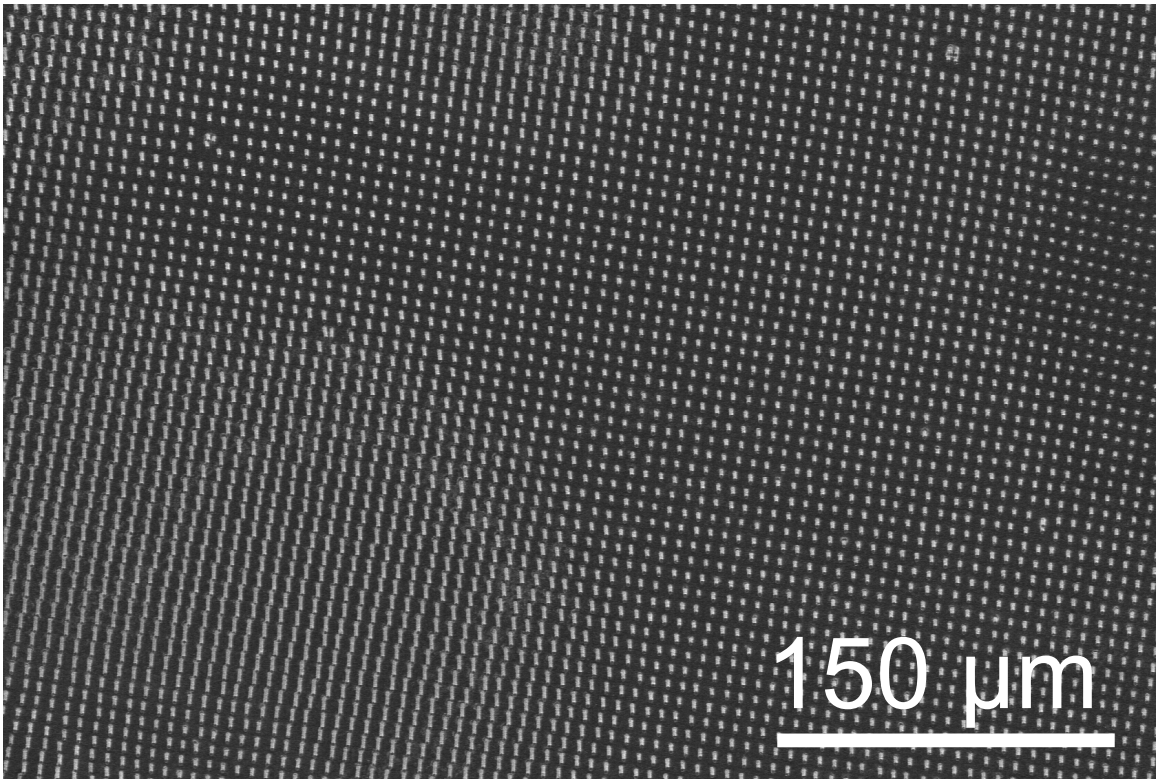


Figure 3.2: Overview of an infilled wire array.

## 3.2 Ni Nanoparticle Direct Contact

After embedding the arrays, the exposed wire tips were coated with ohmic nickel nanoparticle (Ni np) contacts. These nps were formed on the Si wires by immersing the Si in an aqueous solution of nickel chloride, sodium hypophosphite, and sodium succinate (Nickelex, Transene, Inc). The hypophosphite is oxidized at the semiconductor surface, allowing the $Ni^{2+}$ ions to scavenge the resulting electrons and to nucleate on the semiconductor. The temperature of the solution and the deposition time were varied in order to optimize the Ni np coverage. At 80°C, the oxidation occurred selectively at the wire edges, as seen in Figure 3.1. The edge sites likely catalyze the oxidation reaction. By limiting the deposition

time to 30 sec under these conditions, Ni nps could be made to line the edges of the wires without obstructing the wire tops or sidewalls, an important advantage for coupling light into the Si wire solar cells.

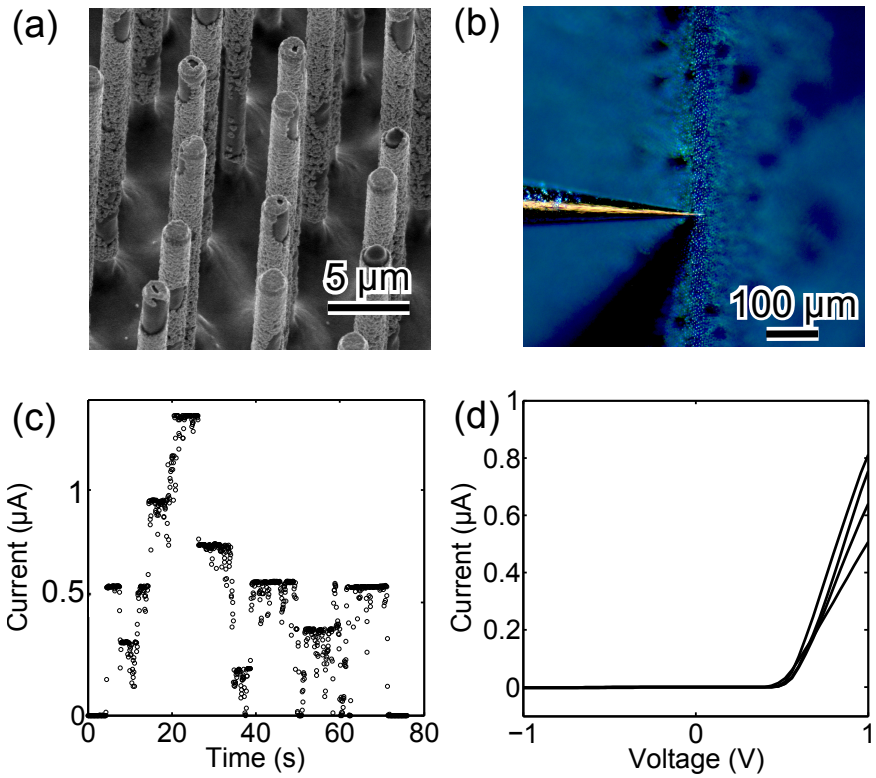


Figure 3.3: Measuring the Si/Ni resistance with a nanoprobe. (a) An array of embedded wires fully coated with Ni nanoparticles. (b) The nanoprobe making contact to a small group of nanowires. (c) Current vs. time for an applied bias of 1V as the nanoprobe is moved into and out of the wire array. The current plateaus correspond to a finite number of wires in contact with the probe. (d) Current vs. voltage curves as measured by the nanoprobe. The top two curves have five wires contacted while the middle curve has four in contact and the bottom curve has three wires in contact.

In order to measure the series resistance of the Ni/Si contact, polymer infilled Si wires with diffused p-n diodes were fully coated with Ni nps by immersing them in the electroless Ni solution for 75 sec, as seen in **Figure 3.3 (a)**. Ga/In was scribed into the wafer for a back contact and groups of wires were contacted with a nanoprobe (miBot Micromanipulators, Imina Technologies). The probe was moved to approach the wires by eye under an optical microscope (Figure 3.3 (b)). When the probe was deemed to be sufficiently close to the

array, a bias of 1 V was applied, and the current was measured as a function of time as the nanoprobe was slowly moved towards the sample in ∼100 nm steps. A jump in current could be seen each time an additional wire was contacted, as shown in Figure 3.3 (c), where the probe was repeatedly moved into and out of the array. After confirming that the device current and hence the contact were stable, the probe voltage was swept from -1 to 1 V and the current was recorded, leading to the traces seen in Figure 3.3 (d). The number of wires that were contacted was estimated by counting the number of discrete steps in the current vs. time curves needed to achieve the current seen at 1 V in the current-voltage plot. The series resistance of the devices was then calculated by performing a linear fit to the 0.6 to 1 V range. Given this resistance, the number of wires estimated to be in contact, and the spacing between wires (7 $\mu$m), the Ni/Si contribution to the wire sheet resistance was estimated to be:

$$R_{sheet} = R_{measured} * \#ofwires * (7\mu m)^2 = 1.38 \pm 0.03\Omega \text{ cm}^2.$$

After measuring the sheet resistance, single wires were removed from the growth substrate and dispersed on a heavily doped ($\rho$ = 0.02 Ωcm) Si substrate. The end of a wire was then removed with a focused ion beam (FIB) (FEI, Nova 600) at 30 kV and 30 pA as seen in **Figure 3.4** in order to investigate the Ni/Si interface. The Ni appears to make continuous contact to the Si with no apparent interface layer, though TEM will be needed to confirm.

## 3.3 Ag Nanowires

Immediately after plating Ni nps onto the wires, Ag nws (Cambrios ClearOhm$^{TM}$) were dropcast onto the embedded array to form an interconnected top contact. Xu and Zhu (93) demonstrated conductive and stretchable Ag nw networks by embedding the Ag nws in the top layer of a film of PDMS, and our approach is thus analogous to their technique. As seen in Figure 3.1, the Ag nws wrap around the Si wires, forming good mechanical contact to the Ni nps. Optical properties of the silicone polymer on glass and Ag nws on polymer on glass can be seen in **Figure 3.5**. Transmission and reflection values were obtained with integrating sphere measurements, and the remainder of the light was assumed to be absorbed. The Ag nws absorb mildly in the blue (< 10% at 400 nm) near their plasmon

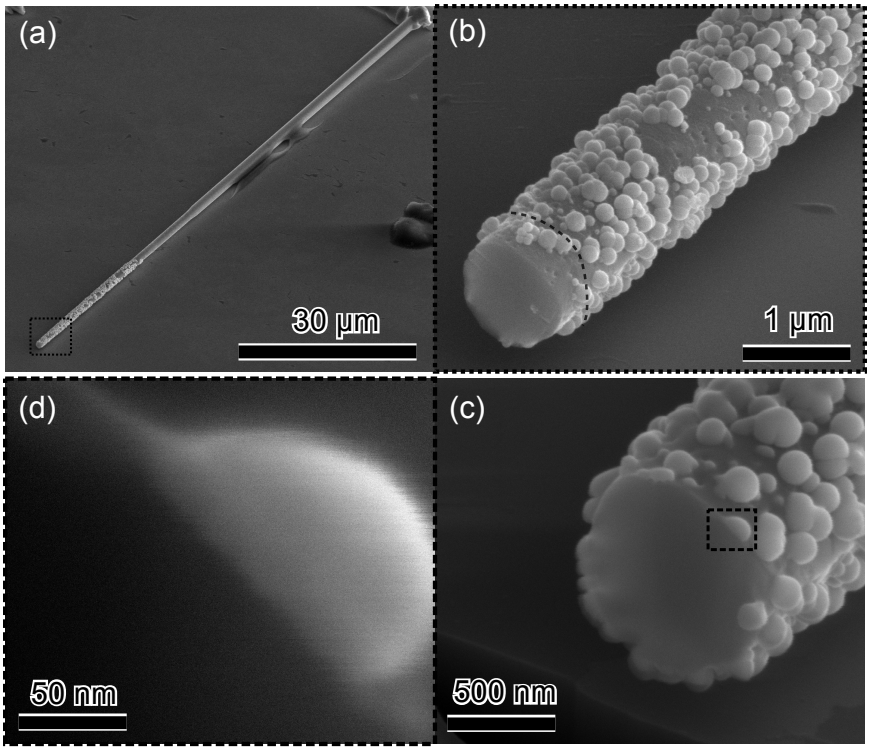


Figure 3.4: Examining the Ni/Si interface. (a) SEM of a Ni coated wire on a Si substrate. The area surrounded by the dotted box is magnified in the next panel. (b) Close up of the wire tip. The dotted line signifies the extent of the FIB cut. (c) The wire after being cut. The area within the dotted box is magnified in the next panel. (d) Close up of the Ni/Si interface.

resonance,(100) but otherwise transmit broadly across the spectrum. Reflection losses come from the polymer/air/glass index contrasts. The Ag nw dispersion on polymer on glass had a sheet resistance of 10 $\Omega/\square$, as measured with a four point probe.

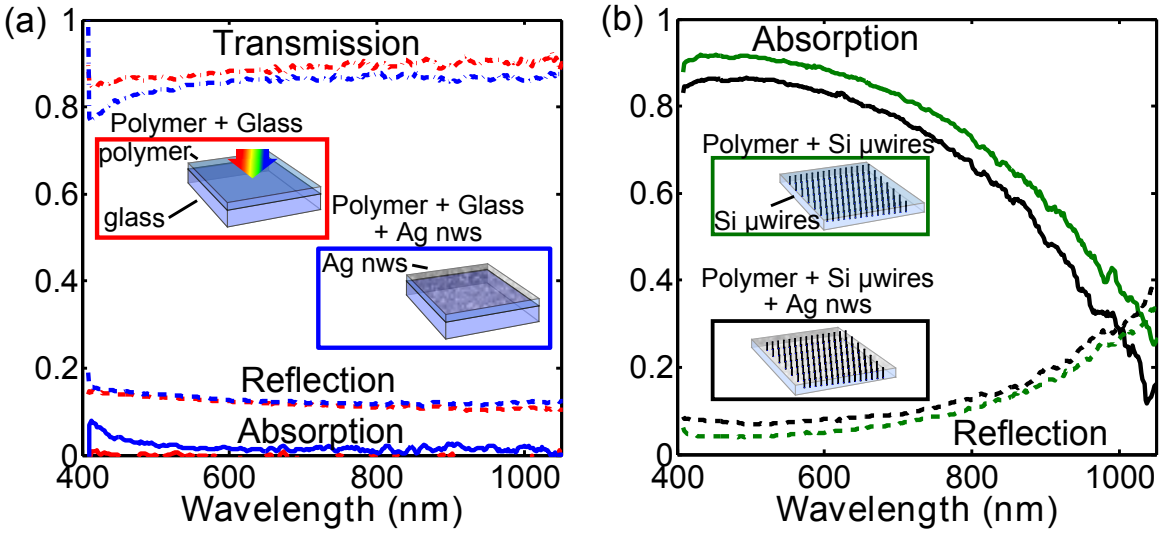


Figure 3.5: Optical properties of the contact components. (a) Transmission, reflection, and absorption for silicone polymer coated glass slides and Ag nw coated polymer covered glass slides. (b) Transmission and reflection for polymer embedded Si wire arrays and Ni np and Ag nw contacted polymer embedded arrays.

The optical properties of polymer embedded Si wire arrays with and without the Ni np and Ag nw contact layer are also contained in Figure 3.5. These arrays were removed from the Si wafer growth substrate by mechanical force with a razor blade, leaving free-standing polymer/wire films. The films were placed on a glass coverslip to keep them flat during integrating sphere measurement. While the measured absorption of the Si wire/Ni np/Ag nw structures are a convolution of absorption from all three of the materials, the absorption profile looks identical to the profile of the Si wires alone, suggesting that the Ag and Ni do not have a large impact on the overall device behavior. The absorption falls by $\sim 10\%$ across the spectrum due to reflection losses introduced by the Ni nps and Ag nws. The Ag nw films are denser on the Si arrays than on the planar polymer coated substrate due to their three-dimensional morphology, leading to higher reflection losses.

## 3.4 On Substrate Performance

In parallel to optical measurements, the current-voltage behavior of wires still on the Si substrate was measured. The wires at the substrate edge were mechanically removed to minimize shunting to the substrate through Ag nws at the edges, and Ga/In was scratched into the wafer to form a back contact. The electrical characteristics of an exemplary sample are shown in **Figure 3.6**. For the purpose of calculating the current density and the series resistance, light beam induced current (LBIC) maps of the device were fed into image analysis software (ImageJ) to set the active area perimeter and to calculate the area. Internal inactive areas (e.g. the small dark spots seen in Figure 3.6 ) were included in the total area. The lower right corner of the device is not contacted as the dropcast polymer completely covers the Si wires in that region. The characteristics of the device are outlined in **Table 3.1**.

Table 3.1: AM 1.5G electrical characteristics of an on-substrate, Ni np/Ag nw contacted Si wire array solar cell.

| Area ($cm^2$) | $J_{SC}$ ($mA/cm^2$) | $V_{OC}$ (V) | Fill Factor (%) | Efficiency (%) | $R_{shunt}$ ($\Omega cm^2$) | $R_{series}$ ($\Omega cm^2$) |
|---|---|---|---|---|---|---|
| 0.103 | 10.0 | 0.505 | 55.5 | 2.80 | 445 | 14.0 |

The series resistance ($R_{series}$) was calculated from the slope at open circuit voltage and and the shunt resistance ($R_{shunt}$) was calculated from the slope at short circuit. Though the overall conversion efficiency is low, at 2.8%, the $V_{OC}$ and $J_{SC}$ can be improved by adding surface passivation and $Al_2O_3$ scattering particles to the wires. In contrast, the fill factor (55.5%) and series resistance (14.0 $\Omega$ $cm^2$) are direct results of the Ni np/Ag nw contacting scheme. The series resistance is likely dominated by the Ni np/Si wire contact. While this resistance was found to be 1.38 $\Omega$ $cm^2$ for wires fully coated with Ni, the measured device has $\sim$ 10 times fewer Ni nanoparticles, leading to the higher resistance. In contrast, the Ag nws contribute at most $\sim$ 1 $\Omega$ $cm^2$ to the overall series resistance (10 $\Omega/\square$ over $\sim$ 0.1 $cm^2$) and the resistance due to transport through the emitter (doped $\sim$ 1 x $10^{19}$ $cm^{-3}$) and base are negligible. The Ag nw/Ni np contact may also be a bottleneck. Optimization of the Ni nanoparticle coverage or annealing the devices may lower the sheet resistance and increase

the fill factor.

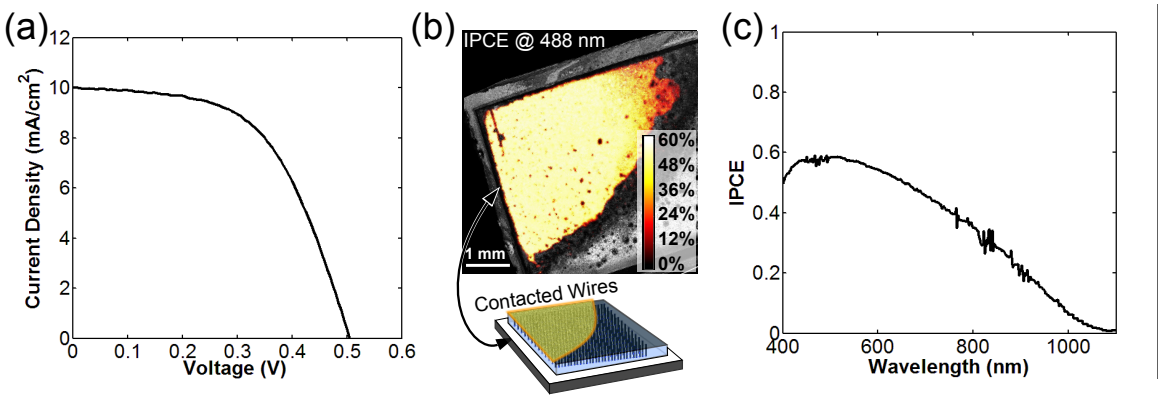


Figure 3.6: Electronic properties of an on substrate Ni np/Ag nw embedded Si wire array solar cell. (a) AM 1.5G current-voltage curve. (b) Incident photon to current efficiency (IPCE) profile map at 488 nm showing the extent of carrier collection. The IPCE map is overlaid on a reflected confocal image. The cartoon demonstrates the contacted area of the device. The Si wires in the lower right corner of the device are completely covered with polymer and hence are not contacted. (c) IPCE across the AM1.5G spectrum.

The incident photon to conversion efficiency (IPCE) curve of Figure 3.6 has a similar shape to the absorption profiles of Figure 3.5, suggesting that most of the aforementioned absorption can, in fact, be attributed to the Si wires. The difference between the IPCE and absorption curves is likely due to the finite diffusion length within the wires which will lead to recombination losses rather than current collection. Additionally, the substrate (not present in the integrating sphere measurements), will absorb some of the light, though it is degenerately doped and thus will not appreciably contribute to the IPCE as any generated carriers will rapidly recombine. Also of note, despite the evident scratch on the upper left hand corner of the sample in Figure 3.6, the shunt resistance is large and the rest of the device collects photocurrent uniformly. In contacting 100,000s of Si nanowires all in parallel, the loss of individual devices does not substantially decrease the overall device performance, in contrast to a defective area in a monolithic cell.

### 3.4.1 Comparison to Indium Tin Oxide Contacts

To compare the Ni np/Ag nw contacting scheme to a more conventional contact for thin film solar cells, 20 nm of Indium Tin Oxide (ITO) ($\rho \approx 7$ x $10^{-4}\Omega$ cm) was sputtered onto

an infilled wire array. The ITO was sputtered onto the wires at room temperature with RF magnetron sputtering under a 1.29% $O_2$, 98.71% Ar plasma at 3 mTorr and 200 W of power. The optical properties of the ITO may be found in the supplementary information of (34). The ITO readily fractured in the polymer infilled area between Si wires and hence Ag nws were spun onto the ITO coated array in order to make contacts over large areas, with the ITO serving to make localized contact to the Si. The cell had comparable performance to the device in Figure 3.6, as shown in **Table 3.2** and **Figure 3.7** with an efficiency of 2.51%, a fill factor of 54.6%, and a series resistance of 9.27 $\Omega$ cm$^{-2}$. However, in some regions the Ag nws fractured along with the ITO, leading to inactive areas, and thus the ITO based contact proved to be less robust than the Ni np scheme and hence was not pursued further.

Table 3.2: AM 1.5G electrical characteristics of an on-substrate, ITO/Ag nw contacted Si wire array solar cell.

| Area ($cm^2$) | $J_{SC}$ ($mA/cm^2$) | $V_{OC}$ (V) | Fill Factor (%) | Efficiency (%) | $R_{shunt}$ ($\Omega cm^2$) | $R_{series}$ ($\Omega cm^2$) |
|---|---|---|---|---|---|---|
| 0.2658 | 10.5 | 0.437 | 54.6 | 2.51 | 448 | 9.27 |

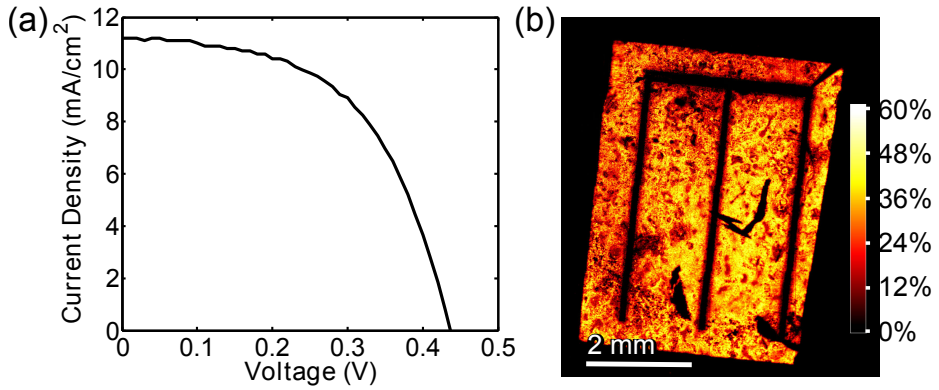


Figure 3.7: Electronic properties of an on-substrate ITO/Ag nw embedded Si wire array solar cell. (a) AM 1.5G current-voltage power curve. (b) Incident photon to current efficiency (IPCE) profile map at 488 nm showing the extent of carrier collection.

### 3.4.2 Thermal Imaging of Shunts

Shunts in solar cells and heat transfer in wires can be visualized through thermal imaging.(101; 102) Under reverse bias, current preferentially flows through the shunt pathways, causing those areas to heat up. To image shunt pathways in a large area wire array cell, the cell was biased and imaged with a FLIR ThermaCAM S6000, resulting in the images shown in **Figure 3.8**. Clear temperature changes and local hot spots were visible, but, unfortunately, the resolution of the camera was not sufficient to make out individual wires. The wires measured in Figure 3.8 were from an early device by Dr. Brendan Kayes. Ag nw/Ni np contacted cells were never imaged due to the limitations encountered when attempting to measure Dr. Kayes' cells.

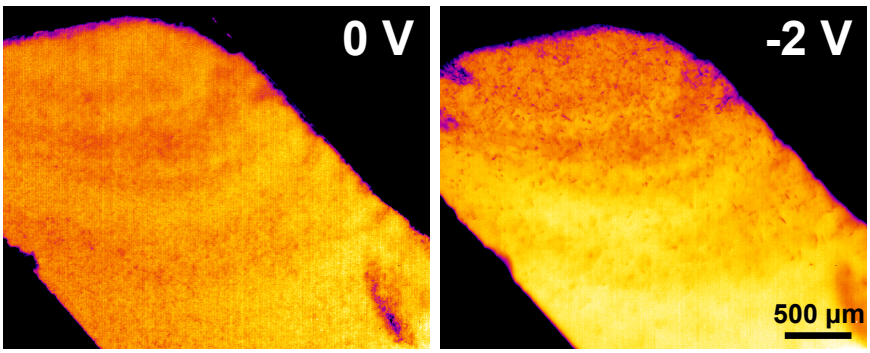


Figure 3.8: Thermal images of a large area Si wire array. (left) Cell at 0 V forward bias. The average temperature is 23.3-25.3°C. (right) Cell at -2 V bias. The average temperature is 45.9-49.9°C.

## 3.5 Peeled Off Cells

Finally, polymer embedded, Ni np/Ag nw contacted Si wire arrays were peeled off of the growth substrate with a razor blade and Au was evaporated on the back to make a free standing, flexible device. A Ag busbar was also added to aid in making contact with an electrical probe. **Figure 3.9** shows LBIC maps and current-voltage curves of the device on and off of the growth substrate. The photoresponse of individual wires can be made out in the magnified region. The ratio of individual wires contacted (as evidenced by a $\sim 3\mu m$ diameter bright spot in the LBIC map) to the total number of wires in the device (1 per 7 x 7 $\mu$m area) yielded a $> 99\%$ contact yield. The wire array electrical performance was

measured both on substrate and after peel-off, and the performance per contacted area is virtually identical before and after. However, the electrical properties are inferior to the device shown in Figure 3.6 due to the lower quality of the Si wire arrays used for this sample. The peeled off curve in Figure 3.9 was measured by flattening the wire array; it naturally rolled into a cylinder with a ∼1 mm diameter due to strain built up during the polymer curing process. This insensitivity to rolling and unrolling alludes to the robustness and flexiblity of the contact. Figure 3.9 shows the cell wrapped around a pencil with radius of 3.61 mm. Attempts to clamp the end of the peeled off film in order to controllably alter the radius of curvature resulted in the film tearing; the $\sim 100\mu m$ thick films yielded under the shear stress. Further encapsulation of the arrays will be needed to measure the performance as a function of radius of curvature and number of cycles of rolling and unrolling.

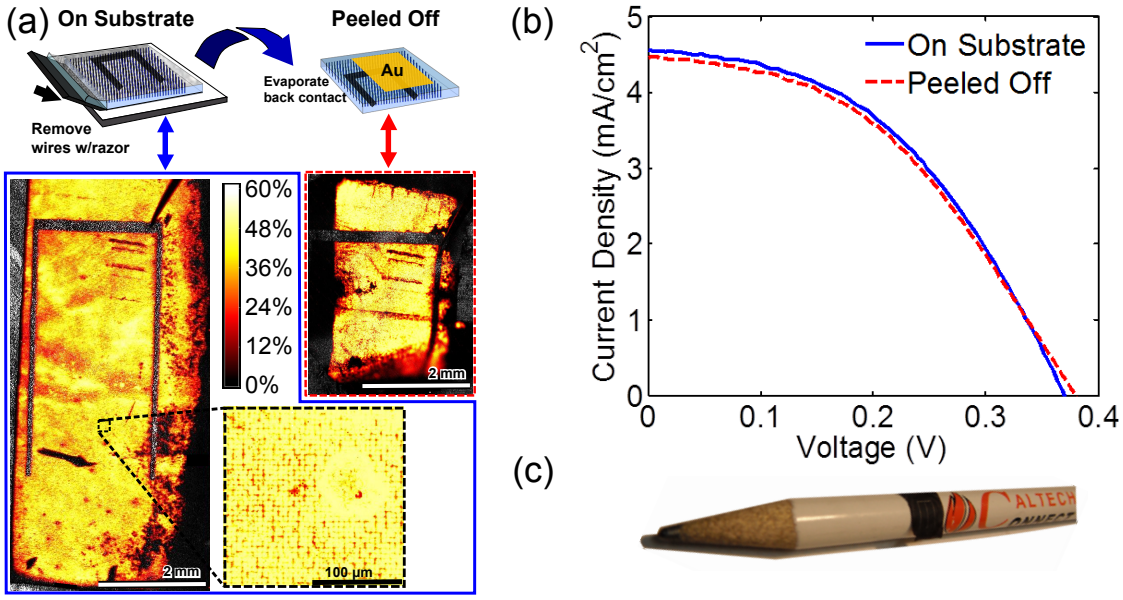


Figure 3.9: Performance of a peeled off wire array. (a) (above) Diagram showing the peel off and back contacting of wire arrays embedded in polymer. (below) IPCE map at 488 nm for a cell on and off the substrate showing the high contact yield both before and after the peel off step. (b) AM 1.5G current-voltage curve for the cell on substrate and peeled off. (c) Peeled off cell wrapped around a pencil demonstrating the device flexibility.

## 3.6 Summary and Outlook

In conclusion, a two step contacting process of Ni nps and Ag nws led to flexible, transparent contacts for use with Si wire arrays and other inorganic materials. Flexible Si wire array solar cells had conversion efficiencies of up to 2.80%, fill factors of up to 55.5%, and series resistances of 14.0 $\Omega$ cm$^2$. Optimization of the Ni np coverage and attempts to anneal the contacts or to "plasmonically weld" (100) them may improve the cell performance. In this "welding" process, the contact is illuminated with high power white light which couples to plasmonic modes at the Ag nw junctions and, hopefully, at the Ni np/Ag nw interfaces, creating high fields and localized heating. The heating will then fuse the metals together to create a lower resistance contact. Full field optical simulations could help with understanding of the Ni np absorption and reflection properties. Experimentally, illuminated the contacts with $\sim$ 1 W/cm$^2$ did not alter the performance and illumination with $\sim$ 1 W/cm$^2$ of 496 nm laser light created a large barrier resistance, likely due to oxidation of the Ni nanoparticles. Thus, an oxygen free atmosphere may be needed to realize plasmonic welding for these contacts.

Though n-Si was contacted through this scheme, Ni is also an ohmic contact for p-Ge, p-Si, n-InGaAs, p-InGaAs, n-InP, n-InSb, and p-SiC, making this technique broadly applicable to a variety of other inorganic semiconductors.(17) A number of other metals can also be readily deposited via electroless deposition, further expanding the range of accessible materials. Deposition along crystal edges, as seen with the Ni nps, should be possible with other micro- or nano-structured semiconductors. Electroless metal deposition on materials may also prove useful for exploring their absorption profiles or may act to selectively deposit catalysts for electrochemical reactions. Overall, this contacting paradigm should be broadly applicable to a wide array of inorganic device geometries and need not be limited to solar applications (i.e. LEDs, transistors, etc. could also take advantage of this scheme).

# Chapter 4

## GaP on Si

### 4.1 Motivation

The demonstration of Si diffusion lengths on the order of 10 $\mu$m and the development of large area Si wire array cells led to the possibility of high effiency multijunction wire array structures. Nominally, heterostructure wire arrays may be fabricated regardless of material quality. However, multijunctions will only outperform their single junction counterparts if each cell is able to perform at a high level. For example, combining a 20% efficient GaAs cell ($V_{OC}$ = 0.9V, $J_{SC}$ = 25mA/cm$^2$, and $FF$ = 89%) with an 11% efficient Ge cell ($V_{OC}$ = 0.3V, $J_{SC}$ = 50mA/cm$^2$, and $FF$ = 75%) leads to a 23% efficient tandem ($V_{OC}$ = 1.2V, $J_{SC}$ = 25mA/cm$^2$, and $FF$ = 77%), an improvement over the stand alone performance of either cell, but still well below the single junction efficiency of GaAs.

Multijunctions not only allow for greater than 30% efficiencies, as will be discussed in the next chapter, but also lead to devices with high voltages, an important requirement for solar photoelectrochemistry (PEC).(103) Solar PEC offers a solution to the challenge of storing solar power. Even if solar module costs drop down to the level of grid parity, solar generated electricity will still not be able to provide more than 20% of the total power for the U.S. due to the variability of sunlight.(104) Long term, low cost, grid scale power storage systems are currently lacking. However, generating fuels such as $H_2$ or syngas ($CO + H_2$) instead of electricity gives flexibility to the power generation process; the fuels can be converted to energy when needed. Additionally, by converting $CO_2$ and water to syngas, excess $CO_2$ is pulled out of the air, helping to mitigate problems caused by this greenhouse gas.(105)

Water splitting ($H_2O \rightarrow H_2 + O_2$) requires at least 1.7 V, including overpotential require-

ments, to drive 10 mA/cm$^2$ and carbon dioxide reduction ($CO_2 + H_2O \rightarrow CO + H_2 + O_2$) requires well over 2 V.(89) Thus, Si alone cannot provide this photovoltage. Higher bandgap materials may be used instead, but due to the limited photon flux in the ultraviolet regime of the solar spectrum, overall device efficiencies and product yields will be low. Tandem structures offer higher voltages and appreciable currents, allowing for greater overall efficiencies despite the voltage constraints.

While wire heterostuctures are not new, previous work has primarily been limited to Si/Ge systems or to III-Vs, and their architectures have been simple radial or coaxial superlattices.(42; 106; 107) Dr. Ross at IBM fabricated Si on GaP or Si/Ge/GaAs axial structures, but only in thin layers and not with the explicit intent of forming active devices.(108) For photoelectrochmical devices, Hwang et al. (109) and Shi et al. (110) used $TiO_2$ on Si wires to generate $H_2$. However, the bandgap of $TiO_2$ is too large to generate appreciable photocurrent from the solar spectrum.

When considering the materials requirements for photoelectrochemistry and for growing heterostructures with a limited number of defects, GaP stands out as an ideal mate for Si wire arrays. GaP is lattice matched to Si, has a large enough bandgap, 2.32 eV, to give the desired voltages in combination with Si, and has been used to reduce both $CO_2$ and $H_2O$.(111–113) Additionally, GaP's material properties have been explored extensively due to its use in light emitting diodes,(114) it can be doped both n-type and p-type,(115; 116) and epitaxial growth on Si has been achieved.(117–127) Thus, we set out to develop GaP/Si wire tandem photoelectrodes.

## 4.2 Device Overview

While a number of different GaP on Si wire array morphologies can be imagined, initial exploration focused on understanding the simplest and most straightforward to fabricate: a Si wire array conformally coated with GaP, as seen in **Figure 4.1**. The GaP shell is assumed to have a built-in p-n junction while the Si wire may be highly doped to serve as a back contact to the GaP or may also include a p-n junction, thus creating a multijunction cell. As seen in the band-diagram in Figure 4.1, the conduction band of Si is theoretically aligned with the conduction band of GaP (the electron affinity difference between the two materials is $0.1 - 0.25$ eV),(89) allowing for ready transfer of electrons between the two. In reality, band offsets at interfaces deviate significantly from those that would be expected

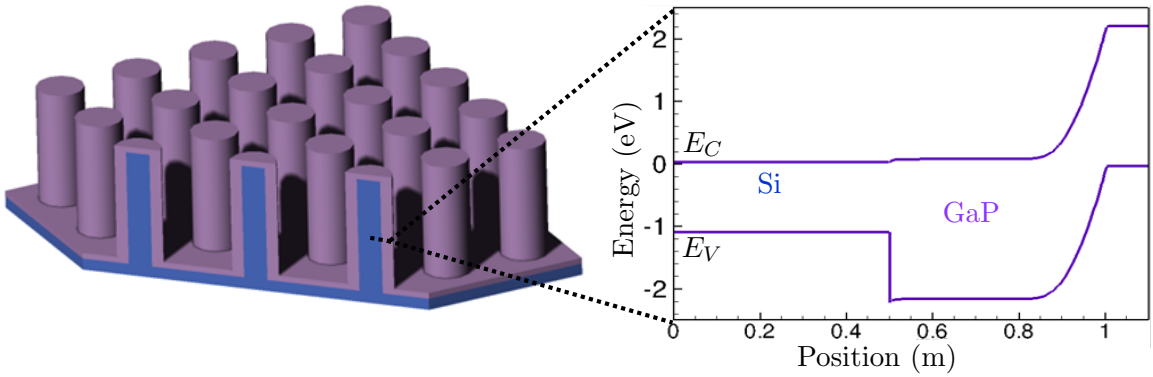


Figure 4.1: GaP/Si device overview and band diagram.

from a simple affinity argument due to charge transfer and dipole formation at the interface. Barriers due to band misalignment at the heterojunction may be mitigated through high doping densities, leading to enhanced tunneling through band spikes.

For stand alone GaP devices, an n+ Si/n GaP/p+ GaP architecture was considered. For tandem devices, a tunnel junction may be formed for either p Si/n+ Si/p+ GaP/p GaP/n+ GaP cells or for n Si/p+ Si/n+ GaP/n GaP/p+ GaP devices. The voltage drop across the tunnel junction will likely be lower for the latter case due to the aforementioned alignment.

## 4.3 Optoelectronic Modeling

### 4.3.1 GaP/Si Full Field Optical Modeling

Integrating the AM 1.5D solar spectrum above the bandgap of GaP leads to a potential photocurrent of 8.0 mA/cm$^2$. Si, on the other hand, has 39.4 mA/cm$^2$ of above bandgap photons available. Thus, even if the outer layer of GaP absorbs all of the available above bandgap light, it will still limit the current of the device. Extending this thinking along the continuum of potential bandgaps, **Figure 4.2** demonstrates regions in which either the top or bottom cell limit the overall device performance. In the upper left corner, the low bandgap core limits the current. In the lower right corner, the high bandgap shell limits the efficiency.

In order to design an outer GaP layer that absorbs as much light as possible and thus maximizes the device performance, the effect of GaP thickness and morphology on absorption were studied through full field, electromagnetic simulations. Finite-difference-

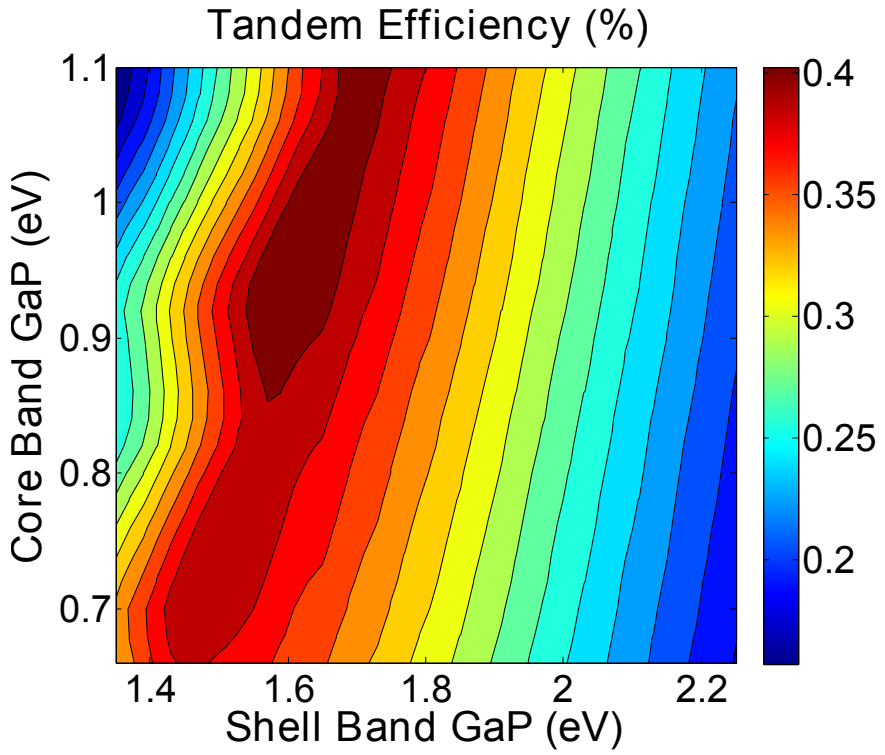


Figure 4.2: Isoefficiency contour plot as a function of core and shell bandgaps.

time-domain (FDTD) simulations with a two dimensional GaP on Si grating gave a rough estimate of the absorption that could be expected for a wire array. The Si core was 1 $\mu$m thick and 20 $\mu$m tall with a 7 $\mu$m center to center spacing. The GaP thickness was varied from 0.5 to 2 $\mu$m in 0.5 $\mu$m increments, as seen in **Figure 4.3 (a)**. Boundary conditions for the top, sides, and bottom were fully absorptive (PML), periodic, and fully reflecting, respectively. Optical constants were taken from Aspnes and Studna (128). A plane wave source at a varying wavelength and incident angle was used for excitation. The power absorbed in the GaP at each wavelength was calculated and normalized to the incident power. Both transverse electric (TE) and transverse magnetic (TM) polarizations were considered, and the two results were averaged.

As seen in Figure 4.3 (b), the outer GaP layer absorbed up to 80% of the above-band gap incident power, with losses primarily due to absorption by the Si core and by reflection, especially at normal incidence where much of the light misses the GaP entirely, simply traveling in between the GaP structures and reflecting back out of the grating. The location of the direct transition in GaP is evidenced by the rapid increase in absorption at shorter wavelengths.

A full three-dimensional, periodic wire array was also simulated. This structure consisted of a 1 $\mu$m diameter, 10 $\mu$m tall Si wire with a 0.5 $\mu$m thick GaP shell, a 7 $\mu$m pitch, and the same boundary conditions used above. Computational limits restricted the device geometry and only allowed for normal incidence to be considered. These conditions give a lower bound for actual absorption, as typical wires can be up to 100 $\mu$m long, can have GaP coatings of more than a micron, and have maximized absorption at oblique angles of incidence. As a point of comparison, the exponentially decaying Beer-Lambert absorption expected for a wire array was also calculated. The results are shown in **Figure 4.4 (a)**.

At 400 nm, where the GaP absorption coefficent is large, the full field absorption cross section is larger than would be expected from mere geometric, Beer-Lambert considerations. The size of the structure is on the order of the wavelength of the incident light, and the high index of the GaP and Si direct light into the wire. This phenomenon of a larger absorption cross section than would be expected from simple geometric considerations is well know, for example, for small Mie scatterers.(129)

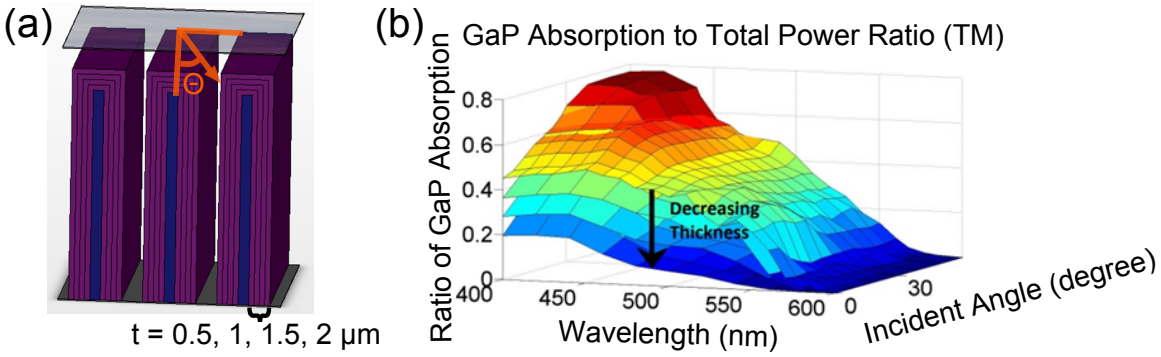


Figure 4.3: Simulations of GaP on a Si grating. (a) Simulation overview. (b) The GaP on Si grating absorption as a function of wavelength, angle, and GaP thickness.

At 500 nm, however, the GaP absorbs less than would be expected from Beer-Lambert theory. This loss of power in the GaP corresponds to an increase in the Si absorption; the GaP refracts and focuses the incident beam, channeling light into the higher index Si core. This Si absorption enhancement extends over much of the spectrum. Thus a relatively thick GaP layer is required to maximize shell absorption before light is lost to the Si core.

In order to further explore the channeling of light into the higher index Si core, two dimensional full field simulations were conducted on the radial cross section of the wire.

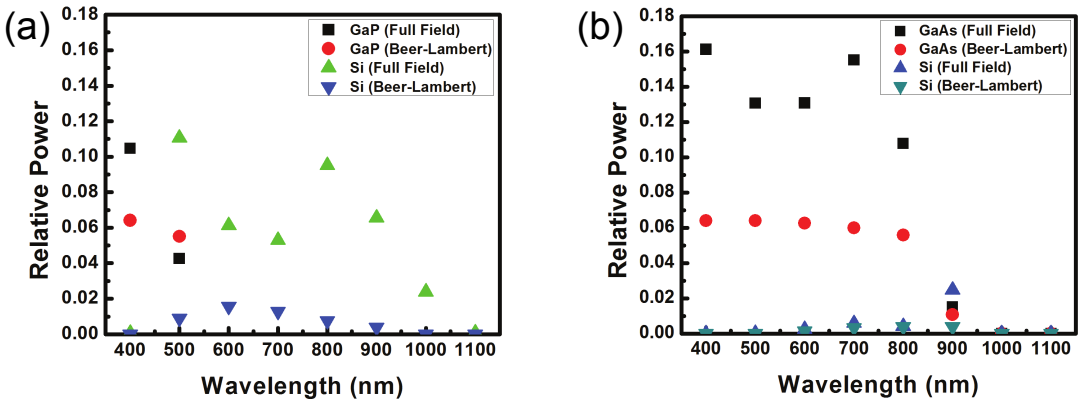


Figure 4.4: Normal incidence (a) GaP/Si and (b) GaAs/Si wire array absorption. Relative power refers to the amount of power absorbed in the listed material as normalized to the total incident power.

Radial absorption becomes relevant if $Al_2O_3$ scattering particles or other optical elements are incorporated into the array to boost scattering parallel to the substrate. A plane wave source, periodic side boundary conditions, a perfectly reflecting bottom, and a perfectly absorbing top were again used. The Si wire was left at 1 $\mu$m and the GaP thickness was varied as before.

Beer-Lambert and full field generation profiles at 500 nm are shown in **Figure 4.5**. The full field profiles clearly show focusing into the Si wire core. A comparison of the power absorbed as a function of wavelength further elucidates the striking difference between the Beer-Lambert and full field values (**Figure 4.6**). The Beer-Lambert model shows the power absorbed in the Si core decreasing consistently as the GaP shell thickness decreases. The full field values, on the other hand, remain high, as the GaP continues to direct light into the Si core.

Overall, the optical simulations suggest that making a GaP/Si tandem wire array will be difficult. Due to the higher index of the Si and the indirect bandgap of GaP, a thick GaP coating will have to be used in order to get reasonably high photocurrents and prevent the light from being absorbed by the Si. However, experimentally measured diffusion lengths of GaP are low, on the order of 100 nm,(130) suggesting that thick layers alone will not be enough. Instead the GaP will have to be highly structured in order to extract photogenerated carriers before they recombine.

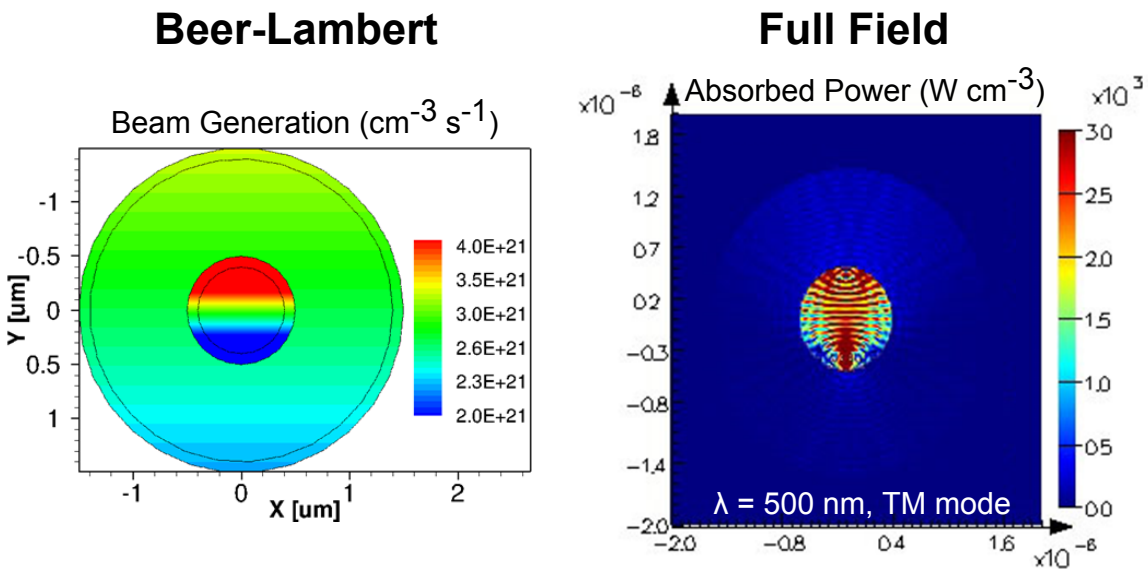


Figure 4.5: Comparison of Beer-Lambert and full field radial optical absorption for GaP/Si wire cross sections.

### 4.3.2 GaAs/Si Optical Modeling

In order to circumvent the severe current mismatch of the GaP/Si material system and the aforementioned conflict between optically thick material requirements and collection lengths, GaP may be alloyed with N or As to create a direct gap material and to lower the bandgap, potentially even to the point of reaching a current matched system.(131–134) GaAsP is a typical ternary alloy. When alloyed with nitrogen, the localized nitrogen states coalesce in to a band, which in turn anticrosses with the conduction band and leads to a smaller, direct bandgap. **Figure 4.7 (a)** demonstrates the relationship between alloy bandgap and lattice constant. By altering the N, P, and As ratios, GaNPAs can remain lattice matched to Si over a broad range of bandgaps. In the lab, GaNPAs has been the source of some study, but so far the material quality has been poor, with diffusion lengths at most on the order of 1 $\mu$m due to hydrogen and carbon incorporation during growth.(135; 136) However, recently, GaAsP single wire cells have been fabricated with >10% efficiencies.(137)

As GaNPAs compounds have a smaller, direct band gap and thus would enable a high efficiency, multijunction, Si wire array-based heterostructure, GaAs was also tested as a potential shell material in the wire geometry. GaP and GaAs provide useful bounds for the

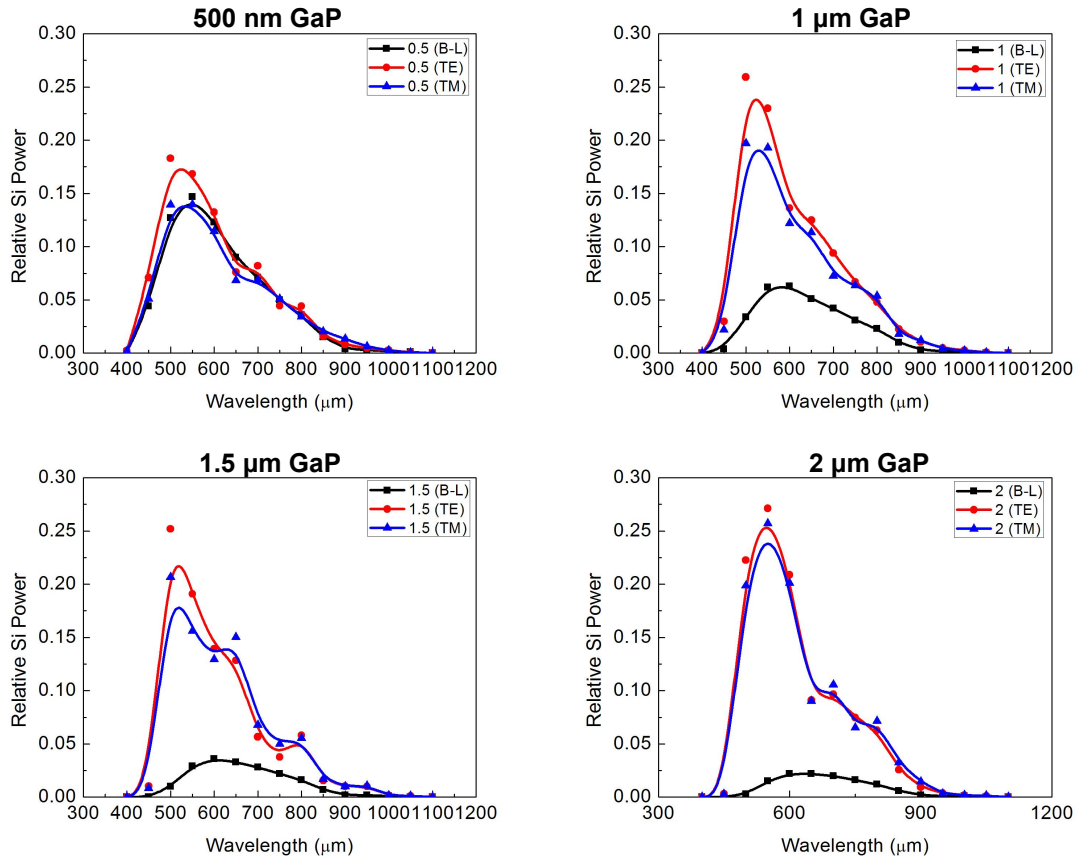


Figure 4.6: Comparison of Beer-Lambert (B-L) and full field optical absorption (TE and TM) as a function of wavelength and GaP thickness for a radial cross section of a GaP on Si wire.

behavior of GaNPAs, as their bandgaps lie on either side of those of GaNPAs, and GaNPAs can be either direct or indirect gap depending on the composition.

GaAs was tested as a shell material in an identical simulation setup to the previously discussed GaP on Si simulations, with only the optical constants changed. As seen in Figure 4.4 (b), the shell absorption increases drastically, and once again, the absorption cross section is much greater than the geometric, analytical value. The direct gap of GaAs is able to much more effectively absorb the incident photons, allowing the GaAs to fully collect all of the above bandgap light that falls on it rather than losing it to the Si core. Beyond the bandgap of GaAs, at 900 nm and greater, the Si benefits slightly from the GaAs channeling light into the wire core, but the Si is poorly absorbing at these wavelengths, leading to low overall collection in the wire.

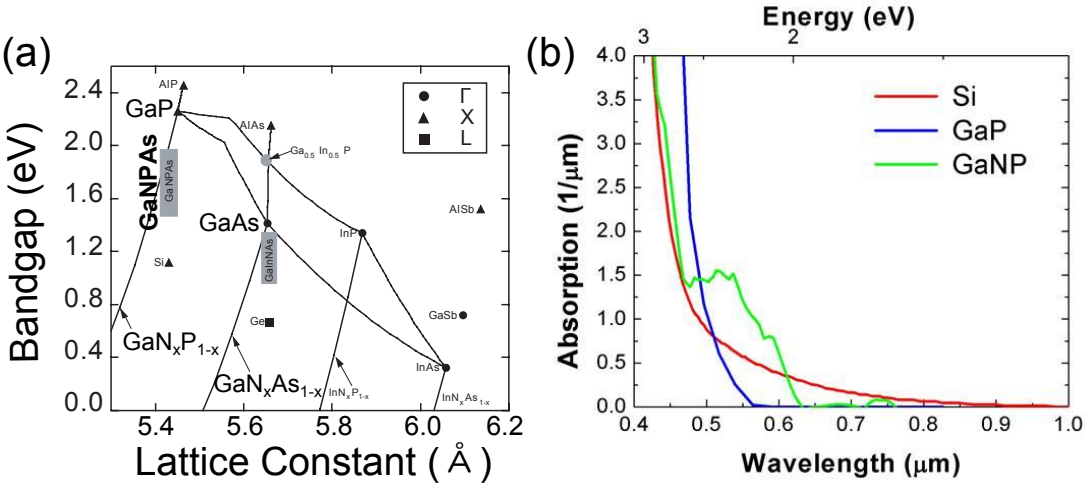


Figure 4.7: Properties of GaNPAs. (a) The bandgap of a variety of materials, including GaNPAs, as a function of lattice constant. ©IOP Publishing. Reproduced by permission of IOP Publishing. All rights reserved. (b) Optical data for GaNP courtesy of Dr. John Geisz (NREL)

Finally, the simulations at individual wavelengths were weighted by the solar spectrum and summed to give an ideal AM 1.5G photocurrent for each layer. The GaP/Si wire array generates 0.63 mA/cm$^2$ in the GaP shell and 2.60 mA/cm$^2$ in the Si core while the GaAs/Si wire array generates 4.20 mA/cm$^2$ in the shell and 0.22 mA/cm$^2$ in the core. Thus, the two structures fall on either side of current matching conditions and suggest that with an intermediate material and appropriate thickness choices, current matching should be possible. Additional light trapping techniques should also be incorporated to increase the overall absorption.

As the simulated structures were only 10 $\mu$m tall and 1.5 $\mu$m in diameter, they absorbed a very small amount of light. Real structures, with thicker layers and significantly longer wires, will likely absorb far more of the incident photons. Unfortunately, the aforementioned simulations were limited by computational power. Nevertheless, they still offered worthwhile understanding of channeling due to index contrast and an estimation for necessary layer thicknesses for full absorption, revealing the importance of direct gap outer layers. The simulations also demonstrated the enhanced absorption cross section of the wires.

### 4.3.3 GaP/Si Device Physics Modeling

When discussing the potential photocurrents from the full field simulations, the internal quantum efficiency was always assumed to be 1. However, real devices will have finite diffusion lengths due to Shockley-Reed-Hall (SRH), Auger, radiative, defect, and surface recombination. Thus, a quasi three-dimensional, GaP/Si wire array device physics model with recombination losses was created. The simulated structure was identical to that used in the three-dimensional optical simulations.

Electronically, the simulated structure consisted of a GaP radial pn junction on a degenerately doped Si support. The GaP cell had an n-type base with a doping of 1 x $10^{17}$ $cm^{-3}$ and a p-type emitter with a doping of 5 x $10^{18}$ $cm^{-3}$. The GaP thickness was varied as in the two-dimensional model. Contacts were placed on the outer GaP emitter and on either the Si or on the GaP base. The location of the base contact was found to have minimal influence on the properties of the cells as the conduction band offset between GaP and Si is small; transport through the Si and across the GaP/Si heterointerface did not inhibit the device performance. Finally, the GaP diffusion length was set by modifying the SRH lifetime in the material and the SRV was assumed to be zero. While a surface recombination velocity of zero is highly unrealistic, the intent of the model was to explore limiting efficiencies as a function of the material diffusion length.

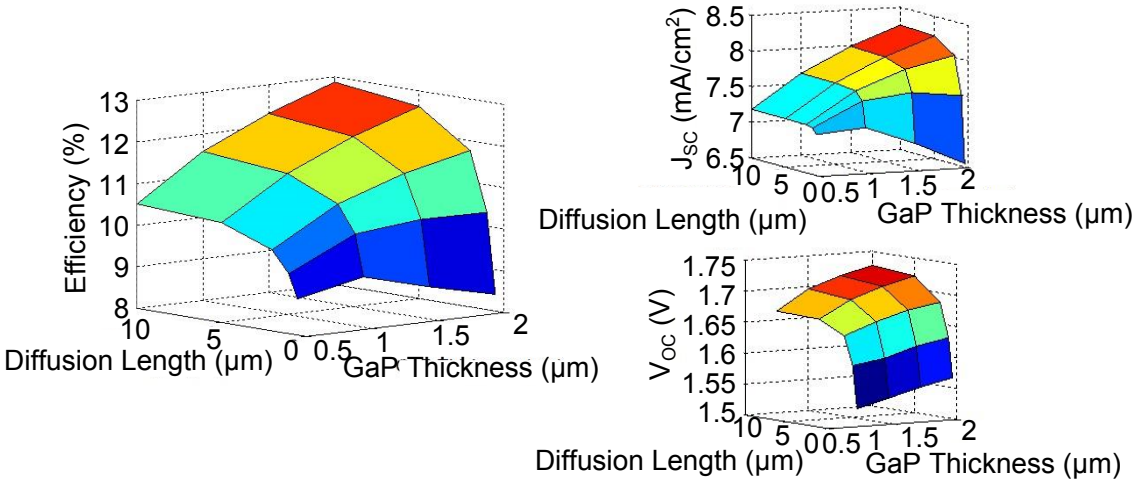


Figure 4.8: Simulated GaP/Si wire array efficiencies, short circuit current densities ($J_{SC}$), open circuit voltages ($V_{OC}$) as a function of GaP diffusion length and conformal shell thickness.

The optical absorption profile was originally assumed to follow Beer-Lambert theory, decaying exponentially into the material in accordance with the material optical absorption length. Additionally, all of the light was assumed to fall on the tops of the wires alone, leading to much higher collection than seen in the optical simulations. More realistic profiles were eventually incorporated, as will shortly be discussed, but the Beer-Lambert assumption helped to put an upper bound on potential efficiencies.

As demonstrated in **Figure 4.8**, optimal efficiencies were found for GaP thicknesses on the order of the material diffusion length, a result also seen in the modeling of Si wires.(27) While the open circuit voltage falls off directly with diffusion length, having little dependence on thickness, the short circuit current reaches a maximum value when the diffusion length is greater than the thickness, as would be expected for a radial junction geometry where generated carriers have to travel the shell thickness to be collected. The GaP thickness was capped at 2 $\mu$m in order to stay within experimentally realizable values. Overall, efficiencies of up to 13% could be achieved, though these would require intense light trapping and higher material quality than has yet been realized experimentally (10 $\mu$m in contrast to the $\sim$ 100 nm that has been measured).

As seen in the aforementioned GaP/Si optical simulations, however, the Beer-Lambert model does not provide a realistic description of the optical absorption behavior of the arrays. Thus, optical generation profiles at a variety of wavelengths were obtained from the full field simulations, weighted appropriately by the solar spectrum, summed, and the whole inserted into the device physics simulation. As the whole wire array was illuminated, much of the light failed to strike the wires and reflected out of the array without being absorbed. This led to a 0.80% efficiency for a 10 $\mu$m diffusion length and 0.5 $\mu$m GaP thickness. Scaling the Beer-Lambert model to also account for the reflection losses led to an efficiency of 0.97%. Again, light trapping is sorely needed.

### 4.3.4 AlP Window Layers

Unlike Si, with its broad array of surface passivation coatings, III-Vs are far more limited in surface passivation techniques. Often, a thin, larger bandgap, heavily doped material is grown on the III-V surface to act as a minority carrier mirror. Ideal window layers have a conduction (valence) band at the same energy as the corresponding band in the n-type (p-type) region, allowing majority carriers to exit to the circuit without a loss of potential

while reflecting minority carriers.

For GaP, AlP serves as a potential window layer.(138) It is type II with respect to GaP and will thus have a conduction band spike at the interface, but the difference is small, as seen in **Figure 4.9**. To test the efficiencies of an AlP window layer, a GaNP cell was simulated, with the use of optical data from John Geisz at NREL (Figure 4.7 (b)), and the cell capped with a 10 nm thick AlP layer, with optical data taken from Monemar (139). All other parameters were identical to those of the simulations in Figure 4.8. The surface recombination velocity was then varied and the device efficiency recorded for cells both with and without the window layer. The results, seen in Figure 4.9, demonstrate the effectiveness of the window layer. The efficiency is almost entirely decoupled from the state of the surface.

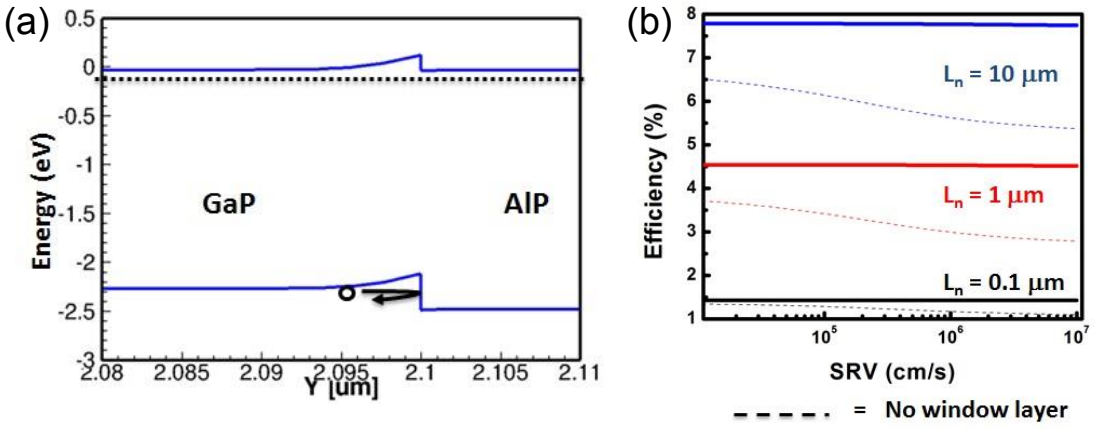


Figure 4.9: Influence of an AlP window layer on GaP on Si cell performance. (a) Band diagram showing holes being reflected from the AlP. (b) Efficiency as a function of the SRV for a GaNP cell with and without an AlP window layer.

## 4.4 Structure Growth and Characterization

Simulating a structure offers valuable physical insight, but nothing compares to actually making and measuring real devices. Thus, GaP coated wire arrays were grown and their performance was analyzed.

### 4.4.1 GaP Growth

Wire arrays were grown as described in Chapter 2 and ranged in height from 10-50 $\mu$m with 1-2 $\mu$m diameters. Metalorganic chemical vapor deposition (MOCVD) using trimethyl gallium and phosphine precursors was then used to grow GaP on the exposed wire sidewalls.(140; 141) By varying the V/III ratio during growth, the layers were made either p-type or n-type, with doping likely coming from P vacancies or interstitials. In each growth, several pieces of planar silicon were included with the wire arrays to compare growth on planar and wire array substrates.

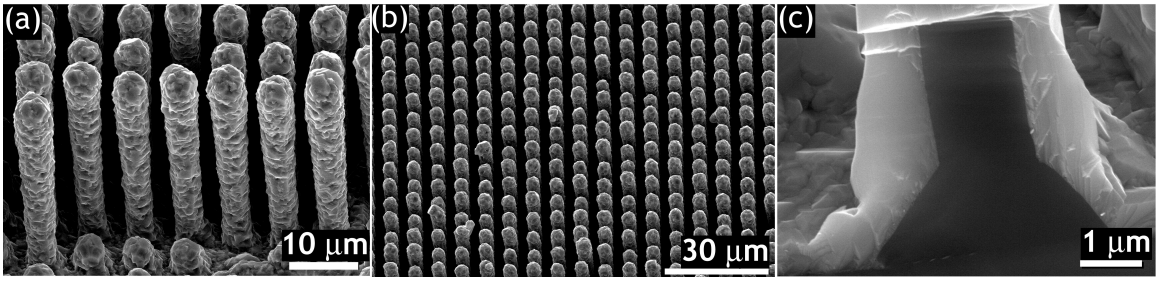


Figure 4.10: SEMs of GaP on a Si wire array.

SEM images of a GaP-coated Si wire array are shown in **Figure 4.10**. A cleaved wire shows the Si core and GaP coating in cross section. The coating was conformal and rough, both on the wire array samples and on the planar Si substrates, indicating that the roughness of the layer is caused by the polar on nonpolar epitaxial growth rather than by the nature of the substrate.(142) X-ray diffraction measurements (XRD), shown in **Figure 4.11** demonstrate that the layers are epitaxial, $< 111 >$ oriented GaP films for both the wire array samples and planar substrates, although there is a small $< 220 >$ peak arising in all the wire array samples. This peak could be a product of misoriented wires that broke off during handling of the samples.

To understand light absorption in GaP/Si arrays, the optical absorption of wires embedded in a transparent polymer and peeled off the substrate was studied with an integrating sphere. Two wire arrays were studied: a Si wire array with 1.5 $\mu$m diameter, 30 $\mu$m long wires in a square array, and a GaP-coated array grown on a Si wire array substrate with the same properties as the bare Si wire array. **Figure 4.12** shows optical absorption in both Si and GaP/Si wire arrays. The optical absorption is significantly enhanced by the addition of

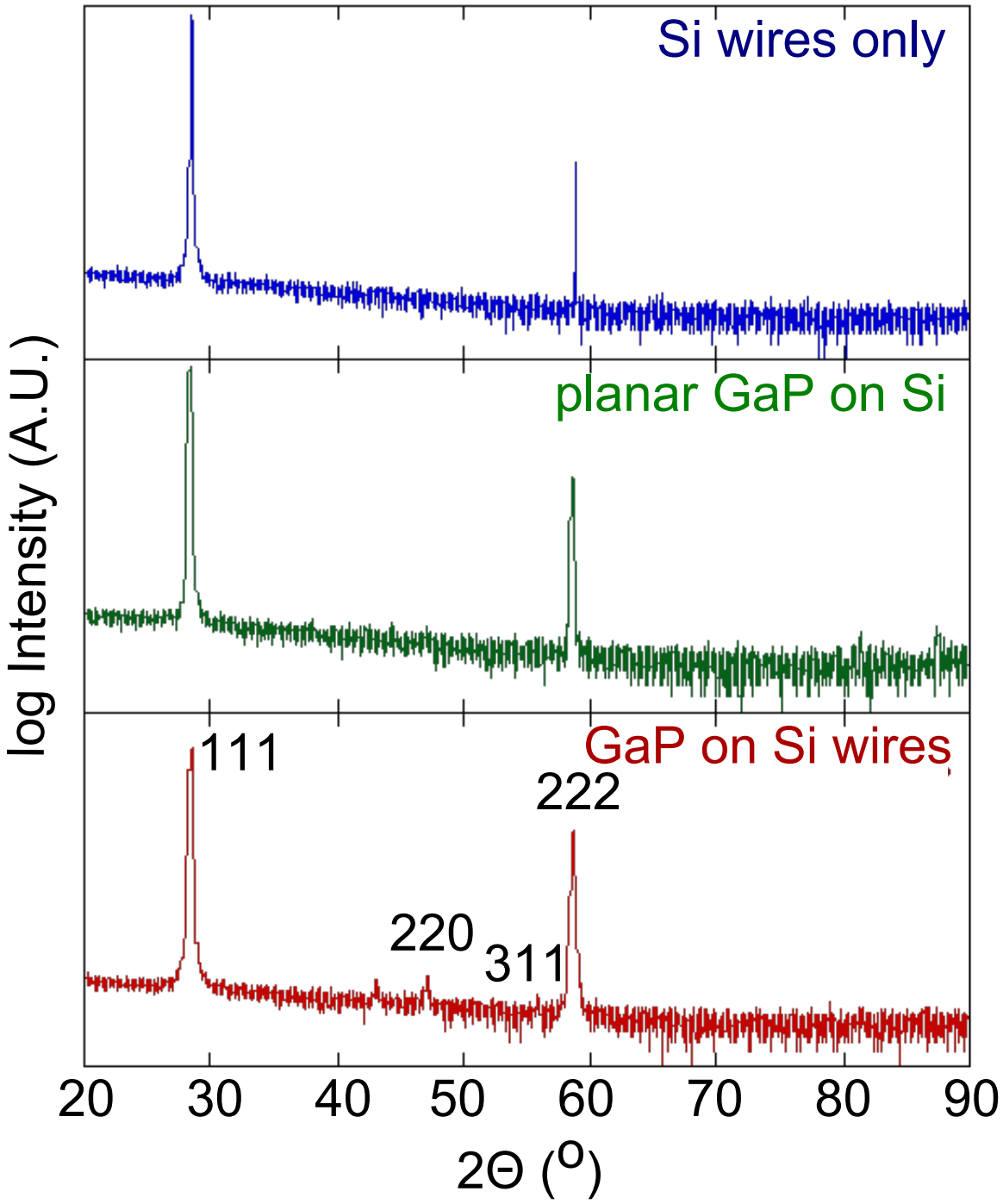


Figure 4.11: XRD plots of Si wires, planar GaP on Si, and GaP on Si wires.

the GaP coating, leading to nearly 100% absorption in the GaP/Si wire arrays without any explicit light trapping structure. The absorption enhancement is likely caused by both the higher fill factor of the GaP coated wires and scattering caused by the rough GaP surface, evidenced by the enhanced absorption even below the band gap of GaP. These experiments validate the optical modeling, further suggesting that the wires exhibit a large absorption cross section and the GaP layer focuses light into the Si core, providing additional pathways for absorption enhancement over simply geometric considerations.

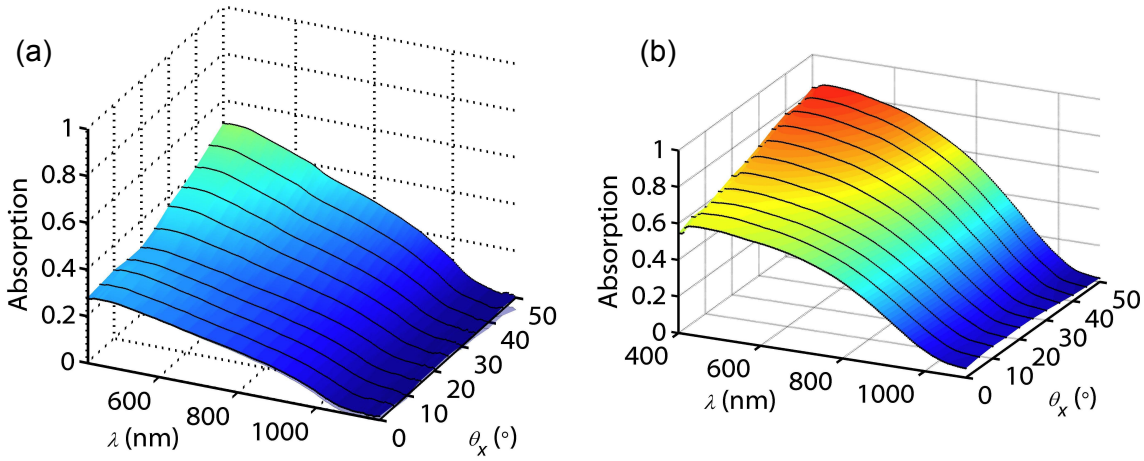


Figure 4.12: Optical absorption of (a) a peeled off Si wire array and (b) a peeled off GaP/Si wire array.

### 4.4.2 Modeling the Optical Effects of Surface Roughness

The morphology of the GaP on Si wires proved to be much rougher than the smooth, conformal layers considered in the initial optoelectronic simulations. Thus, a model was constructed to match the experimental SEMs. Randomly oriented GaP squares (width = 500 nm) were placed inside an envelope function, to follow the overall shape and roughness of the actual wires (see the appendix for the code). The top and bottom boundary conditions were set to produce perfectly matched absorbing layers, while the sides were periodic. A 500 nm plane-wave source was positioned 1 $\mu$m above the top of the wire. An SEM, the model schematic, and absorbed power profiles can be seen in **Figure 4.13**.

At 500 nm,the GaP layer in the textured structure absorbed 33% of the incident power while the Si layer absorbed 45% of the incident power. In contrast, for the conformal

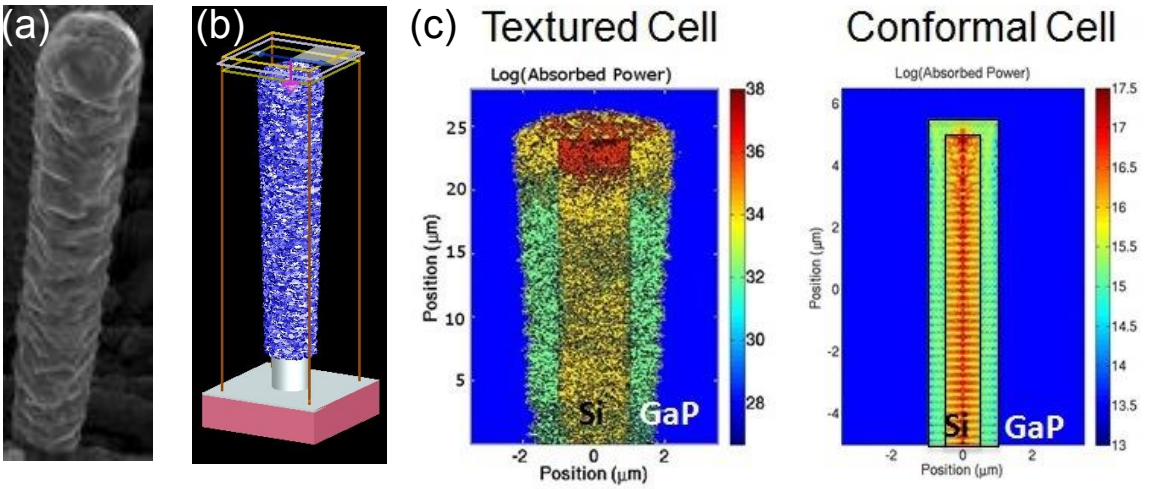


Figure 4.13: Simulation of Rough GaP coated Si wire arrays. (a) SEM of a GaP coated Si wire. (b) Schematic of the simulation setup. (c) Comparison of the absorbed power in a rough GaP coated Si wire and a smooth GaP on Si wire.

structure, the GaP only absorbed 21% of the power while the Si absorbed 29% of the power. In the conformal structure, light was channeled into modes in the higher index Si core whereas the textured structure led to an increased path length in the GaP shell and therefore enhanced shell absorption. Thus, in order to achieve current matching without using a thick shell material, texturing will be beneficial.

The optical model was also used to extract the diffusion length from photoelectrochemical measurements. Spectral response data of GaP coated Si wire arrays was collected under Ar(g) in a sealed glass cell that had a quartz window. The solution contained a low concentration of redox species (0.0050 mM ferrocenium, 0.20 mM ferrocene) which allowed the generated current to be collected. Light intensities were calibrated with a Si photodiode (Thor Labs) that was placed at the same location in the cell as the photoelectrodes. The external quantum efficiency was found at normal incidence for 488 nm illumination and compared to the model described below. The 488 nm wavelength was chosen as it is in the indirect region of the GaP absorption spectrum, resulting in long light penetration depths and thus resulting in significant losses in photocurrent in planar GaP photoelectrodes that have short minority-carrier diffusion lengths.

For the optical model, a 45 $\mu$m tall Si wire on top of a Si substrate was used as such a geometry corresponded more closely to the experimentally measured structure. A plane wave of 500 nm light was incident on the top of an individual wire with periodic side

boundary conditions to account for coupling effects between wires in the square array. The FDTD simulations indicated that the composite GaP/Si microwire photoanodes should absorb a large fraction (88%) of the 500 nm light, with the percentages of 500 nm light absorbed in the GaP and Si calculated to be 20% and 68%, respectively. The majority of the light absorption was calculated to occur near the top of the wire, due to strong scattering arising from the microscale roughness of the MOCVD-grown GaP. Results are shown in **Figure 4.14 (a)**.

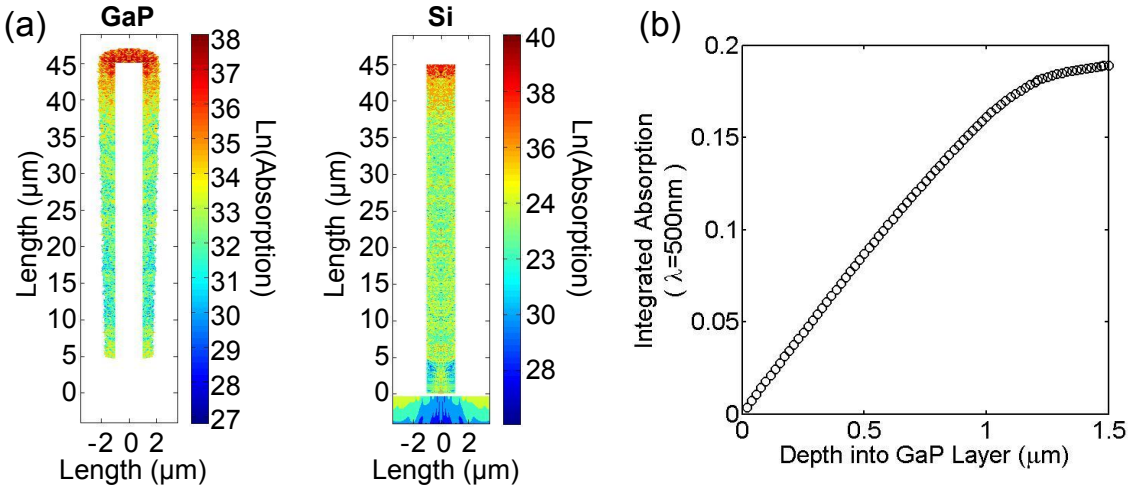


Figure 4.14: Finding the GaP diffusion length. (a) Optical absorption profiles for the GaP and Si layers. (b) Integrated absorption as a function of depth into the GaP layer from all surfaces.

Photoelectrochemical measurements suggested that the photoelectrodes had an incident photon to current efficiency (IPCE) of 1.5% at 488 nm. By integrating the simulated absorption within a set distance of the surface, theoretical IPCE values as a function of the effective carrier collection length, $L_d$, were estimated (Figure 4.14 (b)). This relation suggested that $L_n$ of the material was ~80 nm. Such short $L_d$ values are typical of GaP, and motivate future investigations of smaller absorber layer thicknesses as well as approaches to produce heteroepitaxial GaP with larger $L_d$ values and/or increased absorption coefficients (e.g. by bandstructure modification through alloying with N or As).

### 4.4.3 Single Wire Measurements

Single wire measurements are a useful technique for exploring the electrical properties of the material. While Si wires can be contacted with a simple one step lithography process, contacting heterostructre wires requires a two step lithographic process, as seen in **Figure 4.15**. Different etches and metals are required to contact the core and shell regions. After exposing one side of the wire, the GaP was etched with a 2:5:2 mixture of $HCl:H_2O:H_2O_2$ to expose the Si core, which was then contacted with In. The wire top was then exposed in a separate lithography process, and the GaP surface was cleaned with HCl, and then contacted with Au/Zn. While a few of these single wire devices were fabricated, they suffered from shunting and from poor adhesion of the Au to the substrate. However, the process is sound overall and should be applicable to future experiments. One step lithography was used for the samples of Strandwitz et al. (89), but the Si base of those wires was already protected with an oxide mask and the Al contact layer was not expected to be Ohmic to the GaP.

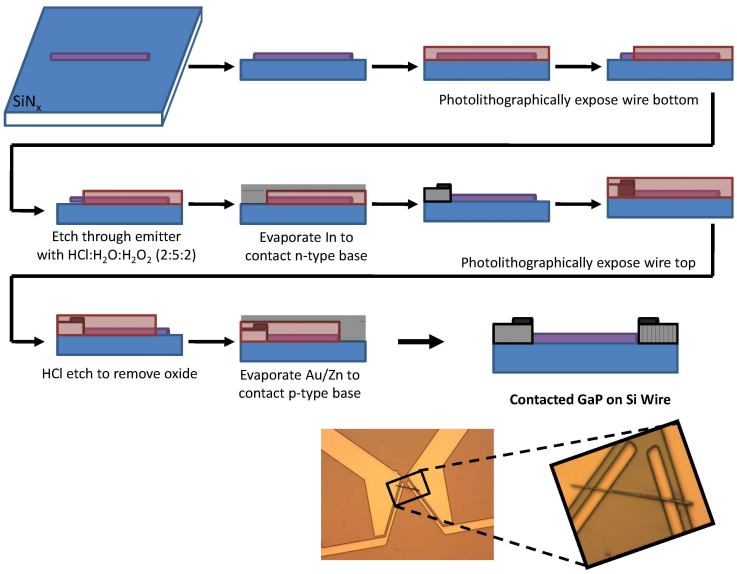


Figure 4.15: Process diagram for single wire measurements of GaP coated Si wires.

## 4.5 Summary and Outlook

The investigation of GaP on Si proved to be an illuminating foray into wire array based heterostructures. Full field modeling revealed that either thick layers or a direct gap alloy is necessary for full absorption in the outer layer. A rough surface also helped to increase absorption in the outer layer. Furthermore, the wire array absorption benefits from the outer cladding, which acts to guide light into the Si. Device physics modeling suggested that efficiencies of greater than 10% could be attained with diffusion lengths on the order of 10 $\mu$m and full absorption, but comparison between photoelectrochemical measurements of epitaxial GaP grown on Si wire arrays and the model suggested that the actual diffusion lengths of the structure were significantly smaller, on the order of 100 nm.

If the diffusion length of the GaP remains small despite further heteroepitaxial refinements, increasingly roughened structures may allow for greater collection despite a limited diffusion length. Additionally, cladding layers could be developed explicitly to channel light into the underlying Si wire. They would need to have a large enough bandgap to not cause significant parasitic absorption and contacting the underlying Si would be a challenge, but they could help the wires to further surpass the Yablonovitch light trapping limit.

In the end, the GaP on Si work revelaed many important lessons for wire array heterostructures, lessons that were invaluable for the tandem wire work of the remaining chapters.

# Chapter 5

## $GaAs_xP_{1-x}$ on $Si_{1-x}Ge_x$: Modeling

### 5.1 Motivation

Multijunction arrays offer the advantages of wire array solar cells along with both higher efficiencies and higher voltages. While the previous chapter explored GaP/Si wire heterostuctures for solar photoelectrochemistry, different constituent materials must be selected in order to obtain high efficiencies for solar electricity generation. The limiting efficiency for a GaP/Si combination is less than that of a single junction Si cell alone due to severe current limiting by the GaP subcell. Additionally, GaP is an indirect gap material and thus thick layers are needed to absorb incident sunlight. Nevertheless, the GaP/Si wire heterostructure revealed that Group IV and III-V materials could be joined in one functional device and that the growth morphology could be controlled through the use of $SiO_x$ masking layers.

The use of lower bandgap III-Vs and the careful tailoring of the geometries could lead to a high efficiency device. With this goal in mind, this chapter focuses on the design of such devices with an analytical model and simulations, and Chapters 6 and 7 will explore the experimental efforts directed towards realizing the proposed designs. $GaAs_xP_{1-x}$ on $Si_{1-x}Ge_x$ was identified as an ideal materials system due to the potential for lattice matching with bandgap combinations that allow for high detailed balance efficiencies. Three architectures were developed and explored: a simple coaxial structure, and structures with hemispherical or spherical $GaAs_xP_{1-x}$ layers seeded off of the $Si_{1-x}Ge_x$ wire tip. An analytical model revealed that these cells have the potential for >34% efficiencies. Optical modeling demonstrated that current matching can be realized. Finally, device physics modeling stressed the importance of achieving high lifetime III-V layers, but also showed that defects at the heterointerface can have minimal impact if doped so as to repel minority carriers.

## 5.2 Material Choice

To achieve a high efficiency device, the bandgaps of the constituent materials must be chosen so that the photocurrent in each layer is matched. Additionally, lattice-matched material systems are desirable as mismatch strain relieving dislocations can act as recombination centers, though recent work suggests that the wire geometry may facilitate high quality growth of lattice mismatched materials.(61) Dislocations due to lattice mismatch can be forced to propagate radially outward from the wire interface, allowing high quality material to be grown axially.

As a first step towards identifying a desirable material system, detailed balance efficiencies for a series connected, two junction cell were calculated by following the treatment of Henry (18) with the exception that the quadrilateral rule was used to solve the thermal radiation and radiative recombination integrals. Band gap and lattice constant data for SiGe, GaAsP, and GaInP was taken from (143–145), respectively and overlaid on the calculated isoefficiency contour plot to create **Figure 5.1**. The plot reveals that $Si_{0.1}Ge_{0.9}$, $GaAs_{0.9}P_{0.1}$, and $Ga_{0.56}In_{0.44}P$ are an almost ideal material system for the core, shell, and window materials of a tandem wire array device. The combination has a detailed balance efficiency of over 40%. However, despite the specific composition choice, the chosen material combination is somewhat flexible; the limiting efficiency is well over 35% across a broad range of alloys: gains in open circuit voltage make up for small losses in short circuit current across this range. Practically, $Si_{1-x}Ge_x$ wires have been successfully synthesized,(146) and both Si and Ge wires can be grown using high temperature chlorosilane chemistry,(24) which has been demonstrated to produce high fidelity, ordered arrays.(63)

## 5.3 Device Architectures

If the $GaAs_{0.9}P_{0.1}$ first fully absorbs all of the available above-bandgap photons from the solar spectrum and the $Si_{0.1}Ge_{0.9}$ then absorbs all of the remaining photons above its bandgap, each will contribute $\sim$28 mA/cm$^2$ of current. Thus, in order to achieve current matching, the incident light must first pass through the $GaAs_{0.9}P_{0.1}$ and the optical path length must be long enough in the $GaAs_{0.9}P_{0.1}$ so that all of the above bandgap photons are absorbed. Combining this constraint with realistic growth geometries led to the three device designs depicted in **Figure 5.2**. In the conformal structure, the III-V layers are deposited directly

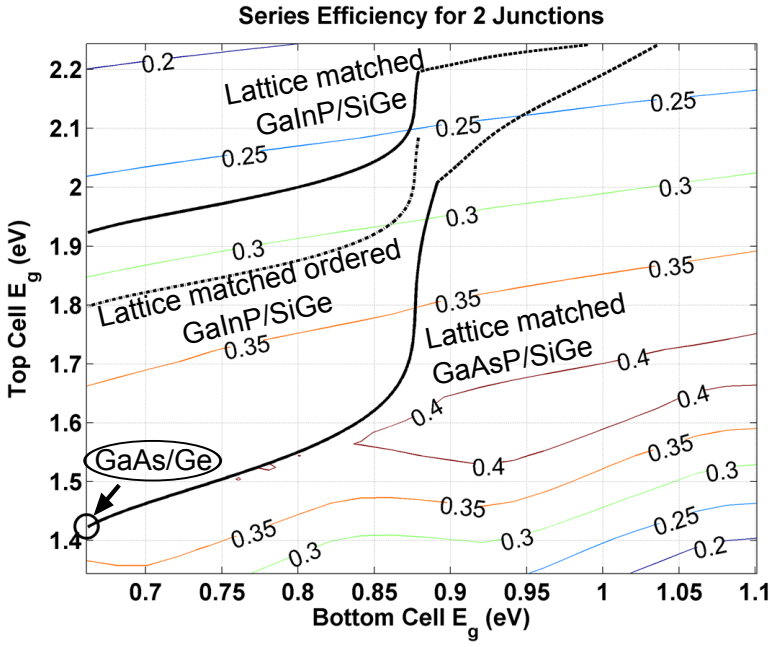


Figure 5.1: Lattice matched material combinations overlaid on an isoefficiency contour plot for series connected, two junction cells.

on a p-n $Si_{0.1}Ge_{0.9}$ radial junction wire array. In the hemisphere structure, the $Si_{0.1}Ge_{0.9}$ wire array is infilled with a dielectric material and growth of the III-V layers is then templated from the wire tips, in a method analogous to epitaxial lateral overgrowth.(62) The ellipsoidal structures allow for a close packed array of $GaAs_{0.9}P_{0.1}$ absorbers at the top of the cell, directing all incident light through the $GaAs_{0.9}P_{0.1}$ material before it reaches the $Si_{0.1}Ge_{0.9}$. Finally, in the sphere structure, the wire sidewalls are protected by a dielectric and III-V growth proceeds in all directions from the seed region near the top of the wire.

## 5.4 Analytical Model

While not as accurate as finite element numerical simulations, a simplified analytical model allows for physical insight into and rapid exploration of the device parameters. An analytical model for the conformal wire array device geometry may be solved by extension of the model of Kayes et al. (27) and is not covered here. Instead, the hemisphere design was chosen as a case study. The spherical design can also be solved through a similar analytical approach, though the absorption profile should be modified. For the hemisphere, the optical absorption and current-voltage curves were calculated for a variety of geometries and recombination

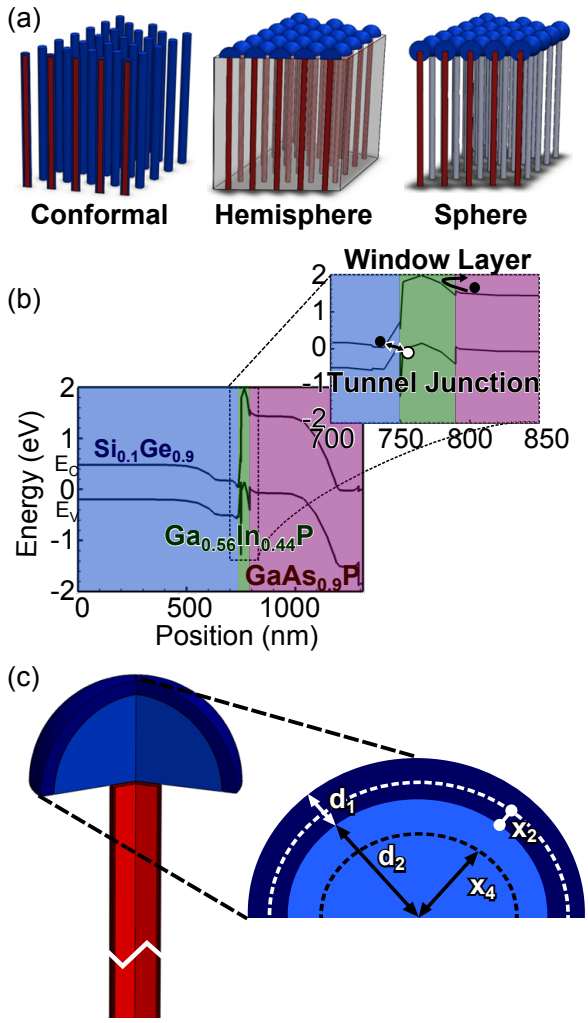


Figure 5.2: Overview of the multijunction wire array geometries and electronic structure. (a) The three multijunction wire array structures under consideration. (b) A representative band diagram showing the $Si_{0.1}Ge_{0.9}$ and $GaAs_{0.9}P_{0.1}$ p-n junctions, and the $Ga_{0.56}In_{0.44}P$ tunnel junction and window layers. The 20 nm of $Si_{0.1}Ge_{0.9}$ closest to the $Ga_{0.56}In_{0.44}P$ is highly doped to serve as part of a tunnel junction and hence experiences bandgap narrowing. (c) Cross section of the $GaAs_{0.9}P_{0.1}$ hemispherical shell showing the parameters used in the analytical model. The depletion region boundaries are marked with dotted lines.

parameters. Optical constants for the $Si_{0.1}Ge_{0.9}$ were taken from Palik (147). Constants for the $GaAs_{0.9}P_{0.1}$ were generated by shifting GaAs n and k vs. energy values by a constant energy such that k fell to zero at the desired bandgap. The optical constants found in the literature were not used as the absorption coefficient did not go to zero at the expected bandgap and as multiple samples with the same composition had different optical constants, suggesting that the material was plagued with defects that altered the optical properties.(148) Electronic material parameters were taken from a database made available by the Ioffe Institute.(149)

First, the III-V top subcell performance was analyzed. The optical absorption profile of the III-V layer was calculated by considering the excitation of a sphere of material by a plane wave, using Mie theory.(129) A polar coordinate grid that covered the hemisphere was discretized into 25 points in both r and $\theta$ and the fields calculated at those points by summing the first 20 normal modes. The code can be found in the appendix. The absorption was then calculated by considering the real part of the divergence of the Poynting vector, $P_{abs} = -\frac{1}{2}\vec{\nabla} \cdot \vec{P} = -\frac{1}{2}\omega|\vec{E}|^2\epsilon''$, where $P_{abs}$ is the absorbed power, $\vec{P}$ is the Poynting vector, $\omega$ is the frequency, $\vec{E}$ is the internal electric field, and $\epsilon''$ is the imaginary part of the dielectric constant. The outer profile converges after summing the first 20 modes, but the inner profile (close to r = 0) continues to oscillate as new modes are added; the modes tend to be highly structured around the origin. Thus, the seven lowest r values around the origin were discarded.

For a 2 $\mu$m radius sphere, the Mie theory results are plotted in **Figure 5.3** alongside a simple Beer-Lambert (B-L) profile. The absorption at each wavelength was evaluated, weighted by the solar spectrum, and summed to yield an optical generation profile. For the Mie model, the plane wave is incident from the x direction ($\theta = 90^\circ$ on the plot), and the X-Z optical generation cross section is shown. The Y-Z cross section is similar. For the B-L absorption profile, the generation is assumed to decay exponentially into the material with a decay length of $\alpha = 2\omega k$, where $\omega$ is the frequency and k is the imaginary part of the index of refraction. The two absorption profiles are similar, as might be expected for direct gap $GaAs_{0.9}P_{0.1}$. Photons are absorbed before they can fully occupy the modes of the structure. Thus, a Beer Lambert photogeneration profile was assumed in the device physics equations in order to make them analytically tractable.

In addition to the Beer Lambert absorption assumption, the device physics model of the

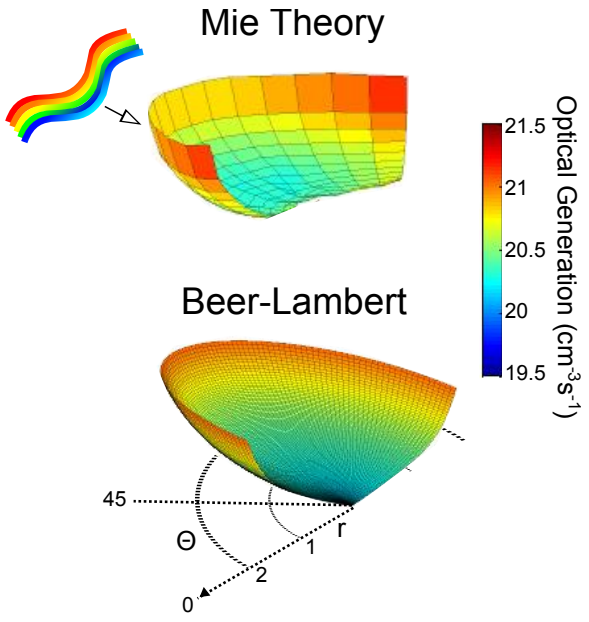


Figure 5.3: Polar coordinate plots comparing Mie Theory and Beer-Lambert absorption for the upper $GaAs_{0.9}P_{0.1}$ cell.

III-V hemisphere relied on three additional assumptions:

1. Transport occurs only in the radial direction.

2. The p-n junction is abrupt.

3. All of the carriers that are generated in the depletion region are collected.

With these assumptions and following the conventions outlined in Figure 5.2, the limits of the depletion region may be found by maintaining charge conservation;

$$N_A(d_2^3 - x_4^3) = N_D((d_2 + x_2)^3 - d_2^3),$$

and by solving Poisson's equation in spherical coordinates (assuming angle invariance);

$$\frac{1}{r^2}\frac{d(r^2\frac{dV}{dr})}{dr} = \frac{\rho}{\epsilon},$$

which leads to;

$$V_{bi} + V = \frac{qd_2^2N_A}{6\epsilon} + \frac{q}{3\epsilon d_2}(N_Ax_4^3 + N_Dx_2^3) + \frac{q}{2\epsilon}(-N_Ax_4^2 + N_Dx_2^2),$$

where $V_{bi} = \frac{kT}{q} \ln(\frac{N_A N_D}{n_i^2})$ is the built in voltage, $V$ is the applied voltage, $N_A$ is the p-type dopant density, $N_D$ is the n-type dopant density, $n_i$ is the intrinsic carrier concentration, $T$ is the temperature, $k$ is Bolzmann's constant, $q$ is the fundamental electrical charge, and $\epsilon$ is the dielectric constant.

Since assumption #3 states that all of the charge carriers in the depletion region are collected,

$$J_g^{dep} = \sum_{\omega} q\Gamma_0(\omega) \frac{d_2^2}{(d_1+d_2)^2} (e^{\alpha(\omega)(x_2-d_1)} - e^{\alpha(\omega)(x_4-d_1-d_2)},$$

and from the model of (150) for recombination:

$$J_r^{dep} = -qU_{max} \frac{r_2(V)^3 - r_1(V)^3}{3(d_1+d_2)^2},$$

where $\Gamma_0(\omega)$ is the incident photon flux, $\alpha = 2\omega k$ is the Beer-Lambert attenuation coefficient, $k$ is the imaginary part of the index of refraction, $U_{max} = \frac{n_i}{\sqrt{\tau_{n,0}\tau_{p,0}}} \sinh \frac{qV}{2kT}$ is the maximum recombination rate of a mid-level trap, $\tau$ is the lifetime in the n or p-type region, $r_1(V) = r(V) - L_C$, $r_2(V) = r(V) + L_C$, $r(V) = x_4 + \frac{\ln \frac{N_A}{n_i}}{\ln \frac{N_A N_D}{n_i^2}}(x_2 + (d_2 - x_4))$ is the point where the Fermi level crosses midgap, and $L_C = \frac{\pi}{2}\frac{kT}{qE} = \frac{\pi kT(x_2+(d_2-x_4))}{2q(V_{bi}+V)}$ is the recombination collection length.

In the two quasi-neutral regions, we must solve the diffusion equation in spherical coordinates (again, assuming angle invariance):

$$\nabla^2 n, p - \frac{n,p}{L_{n,p}^2} = \frac{1}{r^2}\frac{d(r^2 \frac{dn,p}{dr})}{dr} - \frac{n,p}{L_{n,p}^2} = -\frac{\alpha\Gamma_0}{D_{n,p}} e^{\alpha(r-(d_1+d_2))},$$

where $n, p$ is the minority carrier in the given region, $L_{n,p}$ is the diffusion length of the carriers, and $D_{n,p}$ is the diffusion coefficient.

The current may then be found from the relation $J = qD_{n,p}\frac{dn,p}{dr}$, where the current is evaluated at the depletion region boundaries. The boundary conditions are:

1. $n(0) =$ finite,
2. $S_n \cdot n(0) = -D_n \frac{dn}{dr}|_0$,
3. $n(x_4) = n_0(e^{qV/kT} - 1)$,
4. $p(d_2 + x_2) = p_0(e^{qV/kT} - 1)$,

5. $S_p \cdot p(d_1 + d_2) = -D_p \frac{dp}{dr}|_{d_1+d_2}$,

where $S_n$ and $S_p$ are the electron and hole surface recombination velocities, respectively. In the n-type emitter, the differential equation can be solved to give

$$p = A\frac{e^{r/L_p}}{r} + B\frac{e^{-r/L_p}}{r} + e^{\alpha(r-(d_1+d_2))}\frac{\alpha\Gamma_0}{D_p}(\frac{L_p^2}{1-\alpha^2L_p^2})(1 + \frac{2\alpha L_p^2}{r(1-\alpha^2L_p^2)}),$$

where $A$ and $B$ are constants to be determined from the boundary conditions.

The solution takes the same form in the p-type core (with n substituted for p), but an additional term, $\Delta\frac{\sinh r/L_n}{r/L_n}$, where $\Delta$ is a constant, must be included to account for the additional boundary condition. L'Hospitals rule may be used to solve for the limits at r = 0 and combined with the boundary conditions to find the constants.

The device parameters were selected as follows: diffusion lengths of less than 100 nm have been seen for GaP/Si wire heterostructures,(89) but lengths of a few microns are regularly achieved for high quality GaAs and hence a diffusion length range of 10 nm - 100 $\mu$m was explored.(151) The n-type emitter was set to be 100 nm thick with a dopant density of 9 x $10^{17}$ $cm^{-3}$. The p-type base was doped at 5 x $10^{16}$ $cm^{-3}$. Finally, the hole and electron recombination velocities were set to 100 cm/s.

Device characteristics for III-V hemispherical top subcells with varying radii and diffusion lengths are shown in **Figure 5.4**. The $V_{OC}$ is relatively invariant of device diameter, but falls off uniformly with device diffusion length. The $J_{SC}$, on the other hand, is relatively insensitive to diffusion length until the diffusion length approaches the physical dimensions of the device. Overall, for the parameter space surveyed, a maximum efficiency of 29.7% was achieved for a 10 $\mu$m thick device with a 100 $\mu$m diffusion length. Higher efficiencies would be possible with larger radii, but fall outside of the scope of the architectures considered herein.

Furthermore, the top subcells are relatively insensitive to surface recombination velocity. As the radius goes up, the surface to volume ratio goes down, and a sphere is already the shape with minimum surface-to-volume ratio. The model suggests that surface recombination velocities of ~10,000 cm/s could be tolerated with minimal effect on device performance (**Figure 5.5**).

Finally, the hemispherical top subcell was coupled with the wire model of (27) to simulate current voltage curves for tandem solar cell structures. First, current-voltage curves were

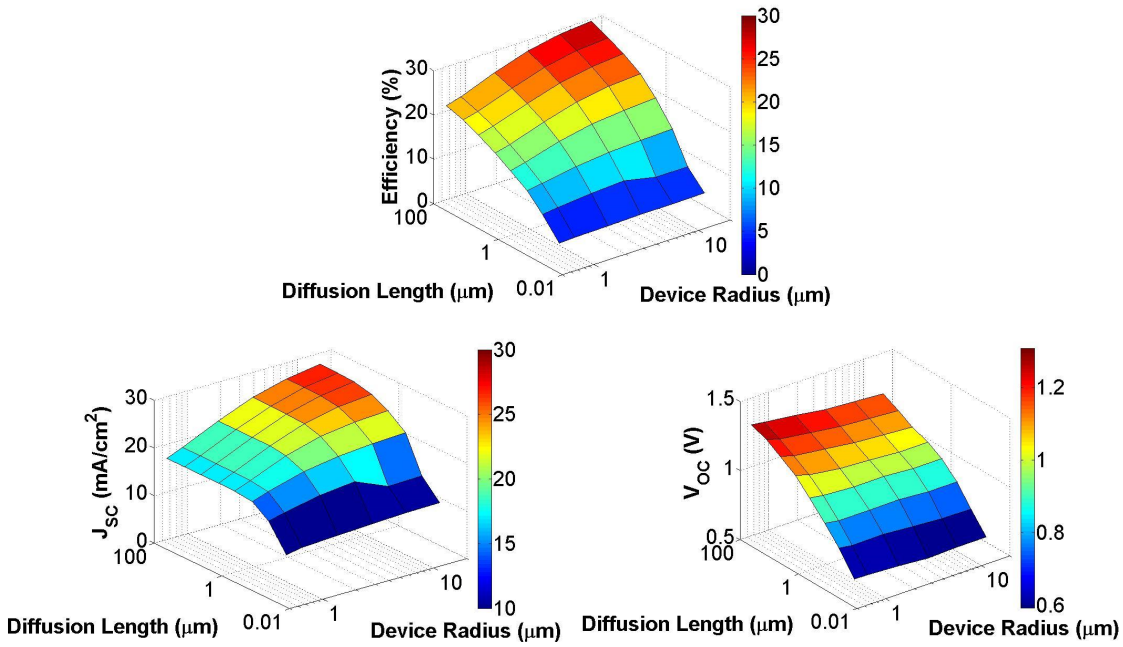


Figure 5.4: Efficiency, short circuit current density, and open circuit voltage of hemispherical $GaAs_{0.9}P_{0.1}$ solar cell structures as a function of device radius and diffusion length.

generated for the hemisphere and for a $Si_{0.1}Ge_{0.9}$ wire. Kirchhoff's circuit laws were then enforced for the two devices in series. **Figure 5.6** shows the evolution of device performance as the dimensions are altered, and **Table 5.1** displays the $V_{OC}$, $J_{SC}$, efficiency, and fill factor for the devices.

The combined performance is primarily limited by the short circuit current density of the $Si_{0.1}Ge_{0.9}$ wire cell, with current matching only achieved by making the $GaAs_{0.9}P_{0.1}$ layer small enough to allow some of the blue light to reach the $Si_{0.1}Ge_{0.9}$ wire and to be absorbed therein or by making the $Si_{0.1}Ge_{0.9}$ wire much longer. $Si_{0.1}Ge_{0.9}$ is a very poor absorber in the infrared and hence the current is 2-4 mA/cm$^2$ lower than possible. As the wire is made longer to absorb more of the incident light, the recombination losses rise and the wire efficiency begins to drop due to voltage losses, limiting the gains beyond a certain point. However, while the model of Kayes et al. (27) assumes Beer-Lambert absorption, experimental studies have demonstrated the enhanced absorption enjoyed by wire arrays,(31) and hence higher efficiencies may be possible in real devices.

Finally, the above model assumed a perfect tunnel junction between the two subcells. However, real devices will experience a finite, though hopefully small, voltage drop across

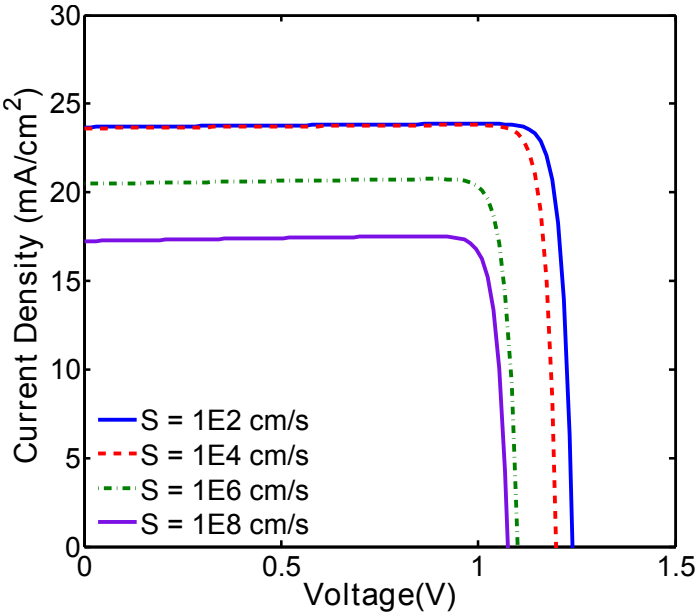


Figure 5.5: Light IV curve of the shell as the outer ($r = d_1 + d_2$) and inner ($r = 0$) surface recombination velocities are varied. The velocities are both set to have the values indicated.

the tunnel junction. Thus, a series resistance was added to the model to account for these losses. For the first cell considered in Table 5.1, as long as the series resistance for the tunnel junction is kept at or below 0.7 $\Omega$ cm$^2$, the tandem efficiency will remain above 32%. For the second cell, the efficiency will remain above 33% for a resistance of up to 1 $\Omega$ cm$^2$. However, for larger values of series resistance, the cell efficiency rapidly began to fall, as seen in **Figure 5.7**.

## 5.5 Optical Modeling

In order to create a more realistic model of all three structures, full optoelectronic finite element simulations were conducted. For all three geometries, a 1.5 $\mu$m diameter, 40 $\mu$m long $Si_{0.1}Ge_{0.9}$ wire served as the base and a square array of varying pitch was assumed. In the conformal structure, the $GaAs_{0.9}P_{0.1}$ shell and the $Ga_{0.56}In_{0.44}P$ layers were set to be 500 nm and 20 nm thick, respectively. In the hemispherical and spherical structures, the III-V semiconductor shell was ellipsoidal, depicting a case in which growth nucleates simultaneously at the sides and the top of the wire and continues outward. The shell thickness was set such that a 500 nm gap was left between adjacent wires.

First, full field optical simulations were run using the finite difference time domain

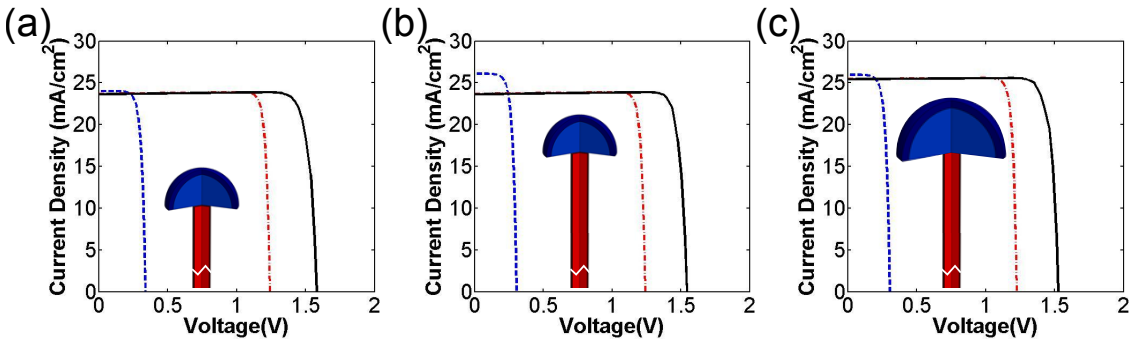


Figure 5.6: Light IV curves of the $Si_{0.1}Ge_{0.9}$ wire (blue dashed), the $GaAs_{0.9}P_{0.1}$ hemisphere (red dot-dashed), and the tandem combination (black solid) as the structure geometry is varied. In (a), the hemisphere has a 3 $\mu$m radius and the wire is 100 $\mu$m long. In (b), the wire length is increased to 400 $\mu$m. In (c), the radius is increased to 5 $\mu$m and the length is 400 $\mu$m.

Table 5.1: Light IV characteristics for subcells and tandem cell as the geometry of the shell and wire are varied.

| | $V_{OC}$ (V) | $J_{SC}$ (mA/cm$^2$) | Eff (%) | FF (%) |
|---|---|---|---|---|
| 3 $\mu$m $GaAs_xP_{1-x}$ shell | 1.24 | 23.7 | 26.7 | 90.7 |
| 100 $\mu$m $Si_{1-x}Ge_x$ wire | 0.33 | 24.0 | 5.94 | 73.9 |
| Tandem | 1.57 | 23.6 | 32.4 | 87.1 |
| 5 $\mu$m $GaAs_xP_{1-x}$ shell | 1.23 | 25.5 | 28.2 | 90.1 |
| 400 $\mu$m $Si_{1-x}Ge_x$ wire | 0.30 | 26.0 | 5.62 | 71.7 |
| Tandem | 1.52 | 25.4 | 33.6 | 86.7 |

method with plane wave incident illumination. Optical constants for $Si_{0.1}Ge_{0.9}$ and $GaAs_{0.9}P_{0.1}$ were found as mentioned in the previous section, and $Ga_{0.56}In_{0.44}P$ values were generated by shifting InP n and k data to the desired bandgap. Optical absorption simulations were performed at 50 nm steps for both a two dimensional model and a full three dimensional model with periodic side boundary conditions, a perfectly absorbing top boundary, and a perfectly reflecting base. Both TE and TM plane wave sources were used and the results for both polarizations were averaged. Previous experiments demonstrated that coherent interface effects were suppressed in wires due to mild diameter tapering and small film variations and hence partial spectral averaging was employed to smooth these frequency

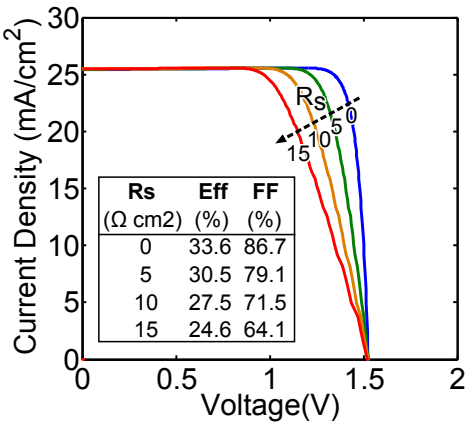


Figure 5.7: The effect of series resistance ($R_s$) on the performance of the second tandem cell in Table 5.1.

specific resonances. Spectral averaging will also more closely represent the surface roughness evidenced in experimental structures, again by smoothing the resonances. Finally, 200 spherical, 50 to 250 nm diameter, $Al_2O_3$ scattering particles were randomly distributed in the empty space to the sides of the wire to scatter light into the structure, and a 100 nm MgF, 60 nm $TiO_x$ dual layer antireflective coating was placed over the outer $Ga_{0.56}In_{0.44}P$ window. The antireflection coating was optimized to allow maximum transmission of the relevant wavelengths of the solar spectrum by using simple transfer matrix method (TMM) calculations on a planar cell. The TMM code may be found in the appendix.

The absorption profiles were calculated as described in Ferry et al. (152) and the cross sections were compared, as seen in **Figure 5.8**. The absorption features that were visible in the 3D structure were mirrored in the 2D model, as demonstrated in Figure 5.8 (b). Overall, the $GaAs_{0.9}P_{0.1}$ absorption for the 2D and 3D models were nearly identical while the $Si_{0.1}Ge_{0.9}$ absorption was appreciably lower in the 850-1100 nm range for the 3D model due to the smaller physical cross section. As experiments have shown that wires can absorb the majority of light within this range with the incorporation of scattering particles and anti-reflective coatings, the higher absorption of the 2D model was assumed to be possible. Thus, though the proposed tandem device structures are three dimensional, two dimensional simulations were employed as they maintain the features seen in three dimensional simulations with greatly reduced computational complexity, allowing for rapid cell design iteration.

Device response to the solar spectrum was characterized by 23 optical simulations,

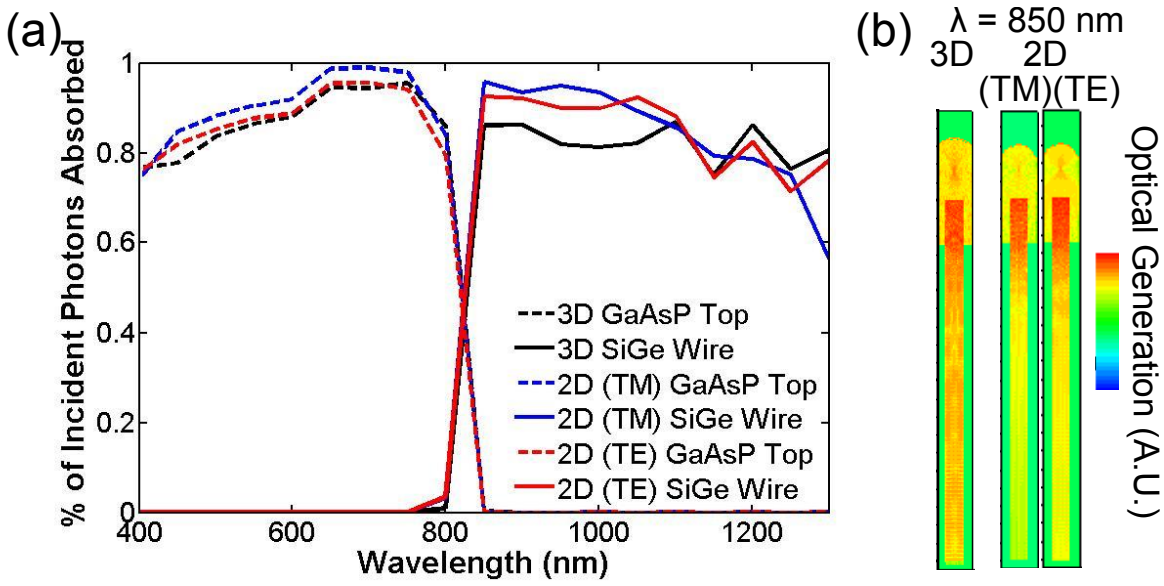


Figure 5.8: 2D vs. 3D optical simulation comparison (a) Comparison of 2D (TE and TM) and 3D absorption rates in the core and shell as a function of wavelength.(b) Absorption profiles at 850 nm for the 2D and 3D cases.

stepped in wavelength throughout the AM1.5G solar spectrum. Due to the length of time required to run the optical simulations and, more significantly, to interpolate the finite-difference-time-domain grid onto the finite element grid, optical simulations were run in 50 nm steps for the optoelectronic simulations. However, to make sure that no significant features were missing in the optical response, optical simulations were also run in 25 nm steps as a check. A comparison of the two absorption profiles for the different wavelength spacings is shown in **Figure 5.9**. The absorption was calculated independently in the $Si_{0.1}Ge_{0.9}$, in the $GaAs_{0.9}P_{0.1}$, and in the $Ga_{0.56}In_{0.44}P$ by considering the real part of the divergence of the Poynting vector. The optical generation was then integrated over the volume and multiplied by the fundamental electric charge, yielding an assumed unity internal quantum efficiency $J_{SC}$. The differences in "ideal" short circuit densities that would be expected for the two profiles are listed in **Table 5.2**. The largest difference between the two values is 1% for the window layers, which do not contribute to the overall current of the device. The difference in shell and wire absorption between the two profiles is less than 1%. Thus, 50 nm steps were used for the remaining simulations.

After validating the use of a 2D model and 50 nm wavelength steps, all three heterostructure geometries were explored with array pitches from 3-7 $\mu$m in 1 $\mu$m steps. For all of

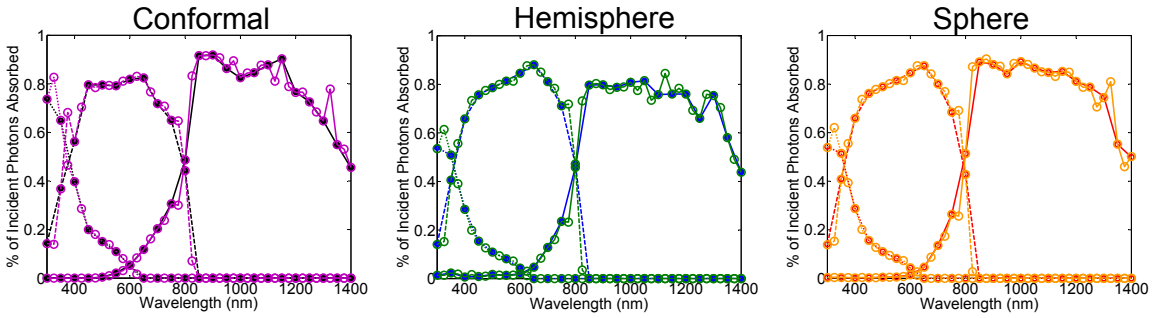


Figure 5.9: Comparison of the absorption profiles for FDTD optical simulations run at 25 nm wavelength steps vs. 50 nm wavelength steps.

the simulations, the window layer was highly absorbing in the ultraviolet wavelengths and accounted for a loss of around ∼2 mA/cm$^2$ of all possible photocurrent. The absorption in the conformal structure was relatively independent of wire pitch. Light incident between the wires scatters off of the $Al_2O_3$ particles and back into the array, allowing for high absorption regardless of packing fraction. The absorption profile, plotted in **Figure 5.10** for the full spectrum, reveals that light is directed into guided modes in the wire core, in contrast to the simple Beer-Lambert absorption assumed for the analytical model. As seen in Figure 5.10, this facilitates high absorption in the infrared part of the solar spectrum despite the fact that 40 $\mu$m of $Si_{0.1}Ge_{0.9}$ is not optically thick for these wavelengths. In the blue part of the spectrum, 500 nm of $GaAs_{0.9}P_{0.1}$ absorbed ∼70% of the incident photons, sufficient for current matching. Simple Beer Lambert absorption gives a slightly higher absorption rate of 74.5%, suggesting that the optical path length is not enhanced for the III-V layer in this structure. As the $Si_{0.9}Ge_{0.9}$ wire core has a higher index than the $GaAs_{0.9}P_{0.1}$ cladding, incoupled light is guided into the $Si_{0.9}Ge_{0.9}$ core rather than residing in modes in the shell.

In contrast to the conformal structure, the hemisphere and sphere designs showed clear pitch dependence. For large wire array pitches, the III-V layers were optically thick and hence absorbed all of the blue light. Additionally, the hemispherical and spherical geometry focused red light onto the wire core where it was absorbed. However the large index contrast between the base of the III-V sphere or hemisphere and the underlying air or lower index dielectric caused red light that reached that interface to be strongly reflected.

Lowering the array pitch at fixed wire diameter decreased the relative fraction of light that impinged on the large index contrast region at the III-V/dielectric rear interface, allowing for greater core absorption. Meanwhile, the lower pitch also led to thinner III-V layers

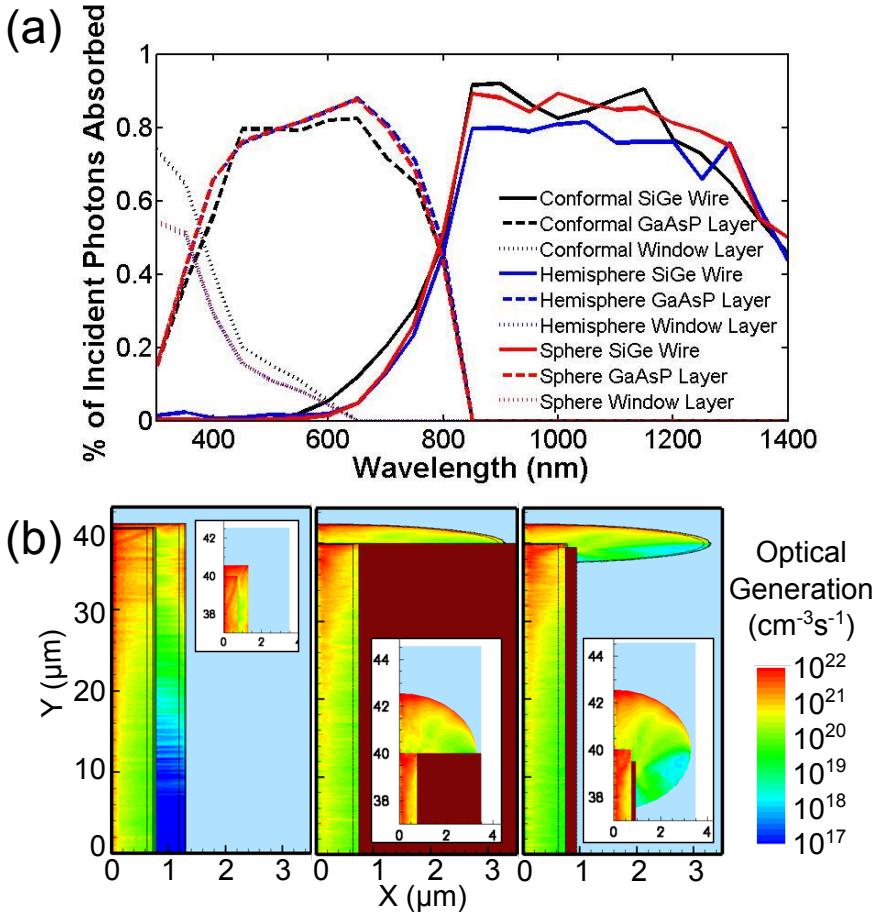


Figure 5.10: Optical properties of multijunction wire arrays (a) Percent of incident photons absorbed as a function of wavelength for the window, shell, and core layers and for all three structures. (b) The overall, AM1.5G, generation profile for the three structures at a 7 $\mu$m pitch. The plots are distorted laterally in order to encompass the full profile. The insets show an undistorted view of the top of the structures.

Table 5.2: Calculated ideal (IQE=1) $J_{SC}$ of layers under course (50 nm wavelength step) and fine (25 nm step) simulations.

| Structure | Region | Course | Fine | Difference |
|---|---|---|---|---|
| | | $J_{SC}$ (mA/cm$^2$) | $J_{SC}$ (mA/cm$^2$) | (%) |
| Conformal | Window | 2.67 | 2.67 | 0 |
| | Shell | 20.49 | 20.59 | 0.5 |
| | Wire | 23.32 | 23.46 | 0.6 |
| Hemisphere | Window | 2.02 | 2.00 | 1 |
| | Shell | 21.53 | 21.52 | 0.04 |
| | Wire | 21.07 | 20.92 | 0.7 |
| Sphere | Window | 2.04 | 2.02 | 1 |
| | Shell | 21.27 | 21.30 | 0.1 |
| | Wire | 22.92 | 22.94 | 0.09 |

which allowed the $Si_{0.1}Ge_{0.9}$ wire to absorb some of the blue light, further aiding in current matching. A compromise was reached for the 4 $\mu$m pitch, allowing for current matching conditions. The spectral profile at this pitch is shown in Figure 5.10. Idealized $J_{SC}$s for all pitches are plotted in **Figure 5.11**, and all optical absorption and loss mechanisms are summarized in **Figure 5.12**. Beer Lambert absorption for the 4 $\mu$m pitch structure suggests roughly equivalent absorption rates, again suggesting that the optical path length is not much altered.

For all structures, the current matched, idealized short circuit current densities were ~21 mA/cm$^2$ in the wire and in the shell. To reach current densities closer to the theoretical maximum values, a series of graded index layers could be added on the back to couple red light out to the wire, longer wires could be used to allow for greater absorption in the red, and window layers with higher bandgaps could be employed to mitigate parasitic absorption.

## 5.6 Electronic Modeling

The photogeneration profile was utilized as data input in a drift-diffusion based device physics simulator (TCAD Sentaurus by Synopsys) to explore photovoltaic device perfor-

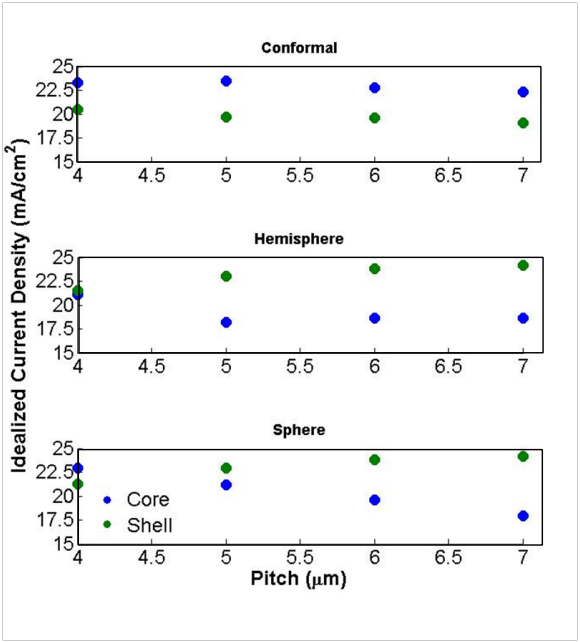


Figure 5.11: Plot of the relative absorption in the core and shell for all three structures for varying pitch.

mance for various geometries. Electronically, all three devices consisted of a base $Si_{0.1}Ge_{0.9}$ wire with a radial p-n junction, a highly doped $Si_{0.1}Ge_{0.9}/Ga_{0.56}In_{0.44}P$ tunnel junction and surface field, a $GaAs_{0.9}P_{0.1}$ p-n junction shell, and a $Ga_{0.56}In_{0.44}P$ front surface field. A representative band diagram is shown in Figure 5.2.

The electrical parameters of the materials were taken from the simulation database,(153) except for the tunnel junction tunneling masses (0.05 and 0.14 for electrons and holes, respectively) and effective Richardson constants (0.21 and 0.4 for electrons and holes, respectively) which were taken from an AlGaAs/GaAs interface model.(154) All interface recombination velocities were set to 100 cm/s for the initial simulations. The $Si_{0.1}Ge_{0.9}$ Shockley-Read Hall lifetime was set to 1 $\mu$sec ($L_n \sim 100\mu$m), comparable to experimentally measured values,(32) and Shockley-Read-Hall lifetimes of 1.25 ps, 5 ps, 20 ps, 500 ps, and 50 ns ($L_n \sim$ 157 nm, 315 nm, 629 nm, 3.15 $\mu$m, and 31.5 $\mu$m) were considered for the $GaAs_{0.9}P_{0.1}$. Auger and radiative recombination were also included. A small contact was located at the bottom center of the $Si_{0.1}Ge_{0.9}$ wire. The $GaAs_{0.9}P_{0.1}$ contact was either located at the outer base for the conformal structure or entirely covered the outside of the window layer for the hemisphere and sphere structures. Finally, cylindrical symmetry was specified, enabling the two-dimensional model to serve as a quasi-three-dimensional simu-

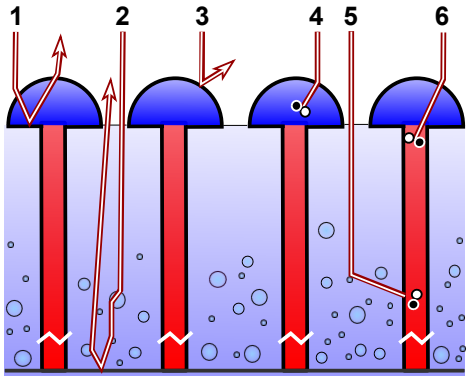


Figure 5.12: Cartoon depicting the loss and absorption mechanisms in a wire array tandem cell. 1: Reflection off of the III-V/infill interface. 2: Light that misses the cell entirely. 3: Reflection off of the wire surface. 4: Light absorbed directly in the III-V. 5: Light scattered into the wire. 6: Light guided through the III-V into the wire and absorbed.

lation. In order to facilitate geometrical correspondence from the two-dimensional optical simulations to the three-dimensional device physics model, after summing and weighting the single wavelength simulations, the overall generation profile was weighted by $\frac{R^2}{r}$ where $R$ is equal to half of the pitch and $r$ is the profile's x coordinate. Thus when integrated cylindrically, the profile yields the same idealized $J_{SC}$ as when integrated in two dimensions. The modified profile was then interpolated onto a finite element grid for device physics simulations.

A simulated voltage variation was imposed at the outer and inner contacts to explore the light current-voltage (I-V) device performance, and the results are plotted in **Figure 5.13**. When the diffusion length becomes comparable to the shell dimensions, a fraction of the generated carriers can no longer reach the junction before recombining, and the overall short circuit current density drops, becoming limited by the shell photocurrent. **Figure 5.14** plots the SRH recombination for one of the scenarios considered. At higher lifetimes, the carriers diffuse throughout the shell, leading to more homogeneous recombination whereas the carriers are more localized for the short diffusion length devices. Since the conformal structure features a uniform, radial junction, the carrier path length is shorter than the path length in the hemisphere or sphere structures and hence the short circuit current density in the conformal structure is reduced less significantly as the minority carrier lifetime decreases.

Looking at the voltage drop as a function of minority carrier lifetime, the decrease in open circuit voltage for the hemisphere structure is slightly less than for the sphere which

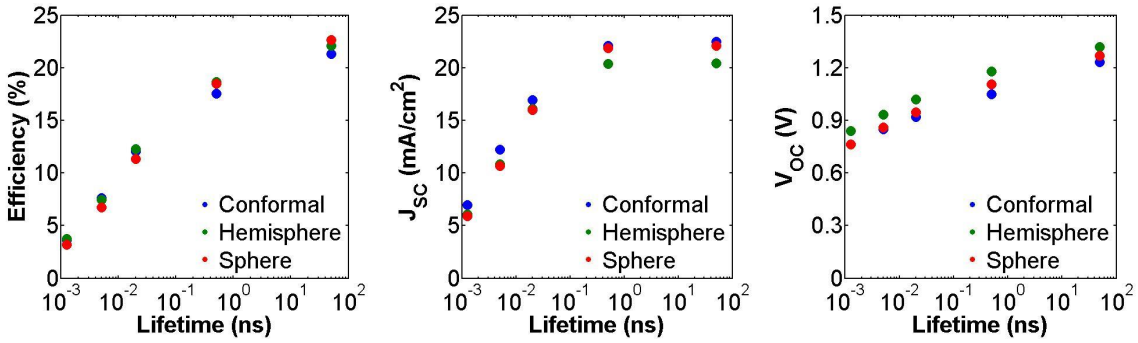


Figure 5.13: Efficiency, short circuit current density, and open circuit voltage of the tandem wire array solar cell structures as a function of the $GaAs_{0.9}P_{0.1}$ lifetime.

in turn is significantly less than the open circuit voltage drop for the conformal structure. The voltage degradation can be directly related to Shockley-Read-Hall recombination and the overall volume of material. For example, for the 7 $\mu$m pitch, the conformal structure contains 133.3 $\mu m^3$ of $GaAs_{0.9}P_{0.1}$ while the hemisphere contains only 57.5 $\mu m^3$ per wire. The larger defective volume leads to a higher dark current in the conformal structure and hence a lower $V_{OC}$ as $V_{OC} = \frac{kT}{q} \ln(\frac{J_{SC}}{J_0} + 1)$. Thus, in comparing the hemisphere and conformal geometries, the former retains a higher voltage as the lifetime decreases due to the lower overall material volume, while the latter shows a smaller incremental current loss due to the shorter distance to the junction.

In order to investigate the effects of the individual subcells, a contact was placed at the interface between the two cells, and each cell was simulated independently. The results from a representative hemispherical tandem structure with a 50 ns lifetime can be found in **Table 5.3**. The $GaAs_{0.9}P_{0.1}$ and the $Si_{0.1}Ge_{0.9}$ bandgaps are 1.54 and 0.79 eV, respectively. Subtracting 0.4 eV from each as an approximation of the potential drop due to unavoidable thermodynamic effects, ideal subcell $V_{OC}$s of ~1.14 and ~0.39 V would be expected. The actual subcell $V_{OC}$s are below this value. In the case of the $GaAs_{0.9}P_{0.1}$, the addition of radiative and auger recombination and window layer resistance account for the ~13 mV difference. For the $Si_{0.1}Ge_{0.9}$ wire, SRH recombination causes the voltage loss. The dimensions of the wire (40 $\mu$m in length) are on the order of the diffusion length (100 $\mu$m) and hence appreciable recombination would be expected and is in fact seen in the simulation. Finally, the simulation compares favorably to the analytical model values of Table 5.1, with a smaller $J_{SC}$ in the $Si_{0.1}Ge_{0.9}$ due to its shorter length of 40 $\mu$m (limited to

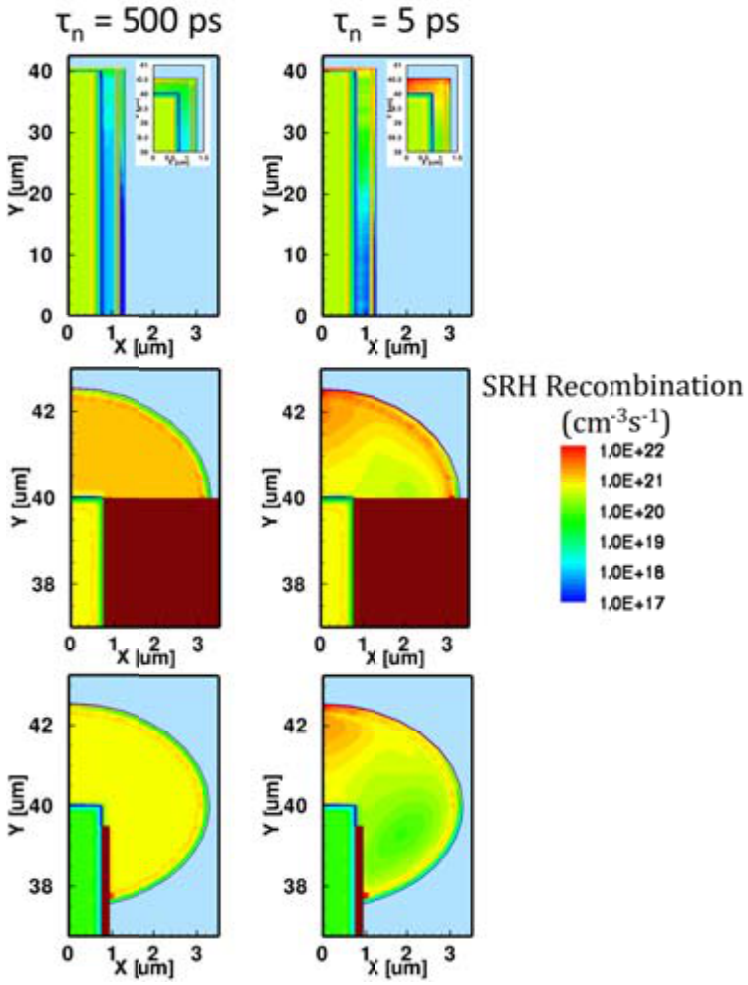


Figure 5.14: Shockley-Reed-Hall recombination for $\tau_n = 500$ or 5 ps in the $GaAs_{0.9}P_{0.1}$ cell for an array with a 7 $\mu$m pitch.

this value by computation memory), reduced $V_{OC}$s due to additional loss mechanisms, and slightly reduced fill factors. Additional simulations will likely bring convergence between the models as the structure and doping profiles are further optimized.

Table 5.3: Light IV characteristics for a representative hemispherical tandem.

| | $V_{OC}$ (V) | $J_{SC}$ (mA/cm$^2$) | Eff (%) | FF (%) |
|---|---|---|---|---|
| 4 $\mu$m pitch | 1.01 | 23.2 | 20.8 | 88.4 |
| $GaAs_{0.9}P_{0.1}$ shell | | | | |
| 40 $\mu$m tall | 0.26 | 20.0 | 3.58 | 67.7 |
| $Si_{0.1}Ge_{0.9}$ wire | | | | |
| Tandem | 1.32 | 20.4 | 22.1 | 82.1 |

The effects of increasing the surface recombination velocity on device performance were also explored. The $Ga_{0.56}In_{0.44}P$ surface, the $Si_{0.1}Ge_{0.9}/Ga_{0.56}In_{0.44}P$ interface, and the $GaAs_{0.9}P_{0.1}$/dielectric interfaces of the sphere and hemisphere structures were given recombination velocities of first $10^4$ and then $10^6$ cm/s. **Table 5.4** lists the device results. The conformal structure's behavior is relatively unaffected by the SRV change as the $GaAs_{0.9}P_{0.1}$ is completely coated with the $Ga_{0.56}In_{0.44}P$ window. In fact, the efficiency goes up slightly at high SRVs due to an increase in fill factor. The contact is set as a small area at the bottom of the wire, but, when the SRV is high, the contact effectively extends to the entire outer surface. Minority carriers are reflected by the window layer, but majority carriers recombine at the surface. The hemisphere and sphere designs, on the other hand, experience a drop in performance with increasing SRV due to increasing recombination at the III-V dielectric interface.

Finally, in light of the work by Falub et al. (61), we also considered a modified hemispherical device in which a defective $GaAs_{0.9}P_{0.1}$ rectangular region was added below the hemisphere, as shown in **Figure 5.15**. The hemisphere was set to have a lifetime of 1 ns. The defective region was set to have a high p-type doping concentration of 1 x $10^{19}$ in order to serve as a back surface field. The SRH lifetime in this region could be varied from 1 ns to 1 ps with only a 4 mV drop in $V_{OC}$ and negligible change in $J_{SC}$, as shown in Figure 5.15. The hemisphere is thick enough to absorb all of the above bandgap light and the high doping of the defective layer repels minority carriers away from the defective region and

Table 5.4: Device performance as a function of surface recombination velocity.

| | SRV (cm/s) | $V_{OC}$ (V) | Eff (%) |
|---|---|---|---|
| Conformal | $10^4$ | 1.23 | 21.3 |
| | $10^6$ | 1.20 | 21.4 |
| Hemisphere | $10^4$ | 1.27 | 20.9 |
| | $10^6$ | 1.11 | 17.0 |
| Sphere | $10^4$ | 1.24 | 21.7 |
| | $10^6$ | 1.06 | 17.6 |

towards the junction. Thus, if defects due to lattice mismatch or polar on nonpolar growth can be grown out within a few microns of the wire base, the cell can achieve high efficiencies despite their presence.

## 5.7 Summary and Outlook

An analytical model suggests that $GaAs_xP_{1-x}$ on $Si_{1-x}Ge_x$ tandem wire array multijunction solar cells can achieve efficiencies approaching 34% with diffusion lengths on the order of 10 $\mu$m, optically thick materials, and a low loss tunnel junction. Full field optical modeling revealed that current matching can be realized for a variety of structures with careful geometric design. The optical modeling also elucidated many of the reflection and absorption loss mechanisms e.g. guiding into the wire and reflection of red light from the lower III-V air/oxide interface. Electronic modeling emphasized the importance of high lifetime material in the active layer, but suggested that defects at the heterointerface can have minimal impact if doped so as to repel minority carriers. Passivating the masking oxide/III-V interface will also be important for attaining high efficiencies.

For actual device fabrication, growing an effective tunnel junction will be important as will fully enveloping the cell with a window layer. The tunneling masses and effective Richardson constants for carriers across the tunnel junction are unknown for the materials that were considered here and hence measuring these values in real devices would be useful information.

Future simulations should consider refining the optical model to take into account the actual geometry of the grown devices and should include defect levels, defect distribution,

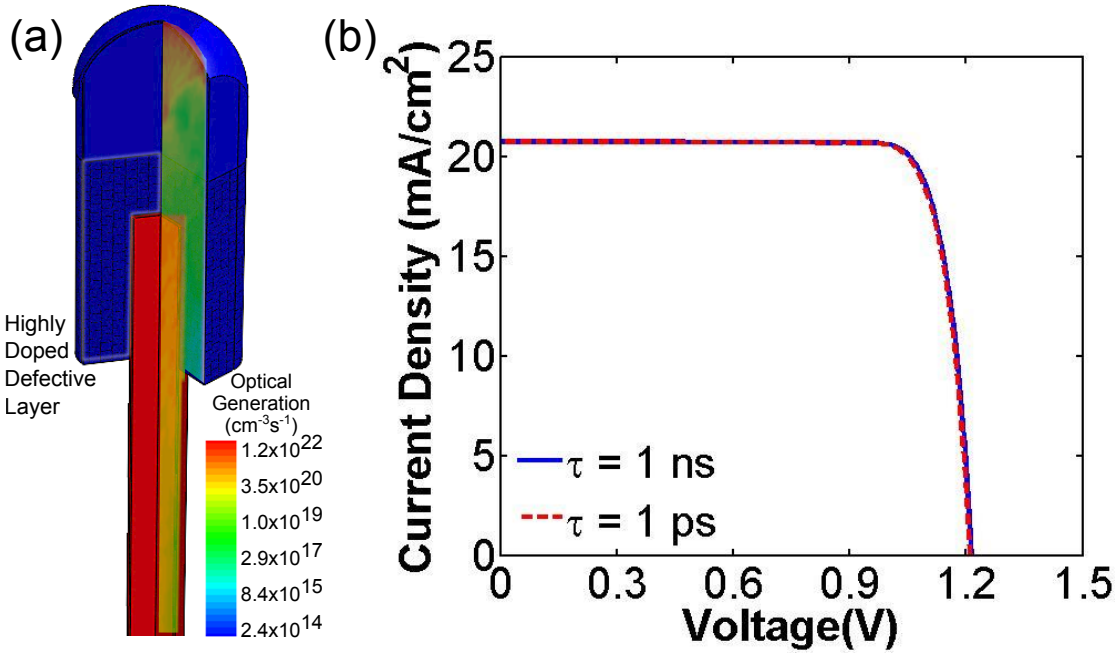


Figure 5.15: The influence of a"defective" layer on device performance. (a) Optical generation profile and overview for a $GaAs_{0.9}P_{0.1}$ on $Si_{0.1}Ge_{0.9}$ cell with a"defective" layer. (b) Light IV curves for 1 ns and 1 ps SRH lifetimes in the "defective" layer.

and measured electrical properties. The properties of cells made with other materials (e.g. $GaIn_{1-x}P_x$) could also be explored as could the addition of a third material to make a triple junction. Additionally, structures other than wires should be considered both in simulations and in actual growth. The proper initial structure may allow for rapid defect mitigation despite the use of greatly mismatched materials.

Finally, while we have specifically explored the implications of III-V on wire growth for creating tandem wire array cells, the mechanism may also be useful for creating flexible, standalone III-V cells, LEDs, or other devices on a reusable Si wafer. Wire arrays may be able to accommodate thicker strained layers than planar films before relaxing through defects, allowing band structure alteration and e.g. higher mobilities.(155)

# Chapter 6

## $Si_{1-x}Ge_x$ Wire Growth

### 6.1 Previous Work and Overview

In order to realize the simulated tandem wire cells in practice, $Si_{1-x}Ge_x$ wire arrays had to be grown. While $Si_{1-x}Ge_x$ nanowires have been synthesized using silane and germane,(146) $Si_{1-x}Ge_x$ wires have not yet been fabricated in ordered arrays or using high temperature Cl chemistry.

On one end of the alloy continuum, the Atwater Group has grown ordered arrays of Si wires for years. Chris Chen and Hal Emmer began at these Si growth conditions and slowly introduced Ge, allowing them to grow wires with up to 10% Ge composition. However, higher Ge concentrations could not be achieved, likely due to a prohibitively high strain energy between the Si substrate and Ge rich alloys, which would inhibit wire nucleation.

On the other end of the continuum, Givargizov (24) demonstrated Ge "whisker" growth from $GeCl_4$ at 650-800°C and Song et al. (156) suggested that Si impurities play a key role in modifying the bulk and surface energetics of the vapor-liquid-solid process for Ge wire growth. With these prior efforts as guides, Ge wires were grown with Au, Cu, and Ni catalysts on Si substrates, though array fidelity was less than 50% for all metals. The addition of small amounts of HCl, $BCl_3$, and $SiCl_4$ clearly modified the growth morphology, but did not improve fidelity. Strain-induced dislocations and nucleation barriers at the wire/substrate interface likely inhibited wire growth normal to the substrate. Further, growth on Ge substrates did not lead to any growth at all, likely due to the formation of a stable Au/Ge alloy.

Thus, to achieve high fidelity Ge wire arrays for the exploration of structured III-V on Ge growth, pillars with a variety of pitches were prepared with reactive ion etching (RIE)

from (111) and (100) Ge substrates using Ti hard masks. Etching was observed to occur preferentially in the $< 111 >$ direction.

Finally, $Si_{1-x}Ge_x$ wire arrays and CVD and RIE Ge wires were covered with a PECVD $SiO_x$ and selectively patterned to expose the tips. These structures were then sent to NREL for GaAs growth as detailed in the next chapter.

## 6.2 Discussion of Ge Chemistry and Catalysts

Theoretically, the growth of Ge wires should follow the physical processes outlined in Chapter 2. **Figure 6.1** shows the phase diagrams for Au/Ge and Cu/Ge, respectively, suggesting that vapor-liquid-solid growth should be possible within these materials; a liquid alloy of Ge and the catalyst will form and, by supersaturating this alloy, crystalline Ge should be deposited. However, the actual growth conditions for Ge wires may be radically different from those optimized for Si wire growth. Ge becomes a liquid at 938°C, forcing the use of a lower growth temperature than was used for growing Si wires. Furthermore, the decomposition of $GeCl_4$ will not produce the same ratios and species of Cl-containing molecules that will result from $SiCl_4$ decomposition,(37) and the kinetics and energetics of the compounds may be very different. Thus, varying conditions will prevail within and around the catalyst alloy and at the growth interface.

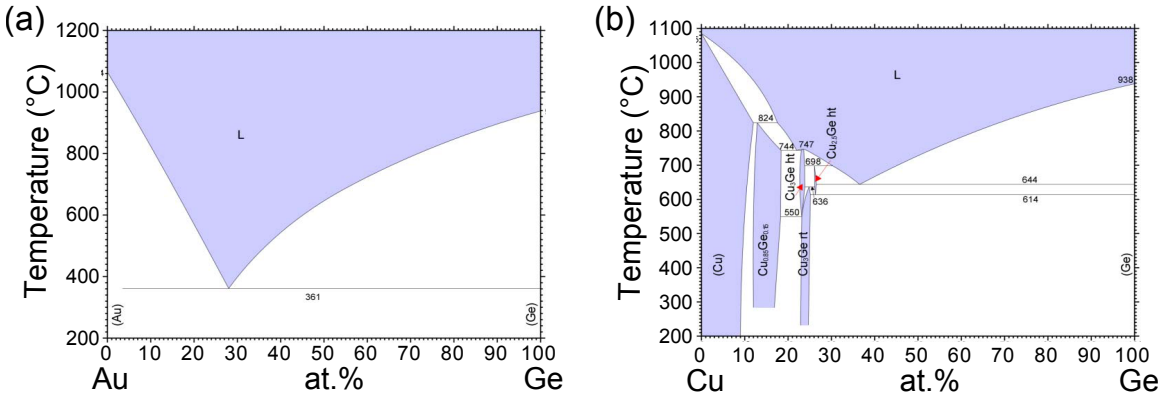


Figure 6.1: Phase diagrams for Ge and Au or Cu. Reprinted with permission of ASM International. All rights reserved. www.asminternational.org (157), (158)

Initial attempts to grow $Si_{1-x}Ge_x$ wires were highly inconsistent. These growths were performed at high temperatures ($\sim 1000$°C) using Cu catalyst on Si substrates and taking

the vapors from heated $GeCl_4$. The wafers were often heavily etched and a liquid condensed on the walls of the reactor. Further investigation suggested that the $GeCl_4$ was decomposing into GeCl and HCl, the former condensing on the walls of the reactor and the latter etching the growth substrates.(159) Givargizov (160) used far less $GeCl_4$ for growth of Ge films, and hence our reactor was modified to bubble $H_2$ through the $GeCl_4$ in order to achieve lower concentrations, as seen in Figure 2.8. Bubbling led to more repeatable growths and allowed for forays into growing $Si_{1-x}Ge_x$ wires.

## 6.3 Au Catalyzed Ge Growth

As the Au/Ge phase diagram has no germanicides, Au was chosen as the initial catalyst for attempting Ge wire growth. The temperature and flow rates were swept over a range from 750-850°C and $GeCl_4/H_2$ = 50/900-100/650 sccm, respectively. Two distinct $GeCl_4$ reactions dominate in this range:

1. $GeCl_4 + Ge \leftrightarrow 2GeCl_2$,
2. $GeCl_4 + H_2 \leftrightarrow GeCl_2 + 2HCl$.

The first reaction etches Ge while the second leads to growth. The competition of these two reactions led to the wide range of morphologies seen in **Figure 6.2**.

At low temperatures, polycrystalline growth dominated. As the temperature was raised, wire-like structures emerged, with the growth appearing to be directed by the catalyst. Finally, for the highest range of temperatures studied, single crystals nucleated at each catalyst site, but the catalyst did not appear to be active in material deposition. Dailey et al. (161) saw similar structures for lower temperature, low digermane partial pressure growth.

By fixing the temperature at 800°C and varying the $GeCl_4$ and $H_2$ flow rates, wires were grown at $GeCl_4/H_2$ = 75/900 sccm. The array fidelity was $\sim$ 40% with defects primarily due to lack of wire nucleation or to wire kinking. Many wires kinked almost immediately after growth and all appeared to diverge from normal at the same height. This height likely is a critical point for defect relaxation stemming from the Si substrate/Ge wire lattice mismatch. At lower $GeCl_4$ flows, wire growth rapidly disappeared. At 100/900 flows, wires were achieved at the sample edge and polygonal crystals were seen in the middle of the sample.

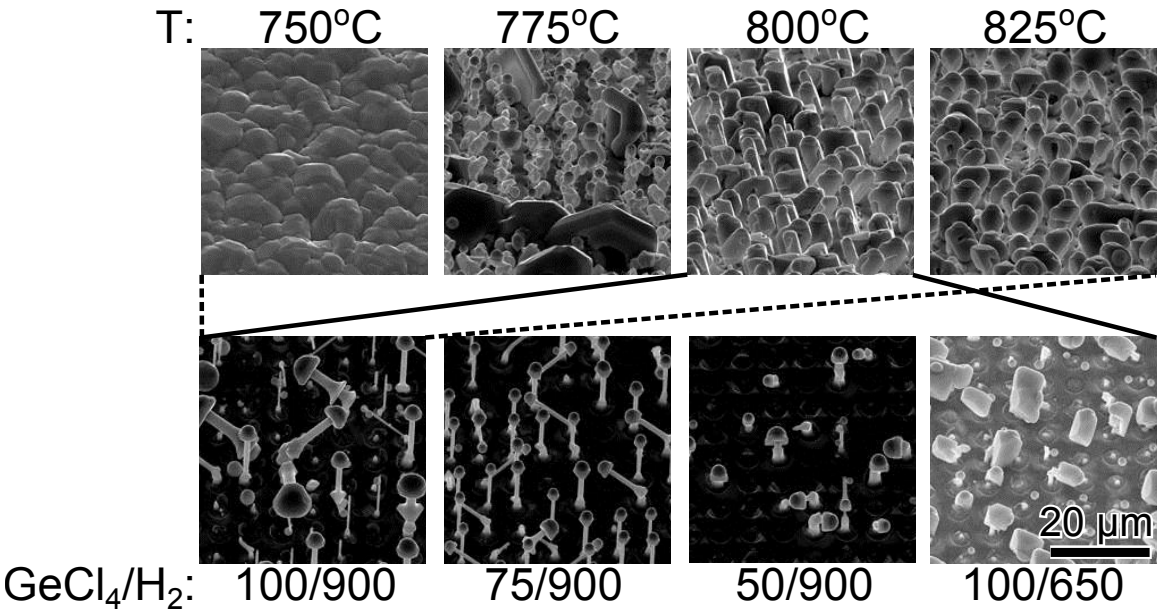


Figure 6.2: Ge on Si growth morphology as a function of growth temperature and $GeCl_4/H_2$ flow rates.

The material properties of the as-grown wires were explored using X-ray diffraction (XRD) and energy dispersive X-ray spectroscopy (EDX) (**Figure 6.3**). $2\Theta$ XRD scans of the wires seen in Figure 6.2 revealed a single crystal Ge peak at 27.3° and a single crystal Si peak at 28.44° from the substrate. The broad peak in between the Ge and Si peaks also suggests the presence of strained Ge or $Si_{1-x}Ge_x$. Overall, however, the Ge peak sharpness and intensity relative to the Si peak suggests that the bulk of the wire is crystalline, relaxed Ge. The EDX scans reinforce that the wires are pure Ge, with a Si peak appearing only at the substrate.

## 6.4 Influence of HCl, $BCl_3$, or $SiCl_4$ on Growth

Since $BCl_3$ and $SiCl_4$ have been found to alter Si and Ge wire growth, respectively, the gases were independently introduced to the growth process to evaluate their effect on morphology.(156) **Figure 6.4** displays the results, along with the effect of adding HCl. Each led to uniquely different structures, but none improved the overall fidelity; they altered the chemistry but not in such a way as to prefer $< 111 >$ oriented wire growth.

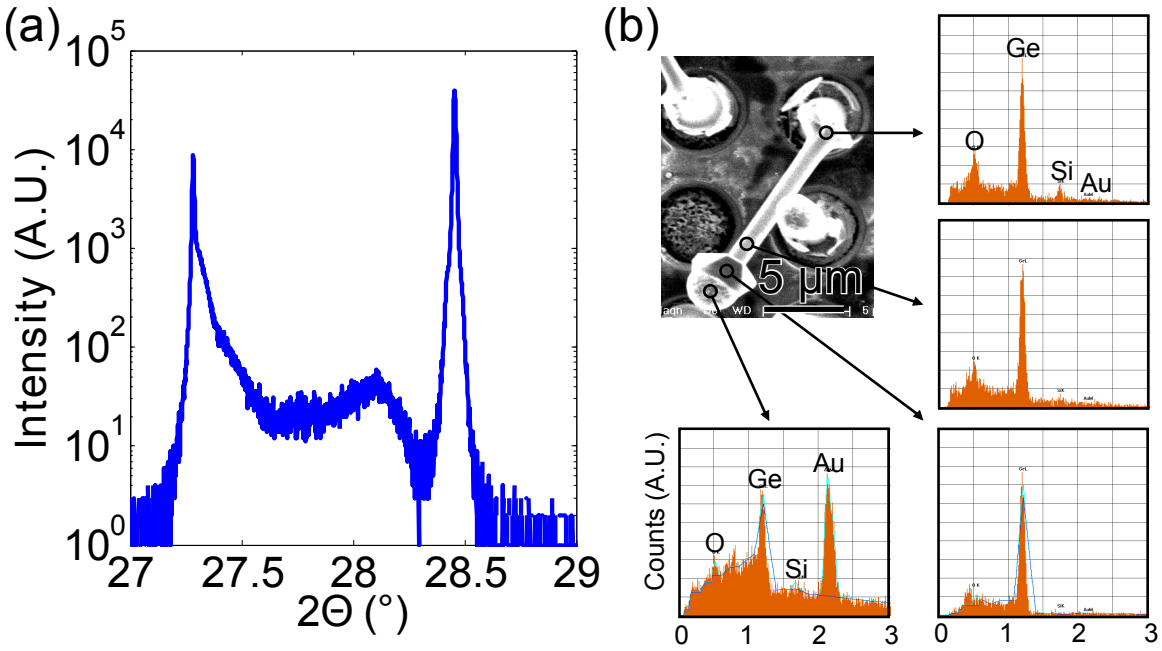


Figure 6.3: (a) XRD plot of Ge wires grown on a Si substrate. (b) EDX of a Au catalyzed Ge wire for a variety of positions along the wire length.

## 6.5 Ni, In, and Cu Catalyzed Ge Growth

Due to the deleterious effects of Au on Si device performance, as well as its scarcity and cost, the above growths were deemed a sufficient demonstration of the feasibility of Ge wire growth, and Ni, In, and Au catalysts were considered with the hope that growth conditions could be found with these metals that would lead to high fidelity arrays. All three have a complicated phase diagram with Ge, as exemplified by Figure 6.1 (b).

The best results from all of the metals can be seen in **Figure 6.5**. Au, Cu, and Ni all led to wire growth, while the high vapor pressure of In caused it to evaporate during the anneal. While the Ni results initially seemed promising, they were not reproducible, and hence Ni was abandoned. Growths with Cu, on the other hand, consistently led to wire formation, though the exact morphology varied with temperature and flow rate as seen in **Figure 6.6**.

Though Cu catalyzed wire growth for a variety of conditions, the fidelity was universally low ($< 50\%$) and normally oriented nanowires often grew alongside their larger counterparts. Furthermore, wire growth could only be initiated if the sample was first annealed at 1000°C. The wire morphology and the prevalence of *nano-* rather than micro- wire growth can

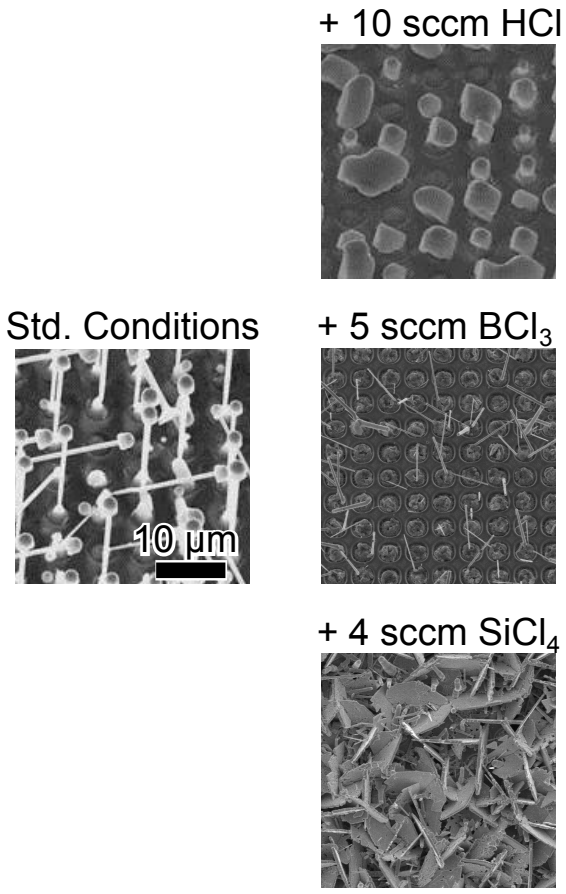


Figure 6.4: The effects of small amounts of $BCl_3$, HCl, or $SiCl_4$ on the Ge growth morphology.

possibly be explained as follows (see **Figure 6.7**):

1. As the sample is annealed at 1000°C, the Cu saturates with Si.
2. The sample is cooled to 800°C, which causes some Si to leave the catalyst alloy and to be deposited on the substrate.
3. $GeCl_4$ is introduced, and Ge penetrates the catalyst particle.
4. Growth only proceeds if the Si/catalyst area is small enough that the strain energy due to lattice mismatch is less than the energy gain from changing the alloy composition by expelling crystalline Ge. This leads to initial growth at small diameters (when the material can relax slightly radially at the interface edges) and explains the abundance of normally oriented *nano*wires.

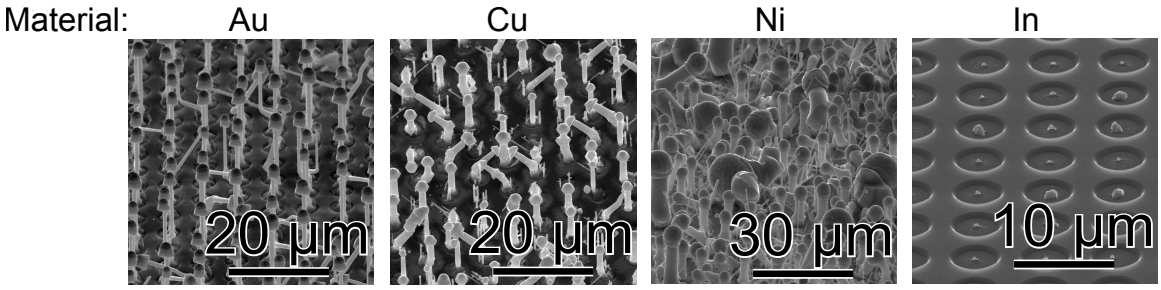


Figure 6.5: Growth attempts with Au, Cu, Ni, and In catalysts.

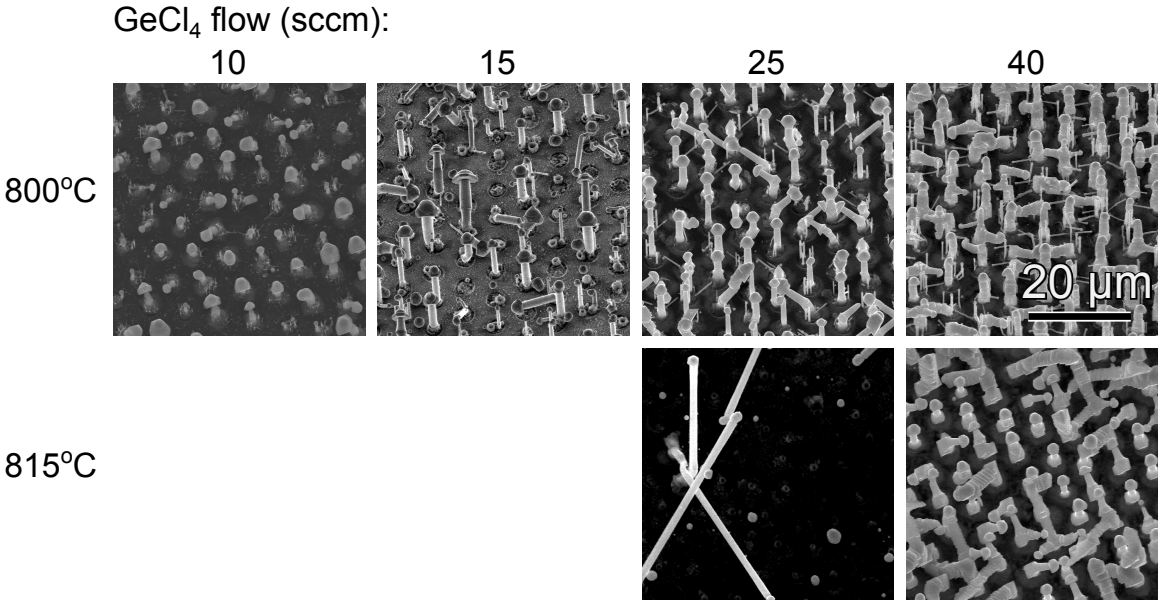


Figure 6.6: The influence of temperature and flow rate on Ge wires grown from Cu.

5. The sample is cooled to 650°C, which causes the remaining Ge to crystallize out of the Cu.

Additionally, as demonstrated by XRD (**Figure 6.8**), the crystal quality of the Cu catalyzed Ge wires was low, inferior to that of the Au grown wires. The Au wires could be seeded directly at 800°C and seemed to grow uniformly after an initial narrowing, likely due to massive defect relaxation at the base. The morphology of the Cu wires, on the other hand, varied along the length, suggesting the continued presence of defects.

To test whether *nano*wire growth might be preferred, nanoscale Cu catalyst particles were deposited on Si substrates.(162) 250 nm holes were patterned by electron beam lithography and filled with 100 nm of Cu. After growth, the substrates were examined, and no wires or metal particles were found at the holes. Cu has a high solubility in Si,(163) and

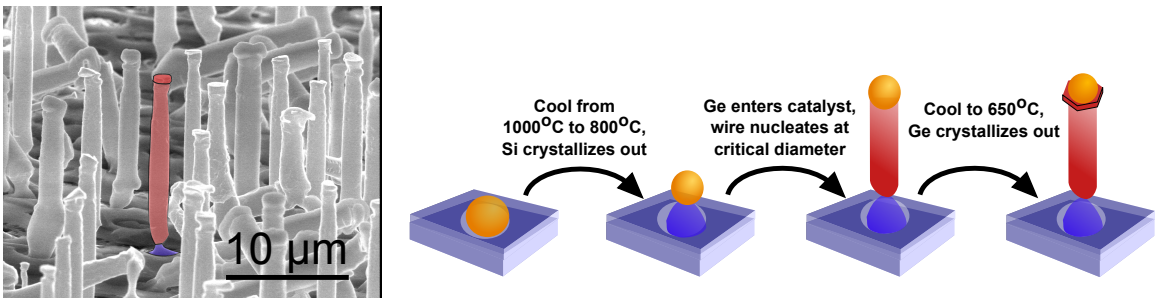


Figure 6.7: Suggested mechanism describing the evolution of the Ge wire morphology.

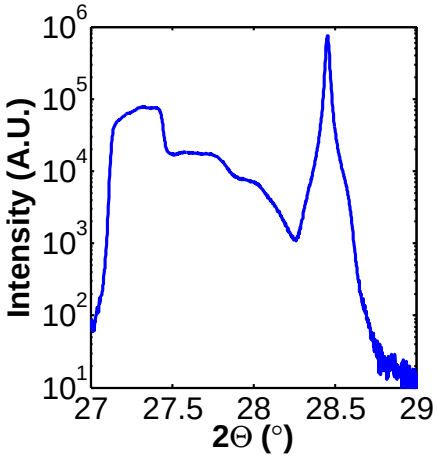


Figure 6.8: XRD plot of Cu catalyzed Ge wires grown on Si.

thus all of the catalyst was likely absorbed by the substrate.

Additionally, growths were attempted directly on a $< 111 >$ Ge substrate to eliminate the effects of strain entirely. Both Au and Cu were used to try to seed growth on the Ge substrate, but no Ge deposition was observed. Instead, the catalyst particle swelled and became spherical. Though no AuGe phases exist on the steady state phase diagram, metastable AuGe phases have been observed during Ge wire growth, and these phases may be preferred under our conditions.(164) As demonstrated in Song et al. (156), additional components may be necessary to change the energetics sufficiently to cause growth to occur.

## 6.6 Cu Catalyzed $Si_{1-x}Ge_x$ Wire Growth

As a final note on growth, when $GeCl_4$ was first installed, $Si_{1-x}Ge_x$ growths were attempted, and, in a few cases, $Si_{1-x}Ge_x$ wires were grown. **Figure 6.9** demonstrates one success with a 20:1 ratio of $SiCl_4$ to $GeCl_4$ and otherwise standard Si wire growth conditions. The fidelity

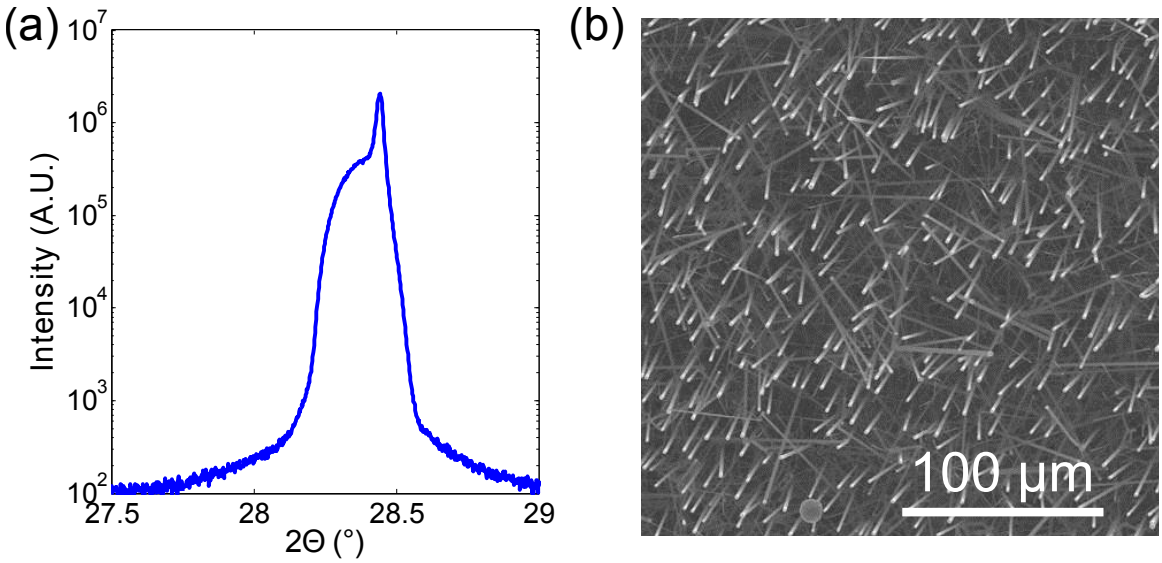


Figure 6.9: $Si_{1-x}Ge_x$ wire growth. (A) XRD plot of Cu catalyzed SiGe wires grown on Si. (b) SEM of $Si_{1-x}Ge_x$ wires.

and crystal quality are both low, but this was the first $Si_{1-x}Ge_x$ success, demonstrating the feasibility of the project. Chris Chen and Hal Emmer went on to refine the growth parameters and to achieve high fidelity, high quality SiGe wires with up to 10% Ge content.

## 6.7 Reactive Ion Etched Ge

Given the difficulties growing $Si_{1-x}Ge_x$ wires, Ge pillars were fabricated using reactive ion etching (RIE) of $< 111 >$ and $< 100 >$ Ge in order to create substrates for exploring the growth of III-Vs on wires.(165) The Ge was patterned as follows:

1. 10 nm of Ti was sputtered onto the wafers to serve as a hard mask.

2. AZ 5214 (a negative resist) was spun onto the samples at 4000 rpm, baked at 95° for 1 min, exposed through the standard wire lithography mask, baked at 115°C for 2 min, flood exposed for 60 s, and developed in CD 026 for 45 sec.

3. The exposed Ti was removed by immersing the samples for 6 sec in an HF based Ti etch from Transene.

4. The samples underwent RIE at 150W in $Cl_2$ for 10 min, forming 3 $\mu$m pillars in a square lattice with 7 $\mu$m spacing.

5. The remaining Ti was removed with the etchant and the Ge was lightly etched by immersion in 6% $H_2O_2$ in $H_2O$ for 5 min in order to clean the surface.

Representative patterned Ge samples can be seen in **Figure 6.10**. The $< 111 >$ direction etched preferentially under the chosen conditions, leading to the rough substrate seen for the (100) sample. Overall, the RIE process was straightforward and led to the desired Ge structures.

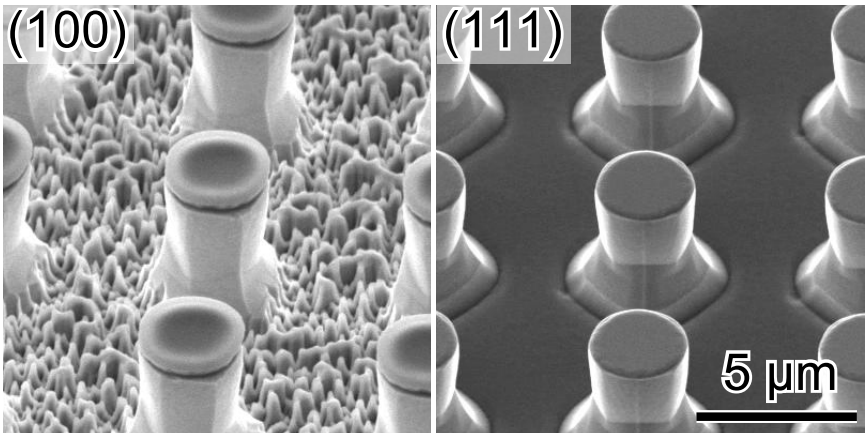


Figure 6.10: Reactive ion etched Ge pillars on (111) and (100) substrates.

## 6.8 Masking Wires

Finally, after growing Ge and $Si_{1-x}Ge_x$ wires and etching Ge pillars, they needed to be masked in order to achieve selective III-V growth at the tips. However, while $SiO_x$ is stable, $GeO_x$ is water soluble and would be rapidly removed under traditional MOCVD growth conditions. Thus, the booting process developed for creating Si pn junctions could not be applied here. Instead, $SiO_x$ was deposited on the wires with PECVD. The wires were then infilled and etched. The overall process proceeded as follows:

1. The etched Ge wires were coated with ~300 nm planar equivalent PECVD $SiO_x$ deposited at 350°C, 20 W of high frequency power, 1000 mT, 42 sccm of $SiH_4/N_2$, and 838 sccm of $N_2O$.

2. The wires were infilled with S1813 by spinning it in three times at 3000 rpm (for the second and third infills, the resist was added while the wafer was spinning). The resist

was then baked at 115°C for 5 min. The samples were ashed at 300 mT of $O_2$ and 300W for 15 min to expose the pillar tips.

3. The $SiO_x$ was removed at the tips by immersion in BHF for 90 sec.

4. The resist was removed with acetone.

A booted Ge can be seen in **Figure 6.11**. Additionally, the $SiO_x$ protective mask is visible over much of the pillars in Figure 6.10, with the exposed Ge tip appearing darker than the oxide.

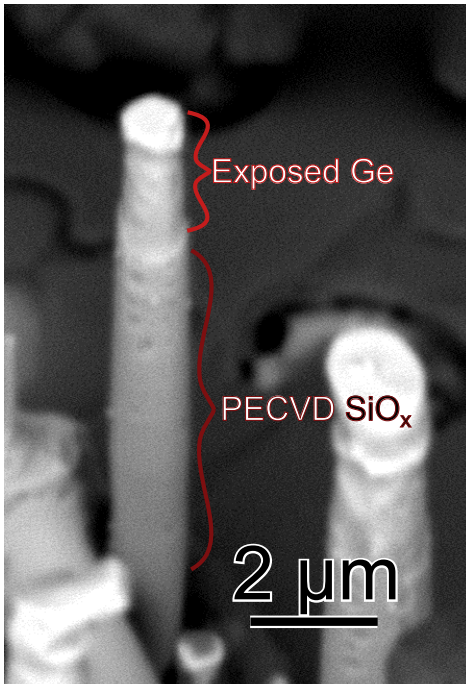


Figure 6.11: A Ge wire masked with PECVD $SiO_x$.

## 6.9 Summary and Outlook

Ge wire growth was attempted under a variety of different flow rates and temperatures for Au, Cu, Ni, and In catalyst, and on both Si and Ge. Wires were grown on Si with Au, Cu, and Ni under select conditions, but the fidelities failed to exceed 40%, likely due to the effects of strain resulting from lattice mismatch. Growth on Ge resulted in spherical alloy particles rather than crystalline Ge growth. $BCl_3$, HCl, and $SiCl_4$ were added to attempt

to alter the growth energetics to favor oriented wire growth to no avail. Thus, pillars were etched out of planar Ge to allow for the exploration of III-V on wire growth.

While the attempts to grow high fidelity arrays of Ge wires in this thesis were unsuccessful, high fidelities should be possible with further efforts. The use of smaller Cu catalyst particles or the addition of impurities may yet prove effective. Exploring different conditions for wire nucleation (and switching conditions for growth) may also be fruitful. TEM studies of the Si/Ge interface and of Ge wires would be invaluable for elucidating the defect distribution and the growth mechanisms. Additionally, physical models for wire nucleation are sorely lacking and should be developed in order to understand the effects of strain, catalyst size, etc. on growth.

Finally, some of the non-wire single crystalline Ge structures of Figure 6.2 may prove useful on their own. If arrays of highly crystalline Ge polygons can be grown and masked to restrict III-V growth to a few points or surfaces, the desired strain relief and defect guidance may still be realizable and allow concepts similar to the tandem design of Chapter 5 to be realized. A broad range of structures could also be made with RIE and other conventional fabrication techniques, again potentially leading to interesting substrates for III-V growth.

# Chapter 7

## GaAs Growth on Ge

### 7.1 Previous Work and Overview

Once structured Ge substrates had been fabricated, III-V growth on these architectures could be explored, bringing the realization of tandem wire array solar cells one step closer to reality. While the wire geometry may mitigate the formation and propagation of defects that originate from lattice mismatched and polar-on-nonpolar growth, leading to long lifetime III-V material, these traits have yet to be demonstrated in practice. Seeded CVD growth of axial Ge/GaAs wire heterostuctures has been performed,(108) but, to our knowledge, conventional epitaxial growth of III-Vs on highly structured $Si_{1-x}Ge_x$ has not been explored. Thus, the work in this chapter set out to experimentally investigate the feasibility of III-V on $Si_{1-x}Ge_x$ wire growth.

While $GaAs_{0.9}P_{0.1}$ was used in the optoelectronic modeling of Chapter 5, GaAs was selected as a representative III-V for these cursory experiments. The detailed balance limiting efficiency of the GaAs/Ge material combination is not the maximum for two cells, but it still exceeds 35% (Figure 5.1). Additionally, the lattice mismatch between GaAs and Ge growth is low ($< 0.1\%$) as is the coefficient of thermal expansion mismatch, and the growth of GaAs on Ge has been extensively explored.(166)

As Caltech does not have the necessary facilities or expertise to grow GaAs, the substrates were sent out for growth. CVD grown $< 111 >$ Ge and $Si_{0.9}Ge_{0.1}$ wires, $< 100 >$ and $< 111 >$ RIE fabricated Ge pillars, and oxide masked, planar (100) and (111) Ge were sent to Dr. Bill McMahon at the National Renewable Energy Lab (NREL) for growth of undoped, $Al_{0.2}Ga_{0.8}As$-cladded GaAs.(167) While these films could not be probed electronically due to the thick, intrinsic window layers, time resolved photoluminesence studies

(TRPL) and X-ray diffraction (XRD) gave insight into the material quality.

Finally, photovoltaic GaAs devices were designed and optimized through optoelectronic simulations, and substrates were sent to Sumika, a commercial foundry, to grow the designed layers.

## 7.2 Structure Overview

CVD grown $< 111 >$ Ge and $Si_{0.9}Ge_{0.1}$ wires, $< 100 >$ and $< 111 >$ RIE fabricated Ge pillars, and oxide masked, planar (100) and (111) Ge were prepared and sent to NREL for GaAs growth. A piece of planar (311) Ge was also included in each growth run to serve as a control.

NREL deposited the following layers on the substrates:

Table 7.1: Overview of GaAs on Ge growth run.

| Layer | Material | Thickness ($\mu$m) |
|---|---|---|
| Superlattice 1 | GaAs | 0.05 |
| Superlattice 2 | $Al_{0.2}Ga_{0.8}As$ | 0.05 |
| Repeat previous pair 10 times | | |
| 21 | $Al_{0.2}Ga_{0.8}As$ | 0.05 |
| 22 | GaAs | 1.5 |
| 23 | $Al_{0.2}Ga_{0.8}As$ | 0.2 |
| 24 | GaAs | 0.01 |

The superlattice serves to mitigate defects stemming from the Ge/GaAs interface due to lattice mismatch and polar-on-nonpolar growth, and the $Al_{0.2}Ga_{0.8}As$ serves as a window layer, confining minority carriers to the bulk. The presence of the window layers allows the material quality to be assessed through TRPL.

## 7.3 Material Characterization

After receiving the samples back from NREL, they were characterized with photoluminescence (PL), TRPL, XRD, and SEM. In order to not degrade the material with the electron beam, SEM was performed last.

**Figure 7.1** shows full characterization of the (311) planar control sample. The GaAs film appeared smooth under optical Nomarksi imaging. XRD of the < 311 > direction revealed the single crystalline, epitaxial nature of the Ge (peak at 53.69°), the GaAs (peak at 53.74°), and the $Al_{0.2}Ga_{0.8}As$ (peak at 53.73°). The lower intensity side peaks stem from the superlattice. Finally, TRPL of the film (635-690 nm excitation, 30 mW, 20 MHz source) yielded a lifetime of ∼7 ns. Thus, the GaAs film grown on the (311) Ge was very high quality.

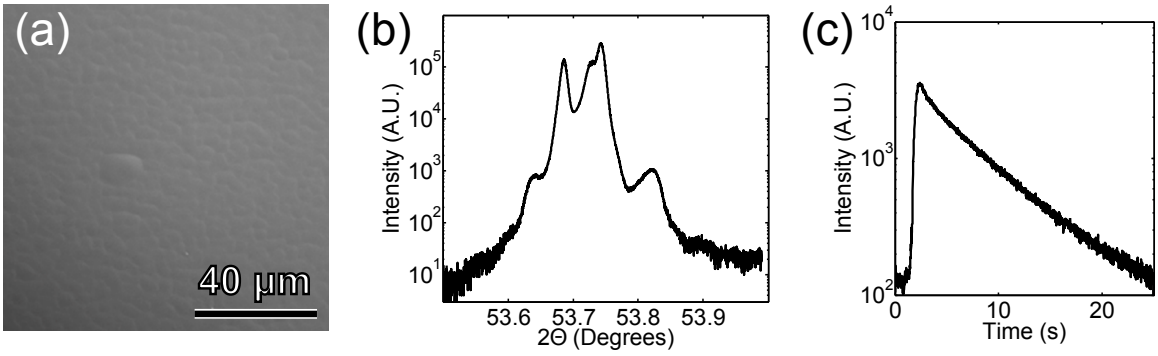


Figure 7.1: GaAs Growth on (311) Ge. (a) Nomarski optical image of GaAs grown on (311) planar Ge. (b) XRD rocking curve of the structure in (a). (c) TRPL of the film.

**Figure 7.2** shows the SEMs of the structured Ge before and after GaAs growth. In general, the GaAs appears rough, though crystalline, with some smoother crystallites arising from the Ge wires. For the RIE wires, the {1 -1 0} planes appear favored from the top down view of the (111) growth while the {1 0 0} planes appear to be favored for the (100) substrate.

### 7.3.1 Patterned, Planar Substrates

As an additional control to the (311) Ge, $SiO_x$ masked (111) and (100) substrates were included in the NREL growth runs. These samples restricted the growth to 3 $\mu$m holes in a 7 $\mu$m pitch square array and either (100) and (111) surfaces, similar to the wire tops.(168) The samples' characteristics are featured in **Figure 7.3**. The films were rough, and the XRD peaks were slightly broader than for the other samples, as seen in the next section, suggesting the presence of defects. The PL showed a broad GaAs peak as well as a red defect peak and a blue peak, likely from the $Al_{0.2}Ga_{0.8}As$.

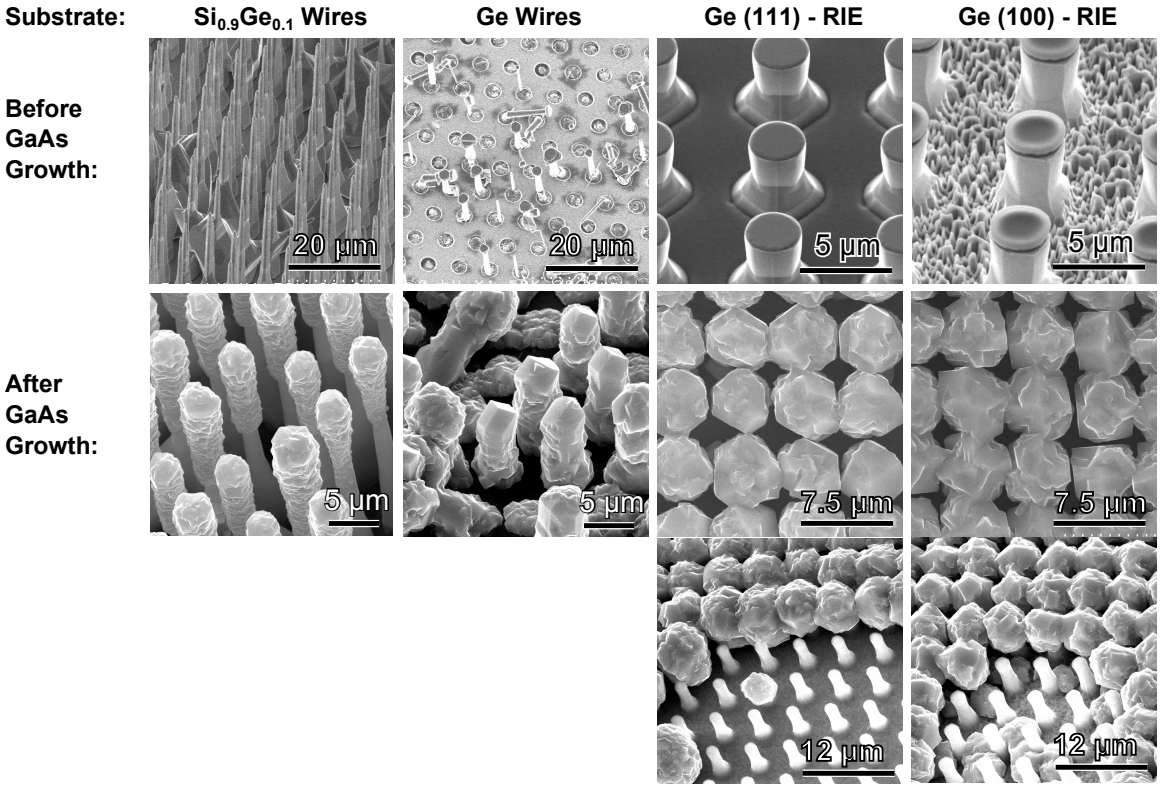


Figure 7.2: SEMs of structured Ge before and after GaAs growth.

### 7.3.2 X-Ray Diffraction

XRD was performed on all of the structured samples and is shown in **Figure 7.4**. In (a), the peak from the Si substrate and from the $Si_{0.9}Ge_{0.1}$ wires are visible along with the GaAs peak. In the other three plots, the Ge, GaAs, and $Al_{0.2}Ga_{0.8}As$ overlap one another. The Ge peak is smaller than the GaAs peak in (b) due to the small number and small size of the CVD grown Ge wires. In (c) and (d), the Ge peak dominates. Overall, the peaks demonstrated that the III-V layers were epitaxial and of reasonably high quality.

### 7.3.3 Photoluminescence

All of the films luminesced at room temperate, suggesting that the defect density was reasonably low in at least a small portion of the material. The PL spectra are displayed in **Figure 7.5**. (a) and (b) feature spectra of the GaAs grown on the CVD wires. These measurements were done at NREL using a 632 nm excitation source, with both visible and NIR detection. Visible spectra were taken with two different gratings and hence the two different PL spectra. The GaAs grown on the $Si_{0.9}Ge_{0.1}$ wires featured defect luminescence

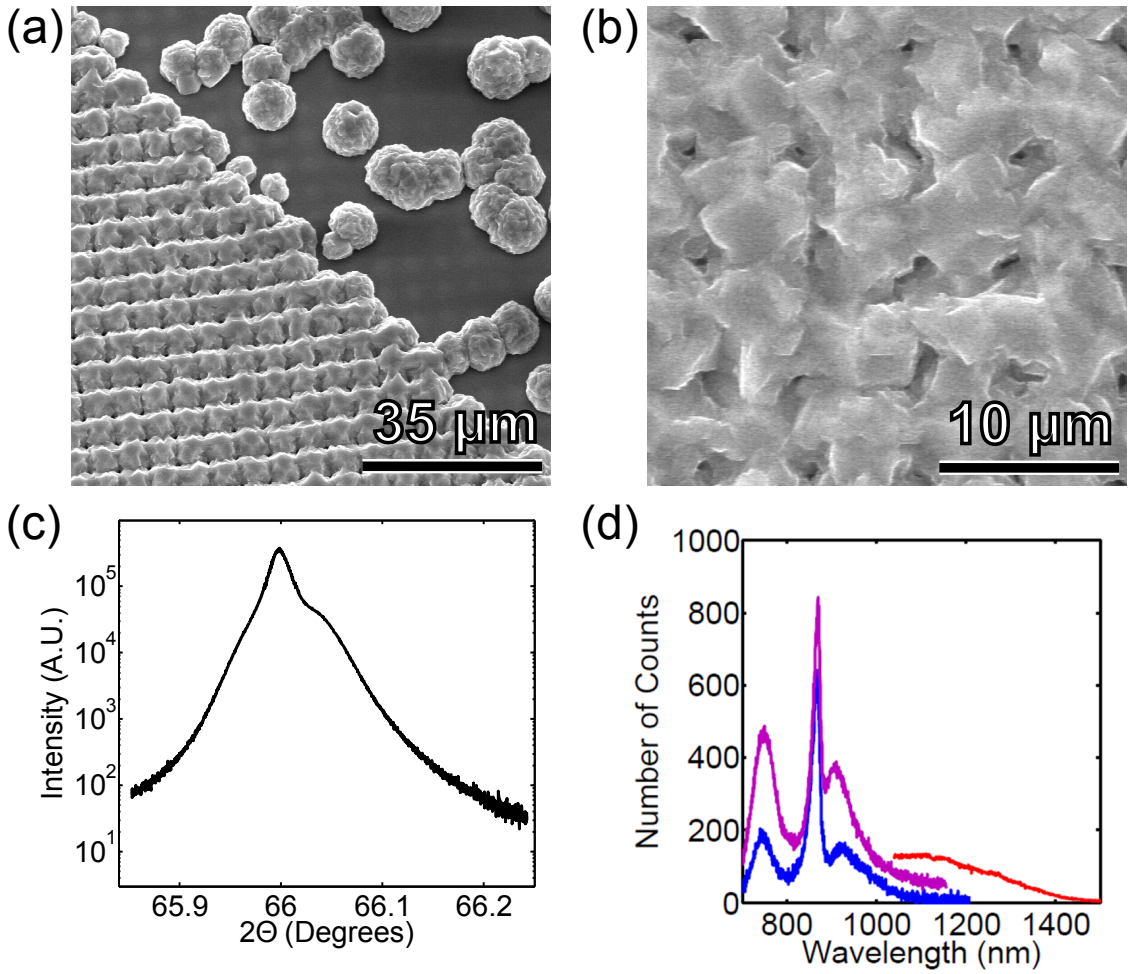


Figure 7.3: GaAs growth on planar, oxide masked Ge. (a) SEM of growth on (111) Ge. The oxide was not fully etched in the area in the upper right. (b) SEM of growth on (100) Ge. (c) XRD of films on (100) Ge. (d) PL of films on (111) Ge.

around 1000 nm, likely due to Si incorporated within the material.(169) PL can also be seen in the NIR. While it is tempting to attribute this peak to the CVD grown wires, the fact that the peaks in (a) and (b) look identical despite the fact that (a) features $Si_{0.9}Ge_{0.1}$ with a nominal bandgap of 1.08 eV while (b) features pure Ge with a bandgap of 0.66 eV suggests that further study is needed. The PL of the RIE etched structures along with PL from the (311) Ge and oxide masked, patterned Ge are shown in (c). These measurements were performed with identical excitation as used for the (311) Ge TRPL and with a 1200 lines/mm grating centered at 870 nm and a visible light CCD. The GaAs film on (311) Ge has a sharp PL peak, indicating that this planar material is high quality with a minimal

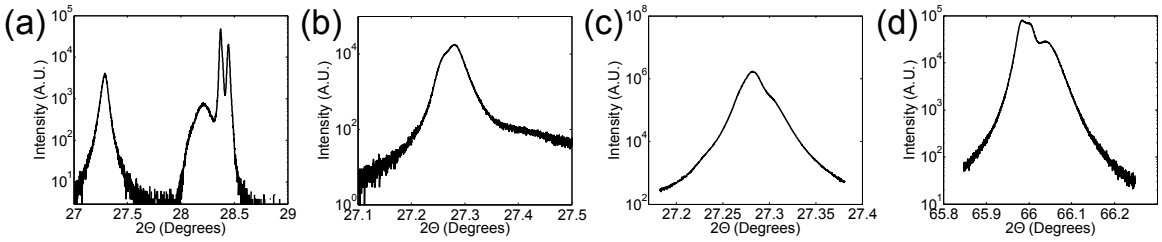


Figure 7.4: XRD of GaAs on structured Ge. (a) GaAs on CVD $Si_{0.9}Ge_{0.1}$ wires. (b) GaAs on CVD Ge wires. (c) GaAs on (111) RIE Ge. (d) GaAs on (100) Ge.

number of defects. The RIE pillars have similarly sharp PL peaks, while the patterned (100) Ge has a broad peak in the sub-bandgap region (between 900-1000 nm) suggesting the presence of defects within the film. Similar peak broadening into the red can be seen for the $Si_{0.9}Ge_{0.1}$ wires.

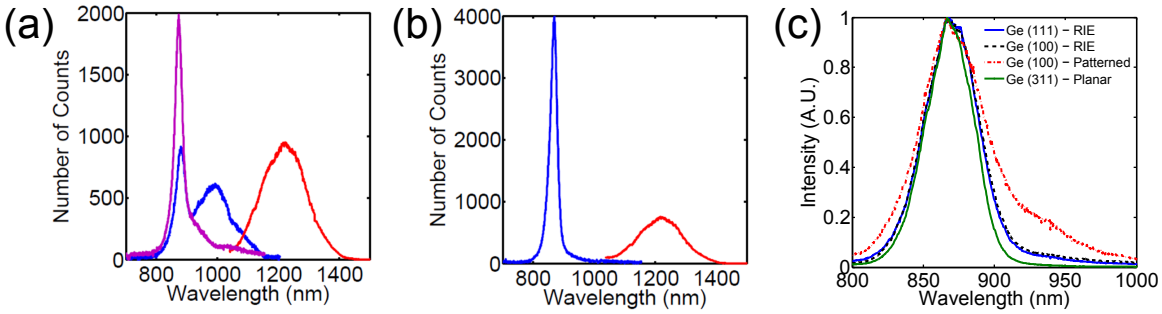


Figure 7.5: PL of GaAs grown on structured Ge. (a) PL of GaAs on CVD $Si_{0.9}Ge_{0.1}$ wires. (b) PL of GaAs on CVD Ge wires. (c) PL of GaAs grown on RIE, oxide masked (patterned), and (311) Ge.

TRPL of the GaAs films allowed for the extraction of radiative lifetimes. **Figure 7.6** shows the time response for the samples. While the curves were highly multiexponential, they all appeared to have ns lifetime components, suggesting that at least some small segments of the films were defect free. (a) features curves obtained at NREL under 780 nm excitation and at 870 nm collection. In (b), the data was obtained as described previously for the (311) sample. The instrument response function was obtained by placing a substrate coated with Lambertian reflecting white paint at the sample position. The signal for $t < 1.5$ sec likely comes from laser scatter within the microscope. More rigorous TRPL experiments for these films are ongoing.

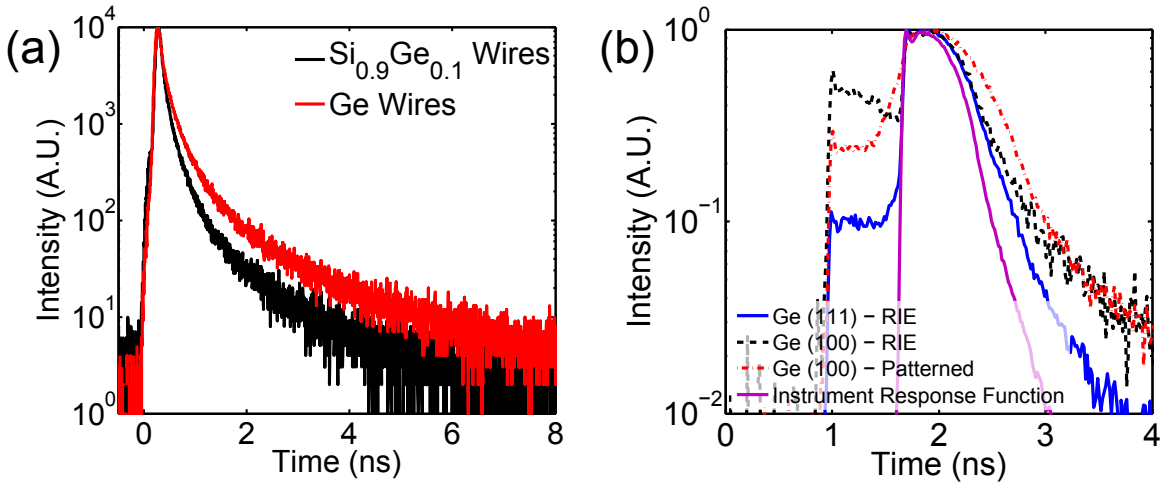


Figure 7.6: TRPL of GaAs grown on structured Ge. (a) TRPL of GaAs on CVD $Si_{0.9}Ge_{0.1}$ and Ge wires. (b) TRPL of GaAs on RIE, oxide masked/patterned, and (311) Ge.

## 7.4 Parameter Optimization for Device Design

Given the promising lifetimes measured for the NREL GaAs growths on Ge, we set out to make full GaAs devices with Sumika, a commercial foundry. Optoelectronic simulations were run in order to optimize the layer thicknesses and doping densities. **Figure 7.7** shows a general schematic of the simulation setup. The initial growth was assumed to be highly defective due to lattice mismatch and polar-on-nonpolar growth and hence the presence of the"defect" layer. The base layer thicknesses was chosen via optical simulations, which suggested that a 2 $\mu$m thick base could generate >26 mA/cm$^2$, ~80% of the maximum value for GaAs. The window and emitter layer thicknesses were chosen to be as thin as possible without risking shunts due to the three-dimensional nature of the growth. The contact layer was set to be as highly doped as possible and, as it will be etched away over most of the sample, was not considered in the model.

For optimizing the doping density,the simulation setup was generally identical to that of Chapter 5. However, doping dependent lifetimes and mobilities were also included. The mobility followed the form:

$$\mu = \mu_0 + \frac{\mu_e}{(1 + \frac{N_A}{N_e})^a},$$

with the specific parameters taken from the Sentuarus parameter file. The lifetimes

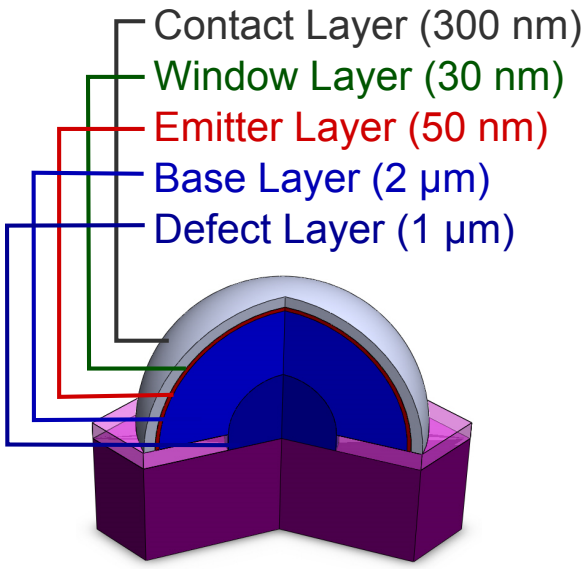


Figure 7.7: Overview of the simulated structure for optimizing the doping levels for a GaAs device grown on Ge.

were roughly fit to Hwang (170) to yield:

$$\tau = \tau_0 (\frac{10^{18}}{N_A})^2,$$

with $\tau_0 = 1$ ns.

**Figure 7.8** displays the device performance as a function of the base and emitter doping for a fixed window and defect doping of 2 x $10^{19}$. The voltage initially increases with emitter and base doping as the Fermi levels split further and further with increasing carrier concentration. However, eventually, the lifetime degradation begins to effect the voltage and increased doping no longer helps. The current, on the other hand, is highest for the lowest doping levels where both the mobility and lifetime are high. The fill factor depends on conductivity which will depend on both the carrier concentration and the mobility. For the range considered, the increase in carrier concentration exceeds the loss in mobility and hence the fill factor increases consistently with doping. Overall, the highest efficiency occurs at a base doping of $\sim$ 1.25 x $10^{17}$ and an emitter of doping of $\sim$ 5 x $10^{18}$ where the increase in voltage is balanced by the loss in current and fill factor.

Having fixed the emitter and base doping, the doping of the window and base were then varied, as seen in **Figure 7.9**. Since the defect layer is assumed to have a low lifetime (1

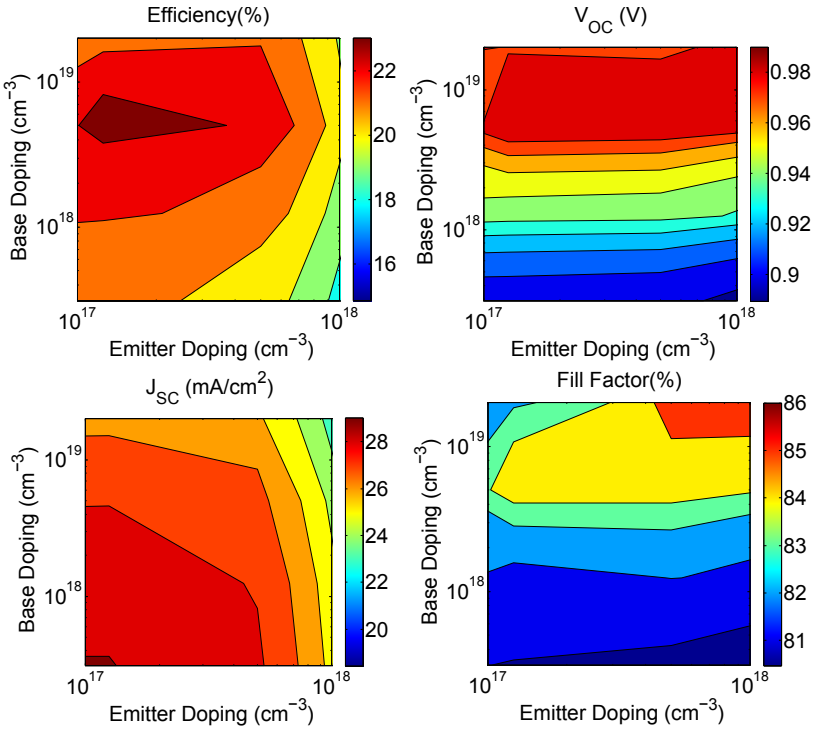


Figure 7.8: Device values for a GaAs hemispherical cell as a function of emitter and base doping (with the window and defect doping set to 2 x $10^{19}$).

ps) and does not absorb much of the incident light and the window layer is also inactive, higher doping leads to higher performance as the generated carriers are further restricted from traveling into defective regions. The fill factor does see some slight drop as the doping is increased due to the loss of mobility in the defective layer, but this small loss is more than made up for by reduced recombination. Hence the window and defect doping were both set at 5 x $10^{18}$ for the growth (the highest level that could be grown without significant material degradation).

Planar (100) and (111) Ge substrates, oxide masked (111) and (100) Ge substrates, RIE, PECVD oxide masked (111) and (100) Ge substrates with 4.5, 5.5, and 7 $\mu$m spacings, and a masked array of Si wires were sent to Sumika for growth of the designed layers. The Ge substrates were all p-type doped at 0.01-0.04 $\Omega$cm, which should allow contact of the GaAs films through the Ge substrates.

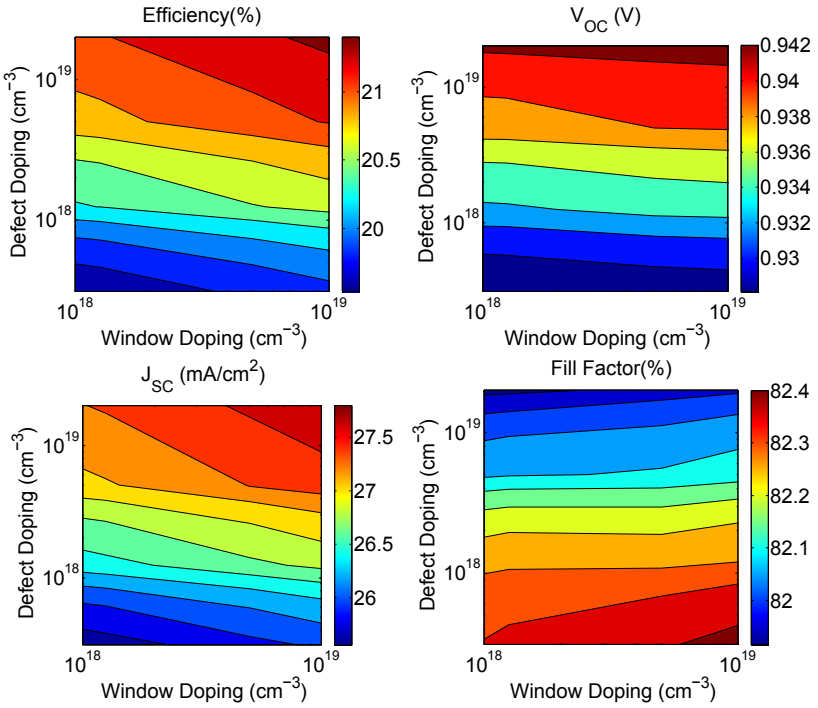


Figure 7.9: Device values for a GaAs hemispherical cell as a function of window and defect doping (with the base doping set to 1.25 x $10^{17}$ and the emitter doping set to 5 x $10^{18}$).

## 7.5 Summary and Outlook

All in all, the initial growths and characterization of GaAs on structured Ge showed promise, with room temperature PL and ns lifetime components. Further characterization will hopefully lead to more insight into the growth e.g. by revealing if certain crystalline planes or geometries are more favorable. Along those lines, TEM characterization is ongoing and should reveal the nature of the defects. If ns lifetimes can be achieved in the films, then high efficiencies should be possible, as outlined in Chapter 5.

Furthermore, investigating the electrical properties of the devices from Sumika should provide a further demonstration of the device feasibility. In order to contact the devices, Au/Ge will be sputtered onto the samples, and they will then be infilled slightly with a polymer (e.g. S1813), allowing the excess metal and contact layer to be removed from the tops of the devices, leaving a ring contact around the outside in the areas that is covered by the polymer. Back contact will be made to the substrates with Ga/In. Individual wires will then be tested with the miBot nanoprobes in the dark and under illumination. The current-voltage curves will be fit with a modified version of the simulation of Chapter 5.

For further work on III-V on Ge wire devices, close iteration between MOCVD growth and TEM characterization would be extremely beneficial. Growth conditions can be tweaked to alter the nucleation and growth, hopefully leading to high quality axial material.

# Chapter 8

# Conclusion

## 8.1 Si Wire Array Solar Cells

### 8.1.1 State of the Art

Over the last six years, Si wire array solar cells have gone from concept to concrete reality. High fidelity arrays of intrinsic, p-type, or n-type wires can be grown from Cu catalyst.(63) They can then be embedded in a transparent, flexible polymer and peeled off of the growth substrate, allowing the Si wafer to be reused for further growths. (12; 13; 35) Furthermore, despite using 100 times less material than conventional Si solar cells, wire arrays can absorb 85% of the sunlight over the course of the day.(31) Building on these advances, the work in Chapter 2 demonstrated that high quality p-n junctions could be fabricated within these arrays and that the wire surfaces could be successfully passivated with a-Si:H and a-$SiN_x$:H. The addition of p-n junctions and surface passivation to the arrays led to the measurement of diffusion lengths of $\sim 10\mu$m, SRVs of $< 500$ cm/s, $V_{OC}$s approaching 600 mV, and single wire efficiencies of 9%. Projecting these results to large area arrays suggests that efficiencies of 17% should be possible. Furthermore, the work of Chapter 3 demonstrated a transparent, flexible top contact for crafting large area devices. Thus, all of the pieces are in place for making $> 10\%$ efficient, large area Si solar cells. With this in mind, in 2010, Dr. Mike Kelzenberg and Dr. Morgan Putnam founded Caelux Corp. with the intent of building on the aforementioned developments to commercialize the Si wire array technology.

More recently, and with a different material, a group at Lund fabricated 13.8% efficient InP wire arrays solar cells. They combined lessons from prior work on the optical properties of InP nanowires and on InP wire growth and took advantage of the innate low surface

recombination velocity of the material to achieve this impressive result.(58) However, their cells are still on the growth substrate and thus further work is required to realize a >10%, *substrate free* wire array cell.

Thus, single junction wire array solar cells have advanced from growth novelties to high performance devices and commercialization. The next few years should reveal if they can truly be competitive with conventional solar technologies in the all-important $/W metric.

### 8.1.2 Future Work

Though semiconductor wires have come a long way from the days of Wagner and Ellis, opportunities abound for further understanding and technological development. First and foremost, the limitations on diffusion length should be understood. Are defects due to stacking faults or point defects limiting the lifetime?(171) Are impurities getting incorporated within the material during growth or processing? TEM and ICP-MS coupled with rigorous lifetime analysis may help to probe the material and reveal if e.g. gettering or annealing are able to improve the material quality.(88)

Furthermore, the junction within the wire could be further optimized. Junction depth, doping, and profile have yet to be widely explored, though Dr. Emily Warren found that thick emitters were limiting the photocurrent within her Si wire array photoelectrodes.(172) If the diffusion lengths can be further improved, axial junctions may allow for better device performance by limiting the junction area. The inverting properties of the nitride could also be exploited to make inverted junction Si wire array cells. For that matter, optimized surface passivation/antireflection coatings should be developed for both the n-type and p-type regions e.g. by combining the a-Si:H and a-$SiN_x$:H or trying ALD layers.

Additionally, while the Ag nw/Ni np contact was able to connect >99% of the wires and proved relatively robust, its resistance was still high and it required that the wire tips be fully exposed and coated with Ni. Plasmonic welding or mild anneals may improve the series resistance. (100) The electroless deposition of other metals may also prove superior to Ni. Finally, other contacting schemes, such as a double back contact should be tested and may prove to have lower resistances and not require that as much of the wire be exposed for contacting, thereby preserving passivation over as much of the surface as possible.

While the Atwater group has focused on Si, much of the research community has begun to shift to III-V wire arrays. Direct gap wires can absorb all above-bandgap light in a small

volume and can take advantage of well developed window layers for surface passivation. For III-V nanowires, axial junctions are needed as radial junctions will fully deplete the wire, but *in situ* MOCVD growth of abrupt junctions is possible.(173) As a final note, wires can exceed the Shockley-Quiesser limit due to their large absorption cross section,(31) and understanding the limit of this phenomenon i.e. how much light can realistically be concentrated in a direct or indirect gap wire, may allow for the fabrication of devices that recapture some of the 7% entropic losses innate to unconcentrated devices, allowing wire arrays to perform more efficiently than conventional planar cells without the use of external optical elements.

## 8.2 Multijunction Wire Array Cells

### 8.2.1 State of the Art

Building on the success of single material wires, heterostructure and multijunction wire arrays are seeing increasing attention in the literature. Heterostructures offer all of the benefits of single material arrays with the possibility for higher voltages and/or higher efficiencies. GaP on Si arrays demonstrated the potential of wire array heterostructures, with the successful epitaxial growth of GaP on Si wires yielding $V_{OC}$s of 750 mV, though performance was limited by the 80 nm diffusion length of the GaP.(89; 141) Optical simulations suggested that the GaP guided light into the higher index Si wire and that the roughness of the GaP surface enhanced the optical path length in the GaP as compared to smooth films.

The desire for higher efficiency, solid state devices led to the consideration of alternate material systems to GaP/Si. $GaAs_xP_{1-x}$ and $Si_{1-x}Ge_x$ are lattice matched and the combination can yield efficiencies approaching 40%. Modeling of conformal, hemispherical, and spherical devices made from these materials reiterated that light is channeled into the high index core at longer wavelengths, but also suggested that only a few $\mu$ms of direct gap material are needed to absorb all of the blue light within the outer layer. The simulations also revealed the need for long diffusion lengths, effective surface passivation, and high doping of defects in order to achieve high efficiencies.

In the lab, significant progress was made towards experimentally realizing the modeled multijunction wire arrays. CVD Ge and $Si_{0.9}Ge_{0.1}$ wires were grown, and GaAs with ns

lifetime components was synthesized on these structures as well as on RIE planar Ge. Much more work remains to develop full tandem devices, but the process is well underway, and GaAs solar cells currently being grown on structured Ge at Sumika should further elucidate the potential and limitations of the technology.

### 8.2.2 Future Work

Work on wire array heterostructures has just begun, and many areas are ripe for further investigation. The growth of Ge and $Si_{1-x}Ge_x$ wire arrays could potentially be improved with the use of additional gases to alter the reaction energetics or with an explicit nucleation step. For that matter, wire nucleation is not well described or understood in the literature, and the development of a rigorous model would help to shed light on the possibilities and limitations of wire growth. Current models simply address steady state growth conditions and not the initial wire nucleation. (174; 175)

As for the growth of outer layers, while epitaxial films have been grown, the films are rough and the lifetimes for both GaP and GaAs can be substantially improved. Iterative experiments with MOCVD growth and TEM and/or TRPL should help to optimize the growth conditions. Other substrate geometries and exposed crystal facets may also improve the growth. Additionally, the opportunity to grow strained layers from a variety of different facets and, potentially, at greater critical thicknesses than planar layers, may allow for bandgap engineering to enable novel new devices with increased mobilities or desirable bandgaps for light absorption or emission.

When making active devices, the optimization of tunnel junctions and window layers for these unique geometries will be essential. The ability to alter the preferred growth directions through diffusion limitations may also prove useful for placing active device layers. If the material preferentially grows radially off of the exposed Ge, placing the exposed Ge structures close to one another can instead force the III-V to grow axially. Thus, after initial deposition, subsequent layers can either grow conformally off of the previous layer, for large spacings, or can be forced to grow axially, by pushing into the diffusion limited regime.

Optically, it may prove interesting to explore the absorption properties of small III-V ellipsoids as they morph from a perfect sphere to an elongated ellipsoid. At one end, the sphere has perfect resonances characterized by whispering gallery modes. On the other

end, all of the modes of the elongated ellipsoid are ergotically populated.(176) In between, rich dynamics exist with some areas of phase space fully sampled, while others have weak localized modes. These "in between" structures may prove useful for absorbing strongly across the solar spectrum.

## 8.3 The Wide World of Wire Arrays

While this thesis focused on the use of wire arrays for photovoltaic applications, they also have potential to be used in a variety of other devices. Semiconductor wires have been used as LEDs or sensors.(177) Additionally, the wire dimensions are on the order of many cell types, and have proved useful for interfacing with neurons e.g. as artificial retinas or as neural probes for recording action potentials.(178; 179) If individual wires can be electronically addressed, as in the work of Ikedo et al. (180), then large area arrays of transistors or memristors could potentially be realized. (181) Wires have also seen use in Li ion batteries, where their geometry allows them to rapidly expand when incorporating Li and then return to pure Si without fracturing.(182) Finally, they have seen use as antimicrobial surfaces, where the wires puncture the cell walls.(183)

Wire array heterostructures also have a number of potentially interesting optical applications. The upper cell of the spherical or hemispherical tandem designs could be replaced by a very high bandgap material, allowing it to serve solely as a lens, directing light to the underlying wire. Exploring the potential for enhanced second harmonic generation (SHG) with wire arrays could also prove interesting. Surfaces and strain lead to the symmetry breaking necessary to observe SHG, (184; 185) and heterostructure wires have both qualities in abundance. By also designing the wire arrays to act as photonic crystals, SHG could be further amplified.

All in all, I expect to see the exploration of semiconductor wires continue to grow in the coming years, as some of the above topics are explored and as new, unforeseen avenues of exploration arise.

# Appendix A

## Si Wire Array Processing Steps

### A.1 Fabricating Arrays with p-n Junctions

The following steps describe how to fabricate p-n junction Si wire arrays:

1. Array Patterning

   (a) Obtain a degenerately doped (<0.001 Ω cm) p-type Si(111) wafer with at least 300 nm of thermal oxide.

   (b) Place the wafer on the spinner and turn on the vacuum. Blow off any dust particles from the wafer surface with a N2 gun. Spin at 3000 rpm and spray with IPA to clean. Allow to spin dry.

   (c) Bake the wafer on a >100°C hotplate for at least 5 min to drive off water.

   (d) Place the wafer in the box for MCC primer, add a few drops of primer to the bottle cap, close the box, and let sit for at least 5 min. The primer promotes resist adhesion.

   (e) Return the wafer to the spinner. Coat the wafer with S1813 photoresist (Microchem), and then spin first at 500 rpm for 5 sec to spread the resist and then at 3000 rpm for 1 min to attain the desired thickness.

   (f) Cure on a hotplate at 115°C for 2 mins.

   (g) Photolithographically pattern the resist using the Karl Suss MA 6 mask aligner. Consult the log and peers to determine the optimal exposure time for a given setup. Different patterns may require different exposure lengths.

(h) Place the sample in MF-319 developer (Microchem) for 60 sec. Check with the optical microscope that the pattern has come out correctly, and, if not, adjust the exposure time accordingly for subsequent patterns.

(i) Cure on a hotplate at 115°C for at least 10 min immediately prior to the next step.

(j) After development of the pattern, the oxide within the patterned holes can be removed by immersion of the samples in buffered HF (BHF), (Transene, Inc.). The etch time depends on the ambient temperature and the oxide thickness. For 500 nm of oxide, $\sim$ 6.5 min will suffice.

(k) Evaporate or sputter 6N Cu to a thickness comparable to or slightly greater than the buffer oxide.

(l) Lift off the resist by submerging the sample in acetone. Rinse sample in acetone, isopropanol, methanol, and finally DI water before drying with nitrogen.

2. Wire Growth

(a) Cleave the patterned samples to the desired size and transfer to the desired $SiCl_4$ CVD reactor. Consult the log and your peers to find appropriate growth conditions. As of 3/31/13, the following conditions were used in the small reactor ("Big Blue"):

i. Load the wafer, positioned in slot 3 of the boat, 77 cm into the reactor at 750°C while purging with $N_2$.

ii. Ramp to 1000°C over 20 min under 500 sccm of $H_2$.

iii. Anneal the wafer for 20 min at 1000°C under $H_2$.

iv. Growth for 25 min under 1000 (995) sccm $H_2$, 12 (13) sccm $SiCl_4$, and 1 (1.05) sccm $BCl_3$. Values in parentheses refer to the actual values as opposed to the setpoints.

v. Cool to 750°C under $N_2$ before pump purging and unloading.

3. Cleaning

(a) Dip the sample in BHF for 10-30 sec to remove the native oxide.

(b) Immerse the sample in an RCA2 clean (6:1:1 DI:HCl:$H_2O_2$ at 75°C) for 10-20 min to remove the Cu.

(c) Dip the sample in BHF for 10-30 sec.

(d) Immerse the sample in 40°C KOH for 30 sec to remove the near surface Si.

4. Barrier Oxide Growth

(a) Immediately after the previous step, place the sample in a tube furnace flowing $N_2$ at 5 lpm.

(b) Allow the furnace to heat up to 1100°C over 90 min and to stabilize for 10 min at 1100°C.

(c) Flow $O_2$ at 5 lpm for 100 min while holding the furnace at 1100°C.

(d) Switch back to $N_2$ while holding the furnace at 1100°C for 10 min before shutting the heaters off.

(e) Allow the sample to cool to $\sim 650 - 750$°C.

5. PDMS Junction Definition

(a) Prepare a mixture of 0.1 g of PDMS curing agent, 1 g of PDMS, and 5 g of toluene.

(b) Cover your sample with the solution and immediately spin at 3000 rpm for 30 sec. Repeat this step twice.

(c) Immediately bake at 60°C for at least 15 min.

(d) Prepare a PDMS etching solution from a 1:1 mixture of 1.0M tetrabutylammonium fluoride in tetrahydrofuran and dimethylformamide.

(e) Coat your sample with the etching solution, let it sit for 2 sec, and rinse.

(f) Place your sample in BHF for 5 min to remove the barrier oxide. MAKE SURE THAT NO BUBBLES ARE TRAPPED IN THE WIRES

(g) Place your sample in the PDMS etch for at least 30 min.

(h) Piranha clean your sample (10 min in 1:3 $H_2SO_4$: $H_2O_2$). Rinse.

(i) Dip your sample in BHF for 5 sec. Rinse.

(j) RCA-2 clean your sample as described previously. Rinse and blow dry.

6. Diffusion

(a) Set the diffusion furnace to 850°C and make sure that the $N_2$ is flowing at 10 slm. When the middle zone reaches 800°C, pull the solid source P wafers to the inlet and allow them to cool for 10 min.

(b) Dip your sample in BHF for 15 sec, rinse, and blow dry. Immediately place it in an open slot between the doping wafers and set the boat back in the tube entrance.

(c) Slowly, over 1 min, push your samples into the doping furnace until the line marked on the side of the pushrod is flush with the end of the tube.

(d) Cap the tube and wait for your desired amount of time minus 2 min.

(e) Slowly, over 1 min, remove the boat from the furnace and allow it to cool at the end of the tube.

(f) Return the furnace to 400°C and the $N_2$ flow rate to 5 lpm. Place the doping wafers back in the furnace

## A.2 Creating Flexible, Contacted Large Area Arrays

The following steps describe how to create flexible, peeled off Si wire array solar cells with a Ag nanowire, Ni nanoparticle top contact:

1. Prepare a solution of 0.1 g Dow Corning 93-500 Space Grade Encapsulant curing agent, 1 g of 93-500 polymer, and 1.5 g of toluene.

2. Drop cast the solution on the wires at 3000 rpm for 30 sec multiple times until the wires are completely covered with polymer. Cover the surface with toluene and spin it off at 3000 rpm to leave $\sim$5 $\mu$m of the tips exposed.

3. Cure the film at 60°C for 10 hours.

4. Dip the wires in a 1:1 solution of 1.0M tetrabutylammonium fluoride in water and dimethylformamide to make the polymer hydrophilic and then immediately rinse.

5. Place the wetted sample in a solution of Nickelex (Transene, Inc.) at 80°C until rapid bubble formation on the wire tips is observed (usually around 30 sec). Rinse and blow dry.

6. Spin on Clear Ohm$^{TM}$ (Cambrios, Inc.) at 3000 rpm for 30 sec.

7. Bake in an oven at 50° for 90 sec. Bake on a hot plate at 150° for 90 sec.

8. (Optional) Evaporate a Ag bus bar on the surface through a shadow mask.

9. Remove the film from the growth substrate with a razor blade. Immediately evaporate 200 nm of Au on the back.

# Appendix B

## Code for Making Rough GaP for FDTD Simulations

**Listing B.1: Code to create a rough textured shell coating (modified from original code by Dr. Mike Kelzenberg)**

```
maxz = 24;
minz = 0;
rad = 1;

unitcellhalfwidth = 3.5;

mint = 0.5;
maxt = 1;
extnt = 0.5;

numXtals = 20000;

num = 0;
isGood = 0;

fid = fopen('Textured\_Rec\_Script.lsf','w');

while (num < numXtals)

    xGuess = rand * unitcellhalfwidth;
    yGuess = rand * unitcellhalfwidth;
    zGuess = minz + (maxz - minz + rad +maxt)*rand;
    if (rand < 0.5)
        xGuess = -xGuess;
    end
    if (rand < 0.5)
        yGuess = -yGuess;
    end
    xRot = rand * 360;
    yRot = rand * 360;
    zRot = rand * 360;



    if (zGuess<maxz)
        if ((maxt-mint)*zGuess/24+mint+rad > (xGuess^2 +yGuess^2)^0.5)
            isGood = 1;
        end
```

```
    else
        if ((xGuess^2 +yGuess^2) + (zGuess - maxz)^2 < (rad + maxt)^2)
            isGood = 1;
        end
    end

    if (isGood)
        num = num+1;
        fprintf(fid,'addrect;\r\nset("name","Rect%d");\r\n', num);
        fprintf(fid,'set("material","GaP - Aspnes and Sedna");\r\nset("set mesh order from
            material database",0);\r\n');
        fprintf(fid,['set("mesh order",2);\r\nset("x",' num2str(1e-6*xGuess) ');\r\nset("y",'
            num2str(1e-6*yGuess) ');\r\n']);
        fprintf(fid,['set("z",' num2str(1e-6*zGuess) ');\r\nset("x span",' num2str(1e-6*extnt) ')
            ;\r\n']);
        fprintf(fid,['set("y span",' num2str(1e-6*extnt) ');\r\nset("z span",' num2str(1e-6*extnt)
             ');\r\n']);
        fprintf(fid,['set("first axis", "x" );\r\nset("rotation 1",' num2str(xRot) ');\r\n']);
        fprintf(fid,['set("second axis", "y" );\r\nset("rotation 2",' num2str(yRot) ');\r\n']);
        fprintf(fid,['set("third axis", "z" );\r\nset("rotation 3",' num2str(zRot) ');\r\n']);
        isGood = 0;
    end

end

fclose(fid);
```

# Appendix C

## Code for the Analytical Tandem Model

### C.1 Code to Plot the Mie Optical Generation Profile

**Listing C.1: Code to calculated and plot Mie absorption for a sphere at a variety of wavelengths and under white light conditions**

```
% Constants that define the problem:
rad = 2; % Particle radius
N_re = 1; % n of the medium
N_im = 0; % k of the medium
steps = 10; % Discretization for plotting
% Build a table of the values for plotting
[th,ph,r] = meshgrid(0:pi/steps:pi,0:pi/steps:2*pi,0:rad/steps:rad);
nmax = 30; % Limit of the sum

% Load the weighting factors for the solar spectrum
load am15g_50nm.txt;

% Load the n and k data for the particle:
load GaAsP.txt;
% Initialize an array to hold the n and k data that matches the spectral
% binning:
nk_GaAsP = zeros(length(am15g_50nm(:,1)),3);

% Define and initialize symbolic variables for use in the calculation
syms E_r_pw E_theta_pw E_phi_pw E_r_I_wl E_theta_I_wl E_phi_I_wl;
E_r_pw = 0;
E_theta_pw = 0;
E_phi_pw = 0;
E_r_I_wl = 0;
E_theta_I_wl = 0;
E_phi_I_wl = 0;

% An array to hold the radial, axial, and azimuthal field values for the
% particle:
Abs = zeros(length(th(:,1,1)),length(ph(1,:,1)),length(r(1,1,:)));

% Populate the n and k array:
for l=1:length(am15g_50nm(:,1))
    nk_GaAsP(l,1) = am15g_50nm(l,1)/1000;
    for p=1:length(GaAsP(:,1))
```

```
        if am15g_50nm(l,1)/1000 < GaAsP(p,1) % Linear interpolation:
            nk_GaAsP(l,2) = (GaAsP(p,2)-GaAsP(p-1,2))/(GaAsP(p,1)-GaAsP(p-1,1))*nk_GaAsP(l,1)+
                GaAsP(p-1,2)-(GaAsP(p,2)-GaAsP(p-1,2))/(GaAsP(p,1)-GaAsP(p-1,1))*GaAsP(p-1,1);
            nk_GaAsP(l,3) = (GaAsP(p,3)-GaAsP(p-1,3))/(GaAsP(p,1)-GaAsP(p-1,1))*nk_GaAsP(l,1)+
                GaAsP(p-1,3)-(GaAsP(p,3)-GaAsP(p-1,3))/(GaAsP(p,1)-GaAsP(p-1,1))*GaAsP(p-1,1);
            break;
        end
    end
end

% Calculate the fields at each wavelength:
% for q=1:length(am15g_50nm(:,1))
for q=1:1
    % Define wavelength specific constants:
    wl = am15g_50nm(q,1)/1000; % The wavelength of interest
    disp(strcat('wl = ',num2str(wl),' um')); % Write the wavelength to the console
    N_re_I = nk_GaAsP(q,2); % n for the particle
    N_im_I = nk_GaAsP(q,3); % k for the particle
    k_pw = 2*pi*(N_re+i*N_im)/wl; % Wave vector of the medium
    k_I = 2*pi*(N_re_I+i*N_im_I)/wl; % Wave vector of the particle
    rh_pw = k_pw*r; % rho for the medium
    rh_I = k_I*r; % rho for the particle
    hbar = 1.05457148E-34; % Planck's constant

    % Get the equation for the field at the given wavelength:
    [E_r_pw,E_theta_pw,E_phi_pw,E_r_I_wl,E_theta_I_wl,E_phi_I_wl] = Mie(am15g_50nm(q,2),rad,N_re,
        N_im,N_re_I,N_im_I,wl,nmax);

    % Initialize arrays to hold the wavelength specific plane wave and
    % particle fields:
    E_pw_wl = zeros(3,length(th(:,1,1)),length(ph(1,:,1)),length(r(1,1,:)));
    E_I_wl = zeros(3,length(th(:,1,1)),length(ph(1,:,1)),length(r(1,1,:)));

    % Convert the symbolic variables to allow calculation of specific
    % values:
    E_r_pw_eval = inline(vectorize(char(E_r_pw)),'theta','phi','rho');
    E_theta_pw_eval = inline(vectorize(char(E_theta_pw)),'theta','phi','rho');
    E_phi_pw_eval = inline(vectorize(char(E_phi_pw)),'theta','phi','rho');
    E_r_I_eval = inline(vectorize(char(E_r_I_wl)),'theta','phi','rho');
    E_theta_I_eval = inline(vectorize(char(E_theta_I_wl)),'theta','phi','rho');
    E_phi_I_eval = inline(vectorize(char(E_phi_I_wl)),'theta','phi','rho');
    for a=1:length(ph(:,1,1))
        for b=1:length(th(1,:,1))
            for c=1:length(r(1,1,:))
                E_pw_wl(1,a,b,c) = E_r_pw_eval(th(a,b,c),ph(a,b,c),rh_pw(a,b,c));
                E_pw_wl(2,a,b,c) = E_theta_pw_eval(th(a,b,c),ph(a,b,c),rh_pw(a,b,c));
                E_pw_wl(3,a,b,c) = E_phi_pw_eval(th(a,b,c),ph(a,b,c),rh_pw(a,b,c));
                E_I_wl(1,a,b,c) = E_r_I_eval(th(a,b,c),ph(a,b,c),rh_I(a,b,c));
                E_I_wl(2,a,b,c) = E_theta_I_eval(th(a,b,c),ph(a,b,c),rh_I(a,b,c));
                E_I_wl(3,a,b,c) = E_phi_I_eval(th(a,b,c),ph(a,b,c),rh_I(a,b,c));
            end
        end
        disp(strcat('    ',num2str(a),'/',num2str(length(ph(:,1,1)))));
    end
    XCPlots(a,wl,(length(th(1,:,1))+1)/2,E_pw_wl,E_I_wl);
    Abs = -N_re_I*N_im_I*squeeze((abs(E_I_wl(1,:,:,:)).^2 + abs(E_I_wl(2,:,:,:)).^2 + abs(E_I_wl
        (3,:,:,:)).^2))/hbar + Abs;

end

if 0
```

```
Log_Abs_plot_xz = log10(-squeeze(Abs(1,:,:)));
Log_Abs_plot_xy = log10(-squeeze(Abs(:,1,:)));
Log_Abs_plot_yz = log10(-squeeze(Abs((length(th(1,:,1))+1)/2,:,:)));

h = figure;
subplot(2,1,1);
polar3d(flipud(Log_Abs_plot_xz'),0,pi,0,rad,1,'surf');
title('XZ','fontsize',14,'fontweight','b');
subplot(2,1,2);
polar3d(flipud(Log_Abs_plot_yz'),0,pi,0,rad,1,'surf');
title('YZ','fontsize',14,'fontweight','b');
fname = 'AM15G.jpeg';
end
```

## C.2 Code to Generate Plots at Each Wavelength

**Listing C.2: Code to plot absorption cross sections for the Mie theory treatment of a sphere**

```
function [] = XCPlots(a,wl,l_yz,E_pw_wl,E_I_wl)

% Plot xy, xz, and yz cross sections
E_r_pw_plot_xz = squeeze(E_pw_wl(1,1,:,:));
E_th_pw_plot_xz = squeeze(E_pw_wl(2,1,:,:));
E_ph_pw_plot_xz = squeeze(E_pw_wl(3,1,:,:));
E_pw_plot_xz = abs(E_r_pw_plot_xz).^2 + abs(E_th_pw_plot_xz).^2 + abs(E_ph_pw_plot_xz).^2;
E_r_I_plot_xz = squeeze(E_I_wl(1,1,:,:));
E_th_I_plot_xz = squeeze(E_I_wl(2,1,:,:));
E_ph_I_plot_xz = squeeze(E_I_wl(3,1,:,:));
E_I_plot_xz = abs(E_r_I_plot_xz).^2 + abs(E_th_I_plot_xz).^2 + abs(E_ph_I_plot_xz).^2;
h = figure;
subplot(2,1,1);
polar3d(flipud(E_pw_plot_xz'),0,pi,0,a,1,'surf');
title('Plane Wave: XZ','fontsize',14,'fontweight','b');
subplot(2,1,2);
polar3d(flipud(E_I_plot_xz'),0,pi,0,a,1,'surf');
title('Internal Field: XZ','fontsize',14,'fontweight','b');
fname = strcat('XZ_',num2str(wl*1000),'nm.jpeg');
print(h,'-djpeg',fname);
close;

E_r_pw_plot_xy = squeeze(E_pw_wl(1,:,1,:));
E_th_pw_plot_xy = squeeze(E_pw_wl(2,:,1,:));
E_ph_pw_plot_xy = squeeze(E_pw_wl(3,:,1,:));
E_pw_plot_xy = abs(E_r_pw_plot_xy).^2 + abs(E_th_pw_plot_xy).^2 + abs(E_ph_pw_plot_xy).^2;
E_r_I_plot_xy = squeeze(E_I_wl(1,:,1,:));
E_th_I_plot_xy = squeeze(E_I_wl(2,:,1,:));
E_ph_I_plot_xy = squeeze(E_I_wl(3,:,1,:));
E_I_plot_xy = abs(E_r_I_plot_xy).^2 + abs(E_th_I_plot_xy).^2 + abs(E_ph_I_plot_xy).^2;
h = figure;
subplot(2,1,1);
polar3d(flipud(E_pw_plot_xy'),0,2*pi,0,a,1,'surf');
title('Plane Wave: XY','fontsize',14,'fontweight','b');
subplot(2,1,2);
polar3d(flipud(E_I_plot_xy'),0,2*pi,0,a,1,'surf');
title('Internal Field: XY','fontsize',14,'fontweight','b');
fname = strcat('XY_',num2str(wl*1000),'nm.jpeg');
print(h,'-djpeg',fname);
```

```
close;

E_r_pw_plot_yz = squeeze(E_pw_wl(1,l_yz,:,:));
E_th_pw_plot_yz = squeeze(E_pw_wl(2,l_yz,:,:));
E_ph_pw_plot_yz = squeeze(E_pw_wl(3,l_yz,:,:));
E_pw_plot_yz = abs(E_r_pw_plot_yz).^2 + abs(E_th_pw_plot_yz).^2 + abs(E_ph_pw_plot_yz).^2;
E_r_I_plot_yz = squeeze(E_I_wl(1,l_yz,:,:));
E_th_I_plot_yz = squeeze(E_I_wl(2,l_yz,:,:));
E_ph_I_plot_yz = squeeze(E_I_wl(3,l_yz,:,:));
E_I_plot_yz = abs(E_r_I_plot_yz).^2 + abs(E_th_I_plot_yz).^2 + abs(E_ph_I_plot_yz).^2;
h = figure;
subplot(2,1,1);
polar3d(flipud(E_pw_plot_yz'),0,pi,0,a,1,'surf');
title('Plane Wave: YZ','fontsize',14,'fontweight','b');
subplot(2,1,2);
polar3d(flipud(E_I_plot_yz'),0,pi,0,a,1,'surf');
title('Internal Field: YZ','fontsize',14,'fontweight','b');
fname = strcat('YZ_',num2str(wl*1000),'nm.jpeg');
print(h,'-djpeg',fname);
close;
```

## C.3 Code to Calculate the Internal Fields of a Particle Given Mie Theory

**Listing C.3: Code to calculated the internal fields and absorption of a sphere using Mie theory**

```
function [E_r_pw,E_theta_pw,E_phi_pw,E_r_I,E_theta_I,E_phi_I] = Mie(E0,a,N_re,N_im,N_re_I,N_im_I,
    wl,nmax)
%                       INTERNAL FIELDS OF A PARTICLE:
%                 MIE THEORY - VECTOR SPHERICAL HARMONICS
%                       Dan Turner-Evans, Jul 2012
%                            dt@caltech.edu
%                    California Institute of Technology
%
% This is a MATLAB tool for calculating the internal fields and hence
% the absorption of a particle illimuniated by a plane wave
%
% E_I = Sum_{n=1}^/inf i^n*E_0*(2n+1)/(n*(n+1))*
%           (c_n*M_o1n^(1) - i*d_n*N_e1n^(1))
%
% E0: Field Intensity (W/m^2)
% a: Particle radius (um)
% N_re: Real part of the index of refraction of the medium
% N_im: Imaginary part of the index of refraction of the medium
% N_re_I: Real part of the index of refraction of the particle
% N_im_I: Imaginary part of the index of refraction of the particle
% wl: The wavelength of interest (um)
% nmax: Upper limit of the sum
% steps: The number of steps between angles, radii in the plot

% Set up the necessary constants:
mu_I = 1; % Permeability of the particle
mu = 1; % Permeability of free space
k_pw = 2*pi*(N_re+i*N_im)/wl; % Wave vector
k_I = 2*pi*(N_re_I+i*N_im_I)/wl; % Wave vector
x_val = k_pw*a; % Size parameter
m_val = (N_re_I+i*N_im_I)/(N_re+i*N_im); % Relative refractive index
% Define symbolic variables to allow for differential calculation:
```

```
syms rho theta phi E_r_pw E_theta_pw E_phi_pw E_r_I E_theta_I E_phi_I x;
% Initialize the radial, zenith, and azimuthal field components for
% the plane wave and the internal field:
E_r_pw = 0;
E_theta_pw = 0;
E_phi_pw = 0;
E_r_I = 0;
E_theta_I = 0;
E_phi_I = 0;

% Calculate the vector components of the electric field.
for n = 1:nmax
    % Set up the Legendre components:
    % P_n^m = (-1)^m/(2^l*l!)*(1-x^2)^(m/2)*d^(l+m)/dx^(l+m)(x^2-1)^l
    % where we substitute in cos(theta) for x
    syms x1;
    pnmial = (x1^2-1)^n;
    pnm = inline(char(pnmial),'x1');
    dpnmail = diff(formula(pnm),x1,n+1);
    dpnmail_cos = subs(dpnmail,x1,cos(theta));
    % m=1 Associated Legendre Polynomial:
    Pn = -1/(2^n*factorial(n))*(1-cos(theta)^2)^0.5*dpnmail_cos;
    dPn = diff(Pn,theta); % derivative of Pn w.r.t. theta

    % Set up the Spherical Bessel function and calculate specific values
    % for the coefficients
    jn = besselj(n+1/2,rho)*sqrt(pi/(2*rho)); % The spherical Bessel Function
    jnr = inline(char(jn*rho));
    djn = diff(formula(jnr),rho); % Take the derivative
    jnI_val = inline(vectorize(char(jn)),'rho');
    jnI = jnI_val(x_val);
    mjnI = jnI_val(m_val*x_val);
    djnIx_val = inline(vectorize(char(djn)),'rho');
    djnI = djnIx_val(x_val);
    dmjni = djnIx_val(m_val*x_val);

    % Set up the Spherical Hankel function
    hnI_val = besselj(n+1/2,x)*sqrt(pi/(2*x)) + i*bessely(n+1/2,x)*sqrt(pi/(2*x));;
    hnIx_val = inline(vectorize(char(hnI_val)),'x');
    hnI = hnIx_val(x_val);
    hnIx = inline(char(x*hnI_val));
    dhnIx = diff(formula(hnIx),x);
    dhnIx_val = inline(vectorize(char(dhnIx)),'x');
    dhnI = dhnIx_val(x_val);

    % Calculate the scattering coefficients
    cn = (mu_I*jnI*dhnI - mu_I*hnI*djnI)/(mu_I*mjnI*dhnI-mu*hnI*dmjni);
    dn = (mu_I*m_val*jnI*dhnI - mu_I*m_val*hnI*djnI)/(mu_I*m_val^2*mjnI*dhnI-mu*hnI*dmjni);

    % Find M and N
    M_theta = 1/sin(theta)*cos(phi)*Pn*jn; % Find the theta component of M
    M_phi = -sin(phi)*dPn*jn; % Find the phi component of M
    N_r = jn/rho*cos(phi)*n*(n+1)*Pn; % Find the radial component of N
    N_theta = cos(phi)*dPn/rho*djn; % Find the theta component of N
    N_phi = -sin(phi)*Pn/sin(theta)/rho*djn; % Find the phi component of N

    % Calculate E for a plane wave
    E_r_pw = E0*(-i^(n+1)*(2*n+1)/(n*(n+1))*N_r + E_r_pw);
    E_theta_pw = E0*(i^n*(2*n+1)/(n*(n+1))*(M_theta -i*N_theta) + E_theta_pw);
    E_phi_pw = E0*(i^n*(2*n+1)/(n*(n+1))*(M_phi -i*N_phi) + E_phi_pw);
```

```
    % Calculate the internal E fields for the particle
    E_r_I = E0*(-i^(n+1)*(2*n+1)/(n*(n+1))*N_r*dn + E_r_I);
    E_theta_I = E0*(i^n*(2*n+1)/(n*(n+1))*(M_theta*cn -i*N_theta*dn) + E_theta_I);
    E_phi_I = E0*(i^n*(2*n+1)/(n*(n+1))*(M_phi*cn -i*N_phi*dn) + E_phi_I);

end
```

## C.4 Code to Plot the Beer-Lambert Optical Generation Profile

**Listing C.4: Code to calculate and plot the absorption of a sphere using the Beer-Lambert approximation**

```
% Constants that define the problem:
a = 2; % Particle radius
N_re = 1; % n of the medium
N_im = 0; % k of the medium
steps = 100; % Discretization for plotting
% Build a table of the values for plotting
[th,r] = meshgrid(0:pi/steps:pi,0:a/steps:a);

% Load the weighting factors for the solar spectrum
load am15g_50nm.txt;

% Load the n and k data for the particle:
load GaAsP.txt;
% Initialize an array to hold the n and k data that matches the spectral
% binning:
nk_GaAsP = zeros(length(am15g_50nm(:,1)),3);

% An array to hold the carrier generation
C_sum = zeros(1,length(th(1,:)),length(r(:,1)));


% Populate the n and k array:
for l=1:length(am15g_50nm(:,1))
    nk_GaAsP(l,1) = am15g_50nm(l,1)/1000;
    for p=1:length(GaAsP(:,1))
        if am15g_50nm(l,1)/1000 < GaAsP(p,1) % Linear interpolation:
            nk_GaAsP(l,2) = (GaAsP(p,2)-GaAsP(p-1,2))/(GaAsP(p,1)-GaAsP(p-1,1))*nk_GaAsP(l,1)+
                GaAsP(p-1,2)-(GaAsP(p,2)-GaAsP(p-1,2))/(GaAsP(p,1)-GaAsP(p-1,1))*GaAsP(p-1,1);
            nk_GaAsP(l,3) = (GaAsP(p,3)-GaAsP(p-1,3))/(GaAsP(p,1)-GaAsP(p-1,1))*nk_GaAsP(l,1)+
                GaAsP(p-1,3)-(GaAsP(p,3)-GaAsP(p-1,3))/(GaAsP(p,1)-GaAsP(p-1,1))*GaAsP(p-1,1);
            break;
        end
    end
end

% Calculate the carrier generation at each wavelength
for q=1:length(am15g_50nm(:,1))
    % Define wavelength specific constants:
    wl = am15g_50nm(q,1)/1000; % The wavelength of interest
    disp(strcat('wl = ',num2str(wl),' um')); % Write the wavelength to the console
    N_im_I = nk_GaAsP(q,3); % k for the particle
    alph = 4*pi*N_im_I/wl;
    hbar = 1.05457148E-34; % Planck's constant
    c = 3E8; % The speed of light
    flux = am15g_50nm(q,2)/1000*wl/(c*hbar); % The incident flux of photons
```

```
    % Initialize arrays to hold the wavelength specific carrier generation
    C_wl = zeros(1,length(th(1,:)),length(r(:,1)));

    for b=1:length(th(1,:))
        for aa=1:length(r(:,1))
            C_wl(1,b,aa) = flux*alph*exp(alph*(r(aa,1)-a));
        end
    end
    C_sum = C_wl + C_sum;
end

Log_C_plot = log10(C_sum);

h = figure;
polar3d(flipud(squeeze(Log_C_plot)'),0,pi,0,a,1,'surf');
title('Ln(Carrier Generation)','fontsize',14,'fontweight','b');
% fname = 'AM15G.jpeg';
% print(h,'-djpeg',fname);

% [X,Y,Z] = sph2cart(th,ph,r);
% E(4,a,b,c) = E_r_eval(th(a,b,c),ph(a,b,c),rh(a,b,c))*sin(th(a,b,c))*cos(ph(a,b,c)) +
    E_theta_eval(th(a,b,c),ph(a,b,c),rh(a,b,c))*cos(th(a,b,c))*cos(ph(a,b,c)) - E_phi_eval(th(a,b,
    c),ph(a,b,c),rh(a,b,c))*sin(ph(a,b,c)); % Compute the x component of the vector
% % x* = sin(theta)cos(phi)r* + cos(theta)cos(phi)theta* - sin(phi)phi*
% E(5,a,b,c) = E_r_eval(a,b,c)*sin(th(a,b,c))*sin(ph(a,b,c)) + E_theta_eval(a,b,c)*cos(th(a,b,c))*
    sin(ph(a,b,c)) + E_phi_eval(a,b,c)*cos(ph(a,b,c)); % Compute the y component of the vector
% % y* = sin(theta)sin(phi)r* + cos(theta)sin(phi)theta* + cos(theta)phi*
% E(6,a,b,c) = E_r_eval(a,b,c)*cos(th(a,b,c)) - E_theta_eval(a,b,c)*sin(th(a,b,c)); % Compute the
    z component of the vector
% % z* = cos(theta)r* - sin(theta)theta*
```

## C.5 Code to Generate Subcell, Tandem J-V Curves

**Listing C.5: Code to calculate the current-voltage characteristics of the subcells and series configuration for a tandem, hemispherical wire array solar cell**

```
% Specify universal constants
numpts = 2001; % The number of points for the IV curves

% Specify constants for the III_V outer cell
d1 = 0.1E-4; % The thickness of the III_V emitter
% d1_vals = [0.05E-4,0.1E-4,0.5E-4];
d2 = 2.9E-4; % The thickness of the III_V base
% d2_vals = [1E-4,3E-4,5E-4];
Sp_III_V = 100; % The III_V p_type SRV
Sn_III_V = 100; % The III_V n_type SRV
Ln_III_V = 1E-2; % The electron diffusion length in the III_V p_type base
Lp_III_V = 1E-2; % The hole diffusion length in the III_V n_type emitter

% Specify the constants for the SiGe wire cell
r1 = 0.1E-4; % The thickness of the wire emitter
r2 = 0.65E-4; % The thickness of the wire base
Sp_wire = 100; % The III_V n_type SRV
Ln_wire = 1E-1; % The electron diffusion length in the III_V p_type base
Lp_wire = 1E-1; % The hole diffusion length in the III_V n_type emitter
L = 1E-2; % The length of the wire
```

```
% Specify the series resistance due to the tunnel junction
Rs = 0; % in Ohm-cm^2

if 0
% Script to get individual IV curves
% Calculate and plot the J_V curves for the III_V cell
Js = zeros(4,numpts);
for cba = 1:length(d1_vals)
    for cb = 1:length(d2_vals)
        d1 = d1_vals(cba);
        d2 = d2_vals(cb);
        figure;
        hold;
        title(strcat('d1 = ',num2str(d1*1E7),'nm, d2 = ',num2str(d2*1E7),'nm'),'FontWeight','b','
            FontSize',24);
        for abc = 1:4
            %Ln = Ln_III_V*10^(abc-1);
            %Lp = Lp_III_V*10^(abc-1);
            Ln = Ln_III_V;
            Lp = Lp_III_V;
            Sp = Sp_III_V*100^(abc-1);
            Sn = Sn_III_V*100^(abc-1);
            wl_data1 = csvread('wl_data_GaAsP.csv');
            J_III_V = zeros(numpts,1);
            V_III_V = zeros(numpts,1);
            for i = 1:numpts
                V_III_V(i,1) = 1.5*(2*i/(numpts+1) - 1);
                Vval = V_III_V(i,1);
                try
                    J_III_V(i,1) = Sphere_IV(Sp,Sn,Ln,Lp,Vval,wl_data1,d1,d2);
                    if J_III_V(i,1) > 0.03 || J_III_V(i,1) < -0.01
                        if J_III_V(i,1) <= 0 && V_III_V(i,1) > 1
                            break
                        else
                            J_III_V(i,1) = 0;
                        end
                    end
                catch
                    continue
                end
            end
            scatter(V_III_V,J_III_V);
            Js(abc,:) = J_III_V;
        end
        %legend(strcat('L = ',num2str(Ln_III_V*1E4),'um'),strcat('L = ',num2str(Ln_III_V*1E5),'um
            '),strcat('L = ',num2str(Ln_III_V*1E6),'um'),strcat('L = ',num2str(Ln_III_V*1E7),'um')
            ,'FontWeight','b','FontSize',24);
        legend(strcat('S = ',num2str(Sn_III_V),'cm/s'),strcat('S = ',num2str(Sn_III_V*100),'cm/s')
            ,strcat('S = ',num2str(Sn_III_V*1E4),'cm/s'),strcat('S = ',num2str(Sn_III_V*1E6),'cm/s
            '),'FontWeight','b','FontSize',24);
        xlabel('Voltage(V)','FontWeight','b','FontSize',24);
        ylabel('Current Density (A/cm^2)','FontWeight','b','FontSize',24);
    end
end
end
if 0
% Calculate and plot the J_V curves for the wire cell
figure;
hold;
for abcd = 1:4
```

```
    Ln = Ln_wire*10^(abcd-1);
    Lp = Lp_wire*10^(abcd-1);

    wl_data2 = csvread('wl_data_SiGe.csv');
    for abcde = 1:length(wl_data1(:,4))
        N_i = wl_data(abcde,3);
        alp = 4*pi*N_i/wl_data(abcde,1); % The absorption coefficent (cm^-1)
        wl_data2(abcde,4)= wl_data2(abcde,4) - wl_data1(abcde,4)*(1-exp(-alp*(d1+d2)));
    end
    J_wire = zeros(numpts,1);
    V_wire = zeros(numpts,1);
    for i = 1:numpts
        V_wire(i,1) = 0.01*(i-(numpts+1)/2);
        Vval = V_wire(i,1);
        try
            J_wire(i,1) = Wire_IV(Sp_wire,Ln,Lp,Vval,wl_data2,r1,r2,L);
            if J_wire(i,1) > 10 || J_wire(i,1) < -0.01
                J_wire(i,1) = 0;
            end
        catch
            continue
        end
    end
    scatter(V_wire,J_wire);
end
end

% Calculated and plot individual and tandem performance
wl_data1 = csvread('wl_data_GaAsP.csv');
wl_data2 = csvread('wl_data_SiGe.csv');
for abcde = 1:length(wl_data1(:,4))
    N_i = wl_data1(abcde,3);
    alp = 4*pi*N_i/wl_data1(abcde,1); % The absorption coefficent (cm^-1)
    wl_data2(abcde,4)= wl_data2(abcde,4) - wl_data1(abcde,4)*(1-exp(-alp*(d1+d2)));
end
J_III_V = zeros(numpts,1);
V_III_V = zeros(numpts,1);
J_wire = zeros(numpts,1);
V_wire = zeros(numpts,1);
for i = 1:numpts
    % Generate IV curves for III-V cell
    V_III_V(i,1) = 1.5*(2*i/(numpts+1) - 1);
    Vval1 = V_III_V(i,1);
    try
        J_III_V(i,1) = Sphere_IV(Sp_III_V,Sn_III_V,Ln_III_V,Lp_III_V,Vval1,wl_data1,d1,d2);
        if J_III_V(i,1) > 0.03 || J_III_V(i,1) < -0.01
            J_III_V(i,1) = 0;
        end
    catch
        continue
    end

    % Generate IV curves for SiGE cell
    V_wire(i,1) = 1.2*(2*i/(numpts+1) - 1);
    Vval2 = V_wire(i,1);
        try
            J_wire(i,1) = Wire_IV(Sp_wire,Ln_wire,Lp_wire,Vval2,wl_data2,r1,r2,L);
            if J_wire(i,1) > 10 || J_wire(i,1) < -0.01
                J_wire(i,1) = 0;
            end
        catch
```

```
            continue
        end
end

% Generate the tandem IV curve
J = zeros(numpts,1);
V = zeros(numpts,1);
if J_wire((numpts+1)/2,1) > J_III_V((numpts+1)/2,1)
    for bc = 1:numpts
        step = 1;
        if J_III_V(bc,1) > J_wire((numpts+1)/2,1) || J_III_V(bc,1) == 0
            continue
        end
        while J_wire(step,1) == 0
            step = step + 1;
        end
        while J_wire(step,1) > J_III_V(bc,1)
            step = step +1;
            if step == numpts
                break
            end
        end
        J(bc,1) = J_III_V(bc,1);
        if abs(J_wire(step,1) - J_III_V(bc,1)) > abs(J_wire(step-1,1) - J_III_V(bc,1))
            V(bc,1) = V_III_V(bc,1) + V_wire(step-1,1)-Rs*(J_wire(step,1)+J_wire(step-1,1))/2;
        else
            V(bc,1) = V_III_V(bc,1) + V_wire(step,1)-Rs*(J_wire(step,1)+J_wire(step-1,1))/2;
        end
    end
else
    for bc = 1:numpts
        step = 1;
        if J_wire(bc,1) > J_III_V((numpts+1)/2,1) || J_wire(bc,1) == 0
            continue
        end
        while J_III_V(step,1) == 0
            step = step + 1;
        end
        while J_III_V(step,1) > J_wire(bc,1)
            step = step +1;
            if step == numpts
                break
            end
        end
        J(bc,1) = J_wire(bc,1);
        if abs(J_III_V(step,1) - J_wire(bc,1)) > abs(J_III_V(step-1,1) - J_wire(bc,1))
            V(bc,1) = V_wire(bc,1) + V_III_V(step-1,1)-Rs*(J_wire(step,1)+J_wire(step-1,1))/2;
        else
            V(bc,1) = V_wire(bc,1) + V_III_V(step,1)-Rs*(J_wire(step,1)+J_wire(step-1,1))/2;
        end
    end
end

% figure;
% hold;
% scatter(V_III_V,J_III_V);
% scatter(V_wire,J_wire);
% scatter(V,J);
% plot(V,J*1000);
set(gca,'fontsize',30,'fontweight','b');
% legend('GaAsP','SiGe','Tandem','Location','South')
```

```
xlabel('Voltage(V)','FontSize',30);
ylabel('Current Density (mA/cm^2)','FontSize',30);
set(gca,'XLim',[0 2],'YLim',[0 30]);
grid on;


% Extract the Eff, JSC, and VOC
eff_overall = max(V.*J)*1000
eff_wire = max(V_wire.*J_wire)*1000;
eff_III_V = max(V_III_V.*J_III_V)*1000;

J_SC_wire = J_wire((numpts+1)/2)*1000;
J_SC_III_V = J_III_V((numpts+1)/2)*1000;
jsc = 1;
while V(jsc,1) < 0 || J(jsc,1) == 0
    jsc = jsc + 1;
end
if abs(V(jsc,1)) < V(jsc+1,1)
    J_SC_overall = J(jsc,1)*1000;
else
    J_SC_overall = J(jsc,1)*1000;
end

voc = 1;
while J_wire(voc,1) > 0 || V_wire(voc,1) <=0
    voc = voc +1;
end
VOC_wire = V_wire(voc,1);
voc = 1;
while J_III_V(voc,1) > 0 || V_III_V(voc,1) < 0
    voc = voc +1;
end
VOC_III_V = V_III_V(voc,1);
voc = 1;
while J(voc,1) >= 0 || V(voc,1) <= 0
    voc = voc +1;
end
VOC_overall = V(voc-1,1);
```

## C.6 Code for the Hemispherical Subcell

**Listing C.6: Code to calculate the current at a given voltage for a hemispherical solar cell**

```
function [J] = Sphere_IV(Sp,Sn,Ln,Lp,V,wl_data,d1,d2)
%
% d1 = 0.1E-4; % The thickness of the III_V emitter
% d2 = 2E-4; % The thickness of the III_V base
% Sp = 100; % The III_V p_type SRV
% Sn = 100; % The III_V n_type SRV
% Ln = 1E-5; % The electron diffusion length in the III_V p_type base
% Lp = 1E-5; % The hole diffusion length in the III_V n_type emitter
% wl_data = csvread('wl_data_GaAsP.csv');
% V = 0;

%               Analytical Model for a Spherical Solar Cell
%                     Dan Turner-Evans, Jul 2012
%                             dt@caltech.edu
```

```
%                  California Institute of Technology
%
% This is a MATLAB tool for calculating the IV curve of a hemi-spherical solar
% cell
%

% Specify the appropriate constants
k = 8.6173324E-5; % The Bolzmann constant (eV/K)
T = 300; % The temperature (K)
q = 1.60219E-19; % The fundamental electrical charge (C)
VT = k*T; % The thermal voltage (eV)
NA = 5E16; % The p-type, core doping (cm^-3)
ND = 9E17; % The n-type, shell doping (cm^-3)
NC = 5.758E17; % Effective density of states in the conduction band (cm^-3)
NV = 9.543E18; % Effective density of states in the valence band (cm^-3)
EG = 1.5389; % The material bandgap (eV)
ni = sqrt(NC*NV)*exp(-EG/(2*VT)); % The intrinsic carrier density (cm^-3)
Phi_0 = VT*log(NA*ND/ni^2); % The built in voltage (eV)
%V = 0; % The applied voltage (V)
% d1 = 0.1E-4; % Emitter thickness (cm)
% d2 = 1.9E-4; % The core radius (cm)
% eps_GaP = 11.1; % The dielectric constant of GaP
% eps_GaAs = 12.9; % The dielectric constant of GaAs
eps0 = 8.854187817620E-14; % Vacuum permittivty in F/cm
eps = (11.1 + 1.8*0.9)*eps0; % The overall permittivity

% First, solve for the limits of the depletion region
syms x2 x4;
x2_val = 0;
x4_val = 0;
S = solve(Phi_0 + V == q/eps*NA*(d2^2/6+x4^3/(3*d2)-x4^2/2)+q/eps*ND*x2^2*(1/2+x2/(3*d2)), NA*(d2
    ^3-x4^3) == ND*((d2+x2)^3-d2^3));
for a = 1:length(S.x2)
    if isreal(S.x2(a)) && S.x2(a)>0 && S.x2(a)<d1 && isreal(S.x4(a)) && S.x4(a)>0 && S.x4(a)<d2
        x2_val = double(S.x2(a));
        x4_val = double(S.x4(a));
    end
end

% Plot the voltage variation across the depletion region
%r1 = x4_val:x4_val/5000:d2;
%V1 = q*NA/(6*eps)*r1.^2+q*NA*x4_val^3/(3*eps)./r1-q*NA/(2*eps)*x4_val^2;
%r2 = d2:x2_val/100:d2+x2_val;
%V2 = -q*ND/(6*eps)*r2.^2-q*ND*(d2+x2_val)^3/(3*eps)./r2+q*ND/(2*eps)*(d2+x2_val)^2+Phi_0+V;
% figure;
% plot(r1,V1);
% hold;
% plot(r2,V2);

% Specify the constants for the quasi-neutral region
%Ln = 1E-5; % The electron diffusion length in the material (cm)
%Lp = 1E-4; % The hole diffusion length in the material (cm)
%N_re = 3; % The real part of index of refraction
%N_im = 0.5; % The imaginary part of the index of refraction
%wl = 6E-5; % The wavelength, in cm.
% alph = 4*pi*N_im/wl; % The absorption coefficent (cm^-1)
%inc_pow = 100; % AM1.5G power (mW/cm^2)
h = 6.626E-34; % Planck's constant (Jsec)
c = 3E10 ; % Speed of light (cm/s)
% flux = inc_pow/1000*wl/(c*h); % The incident photon flux (photons/cm^2/sec)
mup = 367.5; % The hole mobility (cm^2/V/sec)
```

```
Dp = mup*k*T; % The diffusion coefficient for holes (cm^2/sec)
mun = 7661; % The electron mobility (cm^2/V/sec)
Dn = mun*k*T; % The diffusion coefficient for electrons (cm^2/sec)


% Calculate the current in regions 2 and 3
if V > 0
    Umax = ni*sqrt(Dn*Dp)/(Ln*Lp)*sinh(V/(2*k*T));
else
    Umax = 0;
end
kappa = pi*k*T/(Phi_0+V);
rV = x4_val + log(NA/ni)/log(NA*ND/ni^2)*(x2_val+(d2-x4_val));
r1 = rV - (x2_val+(d2-x4_val))/2*kappa;
r2 = rV + (x2_val+(d2-x4_val))/2*kappa;
J23_l = 0;
for i=1:length(wl_data(:,1))
    wl = wl_data(i,1);
    N_im = wl_data(i,3);
    alph = 4*pi*N_im/wl; % The absorption coefficent (cm^-1)
    inc_pow = wl_data(i,4);
    flux = inc_pow/1000*wl/(c*h); % The incident photon flux (photons/cm^2/sec)
    % J23_l = 3*q*flux/(alph^3*(d1+d2)^3)*((alph*(d2+x2_val)*(alph*(d2+x2_val)-2)+2)*exp(alph*(
        x2_val-d1)) - (alph*x4_val*(alph*x4_val-2)+2)*exp(alph*(x4_val-d1-d2))) +J23_l;
    J23_l = q*flux*(exp(alph*(x2_val-d1))-exp(alph*(x4_val-d1-d2))) + J23_l;
end
J23_r = q*Umax/(3*(d1+d2)^2)*(r2^3-r1^3);

% Calculate the current in region 1
% First, solve for the constants given the boundary conditions using
% symbolic logic.

syms A B C;
exp_sum1 = 0;
exp_sum2 = 0;
exp_sum3 = 0;
exp_sum4 = 0;
exp_sum5 = 0;
flux_tot = 0;
for i=1:length(wl_data(:,1))
    wl = wl_data(i,1);
    N_im = wl_data(i,3);
    alph = 4*pi*N_im/wl; % The absorption coefficent (cm^-1)
    inc_pow = wl_data(i,4);
    flux = inc_pow/1000*wl/(c*h); % The incident photon flux (photons/cm^2/sec)
    flux_tot = flux + flux_tot;
    exp_sum1 = exp(-alph*(d1+d2))*2*alph^2*flux*Ln^4/(1-alph^2*Ln^2)^2/Dn + exp_sum1;
    exp_sum2 = exp(alph*(x4_val-(d1+d2)))*alph*flux/Dn*(Ln^2/(1-alph^2*Ln^2))*(1+2*alph*Ln^2/
        x4_val/(1-alph^2*Ln^2)) + exp_sum2;
    exp_sum3 = exp(-alph*(d1+d2))*alph*flux/Dn*Ln^2/(1-alph^2*Ln^2)*(1+2*alph^2*Ln^2/(1-alph^2*Ln
        ^2)) + exp_sum3;
    exp_sum4 = exp(-alph*(d1+d2))*alph^2*flux/Dn*Ln^2/(1-alph^2*Ln^2)*(1+alph^2*Ln^2/(1-alph^2*Ln
        ^2)) + exp_sum4;
    exp_sum5 = exp(alph*(x4_val-(d1+d2)))*alph*flux/Dn*(Ln^2/(1-alph^2*Ln^2))*(alph+2*alph^2*Ln^2/
        x4_val/(1-alph^2*Ln^2)-2*alph*Ln^2/x4_val^2/(1-alph^2*Ln^2))+exp_sum5;
end
S2 = solve(A+B+exp_sum1 == 0, A*exp(x4_val/Ln)/x4_val + B*exp(-x4_val/Ln)/x4_val+ C*sinh(x4_val/Ln
    )/x4_val + exp_sum2 == ni^2/NA*(exp(V/VT)-1), Sn*(A/Ln + B/Ln + C/Ln + exp_sum3) == -Dn*(A/(2*
    Ln^2)+B/(2*Ln^2) + exp_sum4) );
A_val = double(S2.A);
B_val = double(S2.B);
```

```
C_val = double(S2.C);

J1 = -q*Dn*(A_val*exp(x4_val/Ln)/x4_val*(1/Ln-1/x4_val) - B_val*exp(-x4_val/Ln)/x4_val*(1/Ln+1/
     x4_val) + C_val*(cosh(x4_val/Ln)/(x4_val*Ln) - sinh(x4_val/Ln)/x4_val^2) + exp_sum5);

% Calculate the current in region 4
%Sp = 100; % Surface recombination velocity (cm/s)
% First, solve for the constants given the boundary condition.
syms A4 B4;
JH4S = 0;
JD4S = 0;
CBH4S = 0;
CDH4S = 0;
for ii=1:length(wl_data(:,1))
    wl = wl_data(ii,1);
    N_im = wl_data(ii,3);
    alph = 4*pi*N_im/wl; % The absorption coefficent (cm^-1)
    inc_pow = wl_data(ii,4);
    flux = inc_pow/1000*wl/(c*h); % The incident photon flux (photons/cm^2/sec)
    JH4S = alph*(alph*flux/Dp)*(Lp^2/(1-alph^2*Lp^2))*(1+2*alph*Lp^2/((d1+d2)*(1-alph^2*Lp^2))-2*
        Lp^2/((d1+d2)^2*(1-alph^2*Lp^2))) + JH4S;
    JD4S = alph*exp(alph*(x2_val-d1))*(alph*flux/Dp)*(Lp^2/(1-alph^2*Lp^2))*(1+2*alph*Lp^2/((
        x2_val+d2)*(1-alph^2*Lp^2))-2*Lp^2/((x2_val+d2)^2*(1-alph^2*Lp^2))) + JD4S;
    CBH4S = (alph*flux/Dp)*(Lp^2/(1-alph^2*Lp^2))*(1+2*alph*Lp^2/((d1+d2)*(1-alph^2*Lp^2))) +
        CBH4S;
    CDH4S = exp(alph*(x2_val-d1))*(alph*flux/Dp)*(Lp^2/(1-alph^2*Lp^2))*(1+2*alph*Lp^2/((x2_val+d2
        )*(1-alph^2*Lp^2))) + CDH4S;
end
JA4S = A4*exp((d1+d2)/Lp)/(d1+d2)*(1/Lp-1/(d1+d2));
JB4S = -B4*exp(-(d1+d2)/Lp)/(d1+d2)*(1/Lp+1/(d1+d2));
CB = A4*exp((d1+d2)/Lp)/(d1+d2)+B4*exp(-(d1+d2)/Lp)/(d1+d2)+CBH4S;
CD = A4*exp((x2_val+d2)/Lp)/(x2_val+d2)+B4*exp(-(x2_val+d2)/Lp)/(x2_val+d2)+CDH4S;
S3 = solve(Sp*CB == -Dp*(JA4S+JB4S+JH4S), CD == ni^2/ND*(exp(V/VT)-1));

%Now, calculate the carrier distribution and the current.
A4_val = double(S3.A4);
B4_val = double(S3.B4);

% r_vals = x2_val+d2:(d1-x2_val)/100:d1+d2;
% C_vals = zeros(1,length(r_vals));
% CH4S = 0;
% for steppin = 1:length(r_vals)
%     for ii=1:length(wl_data(:,1))
%         wl = wl_data(ii,1);
%         N_im = wl_data(ii,3);
%         alph = 4*pi*N_im/wl; % The absorption coefficent (cm^-1)
%         inc_pow = wl_data(ii,4);
%         flux = inc_pow/1000*wl/(c*h); % The incident photon flux (photons/cm^2/sec)
%         CH4S = exp(alph*(r_vals(steppin)-d1-d2))*(alph*flux/Dp)*(Lp^2/(1-alph^2*Lp^2))*(1+2*alph
    *Lp^2/(r_vals(steppin)*(1-alph^2*Lp^2))) + CH4S;
%     end
%     C_vals(1,steppin) = A4_val*exp(r_vals(steppin)/Lp)/r_vals(steppin)+B4_val*exp(-r_vals(
    steppin)/Lp)/r_vals(steppin)+CH4S;
% end
% figure;
% plot(r_vals,C_vals);

JA4 = A4_val*exp((d2+x2_val)/Lp)/(d2+x2_val)*(1/Lp-1/(d2+x2_val));
JB4 = -B4_val*exp(-(d2+x2_val)/Lp)/(d2+x2_val)*(1/Lp+1/(d2+x2_val));
J4 = q*Dp*(JA4+JB4+JD4S);
```

```
%The total current
J = J1*(x4_val)^2/(d2+d1)^2-J23_r+J23_l*d2^2/(d1+d2)^2+J4*(d2+x2_val)^2/(d2+d1)^2;
```

## C.7 Code for the Wire Subcell

**Listing C.7: Code to calculate the current at a given voltage for a wire solar cell**

```
function [J] = Wire_IV(Sp,Ln,Lp,V,wl_data,r1,r2,L)

%              Analytical Model for a Wire Solar Cell
%                    From work by Brendan Kayes
%                    Dan Turner-Evans, Aug 2012
%                          dt@caltech.edu
%                 California Institute of Technology
%
% This is a MATLAB tool for calculating the IV curve of a radial junction
% solar cell
%

% Specify the appropriate constants
k = 8.6173324E-5; % The Bolzmann constant (eV/K)
T = 300; % The temperature (K)
q = 1.60219E-19; % The fundamental electrical charge (C)
VT = k*T; % The thermal voltage (eV)
NA = 1E16; % The p-type, core doping (cm^-3)
ND = 1E18; % The n-type, shell doping (cm^-3)
NC = 1E19; % Effective density of states in the conduction band (cm^-3)
NV = 6.3E18; % Effective density of states in the valence band (cm^-3)
EG = 0.757; % The material bandgap (eV)
ni = sqrt(NC*NV)*exp(-EG/(2*VT)); % The intrinsic carrier density (cm^-3)
Phi_0 = VT*log(NA*ND/ni^2); % The built in voltage (eV)
% V = 0; % The applied voltage (V)
% r1 = 0.1E-4; % Emitter thickness (cm)
% r2 = 0.65E-4; % The core radius (cm)
% eps0 = 8.854187817620E-14; % Vacuum permittivty in F/cm
% eps = 15.75*eps0; % The overall permittivity
% epsilonp = eps;
% epsilonn = eps;

% First, solve for the limits of the depletion region
x0 = [r1/100 r2-r1];
x = fsolve(@(x)dep_limits(x,r1,r2,V),x0);
x2_val = x(1);
x4_val = x(2);

% Specify the constants for the quasi-neutral region
%Ln = 1E-5; % The electron diffusion length in the material (cm)rci
%Lp = 1E-4; % The hole diffusion length in the material (cm)
%N_re = 3; % The real part of index of refraction
%N_im = 0.5; % The imaginary part of the index of refraction
%wl = 6E-5; % The wavelength, in cm.
% alph = 4*pi*N_im/wl; % The absorption coefficent (cm^-1)
%inc_pow = 100; % AM1.5G power (mW/cm^2)
h = 6.626E-34; % Planck's constant (Jsec)
c = 3E10 ; % Speed of light (cm/s)
% flux = inc_pow/1000*wl/(c*h); % The incident photon flux (photons/cm^2/sec)
mup = 1757; % The hole mobility (cm^2/V/sec)
```

```
Dp = mup*k*T; % The diffusion coefficient for holes (cm^2/sec)
mun = 3652; % The electron mobility (cm^2/V/sec)
Dn = mun*k*T; % The diffusion coefficient for electrons (cm^2/sec)


% Calculate the current in regions 2 and 3
Umax = ni*sqrt(Dn+Dp)/(Ln*Lp)*sinh(q*V/(2*k*T));
kappa = pi*k*T/(Phi_0+V);
rV = x4_val + log(NA/ni)/log(NA*ND/ni^2)*(x2_val+(r2-x4_val));
r1_r = rV - (x2_val+(r2-x4_val))/2*kappa;
r2_r = rV + (x2_val+(r2-x4_val))/2*kappa;
J23_l = 0;
for i=1:length(wl_data(:,1))
    wl = wl_data(i,1);
    N_im = wl_data(i,3);
    alph = 4*pi*N_im/wl; % The absorption coefficent (cm^-1)
    inc_pow = wl_data(i,4);
    flux = inc_pow/1000*wl/(c*h); % The incident photon flux (photons/cm^2/sec)
    J23_l = q*flux*(1-exp(-alph*L))*((r2+x2_val)^2-x4_val^2)/(r1+r2)^2 + J23_l;
end
J23_r = -q*L*Umax/(r1+r2)^2*(r2_r^2-r1_r^2);

% Calculate the current in region 1
% First, solve for the constants given the boundary conditions using
% symbolic logic.
J1_l = 0;
B5 = x4_val/Ln;
B1 = (r1+r2)/Lp;
for i=1:length(wl_data(:,1))
    wl = wl_data(i,1);
    N_im = wl_data(i,3);
    alph = 4*pi*N_im/wl; % The absorption coefficent (cm^-1)
    inc_pow = wl_data(i,4);
    flux = inc_pow/1000*wl/(c*h); % The incident photon flux (photons/cm^2/sec)
    J1_l = 2*q*flux*(1-exp(-alph*L))*Ln^2/Lp^2*B5/B1^2*besseli(1,B5)/besseli(0,B5)+J1_l;
end
J1_r = -2*q*(ni^2/NA)*L*Dn/Lp^2*B5/B1^2*besseli(1,B5)/besseli(0,B5)*(exp(V/VT)-1);


% Calculate the current in region 4
% Sp = 100; % Surface recombination velocity (cm/s)
J4_l = 0;
B2 = (r2 + x2_val)/Lp;
B4 = Lp*Sp/Dp;
f1 = besseli(1,B1)+B4*besseli(0,B1);
f2 = besselk(1,B1)-B4*besselk(0,B1);
for i=1:length(wl_data(:,1))
    wl = wl_data(i,1);
    N_im = wl_data(i,3);
    alph = 4*pi*N_im/wl; % The absorption coefficent (cm^-1)
    inc_pow = wl_data(i,4);
    flux = inc_pow/1000*wl/(c*h); % The incident photon flux (photons/cm^2/sec)
    J4_l = 2*q*flux*(1-exp(-alph*L))*B2/B1^2*((besselk(1,B2)*(f1-B4*besseli(0,B2))-besseli(1,B2)*(
        f2+B4*besselk(0,B2)))/(f1*besselk(0,B2)+f2*besseli(0,B2)))+J4_l;
end
J4_r = -2*q*(ni^2/ND)*L*Dp/Lp^2*B2/B1^2*((f1*besselk(1,B2)-f2*besseli(1,B2))/(f1*besselk(0,B2)+f2*
    besseli(0,B2)))*(exp(V/VT)-1);

%The total current
% J = zeros(7,1);
% J(1,1) = J1_r + J1_l + J23_r + J23_l + J4_r + J4_l;
```

```
% J(2,1) = J1_r;
% J(3,1) = J1_l;
% J(4,1) = J23_r;
% J(5,1) = J23_l;
% J(6,1) = J4_r;
% J(7,1) = J4_l;
J = J1_r + J1_l + J23_r + J23_l + J4_r + J4_l;
```

# Appendix D

## Transmission Matrix Method Code

In order to design an effective anti-reflection coating, I relied on the transmission matrix method. In this technique, the transmission and propagation matrices in each layer of a material stack are calculated and used to find the overall reflection and transmission as follows:

$$T_{layer} = \frac{1}{2}\begin{pmatrix} 1+\frac{n_1}{n_0} & 1-\frac{n_1}{n_0} \\ 1-\frac{n_1}{n_0} & 1+\frac{n_1}{n_0} \end{pmatrix},$$

where $n_0$ and $n_1$ are the real parts of the indexes of refraction of the two materials.

$$P_{layer} = \begin{pmatrix} e^{-in_1(1+ik_1)\frac{\omega}{c}t_1} & 0 \\ 0 & e^{in_1(1+ik_1)\frac{\omega}{c}t_1} \end{pmatrix},$$

where $k_1$ is the imaginary part of the index of the refraction of the material, $t_1$ is the thickness of the material, $\omega$ is the frequency of the light, and $c$ is the speed of light.

$$M = T_1 \cdot P_1 \cdot T_2 \cdot P_2 \cdot ...$$

$$R_{total} = \frac{M(2,1) \cdot M(2,1)^*}{M(1,1) \cdot M(1,1)^*},$$

$$T_{total} = \frac{1}{M(1,1) \cdot M(1,1)^*}.$$

The left plot of **Figure D.1** shows a comparison between the TMM calculations and FDTD simulations for a 500 nm slab of GaAsP cladded with 20 nm of GaInP and coated on top with 100 nm of $TiO_x$ and 60 nm of MgF. The right plot of Figure D.1 demonstrates

the effect of adding the $TiO_x$/MgF coating to the back of the cell.

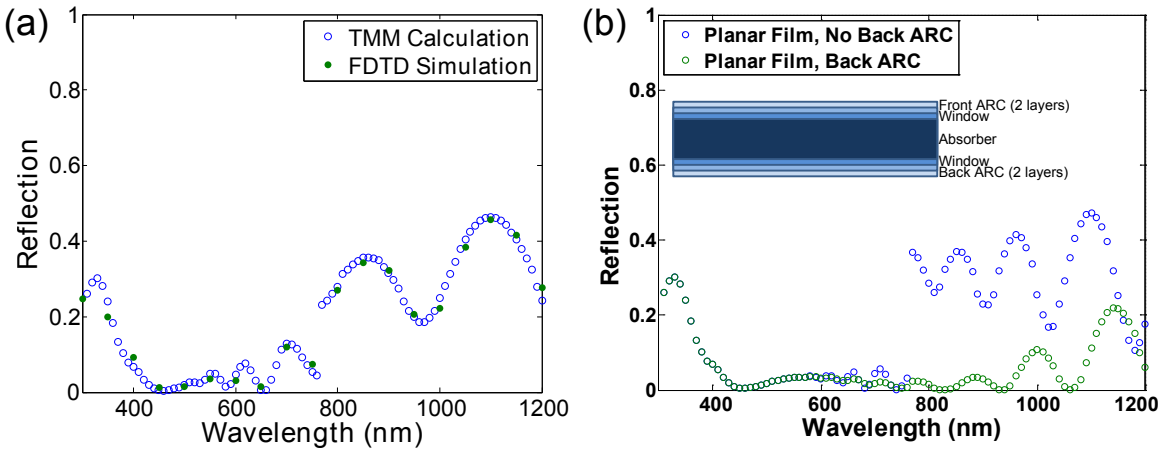


Figure D.1: TMM calculations. (a) Comparison between TMM calculations and FDTD simulations. (b) Change in reflection as a back surface antireflection coating is added.

# Appendix E

## Sentaurus Code

### E.1 Code from the Tandem Simulations

The code for the simulations run in Chapter 5 is included below. Much of it is adapted from the work featured in the thesis of Dr. Mike Kelzenberg.(186) The following code all appeared in the following layout in Sentaurus Workbench.

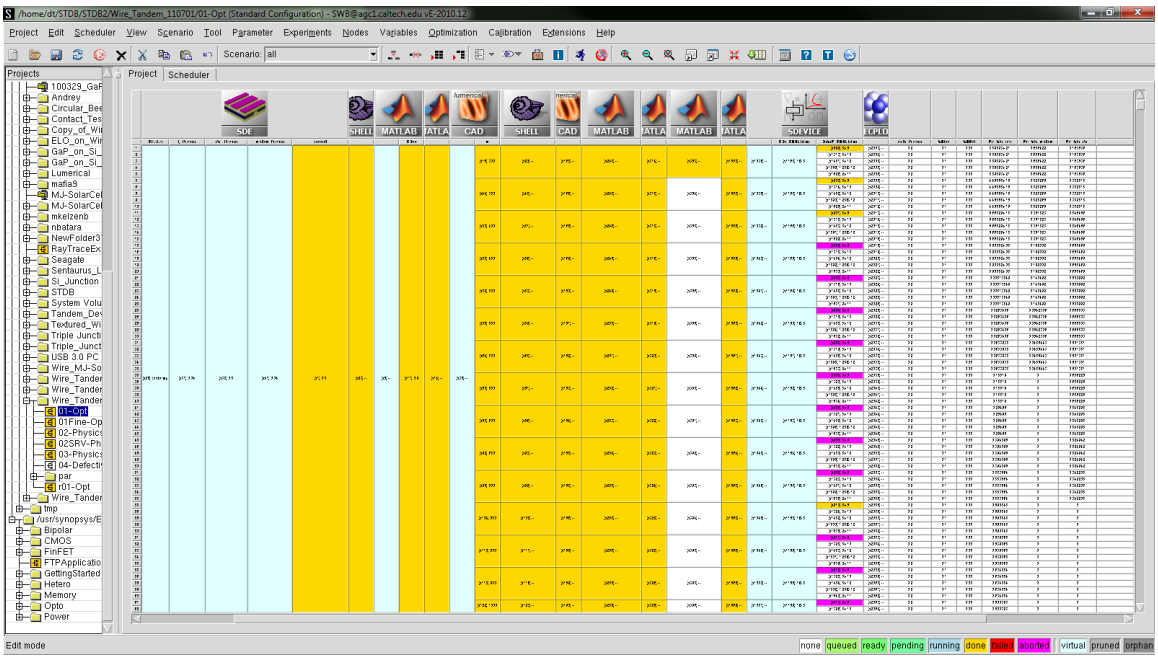


Figure E.1: Layout of Sentaurus simulations for finding the optical generation in tandem wire arrays.

**Listing E.1: Code to generate a tandem wire array FEM grid**

```
##############################################################
```

```
# Dan Turner-Evans                                          #
# 08/02/11                                                  #
# A core shell wire solar cell                              #
#############################################################

#############################################################
# Set the geometric device parameters                       #
#############################################################
#define core_height @core_height@
#define core_radius (* @core_diameter@ 0.5)
#define pitch @pitch@
#define tj_thickness @tj_thickness@
#define shell_thickness @shell_thickness@
#define window_thickness @window_thickness@
#define core_emitter_t 0.1
#define shell_emitter_t 0.1
#define oxide_thickness @oxide_thickness@
#define exposed @exposed@

#############################################################
# Set the doping device parameters                          #
#############################################################
#define window_doping 1e18
#define window_tj_doping 5e19
#define shell_emitter_doping 9e17
#define shell_base_doping 5e16
#define core_tj_doping 5e19
#define core_emitter_doping 9e17
#define core_base_doping 5e16

#############################################################
# Set the grid spacing                                      #
#############################################################
#define DopMaxGrid 0.04
#define DopMinGrid 0.005
#define MatMaxGrid 0.04
#define MatMinGrid 0.002
#define MatRatio 2
#define MBMaxGrid 0.04
#define MBMinGrid 0.005
#define MBRatio 1.5
#define RefMaxGrid 0.04
#define RefMinGrid 0.01
#define RefRatio 1.5
#define window_grid 0.002
#define shell_emitter_grid 0.02
#define shell_base_grid 0.04
#define window_tj_grid 0.002
#define core_tj_grid 0.002
#define core_emitter_grid 0.02
#define core_base_grid 0.04
#define Air_grid 0.5
#define Oxide_grid 0.5

#############################################################
# Create the structure                                      #
#############################################################

# Air
(sdegeo:create-rectangle (position 0 0 0) (position (* pitch 0.5) (+ 2 core_height (* tj_thickness
      0.5) window_thickness shell_thickness ) 0) "Ambient" "Air")
```

```
#if [string compare @Structure@ "conformal"] == 0

# Window
(sdegeo:create-rectangle (position 0 0 0) (position (+ core_radius (* tj_thickness 0.5)
     shell_thickness window_thickness) (+ core_height (* tj_thickness 0.5) window_thickness
     shell_thickness ) 0) "GaInP" "window_outer")

# Shell
(sdegeo:create-rectangle (position 0 0 0) (position (+ core_radius (* tj_thickness 0.5) (*
     window_thickness 0.5) shell_thickness) (+ core_height (* tj_thickness 0.5) (* window_thickness
      0.5) shell_thickness ) 0) "GaAsP" "shell_emitter")
(sdegeo:create-rectangle (position 0 0 0) (position (+ core_radius (* tj_thickness 0.5) (*
     window_thickness 0.5) (- shell_thickness shell_emitter_t) ) (+ core_height (* tj_thickness
     0.5) (* window_thickness 0.5) (- shell_thickness shell_emitter_t) ) 0) "GaAsP" "shell_base")

# TJ
(sdegeo:create-rectangle (position 0 0 0) (position (+ core_radius (* tj_thickness 0.5) (*
     window_thickness 0.5)) (+ core_height (* tj_thickness 0.5) (* window_thickness 0.5) ) 0) "
     GaInP" "window_inner")
(sdegeo:create-rectangle (position 0 0 0) (position (+ core_radius (* tj_thickness 0.5)) (+
     core_height (* tj_thickness 0.5) ) 0) "GaInP" "window_tj")
(sdegeo:create-rectangle (position 0 0 0) (position core_radius core_height 0) "SiliconGermanium"
     "tj_core")

# Core
(sdegeo:create-rectangle (position 0 0 0) (position (- core_radius (* tj_thickness 0.5)) (-
     core_height (* tj_thickness 0.5)) 0) "SiliconGermanium" "core_emitter")
(sdegeo:create-rectangle (position 0 0 0) (position (- core_radius (+ (* tj_thickness 0.5)
     core_emitter_t)) (- core_height (+ (* tj_thickness 0.5) core_emitter_t)) 0) "SiliconGermanium"
      "core_base")
#endif

#if [string compare @Structure@ "hemisphere"] == 0

# Window
(sdegeo:create-elliptical-sheet (position 0 core_height 0) (position (+ core_radius (*
     tj_thickness 0.5) window_thickness shell_thickness) core_height 0) (/ (+ (* tj_thickness 0.5)
     window_thickness shell_thickness ) (+ core_radius (* tj_thickness 0.5) window_thickness
     shell_thickness )) "GaInP" "window_outer")

# Shell
(sdegeo:create-elliptical-sheet (position 0 core_height 0) (position (+ core_radius (*
     tj_thickness 0.5) (* window_thickness 0.5) shell_thickness) core_height 0) (/ (+ (*
     tj_thickness 0.5) (* window_thickness 0.5) shell_thickness ) (+ core_radius (* tj_thickness
     0.5) (* window_thickness 0.5) shell_thickness )) "GaAsP" "shell_emitter")
(sdegeo:create-elliptical-sheet (position 0 core_height 0) (position (+ core_radius (*
     tj_thickness 0.5) (* window_thickness 0.5) (- shell_thickness shell_emitter_t)) core_height 0)
      (/ (+ (* tj_thickness 0.5) (* window_thickness 0.5) (- shell_thickness shell_emitter_t) ) (+
     core_radius (* tj_thickness 0.5) (* window_thickness 0.5) (- shell_thickness shell_emitter_t)
     )) "GaAsP" "shell_base")

# TJ, etc...
(sdegeo:create-elliptical-sheet (position 0 core_height 0) (position (+ core_radius (*
     tj_thickness 0.5) (* window_thickness 0.5)) core_height 0) (/ (+ (* tj_thickness 0.5) (*
     window_thickness 0.5) ) (+ core_radius (* tj_thickness 0.5) (* window_thickness 0.5) )) "GaInP
     " "window_inner")
(sdegeo:create-elliptical-sheet (position 0 core_height 0) (position (+ core_radius (*
     tj_thickness 0.5) ) core_height 0) (/ (* tj_thickness 0.5) (+ core_radius (* tj_thickness 0.5)
      )) "GaInP" "window_tj")
```

```
(sdegeo:define-contact-set "Top_contact" 4  (color:rgb 0 1 0 ) "##" )
(sdegeo:define-2d-contact (find-edge-id (position (+ core_radius (* tj_thickness 0.5)
    shell_thickness window_thickness) core_height 0)) "Top_contact")

(define removeMe (sdegeo:create-rectangle (position 0 core_height 0) (position (* pitch 0.5) (-
    core_height (* pitch 0.5))  0) "GaAs" "temp"))
(entity:delete removeMe)

(define removeMeToo (sdegeo:create-rectangle (position 0 (- core_height (* pitch 0.5)) 0) (
    position (* pitch -0.5) (+ core_height (* pitch 0.5))  0) "GaAs" "temp"))
(entity:delete removeMeToo)

(sdegeo:create-rectangle (position 0 0 0) (position (* pitch 0.5) core_height 0) "Oxide" "Oxide")

(sdegeo:create-rectangle (position 0 0 0) (position core_radius core_height 0) "SiliconGermanium"
    "tj_core")

# Core
(sdegeo:create-rectangle (position 0 0 0) (position core_radius (- core_height (* tj_thickness
    0.5)) 0) "SiliconGermanium" "core_emitter")
(sdegeo:create-rectangle (position 0 0 0) (position (- core_radius core_emitter_t) (- core_height
    (+ (* tj_thickness 0.5) core_emitter_t)) 0) "SiliconGermanium" "core_base")

#endif

#if [string compare @Structure@ "sphere"] == 0
# Window
(sdegeo:create-elliptical-sheet (position 0 core_height 0) (position (+ core_radius (*
    tj_thickness 0.5) window_thickness shell_thickness) core_height 0) (/ (+ (* tj_thickness 0.5)
    window_thickness shell_thickness ) (+ core_radius (* tj_thickness 0.5) window_thickness
    shell_thickness )) "GaInP" "window_outer")

# Shell
(sdegeo:create-elliptical-sheet (position 0 core_height 0) (position (+ core_radius (*
    tj_thickness 0.5) (* window_thickness 0.5) shell_thickness) core_height 0) (/ (+ (*
    tj_thickness 0.5) (* window_thickness 0.5) shell_thickness ) (+ core_radius (* tj_thickness
    0.5) (* window_thickness 0.5) shell_thickness )) "GaAsP" "shell_emitter")
(sdegeo:create-elliptical-sheet (position 0 core_height 0) (position (+ core_radius (*
    tj_thickness 0.5) (* window_thickness 0.5) (- shell_thickness shell_emitter_t)) core_height 0)
     (/ (+ (* tj_thickness 0.5) (* window_thickness 0.5) (- shell_thickness shell_emitter_t) ) (+
    core_radius (* tj_thickness 0.5) (* window_thickness 0.5) (- shell_thickness shell_emitter_t)
    )) "GaAsP" "shell_base")

# TJ, etc...
(sdegeo:create-elliptical-sheet (position 0 core_height 0) (position (+ core_radius (*
    tj_thickness 0.5) (* window_thickness 0.5)) core_height 0) (/ (+ (* tj_thickness 0.5) (*
    window_thickness 0.5) ) (+ core_radius (* tj_thickness 0.5) (* window_thickness 0.5) )) "GaInP
    " "window_inner")
(sdegeo:create-rectangle (position 0 (- core_height exposed) 0) (position (+ core_radius (*
    tj_thickness 0.5) (* window_thickness 0.5) ) core_height 0) "GaInP" "window_inner2")
(sdegeo:create-elliptical-sheet (position 0 core_height 0) (position (+ core_radius (*
    tj_thickness 0.5) ) core_height 0) (/ (* tj_thickness 0.5) (+ core_radius (* tj_thickness 0.5)
     )) "GaInP" "window_tj")
(sdegeo:create-rectangle (position 0 (- core_height exposed) 0) (position (+ core_radius (*
    tj_thickness 0.5) ) core_height 0) "GaInP" "window_tj2")

(define removeMeToo (sdegeo:create-rectangle (position 0 (- core_height (* pitch 0.5)) 0) (
    position (* pitch -0.5) (+ core_height (* pitch 0.5))  0) "GaAs" "temp"))
(entity:delete removeMeToo)

(sdegeo:create-rectangle (position 0 0 0) (position (+ core_radius oxide_thickness) (- core_height
```

```
      exposed ) 0) "Oxide" "Oxide")
(sdegeo:create-rectangle (position 0 0 0) (position core_radius core_height 0) "SiliconGermanium"
    "tj_core")

# Core
(sdegeo:create-rectangle (position 0 0 0) (position (- core_radius (* tj_thickness 0.5)) (-
    core_height (* tj_thickness 0.5)) 0) "SiliconGermanium" "core_emitter")
(sdegeo:create-rectangle (position 0 0 0) (position core_radius (- core_height exposed) 0) "
    SiliconGermanium" "core_emitter2")
(sdegeo:create-rectangle (position 0 0 0) (position (- core_radius (+ core_emitter_t (*
    tj_thickness 0.5)) ) (- core_height (+ (* tj_thickness 0.5) core_emitter_t)) 0) "
    SiliconGermanium" "core_base")

#endif


#################################################################
# Define the doping                                             #
#################################################################
(sdedr:define-constant-profile "ConstantProfileDefinition_for_Window_Outer" "
    NDopantActiveConcentration" window_doping)
(sdedr:define-constant-profile-region "ConstantProfilePlacement_for_Window_Outer" "
    ConstantProfileDefinition_for_Window_Outer" "window_outer")
(sdedr:define-constant-profile "ConstantProfileDefinition_for_Window_Inner" "
    PDopantActiveConcentration" window_doping)
(sdedr:define-constant-profile-region "ConstantProfilePlacement_for_Window_Inner" "
    ConstantProfileDefinition_for_Window_Inner" "window_inner")
(sdedr:define-constant-profile "ConstantProfileDefinition_for_Shell_Emitter" "
    NDopantActiveConcentration" shell_emitter_doping)
(sdedr:define-constant-profile-region "ConstantProfilePlacement_for_Shell_Emitter" "
    ConstantProfileDefinition_for_Shell_Emitter" "shell_emitter")
(sdedr:define-constant-profile "ConstantProfileDefinition_for_Shell_Base" "
    PDopantActiveConcentration" shell_base_doping)
(sdedr:define-constant-profile-region "ConstantProfilePlacement_for_Shell_Base" "
    ConstantProfileDefinition_for_Shell_Base" "shell_base")
(sdedr:define-constant-profile "ConstantProfileDefinition_for_Window_TJ" "
    PDopantActiveConcentration" window_tj_doping)
(sdedr:define-constant-profile-region "ConstantProfilePlacement_for_Window_TJ" "
    ConstantProfileDefinition_for_Window_TJ" "window_tj")
#if [string compare @Structure@ "sphere"] == 0
(sdedr:define-constant-profile "ConstantProfileDefinition_for_Window_Inner2" "
    PDopantActiveConcentration" window_doping)
(sdedr:define-constant-profile-region "ConstantProfilePlacement_for_Window_Inner2" "
    ConstantProfileDefinition_for_Window_Inner2" "window_inner2")
(sdedr:define-constant-profile "ConstantProfileDefinition_for_Window_TJ2" "
    PDopantActiveConcentration" window_tj_doping)
(sdedr:define-constant-profile-region "ConstantProfilePlacement_for_Window_TJ2" "
    ConstantProfileDefinition_for_Window_TJ2" "window_tj2")
(sdedr:define-constant-profile "ConstantProfileDefinition_for_Core_Emitter2" "
    PhosphorusActiveConcentration" core_emitter_doping)
(sdedr:define-constant-profile-region "ConstantProfilePlacement_for_Core_Emitter2" "
    ConstantProfileDefinition_for_Core_Emitter2" "core_emitter2")
#endif
(sdedr:define-constant-profile "ConstantProfileDefinition_for_Core_TJ" "NDopantActiveConcentration
    " core_tj_doping)
(sdedr:define-constant-profile-region "ConstantProfilePlacement_for_Core_TJ" "
    ConstantProfileDefinition_for_Core_TJ" "tj_core")
(sdedr:define-constant-profile "ConstantProfileDefinition_for_Core_Emitter" "
    PhosphorusActiveConcentration" core_emitter_doping)
(sdedr:define-constant-profile-region "ConstantProfilePlacement_for_Core_Emitter" "
    ConstantProfileDefinition_for_Core_Emitter" "core_emitter")
```

```
(sdedr:define-constant-profile "ConstantProfileDefinition_for_Core_Base" "BoronActiveConcentration
    " core_base_doping)
(sdedr:define-constant-profile-region "ConstantProfilePlacement_for_Core_Base" "
    ConstantProfileDefinition_for_Core_Base" "core_base")

#############################################################
# Define the contacts                                       #
#############################################################
(sdegeo:define-contact-set "Top_contact" 4  (color:rgb 0 1 0 ) "##" )
(sdegeo:define-contact-set "Bottom_contact" 4  (color:rgb 0 0 1 ) "##" )

(sdegeo:insert-vertex (position (* core_radius 0.5) 0 0))

(sdegeo:set-current-contact-set "Top_contact")
#if [string compare @Structure@ "conformal"] == 0
(sdegeo:insert-vertex (position (+ core_radius (* tj_thickness 0.5) shell_thickness
    window_thickness) 0.5 0))
(sdegeo:define-2d-contact (find-edge-id (position (+ core_radius (* tj_thickness 0.5)
    shell_thickness window_thickness) 0.25 0)) "Top_contact")
#endif

#if [string compare @Structure@ "hemisphere"] == 0
# (sdegeo:define-2d-contact (find-edge-id (position (+ core_radius (* tj_thickness 0.5)
    shell_thickness window_thickness) core_height 0)) "Top_contact")
#endif

#if [string compare @Structure@ "sphere"] == 0
(sdegeo:define-2d-contact (find-edge-id (position (+ core_radius (* tj_thickness 0.5)
    shell_thickness window_thickness) core_height 0)) "Top_contact")
#endif

(sdegeo:set-current-contact-set "Bottom_contact")
(sdegeo:define-2d-contact (find-edge-id (position (* core_radius 0.25) 0 0)) "Bottom_contact")

# Intermediate contacts for subcell IV
(sdegeo:define-contact-set "Mid_contact" 4  (color:rgb 1 0 0 ) "##" )
(sdegeo:set-current-contact-set "Mid_contact")
#if [string compare @Structure@ "conformal"] == 0
(sdegeo:define-2d-contact (find-edge-id (position core_radius (* core_height 0.5) 0)) "Mid_contact
    ")
(sdegeo:define-2d-contact (find-edge-id (position (* core_radius 0.5) core_height 0)) "Mid_contact
    ")
#endif
#if [string compare @Structure@ "hemisphere"] == 0
(sdegeo:define-2d-contact (find-edge-id (position (* core_radius 0.5) core_height 0)) "Mid_contact
    ")
#endif
#if [string compare @Structure@ "sphere"] == 0
(sdegeo:define-2d-contact (find-edge-id (position core_radius (- core_height (* exposed 0.5)) 0))
    "Mid_contact")
(sdegeo:define-2d-contact (find-edge-id (position (* core_radius 0.5) core_height 0)) "Mid_contact
    ")
#endif

#############################################################
# Refine the grid between doping levels                     #
#############################################################
#if [string compare @Structure@ "conformal"] == 0
(sdedr:define-refinement-window "Win.All" "Rectangle" (position 0 0 0 ) (position (* pitch 0.5) (+
     2 core_height shell_thickness) 0))
(sdedr:define-refinement-size "Ref.All" DopMaxGrid DopMaxGrid 0 DopMinGrid DopMinGrid 0 )
```

```
(sdedr:define-refinement-function "Ref.All" "DopingConcentration" "MaxTransDiff" 1)
(sdedr:define-refinement-placement "Ref.All" "Ref.All" "Win.All")
#endif

#############################################################
# Further refine the grid between materials                 #
#############################################################
#if [string compare @Structure@ "conformal"] == 0
(sdedr:define-refinement-window "Win.Hetero" "Rectangle" (position 0 0 0 ) (position (* pitch 0.5)
      (+ 2 core_height shell_thickness) 0))
(sdedr:define-refinement-size "Ref.Hetero1" MatMaxGrid MatMaxGrid 0 MatMinGrid MatMinGrid 0 )
(sdedr:define-refinement-function "Ref.Hetero1" "MaxLenInt" "Germanium" "GaAs" MatMinGrid MatRatio
      "DoubleSide")
(sdedr:define-refinement-placement "Ref.Hetero1" "Ref.Hetero1" "Win.Hetero")
#endif

#############################################################
# Refine the grid according to region                       #
#############################################################
#if [string compare @Structure@ "conformal"] == 0
(sdedr:define-refinement-window "Win1" "Rectangle" (position 0 0 0 ) (position (+ core_radius (*
     tj_thickness 0.5) shell_thickness window_thickness) (+ core_height (* tj_thickness 0.5)
     window_thickness shell_thickness ) 0))
(sdedr:define-multibox-size "Size.Top1" MBMaxGrid MBMaxGrid MBMinGrid MBMinGrid -MBRatio -MBRatio)
(sdedr:define-multibox-placement "Placement.Top1" "Size.Top1" "Win1")
#if 0
(sdedr:define-refinement-window "Win7" "Rectangle" (position (- core_radius (* tj_thickness 0.5))
     0 0 ) (position (+ core_radius (* tj_thickness 0.5) (* window_thickness 0.5)) core_height 0))
(sdedr:define-multibox-size "Size.Top7" MatMinGrid MatMaxGrid MatMinGrid MatMaxGrid 1 1)
(sdedr:define-multibox-placement "Placement.Top7" "Size.Top7" "Win7")

(sdedr:define-refinement-window "Win8" "Rectangle" (position 0 (- core_height (* tj_thickness 0.5)
     ) 0 ) (position (+ core_radius (* tj_thickness 0.5) (* window_thickness 0.5)) (+ core_height
     (* tj_thickness 0.5) (* window_thickness 0.5)) 0))
(sdedr:define-multibox-size "Size.Top8" MatMaxGrid MatMinGrid MatMaxGrid MatMinGrid 1 1)
(sdedr:define-multibox-placement "Placement.Top8" "Size.Top8" "Win8")
#endif
(sdedr:define-refinement-window "Win2" "Rectangle" (position core_radius core_height 0 ) (position
      (+ core_radius (* tj_thickness 0.5) shell_thickness window_thickness) (+ core_height (*
     tj_thickness 0.5) window_thickness shell_thickness ) 0))
(sdedr:define-multibox-size "Size.Top2" RefMaxGrid RefMaxGrid RefMinGrid RefMinGrid -RefRatio -
     RefRatio)
(sdedr:define-multibox-placement "Placement.Top2" "Size.Top2" "Win2")

(sdedr:define-refinement-window "Win3" "Rectangle" (position 0 (- core_height core_radius) 0 ) (
     position (+ core_radius tj_thickness) (+ core_height tj_thickness) 0))
(sdedr:define-multibox-size "Size.Top3" RefMaxGrid RefMaxGrid RefMinGrid RefMinGrid -RefRatio -
     RefRatio)
(sdedr:define-multibox-placement "Placement.Top3" "Size.Top3" "Win3")

#else
(sdenoffset:create-noffset-block "region" "window_outer" "maxedgelength" window_grid)
(sdenoffset:create-noffset-block "region" "window_inner" "maxedgelength" window_grid)
(sdenoffset:create-noffset-block "region" "shell_emitter" "maxedgelength" shell_emitter_grid)
(sdenoffset:create-noffset-block "region" "shell_base" "maxedgelength" shell_base_grid)
(sdenoffset:create-noffset-block "region" "window_tj" "maxedgelength" window_tj_grid)
#if [string compare @Structure@ "sphere"] == 0
(sdenoffset:create-noffset-block "region" "window_inner2" "maxedgelength" window_grid)
(sdenoffset:create-noffset-block "region" "window_tj2" "maxedgelength" window_tj_grid)
(sdenoffset:create-noffset-block "region" "core_emitter2" "maxedgelength" core_emitter_grid)
#endif
```

```
(sdenoffset:create-noffset-block "region" "tj_core" "maxedgelength" core_tj_grid)
(sdenoffset:create-noffset-block "region" "core_emitter" "maxedgelength" core_emitter_grid)
(sdenoffset:create-noffset-block "region" "core_base" "maxedgelength" core_base_grid)
(sdenoffset:create-noffset-block "region" "Air" "maxedgelength" Air_grid)
(sdenoffset:create-noffset-block "region" "Oxide" "maxedgelength" Oxide_grid)
#endif


#############################################################
# Generate the mesh                                         #
#############################################################

(sde:save-model "n@node@")
(sdedr:append-cmd-file "xy.cmd")
#if [string compare @Structure@ "conformal"] == 0
(sde:build-mesh "snmesh" "-a -c boxmethod" "n@node@")
#else
(sde:build-mesh "noffset" "" "n@node@")
#endif
```

**Listing E.2: Code to create DF-ISE files from the generated .tdr file**

```
# Create a DF-ISE file from the .tdr file

#if [string compare @Structure@ "conformal"] == 0
tdx -dd -M 0 -S 0 n@node|sde@_msh.tdr n@node|sde@_msh

#else

tdx -dd -M 0 -S 0 n@node|sde@_msh_pof.tdr n@node|sde@_msh

#endif
```

**Listing E.3: Code to generate optical data for SiGe and GaAsP**

```
% Program to identify the GaInP and GaAsP compositions that are lattice
% matched to SiGe at a given composition and to then create optical data
% for GaAsP by shifting the optical data of GaAs and to create optical data
% for GaInP by shifting the optical data of InP

% 7/25/11
% Dan Turner-Evans

% Navigate to the appropriate directory
cd nk;

% Import the tabulated data relating the GaInP and GaAsP material parameters
% to a given composition of SiGe
lma = importdata('lattice_matched_alloys.txt');
SiGe_x = lma.data(:,1);
SiGe_Eg = lma.data(:,3);
GaInP_x = lma.data(:,4);
GaInP_Eg = lma.data(:,6);
GaAsP_x = lma.data(:,7);
GaAsP_Eg = lma.data(:,9);

% Import the GaAs optical data
GaAs_Eg = 1.43;
GaAs_data = importdata('GaAs.txt');
```

```
% Import the InP optical data
InP_Eg = 1.35;
InP_data = importdata('InP.txt');

% Specify the SiGe composition
ChosenSiGex = @SiGex@;

% Identify the GaInP and GaAsP composition that are lattice matched to the
% chosen SiGe composition
found = 0;
for i=1:length(SiGe_x),
    find = ChosenSiGex - SiGe_x(i,1);
    if find < 0,
        if abs(ChosenSiGex - SiGe_x(i,1)) < abs(ChosenSiGex - SiGe_x(i-1,1)),
            found = i;
            break
        else
            found = i-1;
            break
        end
    end
end

% Create GaInP optical data from InP
GaInP = InP_data;
for i=1:length(GaInP(:,1)),
    GaInP(i,1) = 1.240/(1.240./GaInP(i,1) + GaInP_Eg(found,1) - InP_Eg);
end

% Create GaAsP optical data from GaAs
GaAsP = GaAs_data;
for i=1:length(GaAsP(:,1)),
    GaAsP(i,1) = 1.240/(1.240./GaAsP(i,1) + GaAsP_Eg(found,1) - GaAs_Eg);
end

% Write the generated data to a csv .txt file
xlswrite('GaAsP.txt',GaAsP)
xlswrite('GaInP.txt',GaInP)
```

**Listing E.4: Code to add scattering particles to optical simulations**

```
#if [string compare @Structure@ "conformal"] == 0
maxz = @core_height@ + @tj_thickness@ + @shell_thickness@ + @window_thickness@ + @ARBot@ + @ARTop@
    ;
excludeZone = @core_diameter@/2 + @tj_thickness@ + @shell_thickness@ +@window_thickness@ + @ARBot@
     + @ARTop@;
#endif
#if [string compare @Structure@ "hemisphere"] == 0
maxz = @core_height@;
excludeZone = @core_diameter@/2;
#endif
#if [string compare @Structure@ "sphere"] == 0
maxz = @core_height@ -@exposed@;
excludeZone = @core_diameter@/2 + @oxide_thickness@;
#endif
minz = 0;
noz = 4;

unitcellhalfwidth = @pitch@/2;

minRad = 0.05;
```

```
maxRad = 0.25;

numSpheres = 50*@core_height@/10;

num = 0;
failc = 0;

xes = zeros(1,numSpheres);
zes = zeros(1,numSpheres);
rads = zeros(1,numSpheres);

fid = fopen('Scatterer_Script_n@node@.lsf','w');

while (num < numSpheres)

    failc = failc + 1;
    if (failc > 10000)
        break;
    end

    xGuess = rand * unitcellhalfwidth;
    zGuess = minz + (maxz - minz)*rand*(1-rand);
    radGuess = minRad + (maxRad - minRad)*rand;

    if ( xGuess - radGuess < excludeZone )
        continue;
    end

    if ( maxz - xGuess * noz / unitcellhalfwidth < zGuess )
        continue;
    end

    isGood = 1;
    for n=1:num
        if ( (xGuess - xes(n) ) ^ 2 + ( zGuess - zes(n) ) ^ 2 ) ^ 0.5 < (rads(n) + radGuess)
            isGood = 0;
            break;
        end
    end

    if (isGood)
        num = num+1;
        xes(num) = xGuess;
        zes(num) = zGuess;
        rads(num) = radGuess;
        extnt = (2*radGuess) ^ (1/3);

       fprintf(fid,'addcircle;\r\nset("name","Sphere%d");\r\n', num );
       fprintf(fid,'set("material","Al2O3 - Palik");\r\nset("set mesh order from material database
            ",0);\r\n');
       fprintf(fid,['set("mesh order",3);\r\nset("x",' num2str(1e-6*xGuess) ');\r\nset("y",'
            num2str(1e-6*zGuess) ');\r\n']);
       fprintf(fid,['set("radius",' num2str(1e-6*radGuess) ');\r\n\r\n']);

    end

end

fclose(fid);
```

**Listing E.5: Code to modify Lumerical simulation for the specific structure**

```
########################################################################################
# Dan Turner-Evans                                                                     #
# 07/25/11                                                                             #
# 3D Simulation of core-shell wire structure                                           #
########################################################################################
clear;


# Load the initial simulation file upon which all future simulations are based
load("lumcad_template.fsp");

switchtolayout;
redrawoff;

# Modify the wire structure for the given parameters

select("core");
set("x span",@core_diameter@*1e-6);
set("y max",@core_height@*1e-6);

# Create a conformal, layered cylindrical wire structure

#if [string compare @Structure@ "conformal"] == 0

select("tj/window");
set("x span",(@core_diameter@ + @tj_thickness@ + @window_thickness@)*1e-6);
set("y max", (@core_height@ + @tj_thickness@/2 + @window_thickness@/2)*1e-6);

select("shell");
set("x span", (@core_diameter@ + @tj_thickness@ + @window_thickness@ + @shell_thickness@*2)*1e-6);
set("y max", (@core_height@ + @tj_thickness@/2 + @window_thickness@/2 + @shell_thickness@)*1e-6);

select("window");
set("x span", (@core_diameter@ + @tj_thickness@ + @window_thickness@*2 + @shell_thickness@*2)*1e
    -6);
set("y max", (@core_height@ + @tj_thickness@/2 + @window_thickness@ + @shell_thickness@)*1e-6);

select("ARBottom");
set("x span", (@core_diameter@ + @tj_thickness@ + @window_thickness@*2 + @shell_thickness@*2 +
    @ARBot@)*1e-6);
set("y max", (@core_height@ + @tj_thickness@/2 + @window_thickness@ + @shell_thickness@ + @ARBot@)
    *1e-6);

select("ARTop");
set("x span", (@core_diameter@ + @tj_thickness@ + @window_thickness@*2 + @shell_thickness@*2 +
    @ARBot@ + @ARTop@)*1e-6);
set("y max", (@core_height@ + @tj_thickness@/2 + @window_thickness@ + @shell_thickness@ + @ARBot@
    + @ARTop@)*1e-6);

#endif

#if [string compare @Structure@ "hemisphere"] == 0

select("tj/window");
delete;
select("shell");
delete;
select("window");
delete;
select("ARBottom");
```

```
delete;
select("ARTop");
delete;

addcustom("tj/window");
set("x",0);
set("x span",(@core_diameter@ + @tj_thickness@ + @window_thickness@)*1e-6);
set("y min",(@core_height@ - @tj_thickness@/2 - @window_thickness@/2)*1e-6);
set("y max",(@core_height@ + @tj_thickness@/2 + @window_thickness@/2)*1e-6);
set("equation 1","(@tj_thickness@/2 + @window_thickness@/2)/(@core_diameter@/2 + @tj_thickness@/2
    + @window_thickness@/2)*sqrt((@core_diameter@/2 + @tj_thickness@/2 + @window_thickness@/2)^2-x
    ^2)");
set("make nonsymmetric",1);
set("equation 2","0");
set("material","GaInP");
set("set mesh order from material database",0);
set("mesh order",3);

addcustom("shell");
set("x",0);
set("x span",(@core_diameter@ + @tj_thickness@ + @window_thickness@ + @shell_thickness@*2)*1e-6);
set("y min",(@core_height@ - @tj_thickness@/2 - @window_thickness@/2 - @shell_thickness@)*1e-6);
set("y max",(@core_height@ + @tj_thickness@/2 + @window_thickness@/2 + @shell_thickness@)*1e-6);
set("equation 1","(@tj_thickness@/2 + @window_thickness@/2 + @shell_thickness@)/(@core_diameter@/2
     + @tj_thickness@/2 + @window_thickness@/2 + @shell_thickness@)*sqrt((@core_diameter@/2 +
    @tj_thickness@/2 + @window_thickness@/2 + @shell_thickness@)^2-x^2)");
set("make nonsymmetric",1);
set("equation 2","0");
set("material","GaAsP");
set("set mesh order from material database",0);
set("mesh order",4);

addcustom("window");
set("x",0);
set("x span",(@core_diameter@ + @tj_thickness@ + @window_thickness@*2 + @shell_thickness@*2)*1e-6)
    ;
set("y min",(@core_height@ - @tj_thickness@/2 - @window_thickness@ - @shell_thickness@)*1e-6);
set("y max",(@core_height@ + @tj_thickness@/2 + @window_thickness@ + @shell_thickness@)*1e-6);
set("equation 1","(@tj_thickness@/2 + @window_thickness@ + @shell_thickness@)/(@core_diameter@/2 +
     @tj_thickness@/2 + @window_thickness@ + @shell_thickness@)*sqrt((@core_diameter@/2 +
    @tj_thickness@/2 + @window_thickness@ + @shell_thickness@)^2-x^2)");
set("make nonsymmetric",1);
set("equation 2","0");
set("material","GaInP");
set("set mesh order from material database",0);
set("mesh order",5);

addcustom("ARBottom");
set("x",0);
set("x span",(@core_diameter@ + @tj_thickness@ + @window_thickness@*2 + @shell_thickness@*2 +
    @ARBot@*2)*1e-6);
set("y min",(@core_height@ - @tj_thickness@/2 - @window_thickness@ - @shell_thickness@ - @ARBot@)
    *1e-6);
set("y max",(@core_height@ + @tj_thickness@/2 + @window_thickness@ + @shell_thickness@ + @ARBot@)
    *1e-6);
set("equation 1","(@tj_thickness@/2 + @window_thickness@ + @shell_thickness@ + @ARBot@)/(
    @core_diameter@/2 + @tj_thickness@/2 + @window_thickness@ + @shell_thickness@ + @ARBot@)*sqrt
    ((@core_diameter@/2 + @tj_thickness@/2 + @window_thickness@ + @shell_thickness@ + @ARBot@)^2-x
    ^2)");
set("make nonsymmetric",1);
set("equation 2","0");
```

```
set("material","TiOx - Sentaurus");
set("set mesh order from material database",0);
set("mesh order",6);

addcustom("ARTop");
set("x",0);
set("x span",(@core_diameter@ + @tj_thickness@ + @window_thickness@*2 + @shell_thickness@*2 +
    @ARBot@*2 + @ARTop@*2)*1e-6);
set("y min",(@core_height@ - @tj_thickness@/2 - @window_thickness@ - @shell_thickness@ - @ARBot@ -
    @ARTop@)*1e-6);
set("y max",(@core_height@ + @tj_thickness@/2 + @window_thickness@ + @shell_thickness@ + @ARBot@ +
    @ARTop@)*1e-6);
set("equation 1","(@tj_thickness@/2 + @window_thickness@ + @shell_thickness@ + @ARBot@ + @ARTop@)
    /(@core_diameter@/2 + @tj_thickness@/2 + @window_thickness@ + @shell_thickness@ + @ARBot@ +
    @ARTop@)*sqrt((@core_diameter@/2 + @tj_thickness@/2 + @window_thickness@ + @shell_thickness@ +
    @ARBot@ + @ARTop@)^2-x^2)");
set("make nonsymmetric",1);
set("equation 2","0");
set("material","MgF - Sentaurus");
set("set mesh order from material database",0);
set("mesh order",7);


addrect("infill");
set("x",0);
set("x span",@pitch@*1e-6);
set("y min",0);
set("y max",@core_height@*1e-6);
set("material","SiO2 (Glass) - Palik");
set("set mesh order from material database",0);
set("mesh order",8);

#endif

#if [string compare @Structure@ "sphere"] == 0

select("tj/window");
delete;
select("shell");
delete;
select("window");
delete;
select("ARBottom");
delete;
select("ARTop");
delete;

addrect("boot");
set("x",0);
set("x span",(@core_diameter@ + @oxide_thickness@*2)*1e-6);
set("y min",0);
set("y max",(@core_height@ - @exposed@)*1e-6);
set("material","SiO2 (Glass) - Palik");
set("set mesh order from material database",0);
set("mesh order",3);

addcustom("tj/window");
set("x",0);
set("x span",(@core_diameter@ + @tj_thickness@ + @window_thickness@)*1e-6);
set("y min",(@core_height@ - @tj_thickness@/2 - @window_thickness@/2)*1e-6);
set("y max",(@core_height@ + @tj_thickness@/2 + @window_thickness@/2)*1e-6);
```

```
set("equation 1","(@tj_thickness@/2 + @window_thickness@/2)/(@core_diameter@/2 + @tj_thickness@/2
    + @window_thickness@/2)*sqrt((@core_diameter@/2 + @tj_thickness@/2 + @window_thickness@/2)^2-x
    ^2)");
set("material","GaInP");
set("set mesh order from material database",0);
set("mesh order",4);

addrect("tj/window side");
set("x",0);
set("x span",(@core_diameter@ + @tj_thickness@ + @window_thickness@)*1e-6);
set("y min",(@core_height@ - @exposed@)*1e-6);
set("y max",@core_height@*1e-6);
set("material","GaInP");
set("set mesh order from material database",0);
set("mesh order",4);

addcustom("shell");
set("x",0);
set("x span",(@core_diameter@ + @tj_thickness@ + @window_thickness@ + @shell_thickness@*2)*1e-6);
set("y min",(@core_height@ - @tj_thickness@/2 - @window_thickness@/2 - @shell_thickness@)*1e-6);
set("y max",(@core_height@ + @tj_thickness@/2 + @window_thickness@/2 + @shell_thickness@)*1e-6);
set("equation 1","(@tj_thickness@/2 + @window_thickness@/2 + @shell_thickness@)/(@core_diameter@/2
     + @tj_thickness@/2 + @window_thickness@/2 + @shell_thickness@)*sqrt((@core_diameter@/2 +
    @tj_thickness@/2 + @window_thickness@/2 + @shell_thickness@)^2-x^2)");
set("material","GaAsP");
set("set mesh order from material database",0);
set("mesh order",5);

addcustom("window");
set("x",0);
set("x span",(@core_diameter@ + @tj_thickness@ + @window_thickness@*2 + @shell_thickness@*2)*1e-6)
    ;
set("y min",(@core_height@ - @tj_thickness@/2 - @window_thickness@ - @shell_thickness@)*1e-6);
set("y max",(@core_height@ + @tj_thickness@/2 + @window_thickness@ + @shell_thickness@)*1e-6);
set("equation 1","(@tj_thickness@/2 + @window_thickness@ + @shell_thickness@)/(@core_diameter@/2 +
     @tj_thickness@/2 + @window_thickness@ + @shell_thickness@)*sqrt((@core_diameter@/2 +
    @tj_thickness@/2 + @window_thickness@ + @shell_thickness@)^2-x^2)");
set("material","GaInP");
set("set mesh order from material database",0);
set("mesh order",6);

addcustom("ARBottom");
set("x",0);
set("x span",(@core_diameter@ + @tj_thickness@ + @window_thickness@*2 + @shell_thickness@*2 +
    @ARBot@*2)*1e-6);
set("y min",(@core_height@ - @tj_thickness@/2 - @window_thickness@ - @shell_thickness@ - @ARBot@)
    *1e-6);
set("y max",(@core_height@ + @tj_thickness@/2 + @window_thickness@ + @shell_thickness@ + @ARBot@)
    *1e-6);
set("equation 1","(@tj_thickness@/2 + @window_thickness@ + @shell_thickness@ + @ARBot@)/(
    @core_diameter@/2 + @tj_thickness@/2 + @window_thickness@ + @shell_thickness@ + @ARBot@)*sqrt
    ((@core_diameter@/2 + @tj_thickness@/2 + @window_thickness@ + @shell_thickness@ + @ARBot@)^2-x
    ^2)");
set("make nonsymmetric",1);
set("equation 2","0");
set("material","TiOx - Sentaurus");
set("set mesh order from material database",0);
set("mesh order",7);

addcustom("ARTop");
set("x",0);
```

```
set("x span",(@core_diameter@ + @tj_thickness@ + @window_thickness@*2 + @shell_thickness@*2 +
    @ARBot@*2 + @ARTop@*2)*1e-6);
set("y min",(@core_height@ - @tj_thickness@/2 - @window_thickness@ - @shell_thickness@ - @ARBot@ -
    @ARTop@)*1e-6);
set("y max",(@core_height@ + @tj_thickness@/2 + @window_thickness@ + @shell_thickness@ + @ARBot@ +
    @ARTop@)*1e-6);
set("equation 1","(@tj_thickness@/2 + @window_thickness@ + @shell_thickness@ + @ARBot@ + @ARTop@)
    /(@core_diameter@/2 + @tj_thickness@/2 + @window_thickness@ + @shell_thickness@ + @ARBot@ +
    @ARTop@)*sqrt((@core_diameter@/2 + @tj_thickness@/2 + @window_thickness@ + @shell_thickness@ +
    @ARBot@ + @ARTop@)^2-x^2)");
set("make nonsymmetric",1);
set("equation 2","0");
set("material","MgF - Sentaurus");
set("set mesh order from material database",0);
set("mesh order",8);

#endif


# Edit simulation region

select("FDTD");
set("simulation time",1e-6);
set("x",0);
set("x span",@pitch@*1e-6);
set("y min",0);
set("y max",(@core_height@ + @tj_thickness@/2 + @window_thickness@ + @shell_thickness@ + @ARBot@ +
    @ARTop@)*1e-6+2e-6);


# Edit sources

select("pw");
set("wavelength start",@wl@*1e-9);
set("wavelength stop",@wl@*1e-9);
set("x",0);
set("x span",@pitch@*1e-6+0.5e-6);
set("y",(@core_height@ + @tj_thickness@/2 + @window_thickness@ + @shell_thickness@ + @ARBot@ +
    @ARTop@)*1e-6+1e-6);
cwnorm;


# Edit monitors

select("power");
set("x",0);
set("x span",@pitch@*1e-6);
set("y min",0);
set("y max",(@core_height@ + @tj_thickness@/2 + @window_thickness@ + @shell_thickness@ + @ARBot@ +
    @ARTop@)*1e-6+2e-6);
set("partial spectral average",1);
set("delta",50e+12);

select("n_all");
set("x",0);
set("x span",@pitch@*1e-6);
set("y min",0);
set("y max",(@core_height@ + @tj_thickness@/2 + @window_thickness@ + @shell_thickness@ + @ARBot@ +
    @ARTop@)*1e-6+2e-6);

select("n_window");
```

```
set("x",0);
set("x span",0.01*1e-6);
set("y min",(@core_height@ +@tj_thickness@/10)*1e-6);
set("y max",(@core_height@ +3*@tj_thickness@/10)*1e-6);

select("n_shell");
set("x",0);
set("x span",0.01*1e-6);
set("y min",(@core_height@ +@shell_thickness@)*1e-6);
set("y max",(@core_height@ +@shell_thickness@ + 0.01)*1e-6);

# Add scatterers
Scatterer_Script_n@node|matlab1@;


for(x=1:2)
{
if(x==1)
{
FileDscr = "n@node@_" + "Tandem_Cell_WL" + num2str(@wl@) + "_TE_@Structure@";
select("pw");
set("polarization","TE");
}
if(x==2)
{
FileDscr = "n@node@_" + "Tandem_Cell_WL" + num2str(@wl@) + "_TM_@Structure@";
select("pw");
set("polarization","TM");
}
save(FileDscr + ".fsp");
}

exit(2);
```

**Listing E.6: Code to run Lumerical simulations**

```
nohup /opt/lumerical/fdtd/mpich/ch_p4/bin/mpirun -n 16 /opt/lumerical/fdtd/bin/fdtd-engine-mpichp4
      n@node|lumcad@_Tandem_Cell_WL@wl@_TE_@Structure@.fsp
nohup /opt/lumerical/fdtd/mpich/ch_p4/bin/mpirun -n 16 /opt/lumerical/fdtd/bin/fdtd-engine-mpichp4
      n@node|lumcad@_Tandem_Cell_WL@wl@_TM_@Structure@.fsp
```

**Listing E.7: Code to extract data from Lumerical simulations**

```
########################################################################################
# Dan Turner-Evans                                                                     #
# 7/27/11                                                                              #
# Generates an output file showing the relative absorption of the materials            #
########################################################################################

########################################################################################
# Create an output file                                                                #
########################################################################################

clear;

prefix_filename = "Tandem_Cell";

for(x=1:2)
{
if(x==1)
```

```
{
FileDscr = "n@node|lumcad@_" + prefix_filename + "_WL" + num2str(@wl@) + "_TE_@Structure@";
JPGDscr = "n@node|lumcad@_" + prefix_filename + "_WL" + num2str(@wl@) + "_TE_@Structure@";
MatlabOut = "n@node|lumcad@_OptGen" + num2str(@wl@) + "nm" + "_TE_@Structure@" + ".mat";

load( FileDscr + ".fsp" );

################################################################################
# Get data from the monitors                                                   #
################################################################################

f = getdata("power","f"); # Frequency vector
x = getdata("n_all","x"); # Position vectors associated with E fields
y = getdata("n_all","y"); # Position vectors associated with E fields
E = getelectric("power");

# Create an empty matrix of the appropriate size
BlankMatrix = matrix(length(x),length(y),1);

E2 = BlankMatrix;
E2(1:length(x),1:length(y),1) = E(1:length(x),1:length(y),1);

index_overall0 = getdata("n_all", "index_x"); # The overall matrix of index values
index_core = getdata("n_core","index_x"); # The core index
index_window = getdata("n_window","index_x"); # The window index
index_shell = getdata("n_shell","index_x"); # The shell index

################################################################################
# Calculate Absorption per unit volume = -0.5*w*|E|^2*imag(eps)                #
################################################################################

# Create matrices that will define the regions of interest
Abs_core = BlankMatrix;
Abs_window = BlankMatrix;
Abs_shell = BlankMatrix;

index_overall = BlankMatrix;
index_overall(1:length(x),1:length(y),1) = index_overall0(1:length(x),1:length(y),1); # Make sure
    that the dimensions are right
Abs_core(1:length(x),1:length(y),1) = (index_overall(1:length(x),1:length(y),1) == index_core
    (1,1,1)); # Specify the core region
Abs_window(1:length(x),1:length(y),1) = (index_overall(1:length(x),1:length(y),1) == index_window
    (1,1,1)); # Specify the window region
Abs_shell(1:length(x),1:length(y),1) = (index_overall(1:length(x),1:length(y),1) == index_shell
    (1,1,1)); # Specify the shell region

# Create a matrix with w, the frequency, at every point
w0 = BlankMatrix;
w0(1:length(x),1:length(y),1) = BlankMatrix(1:length(x),1:length(y),1)+2*pi*f(1);

# Calculate the absorption
Absorbed_core = real(Abs_core*0.5*w0*(2*real(index_overall)*imag(index_overall)*eps0)*E2);
Absorbed_window = real(Abs_window*0.5*w0*(2*real(index_overall)*imag(index_overall)*eps0)*E2);
Absorbed_shell = real(Abs_shell*0.5*w0*(2*real(index_overall)*imag(index_overall)*eps0)*E2);

# Normalize the absorbed power relative to the input power
Absorbed_core_Norm = Absorbed_core/(@pitch@*1e-6*0.5*eps0*c);
Absorbed_shell_Norm = Absorbed_shell/(@pitch@*1e-6*0.5*eps0*c);
Absorbed_window_Norm = Absorbed_window/(@pitch@*1e-6*0.5*eps0*c);

# Calculate the average ratio of light absorbed in the Ge and in the GaAs.
```

```
AvePow_core_TE_@Structure@ = integrate(Absorbed_core_Norm,1:2,x,y);
AvePow_shell_TE_@Structure@ = integrate(Absorbed_shell_Norm,1:2,x,y);
AvePow_window_TE_@Structure@ = integrate(Absorbed_window_Norm,1:2,x,y);

image(x,y,Absorbed_core(1:length(x),1:length(y),1));
exportfigure(JPGDscr + "_core.jpg");
image(x,y,Absorbed_shell(1:length(x),1:length(y),1));
exportfigure(JPGDscr + "_shell.jpg");
image(x,y,Absorbed_window(1:length(x),1:length(y),1));
exportfigure(JPGDscr + "_window.jpg");
image(x,y,E2(1:length(x),1:length(y),1));
exportfigure(JPGDscr + "_E_Mag" + ".jpg");
image(x,y,index_overall(1:length(x),1:length(y),1));
exportfigure("@Structure@.jpg");

matlabsave(MatlabOut,x,y,f,Absorbed_core_Norm,Absorbed_shell_Norm,Absorbed_window_Norm);
}
if(x==2)
{
FileDscr = "n@node|lumcad@_" + prefix_filename + "_WL" + num2str(@wl@) + "_TM_@Structure@";
JPGDscr = "n@node|lumcad@_" + prefix_filename + "_WL" + num2str(@wl@) + "_TM_@Structure@";
MatlabOut = "n@node|lumcad@_OptGen" + num2str(@wl@) + "nm" + "_TM_@Structure@" + ".mat";

load( FileDscr + ".fsp" );

################################################################################
# Get data from the monitors                                                   #
################################################################################

f = getdata("power","f"); # Frequency vector
x = getdata("n_all","x"); # Position vectors associated with E fields
y = getdata("n_all","y"); # Position vectors associated with E fields
E = getelectric("power");

# Create an empty matrix of the appropriate size
BlankMatrix = matrix(length(x),length(y),1);

E2 = BlankMatrix;
E2(1:length(x),1:length(y),1) = E(1:length(x),1:length(y),1);

index_overall0 = getdata("n_all", "index_z"); # The overall matrix of index values
index_core = getdata("n_core","index_z"); # The core index
index_window = getdata("n_window","index_z"); # The window index
index_shell = getdata("n_shell","index_z"); # The shell index

################################################################################
# Calculate Absorption per unit volume = -0.5*w*|E|^2*imag(eps)                #
################################################################################

# Create matrices that will define the regions of interest
Abs_core = BlankMatrix;
Abs_window = BlankMatrix;
Abs_shell = BlankMatrix;

index_overall = BlankMatrix;
index_overall(1:length(x),1:length(y),1) = index_overall0(1:length(x),1:length(y),1); # Make sure
    that the dimensions are right
Abs_core(1:length(x),1:length(y),1) = (index_overall(1:length(x),1:length(y),1) == index_core
    (1,1,1)); # Specify the core region
Abs_window(1:length(x),1:length(y),1) = (index_overall(1:length(x),1:length(y),1) == index_window
    (1,1,1)); # Specify the window region
```

```
Abs_shell(1:length(x),1:length(y),1) = (index_overall(1:length(x),1:length(y),1) == index_shell
    (1,1,1)); # Specify the shell region

# Create a matrix with w, the frequency, at every point
w0 = BlankMatrix;
w0(1:length(x),1:length(y),1) = BlankMatrix(1:length(x),1:length(y),1)+2*pi*f(1);

# Calculate the absorption
Absorbed_core = real(Abs_core*0.5*w0*(2*real(index_overall)*imag(index_overall)*eps0)*E2);
Absorbed_window = real(Abs_window*0.5*w0*(2*real(index_overall)*imag(index_overall)*eps0)*E2);
Absorbed_shell = real(Abs_shell*0.5*w0*(2*real(index_overall)*imag(index_overall)*eps0)*E2);

# Normalize the absorbed power relative to the input power
Absorbed_core_Norm = Absorbed_core/(@pitch@*1e-6*0.5*eps0*c);
Absorbed_shell_Norm = Absorbed_shell/(@pitch@*1e-6*0.5*eps0*c);
Absorbed_window_Norm = Absorbed_window/(@pitch@*1e-6*0.5*eps0*c);

# Calculate the average ratio of light absorbed in the Ge and in the GaAs.
AvePow_core_TM_@Structure@ = integrate(Absorbed_core_Norm,1:2,x,y);
AvePow_shell_TM_@Structure@ = integrate(Absorbed_shell_Norm,1:2,x,y);
AvePow_window_TM_@Structure@ = integrate(Absorbed_window_Norm,1:2,x,y);

image(x,y,Absorbed_core(1:length(x),1:length(y),1));
exportfigure(JPGDscr + "_core.jpg");
image(x,y,Absorbed_shell(1:length(x),1:length(y),1));
exportfigure(JPGDscr + "_shell.jpg");
image(x,y,Absorbed_window(1:length(x),1:length(y),1));
exportfigure(JPGDscr + "_window.jpg");
image(x,y,E2(1:length(x),1:length(y),1));
exportfigure(JPGDscr + "_E_Mag" + ".jpg");
image(x,y,index_overall(1:length(x),1:length(y),1));
exportfigure("@Structure@.jpg");

matlabsave(MatlabOut,x,y,f,Absorbed_core_Norm,Absorbed_shell_Norm,Absorbed_window_Norm);
}
}
AvePow_core_Total = (AvePow_core_TE_@Structure@ + AvePow_core_TM_@Structure@)/2;
AvePow_shell_Total = (AvePow_shell_TE_@Structure@ + AvePow_shell_TM_@Structure@)/2;
AvePow_window_Total = (AvePow_window_TE_@Structure@ + AvePow_window_TM_@Structure@)/2;
write("gvars.dat", "1 @node@ Per_Abs_core " + num2str(AvePow_core_Total));
write("gvars.dat", "1 @node@ Per_Abs_window " + num2str(AvePow_window_Total));
write("gvars.dat", "1 @node@ Per_Abs_shell " + num2str(AvePow_shell_Total));

exit(2);
```

**Listing E.8: Code to convert extracted Lumerical data to the appropraite form for interpolation**

```
FDTDFile1 = strcat('n', num2str(@node|lumcad@), '_OptGen',num2str(@wl@), 'nm_TE_@Structure@.mat');
FDTDFile2 = strcat('n', num2str(@node|lumcad@), '_OptGen',num2str(@wl@), 'nm_TM_@Structure@.mat');

OutputFile = strcat('n',num2str(@node@),'_OptGen',num2str(@wl@),'nm.mat');

load(FDTDFile1);
Pabs_x = x;
Pabs_y = y;
Ngen_pavg = 0.5*squeeze(Absorbed_core_Norm + Absorbed_shell_Norm + Absorbed_window_Norm);

load(FDTDFile2);
```

```
Ngen_pavg = Ngen_pavg + 0.5*squeeze(Absorbed_core_Norm + Absorbed_shell_Norm +
    Absorbed_window_Norm);

save(OutputFile, 'Pabs_x', 'Pabs_y', 'Ngen_pavg');
```

**Listing E.9: Code to interpolate the Lumerical data onto the FEM grid**

```
#MATLAB optical generation grid conversion for Lumerical -> Sentaurus project
#Michael Kelzenberg, 2009

#setdep @previous@
#setdep @node|sde@

%DAT file %%%%%%%%%%%%%%%%%%%%%%%%%%%%%%%%%%%%%%%%%%%%%%%%%%%%%%%%%%%%%%%%%%%%%%%
%This should be a valid DF-ISE .dat file (i.e. generated by mesh or
%noffset3d. The meshing program must be scripted to store the x- and y-
%position of each vertex of the grid as "PMIUserField0" and
%"PMIUserField1", respectively.
%%%%%%%%%%%%%%%%%%%%%%%%%%%%%%%%%%%%%%%%%%%%%%%%%%%%%%%%%%%%%%%%%%%%%%%%%%%%%%%%

datFile = 'n@node|sde@_msh.dat';
grdFile = 'n@node|sde@_msh.grd';

%FDTD MAT file %%%%%%%%%%%%%%%%%%%%%%%%%%%%%%%%%%%%%%%%%%%%%%%%%%%%%%%%%%%%%%%%%%
%This should be the Matlab MAT file generated by the Lumerical CAD script
%including:
% Pabs_x,Pabs_y          X and Y specification of grid (m)
% freq                   Freq. of simulation (Hz)
% Pabs *                 Matrix of power absorption (W/m3)
% Ngen *                 Matrix of optical generation rate (per cm3 per s)
% IntgPwr *              Total power absorption (W/m)
% Current *              Total photocurrent (A per um device length)
% Absfrac *              Fraction of absorbed light, i.e. Absorption Quantum Efficiency
%   * these variables, followed by "_pavg", corespond to partial spectral averaging
%
%  Note that presently, only Pabs_x, Pabs_y, and Ngen_pavg are used by this script.
%%%%%%%%%%%%%%%%%%%%%%%%%%%%%%%%%%%%%%%%%%%%%%%%%%%%%%%%%%%%%%%%%%%%%%%%%%%%%%%%

FDTDFile = strcat('n',num2str(@node|matlab2@),'_OptGen',num2str(@wl@),'nm.mat');

%Regions to process %%%%%%%%%%%%%%%%%%%%%%%%%%%%%%%%%%%%%%%%%%%%%%%%%%%%%%%%%%%%%
%These are the regions to perform the optical generation mesh conversion.
%This must be a cell array of region names, including double-quotes (")
%around each region name!!!
%  Example syntax: regionsToProcess = {'"Base_region"', "Emitter_region"' };
%%%%%%%%%%%%%%%%%%%%%%%%%%%%%%%%%%%%%%%%%%%%%%%%%%%%%%%%%%%%%%%%%%%%%%%%%%%%%%%%

#if [string compare @Structure@ "sphere"] == 0
regionsToProcess = {'"window_outer"' '"window_inner"' '"shell_emitter"' '"shell_base"' '"window_tj
    "' '"tj_core"' '"core_emitter"' '"core_base"' '"window_inner2"' '"window_tj2"' '"core_emitter2
    "'};
#else
regionsToProcess = {'"window_outer"' '"window_inner"' '"shell_emitter"' '"shell_base"' '"window_tj
    "' '"tj_core"' '"core_emitter"' '"core_base"'};
#endif

%Optical generation profile function %%%%%%%%%%%%%%%%%%%%%%%%%%%%%%%%%%%%%%%%%%%%
% The optical generation profile mapping function is located near line 270.
%%%%%%%%%%%%%%%%%%%%%%%%%%%%%%%%%%%%%%%%%%%%%%%%%%%%%%%%%%%%%%%%%%%%%%%%%%%%%%%%
%%%%%%%%%%%%%%%%%%%%%%%%%%%%%%%%%%%%%%%%%%%%%%%%%%%%%%%%%%%%%%%%%%%%%%%%%%%%%%%%
```

```
outputFile = 'n@node|sde@_@wl@nm_optgen.dat';
outputGrid = 'n@node|sde@_@wl@nm_optgen.grd';
exportFile = strcat('n',num2str(@node|sde@),'og',num2str(@wl@),'.mat');

%Number of data values to output per line in output DAT file
numperline = 10;


try

disp('------------------------------------------------------------------------');
disp(['OptGenConverter Version 2']);
disp(['(c) 2009 Michael Kelzenberg']);
disp(['California Institute of Technology']);
disp('------------------------------------------------------------------------');


disp(' ');
disp(['Opening DAT file ' datFile ]);

grd = fopen(datFile);
if (grd < 1)
    error(['Error opening file ' datFile ' for reading.']);
    %exit
end

if ( ~isequal( fgetl(grd), 'DF-ISE text'))
    disp('Error with grid file format: It might not be a DF_ISE text file.');
    disp('Please double-check input file.  The first line should read:');
    disp('     DF-ISE text');
    error('File parse error');
    % exit
end
fln = 1;

verts = [];
regions = {};

nl = fgetl(grd); fln=fln+1;
while( isempty( regexp(nl, 'nb_vertices *= *[0-9]+') ) && ~feof(grd) )
    nl = fgetl(grd); fln=fln+1;
end
tmp=regexp(nl, '[0-9]+','match');
numverts = str2num(tmp{1});
disp(['  File reports ' num2str(numverts) ' vertices']);

nl = fgetl(grd); fln=fln+1;
while( isempty( regexp(nl, 'nb_edges *= *[0-9]+') ) && ~feof(grd) )
    nl = fgetl(grd); fln=fln+1;
end
tmp=regexp(nl, '[0-9]+','match');
numedges = str2num(tmp{1});
disp(['  File reports ' num2str(numedges) ' edges']);

nl = fgetl(grd); fln=fln+1;
while( isempty( regexp(nl, 'nb_elements *= *[0-9]+') ) && ~feof(grd) )
    nl = fgetl(grd); fln=fln+1;
end
tmp=regexp(nl, '[0-9]+','match');
numelems = str2num(tmp{1});
disp(['  File reports ' num2str(numelems) ' elements']);
```

```
nl = fgetl(grd); fln=fln+1;
while( isempty( regexp(nl, 'nb_regions *= *[0-9]+') ) && ~feof(grd) )
    nl = fgetl(grd); fln=fln+1;
end
tmp = regexp(nl, '[0-9]+','match');
numregions = str2num(tmp{1});
disp(['  File reports ' num2str(numregions) ' regions']);

%Advance to data section of file...
nl = fgetl(grd); fln=fln+1;
while( isempty( regexp(nl, 'Data.*\{', 'once') ) && ~feof(grd) )
    nl = fgetl(grd); fln=fln+1;
end

if ( feof(grd) )
    disp('Unexpected end-of-file, no data processed.');
    disp(['Line: ' num2st--r(fln)]);
    error('File parse error.');
end


regionArray = [];
disp(' ');
disp('Reading data points...');
%Main reading loop.  Look for PMIUserField 0 or 1 data sets...
while ~feof(grd)

    nl = fgetl(grd); fln=fln+1;
    while ( isempty( regexpi(nl, '\s*function\s*=\s*PMIUserField[01]', 'once') ) && ~feof(grd) )
        nl = fgetl(grd); fln=fln+1;
    end
    if (feof(grd))
        break
    end

    tmp = regexp(nl, '[01]','match');
    axisNumber = str2num(tmp{1});

    nl = fgetl(grd); fln=fln+1;
    while ( isempty( regexpi(nl, '\s*validity\s*=\s*\[\s*".*"\s*\]', 'once') ) && ~feof(grd) )
        nl = fgetl(grd); fln=fln+1;
    end

    if (feof(grd))
        error(['File Parse Error near line ' num2str(fln)]);
        break
    end
    tmp = regexp(nl, '".*"','match');
    regionName = tmp{1};

    nl = fgetl(grd); fln=fln+1;
    while ( isempty( regexpi(nl, '\s*Values\s*\(\s*[0-9]+\s*\)', 'once') ) && ~feof(grd) )
        nl = fgetl(grd); fln=fln+1;
    end

    if (feof(grd))
        disp(['File Parse Error near line ' num2str(fln)]);
        break
    end
    tmp = regexp(nl, '[0-9]+','match');
```

```
numElems = str2num(tmp{1});

dataPoints = [];
while (1)
    nl = fgetl(grd); fln = fln+1;
    if(isempty(regexp(nl,'[0-9]+') ) )
        break
    else
        thisline = regexp(nl,'[\.\-\e\E\+0-9][\s\.\-\e\E\+0-9]*','match');
        thisline = thisline{1};
        dataPoints = [dataPoints str2num(thisline)];
    end
    if ( ~isempty(regexp(nl,'}','once') ))
        break
    end
end

disp(['  Region ' regionName ' read ' num2str(length(dataPoints)) '/' ...
    num2str(numElems) ' elements for axis ' num2str(axisNumber) ]);

%data points more or less than stated in header
if ( numElems ~= length(dataPoints) )
    disp(['Error: number of data points does not match file header']);
    disp(['Parse error near line ' num2str(fln)]);
    error(['File structure error in region ' regionName]);
end

existingRegion = 0;
for n=1:length(regionArray)
    canRegion = regionArray{n};
    if (isequal(regionName,canRegion.name))
        existingRegion = n;
    end
end

if (existingRegion)
    if (axisNumber == 0)
        regionArray{existingRegion}.xdata = dataPoints;
    else
        regionArray{existingRegion}.ydata = dataPoints;
    end

    if ~isequal( length(regionArray{existingRegion}.xdata), length(regionArray{existingRegion
        }.ydata) )
        disp('Error: number of x data points does not match number of y data points');
        error(['File structure error in region ' regionName ]);
    end

else
    newRegion.name = regionName;
    if (axisNumber == 0)
        newRegion.xdata = dataPoints;
        newRegion.ydata = [];
    else
        newRegion.ydata = dataPoints;
        newRegion.xdata = [];
    end
    newRegion.gdata = zeros(size(dataPoints));
    regionArray{end+1} = newRegion;
end
```

```
end

for n=1:length(regionArray)
    if ~isequal( length(regionArray{n}.xdata), length(regionArray{n}.ydata) )
            disp('Error: number of x data points does not match number of y data points');
            error(['File structure error in region ' regionArray{n}.name ]);
    end
end

disp(' ');
disp('Completed reading DAT file');
disp(['  Read ' num2str(length(regionArray)) ' region(s)']);
disp(' ');
fclose(grd);

regionsToProcess = unique(regionsToProcess);
for n=1:length(regionsToProcess)
    reqName = regionsToProcess{n};
    hasRegion = 0;
    for m=1:length(regionArray)
        if isequal( reqName, regionArray{m}.name )
            hasRegion=1;
            break;
        end
    end
    if ~hasRegion
        disp(['Error: Vertex position information for requested region ' reqName ]);
        disp(['  not contained within this grid.']);
        error(['Unable to process region: ' reqName ]);
    end
end

disp(' ');

%Optical generation profile function %%%%%%%%%%%%%%%%%%%%%%%%%%%%%%%%%%%%%%%%%%%%%%%%
%This function determines the OpticalGeneration value at each spatial
% coordinate (xi, yi).
%
%The function must be called newoptgen, and take as arguments xi and yi
%
%Load any external data sets in this area.
%%%%%%%%%%%%%%%%%%%%%%%%%%%%%%%%%%%%%%%%%%%%%%%%%%%%%%%%%%%%%%%%%%%%%%%%%%%%%%%%%%%%%%%
disp(['Loading MAT file ' FDTDFile ]);
load(FDTDFile);
optGenMatrix = Ngen_pavg';
newoptgen = @(xi, yi) interp2( Pabs_x, Pabs_y, optGenMatrix, xi*1e-6, yi*1e-6 );
%%%%%%%%%%%%%%%%%%%%%%%%%%%%%%%%%%%%%%%%%%%%%%%%%%%%%%%%%%%%%%%%%%%%%%%%%%%%%%%%%%%%%%%
%%%%%%%%%%%%%%%%%%%%%%%%%%%%%%%%%%%%%%%%%%%%%%%%%%%%%%%%%%%%%%%%%%%%%%%%%%%%%%%%%%%%%%%

disp(['Opening output file ' outputFile ]);

ogo = fopen(outputFile,'w');
if (ogo < 1)
    error(['Error opening file ' outputFile ' for writing.']);
    %exit
end

fprintf(ogo, 'DF-ISE text\n\n');
fprintf(ogo, 'Info {\n  version     = 1.0\n  type        = dataset\n  dimension   = 2\n');
fprintf(ogo, '  nb_vertices = %d\n  nb_edges    = %d\n  nb_faces    = 0\n', numverts, numedges);
fprintf(ogo, '  nb_elements = %d\n  nb_regions  = %d\n  datasets    = [ ', numelems, numregions);
```

```
    for n=1:length(regionsToProcess)
        fprintf(ogo,'"OpticalGeneration" ');
    end
fprintf(ogo, ']\n  functions   = [ ');
    for n=1:length(regionsToProcess)
        fprintf(ogo,'OpticalGeneration ');
    end
fprintf(ogo, ']\n}\n\nData {\n\n');

for n=1:length(regionsToProcess)
    reqName = regionsToProcess{n};
    hasRegion = 0;
    for m=1:length(regionArray)
        if isequal( reqName, regionArray{m}.name )
            hasRegion=m;
            break;
        end
    end
    if (hasRegion)
        reg = regionArray{hasRegion};

        disp( ['Proessing Optical Generation for region ' reg.name '...'] );

        fprintf(ogo,'Dataset ("OpticalGeneration") {\n  function  = OpticalGeneration\n  type
                = scalar\n');
        fprintf(ogo, ['  dimension = 1\n  location  = vertex\n  validity  = [ ' reg.name ' ]\n' ]
            );
        fprintf(ogo, '  Values (%d) {\n', length(reg.xdata) );

        gdata = zeros(size(reg.xdata));
        nl = 1;
        for nv=1:length(reg.xdata)

            ogi = newoptgen(reg.xdata(nv), reg.ydata(nv));
            fprintf(ogo, ' %22e', ogi);
            gdata(nv) = ogi;
            nl = nl + 1;
            if (nl > 10)
                fprintf(ogo, '\n');
                nl = 1;
            end
        end
        if (nl > 1)
            fprintf(ogo,'\n');
        end
        fprintf(ogo, '  }\n}\n\n');

        disp( ['    ' num2str(length(reg.xdata))  ' processed'] );
        regionArray{hasRegion}.gdata = gdata;
      end
 end

fprintf(ogo,'\n\n}');
fclose(ogo);
disp(['Finished writing output file ' outputFile ]);

disp(' ');
disp(['Copying from grid file: ' grdFile]);
copyfile(grdFile,outputGrid);
disp(['To grid file: ' outputGrid]);
```

```
disp(' ');
disp(['Exporting generation profile: ' exportFile ]);
save( exportFile , 'regionArray', 'numverts', 'numedges', 'numelems', 'numregions');


disp(' ');
disp('Processing complete!');


exit(0);

catch ME
    disp(ME);
    exit(1);
end

#end
```

**Listing E.10: Code to weigh and sum the single frequency simulations to get an AM 1.5G profile**

```
% MATLAB file for weighing and summing the single frequency simulations to
% create an AM1.5 g absorption profile.

wllow = 300;
wlspacing = 50;
wlnum = 22;
weight = [0.0703,0.7361,1.5354,2.5834,3.1045,3.3755,3.5473,3.6835,3.5516,3.2895,
    3.4004,3.3025,2.8433,1.6354,2.8614,2.7587,1.9358,1.2055,2.1215,2.1937, 1.9071,0.4237,0.0241]*(
    @pitch@*0.5)^2*1E-20/1.609E-19;

exportFile = strcat('n',num2str(@node|sde@),'ogAM1.5.mat');

AM15regionArray = [];

for j=0:wlnum
        wl = wllow + j*wlspacing;
        GenFile = strcat('n',num2str(@node|sde@),'og',num2str(wl),'.mat');
        load(GenFile);
        dim = size(regionArray);
        for i=1:dim(2)
                AM15regionArray{i}.name = regionArray{i}.name;
                AM15regionArray{i}.xdata = regionArray{i}.xdata;
                AM15regionArray{i}.ydata = regionArray{i}.ydata;
                if j == 0
                        for l=1:length(regionArray{i}.gdata(1,:))
                                if regionArray{i}.xdata(1,l) == 0
                                        AM15regionArray{i}.gdata(1,l) = 0;
                                else
                                        AM15regionArray{i}.gdata(1,l) = regionArray{i}.gdata(1,l)*
                                            weight(j+1)*1000*1E6/regionArray{i}.xdata(1,l);
                                end
                        end
                else
                        for l=1:length(regionArray{i}.gdata(1,:))
                                if regionArray{i}.xdata(1,l) == 0
                                        AM15regionArray{i}.gdata(1,l) = 0;
                                else
                                        AM15regionArray{i}.gdata(1,l) = regionArray{i}.gdata(1,l)*
                                            weight(j+1)*1000*1E6/regionArray{i}.xdata(1,l) +
```

```
                                        AM15regionArray{i}.gdata(1,l);
                                end
                        end
                end
        end
        disp(['Initializing']);
        disp(['Copying from dat file: ' GenFile]);
end

grdFile = 'n@node|sde@_@wl@nm_optgen.grd';

outputFile = 'n@node|sde@_AM15g_optgen.dat';
outputGrid = 'n@node|sde@_AM15g_optgen.grd';

#if [string compare @Structure@ "sphere"] == 0
regionsToProcess = {'"window_outer"' '"window_inner"' '"shell_emitter"' '"shell_base"' '"window_tj
    "' '"tj_core"' '"core_emitter"' '"core_base"' '"window_inner2"' '"window_tj2"' '"core_emitter2
    "'};
#else
regionsToProcess = {'"window_outer"' '"window_inner"' '"shell_emitter"' '"shell_base"' '"window_tj
    "' '"tj_core"' '"core_emitter"' '"core_base"'};
#endif

disp(['Opening output file ' outputFile ]);

ogo = fopen(outputFile,'w');
if (ogo < 1)
    error(['Error opening file ' outputFile ' for writing.']);
    %exit
end

fprintf(ogo, 'DF-ISE text\n\n');
fprintf(ogo, 'Info {\n  version     = 1.0\n  type        = dataset\n  dimension   = 2\n');
fprintf(ogo, '  nb_vertices = %d\n  nb_edges    = %d\n  nb_faces    = 0\n', numverts, numedges);
fprintf(ogo, '  nb_elements = %d\n  nb_regions  = %d\n  datasets    = [ ', numelems, numregions);
    for n=1:length(regionsToProcess)
        fprintf(ogo,'"OpticalGeneration" ');
    end
fprintf(ogo, ']\n  functions   = [ ');
    for n=1:length(regionsToProcess)
        fprintf(ogo,'OpticalGeneration ');
    end
fprintf(ogo, ']\n}\n\nData {\n\n');

for n=1:length(regionsToProcess)
    reqName = regionsToProcess{n};
    hasRegion = 0;
    for m=1:length(AM15regionArray)
        if isequal( reqName, AM15regionArray{m}.name )
            hasRegion=m;
            break;
        end
    end
    if (hasRegion)
        reg = AM15regionArray{hasRegion};

        disp( ['Processing Optical Generation for region ' reg.name '...'] );

        fprintf(ogo,'Dataset ("OpticalGeneration") {\n  function  = OpticalGeneration\n  type
                = scalar\n');
```

```
        fprintf(ogo, ['  dimension = 1\n  location  = vertex\n  validity  = [ ' reg.name ' ]\n' ]
            );
        fprintf(ogo, '  Values (%d) {\n', length(reg.xdata) );

        nl = 1;
        for nv=1:length(reg.xdata)

            ogi = AM15regionArray{hasRegion}.gdata(nv);
            fprintf(ogo, ' %22e', ogi);
            nl = nl + 1;
            if (nl > 10)
                fprintf(ogo, '\n');
                nl = 1;
            end
        end
        if (nl > 1)
            fprintf(ogo,'\n');
        end
        fprintf(ogo, '  }\n}\n\n');

        disp( ['    ' num2str(length(reg.xdata))  ' processed'] );
      end
 end

fprintf(ogo,'\n\n}');
fclose(ogo);
disp(['Finished writing output file ' outputFile ]);

disp(' ');
disp(['Copying from grid file: ' grdFile]);
copyfile(grdFile,outputGrid);
disp(['To grid file: ' outputGrid]);

disp(' ');
disp(['Exporting generation profile: ' exportFile ]);
save( exportFile , 'AM15regionArray', 'numverts', 'numedges', 'numelems', 'numregions');

disp(' ');
disp('Processing complete!');


exit(0);

catch ME
    disp(ME);
    exit(1);
end
```

**Listing E.11: Code to place weighted data on FEM grid**

```
exportFile = strcat('n',num2str(@node|sde@),'_@wl@nm_EQE.mat');

AM15regionArray = [];

GenFile = strcat('n',num2str(@node|sde@),'og',num2str(@wl@),'.mat');
load(GenFile);
dim = size(regionArray);
for i=1:dim(2)
        AM15regionArray{i}.name = regionArray{i}.name;
        AM15regionArray{i}.xdata = regionArray{i}.xdata;
```

```
        AM15regionArray{i}.ydata = regionArray{i}.ydata;
        for l=1:length(regionArray{i}.gdata(1,:))
                if regionArray{i}.xdata(1,l) == 0
                        AM15regionArray{i}.gdata(1,l) = 0;
                else
                        AM15regionArray{i}.gdata(1,l) = regionArray{i}.gdata(1,l)*(@pitch@/2)^2*1E
                            -11*68.99/(1.609E-19*regionArray{i}.xdata(1,l));
                end
        end
end
        disp(['Initializing']);
        disp(['Copying from dat file: ' GenFile]);

grdFile = 'n@node|sde@_@wl@nm_optgen.grd';

outputFile = 'n@node|sde@_@wl@nm_EQE.dat';
outputGrid = 'n@node|sde@_@wl@nm_EQE.grd';

#if [string compare @Structure@ "sphere"] == 0
regionsToProcess = {'"window_outer"' '"window_inner"' '"shell_emitter"' '"shell_base"' '"window_tj
    "' '"tj_core"' '"core_emitter"' '"core_base"' '"window_inner2"' '"window_tj2"' '"core_emitter2
    "'};
#else
regionsToProcess = {'"window_outer"' '"window_inner"' '"shell_emitter"' '"shell_base"' '"window_tj
    "' '"tj_core"' '"core_emitter"' '"core_base"'};
#endif

disp(['Opening output file ' outputFile ]);

ogo = fopen(outputFile,'w');
if (ogo < 1)
    error(['Error opening file ' outputFile ' for writing.']);
    %exit
end

fprintf(ogo, 'DF-ISE text\n\n');
fprintf(ogo, 'Info {\n  version     = 1.0\n  type        = dataset\n  dimension   = 2\n');
fprintf(ogo, '  nb_vertices = %d\n  nb_edges    = %d\n  nb_faces    = 0\n', numverts, numedges);
fprintf(ogo, '  nb_elements = %d\n  nb_regions  = %d\n  datasets    = [ ', numelems, numregions);
    for n=1:length(regionsToProcess)
        fprintf(ogo,'"OpticalGeneration" ');
    end
fprintf(ogo, ']\n  functions   = [ ');
    for n=1:length(regionsToProcess)
        fprintf(ogo,'OpticalGeneration ');
    end
fprintf(ogo, ']\n}\n\nData {\n\n');

for n=1:length(regionsToProcess)
    reqName = regionsToProcess{n};
    hasRegion = 0;
    for m=1:length(AM15regionArray)
        if isequal( reqName, AM15regionArray{m}.name )
            hasRegion=m;
            break;
        end
    end
    if (hasRegion)
        reg = AM15regionArray{hasRegion};

        disp( ['Processing Optical Generation for region ' reg.name '...'] );
```

```
        fprintf(ogo,'Dataset ("OpticalGeneration") {\n  function  = OpticalGeneration\n  type
                = scalar\n');
        fprintf(ogo, ['  dimension = 1\n  location  = vertex\n  validity  = [ ' reg.name ' ]\n' ]
            );
        fprintf(ogo, '  Values (%d) {\n', length(reg.xdata) );

        nl = 1;
        for nv=1:length(reg.xdata)

            ogi = AM15regionArray{hasRegion}.gdata(nv);
            fprintf(ogo, ' %22e', ogi);
            nl = nl + 1;
            if (nl > 10)
                fprintf(ogo, '\n');
                nl = 1;
            end
        end
        if (nl > 1)
            fprintf(ogo,'\n');
        end
        fprintf(ogo, '  }\n}\n\n');

        disp( ['    ' num2str(length(reg.xdata))  ' processed'] );
      end
 end

fprintf(ogo,'\n\n}');
fclose(ogo);
disp(['Finished writing output file ' outputFile ]);

disp(' ');
disp(['Copying from grid file: ' grdFile]);
copyfile(grdFile,outputGrid);
disp(['To grid file: ' outputGrid]);

disp(' ');
disp(['Exporting generation profile: ' exportFile ]);
save( exportFile , 'AM15regionArray', 'numverts', 'numedges', 'numelems', 'numregions');

disp(' ');
disp('Processing complete!');


exit(0);

catch ME
    disp(ME);
    exit(1);
end
```

The next two sets of code appeared in another Workbench layout.

**Listing E.12: Code to run the device physics simulations for tandem wire array cells**

```
File{
*-Input
#if @core_height@ == 40
        #if @pitch@ == 7
                #if [string compare @Structure@ "conformal"] == 0
```

```
        Grid     = "../01-Opt/n1_msh.grd"
        Doping   = "../01-Opt/n1_msh.dat"
        OpticalGenerationInput = "../01-Opt/n1_AM15g_optgen.dat"
      #endif
      #if [string compare @Structure@ "hemisphere"] == 0
        Grid     = "../01-Opt/n3_msh.grd"
        Doping   = "../01-Opt/n3_msh.dat"
        OpticalGenerationInput = "../01-Opt/n3_AM15g_optgen.dat"
      #endif
      #if [string compare @Structure@ "sphere"] == 0
        Grid     = "../01-Opt/n4_msh.grd"
        Doping   = "../01-Opt/n4_msh.dat"
        OpticalGenerationInput = "../01-Opt/n4_AM15g_optgen.dat"
      #endif
#endif
#if @pitch@ == 4
      #if [string compare @Structure@ "conformal"] == 0
        Grid     = "../01-Opt/n6272_msh.grd"
        Doping   = "../01-Opt/n6272_msh.dat"
        OpticalGenerationInput = "../01-Opt/n6272_AM15g_optgen.dat"
      #endif
      #if [string compare @Structure@ "hemisphere"] == 0
        Grid     = "../01-Opt/n6719_msh.grd"
        Doping   = "../01-Opt/n6719_msh.dat"
        OpticalGenerationInput = "../01-Opt/n6719_AM15g_optgen.dat"
      #endif
      #if [string compare @Structure@ "sphere"] == 0
        Grid     = "../01-Opt/n7166_msh.grd"
        Doping   = "../01-Opt/n7166_msh.dat"
        OpticalGenerationInput = "../01-Opt/n7166_AM15g_optgen.dat"
      #endif
#endif
#if @pitch@ == 5
      #if [string compare @Structure@ "conformal"] == 0
        Grid     = "../01-Opt/n9846_msh.grd"
        Doping   = "../01-Opt/n9846_msh.dat"
        OpticalGenerationInput = "../01-Opt/n9846_AM15g_optgen.dat"
      #endif
      #if [string compare @Structure@ "hemisphere"] == 0
        Grid     = "../01-Opt/n10293_msh.grd"
        Doping   = "../01-Opt/n10293_msh.dat"
        OpticalGenerationInput = "../01-Opt/n10293_AM15g_optgen.dat"
      #endif
      #if [string compare @Structure@ "sphere"] == 0
        Grid     = "../01-Opt/n10740_msh.grd"
        Doping   = "../01-Opt/n10740_msh.dat"
        OpticalGenerationInput = "../01-Opt/n10740_AM15g_optgen.dat"
      #endif
#endif
#if @pitch@ == 6
      #if [string compare @Structure@ "conformal"] == 0
        Grid     = "../01-Opt/n13420_msh.grd"
        Doping   = "../01-Opt/n13420_msh.dat"
        OpticalGenerationInput = "../01-Opt/n13420_AM15g_optgen.dat"
      #endif
      #if [string compare @Structure@ "hemisphere"] == 0
        Grid     = "../01-Opt/n13867_msh.grd"
        Doping   = "../01-Opt/n13867_msh.dat"
        OpticalGenerationInput = "../01-Opt/n13867_AM15g_optgen.dat"
      #endif
      #if [string compare @Structure@ "sphere"] == 0
```

```
                  Grid     = "../01-Opt/n14314_msh.grd"
                  Doping   = "../01-Opt/n14314_msh.dat"
                  OpticalGenerationInput = "../01-Opt/n14314_AM15g_optgen.dat"
                 #endif
        #endif
#endif
#if @core_height@ == 80
        #if [string compare @Structure@ "hemisphere"] == 0
          Grid     = "../01-Opt/n607_msh.grd"
          Doping   = "../01-Opt/n607_msh.dat"
          OpticalGenerationInput = "../01-Opt/n607_AM15g_optgen.dat"
        #endif
#endif

    Parameters ="@parameter@"
*-Output
    Plot     = "@tdrdat@"
    Current  = "@plot@"
    Output   = "@log@"
    NonLocalPlot = "n@node@_nl"
}


Electrode{
  { Name="Top_contact"  Voltage=0 hRecVelocity = 100}
  { Name="Bottom_contact"  Voltage=0 eRecVelocity = 100}
}

#if 0
Physics {
  MoleFraction(RegionName = ["window_outer" "window_inner" "window_tj"]
    xFraction=0.56
  )
  MoleFraction(RegionName = ["shell_emitter" "shell_base"]
    xFraction= 0.9
  )
  MoleFraction(RegionName = ["tj_core" "core_emitter" "core_base"]
    xFraction= 0.9
  )
#if [string compare @Structure@ "sphere"] == 0
  MoleFraction(RegionName = ["window_inner2" "window_tj2"]
    xFraction=
  )
#endif
}
#endif

Physics {
  AreaFactor = @< 1E11/(3.141592*(@pitch@*0.5)*(@pitch@*0.5)) >@ * to get current in mA/cm^2
  Fermi
  Recombination(
    SRH
  )
  Mobility(
#     DopingDep
    HighFieldSat
  )

  ThermionicEmission

  eBarrierTunneling "TD_NLM" (
```

```
      Band2Band
      TwoBand
  )

  hBarrierTunneling "TD_NLM"(
      Band2Band
      TwoBand
  )

  Optics(
    OpticalGeneration(
      ReadFromFile(Scaling =0
        TimeDependence(
          WaveTime = (0.9, 10)
          Scaling = 1.0
        )
      )
    )
  )

}

Physics (materialInterface="SiliconGermanium/GaInP") {
  Recombination(surfaceSRH)
}

Physics (materialInterface="Ambient/GaInP") {
  Recombination(surfaceSRH)
}

#if [string compare @Structure@ "hemisphere"] == 0
Physics (materialInterface="Oxide/SiliconGermanium") {
  Recombination(surfaceSRH)
}

Physics (materialInterface="Oxide/GaInP") {
  Recombination(surfaceSRH)
}

Physics (materialInterface="Oxide/GaAsP") {
  Recombination(surfaceSRH)
}
#endif

#if [string compare @Structure@ "sphere"] == 0
Physics (materialInterface="Oxide/SiliconGermanium") {
  Recombination(surfaceSRH)
}

Physics (materialInterface="Oxide/GaInP") {
  Recombination(surfaceSRH)
}

Physics (materialInterface="Oxide/GaAsP") {
  Recombination(surfaceSRH)
}
#endif

Physics (material = "GaInP") {
  Recombination(
    Radiative
```

```
    Auger
  )
}

Physics (material = "GaAsP") {
  Recombination(
    Radiative
    Auger
  )
}

Plot {
  xMoleFraction Doping DonorConcentration AcceptorConcentration
  eEffectiveStateDensity hEffectiveStateDensity EffectiveIntrinsicDensity IntrinsicDensity
  eDensity hDensity SpaceCharge
  eQuasiFermiPotential hQuasiFermiPotential BandGap ConductionBandEnergy ValenceBandEnergy
      ElectronAffinity
  ElectricField ElectricField/vector ElectrostaticPotential
  eLifetime hLifetime SRH Auger TotalRecombination SurfaceRecombination RadiativeRecombination
  eCurrent/Vector hCurrent/Vector current/vector
  eMobility hMobility eVelocity hVelocity
  SRH Auger TotalRecombination SurfaceRecombination RadiativeRecombination
  BarrierTunneling
  eBarrierTunneling hBarrierTunneling
  NonLocal
  OpticalGeneration
}

NonLocalPlot ((0, 0)) {
  ConductionBand  ValenceBand
  hDensity  eDensity
  hQuasiFermi  eQuasiFermi
  NonLocal
}




Math{
  RhsMin = 1E-12
  Extrapolate
  Derivatives
  RelErrControl
  Iterations=20
  ExtendedPrecision
  Digits=7
  Notdamped=100
  ErrRef(electron) = 1E0
  ErrRef(hole) = 1E0
  ExitOnFailure
  Number_of_Threads = maximum
  StackSize = 20000000  * 20MB; needed for NewRayTracer
  Method=Super
  NonLocal "TD_NLM" (
    MaterialInterface = "SiliconGermanium/GaInP"
    Length=15e-7          # [cm] distance to anchor point
    Permeation = 15e-7
  )
  DirectCurrent
  Cylindrical(0.0)
```

```
  Transient=BE
  TransientDigits=7
  TransientErrRef(electron) = 1E0
  TransientErrRef(hole) = 1E0

*   CNormPrint
}


Solve{
                NewCurrentPrefix = "tmp_"

                Coupled  { poisson }
                Plot( FilePrefix = "n@node@_Banddgm")
#               Coupled  { poisson electron }
#               Coupled  { poisson hole }
#               Coupled  { poisson electron hole }

                Transient (
                  InitialStep=1e-10 MaxStep =0.2 MinStep = 1e-40 Increment=2
                  InitialTime=0 FinalTime=1
                ){ Coupled (Iterations=20) {Poisson Electron Hole  } }

                NewCurrentPrefix = "Light_IV"

                Quasistationary (
                  InitialStep=1e-4 MaxStep =1e-3 MinStep = 1e-30 Increment=1.7 DoZero
#if @GaAsP_SRHLifeTime@ > 1e-8
                  Goal{ voltage = 1.5 Name="Bottom_contact" }
                ){ Coupled {Poisson Electron Hole  }
                   Plot( FilePrefix = "n@node@_Banddgm_Jsc" Time = (0) )
                 }
#endif
#if @GaAsP_SRHLifeTime@ < 1e-8 && @GaAsP_SRHLifeTime@ > 1e-10
                  Goal{ voltage = 1.3 Name="Bottom_contact" }
                ){ Coupled {Poisson Electron Hole  }
                   Plot( FilePrefix = "n@node@_Banddgm_Jsc" Time = (0) )
                 }
#endif
#if @GaAsP_SRHLifeTime@ < 1e-10
                  Goal{ voltage = 1.2 Name="Bottom_contact" }
                ){ Coupled {Poisson Electron Hole  }
                   Plot( FilePrefix = "n@node@_Banddgm_Jsc" Time = (0) )
                 }
#endif



                NewCurrentPrefix = "tmp_2"

                Quasistationary (
                  InitialStep=1e-2 MaxStep =0.1 MinStep = 1e-30 Increment=1.5 DoZero
                  Goal{ current = 0 Name="Bottom_contact" }
                ){ Coupled {Poisson Electron Hole  }
                 }
                   Plot( FilePrefix = "n@node@_Banddgm_Voc")

  System("rm -f tmp*") *remove the plot we dont need anymore.
  System("rm -f tmp2*") *remove the plot we dont need anymore.
}
```

Only modifications to the parameter file are shown:

**Listing E.13: Parameter file for the device physics simulations**

```
Material = "GaInP" {

...

# Taken from Silicon

Scharfetter * relation and trap level for SRH recombination:
{ * tau = taumin + ( taumax - taumin ) / ( 1 + ( N/Nref )^gamma)
  * tau(T) = tau * ( (T/300)^Talpha )           (TempDep)
  * tau(T) = tau * exp( Tcoeff * ((T/300)-1) ) (ExpTempDep)
        taumin  = 0.0000e+00 ,  0.0000e+00      # [s]
        taumax  = 1.0000e-05 ,  3.0000e-06      # [s]
        Nref    = 1.0000e+16 ,  1.0000e+16      # [cm^(-3)]
        gamma   = 1 ,   1       # [1]
        Talpha  = -1.5000e+00 , -1.5000e+00     # [1]
        Tcoeff  = 2.55 ,        2.55    # [1]
        Etrap   = 0.0000e+00    # [eV]
}

Auger * coefficients:
{ * R_Auger = ( C_n n + C_p p ) ( n p - ni_eff^2)
  * with C_n,p = (A + B (T/T0) + C (T/T0)^2) (1 + H exp(-{n,p}/N0))
        A       = 1.0000e-30 ,  1.0000e-30      # [cm^6/s]
        B       = 0.0000e+00 ,  0.0000e+00      # [cm^6/s]
        C       = 0.0000e+00 ,  0.0000e+00      # [cm^6/s]
        H       = 0.0000e+00 ,  0.0000e+00      # [1]
        N0      = 1.0000e+18 ,  1.0000e+18      # [cm^(-3)]
}

# Taken from GaAs

BarrierTunneling
{ * Non Local Barrier Tunneling
  * G(r) = g*A*T/kB*F(r)*Pt(r)*ln[(1+exp((E(r)-Es)/kB/T))/(1+exp((E(r)-Em)/kB/T))]
  * where:
  *     Pt(r) is WKB approximation for the tunneling probability
  *     g = As/A, As is the Richardson constant for carriers in semiconductor
  *     A is the Richardson constant for free electrons
  *     F(r) is the electric field
  *     E(r) is carrier energy
  *     Es is carrier quasi fermi energy in semiconductor
  *     Em is carrier fermi energy in metal
        mt      = 0.05 ,        0.14    # [1]
}
}

MaterialInterface = "Oxide/GaAsP" {
SurfaceRecombination {
    S0 = @SRV@, @SRV@ * [cm/s]
    Sref = 0 * [1]
  }
}

MaterialInterface = "Oxide/GaInP" {
SurfaceRecombination {
    S0 = @SRV@, @SRV@ * [cm/s]
    Sref = 0 * [1]
  }
}
```

```
MaterialInterface = "Oxide/SiliconGermanium" {
SurfaceRecombination {
    S0 = 100, 100 * [cm/s]
    Sref = 0 * [1]
  }
}

MaterialInterface = "SiliconGermanium/GaInP" {
ThermionicEmission {
        A = 2, 2  # [1]
        B = 4, 4  # [1]
        C = 1, 1  # [1]
}

SurfaceRecombination {
    S0 = @SRV@, @SRV@ * [cm/s]
    Sref = 0 * [1]
  }

BarrierTunneling
{ * Non Local Barrier Tunneling
  * G(r) = g*A*T/kB*F(r)*Pt(r)*ln[(1+exp((E(r)-Es)/kB/T))/(1+exp((E(r)-Em)/kB/T))]
  * where:
  *     Pt(r) is WKB approximation for the tunneling probability
  *     g = As/A, As is the Richardson constant for carriers in semiconductor
  *     A is the Richardson constant for free electrons
  *     F(r) is the electric field
  *     E(r) is carrier energy
  *     Es is carrier quasi fermi energy in semiconductor
  *     Em is carrier fermi energy in metal
        g       = 0.21 ,        0.4     # [1]
}
}

Material = "SiliconGermanium" {

...

# Taken from Silicon

Scharfetter * relation and trap level for SRH recombination:
{ * tau = taumin + ( taumax - taumin ) / ( 1 + ( N/Nref )^gamma)
  * tau(T) = tau * ( (T/300)^Talpha )           (TempDep)
  * tau(T) = tau * exp( Tcoeff * ((T/300)-1) ) (ExpTempDep)
        taumin  = 0.0000e+00 ,  0.0000e+00      # [s]
#       taumax  = 1.0000e-05 ,  3.0000e-06      # [s]
        taumax  = @SiGe_SRHLifeTime@ ,  @SiGe_SRHLifeTime@      # [s]
        Nref    = 1.0000e+16 ,  1.0000e+16      # [cm^(-3)]
        gamma   = 1 ,   1       # [1]
        Talpha  = -1.5000e+00 , -1.5000e+00     # [1]
        Tcoeff  = 2.55 ,        2.55    # [1]
        Etrap   = 0.0000e+00    # [eV]
}

# Taken from GaAs

BarrierTunneling
{ * Non Local Barrier Tunneling
  * G(r) = g*A*T/kB*F(r)*Pt(r)*ln[(1+exp((E(r)-Es)/kB/T))/(1+exp((E(r)-Em)/kB/T))]
  * where:
  *     Pt(r) is WKB approximation for the tunneling probability
```

```
  *     g = As/A, As is the Richardson constant for carriers in semiconductor
  *     A is the Richardson constant for free electrons
  *     F(r) is the electric field
  *     E(r) is carrier energy
  *     Es is carrier quasi fermi energy in semiconductor
  *     Em is carrier fermi energy in metal
        mt      = 0.05 ,        0.14    # [1]
}

}


Material = "GaAsP" {

...

# Taken from Silicon

Scharfetter * relation and trap level for SRH recombination:
{ * tau = taumin + ( taumax - taumin ) / ( 1 + ( N/Nref )^gamma)
  * tau(T) = tau * ( (T/300)^Talpha )           (TempDep)
  * tau(T) = tau * exp( Tcoeff * ((T/300)-1) ) (ExpTempDep)
        taumin  = 0.0000e+00 ,  0.0000e+00      # [s]
#       taumax  = 1.0000e-05 ,  3.0000e-06      # [s]
        taumax  = @GaAsP_SRHLifeTime@ , @GaAsP_SRHLifeTime@     # [s]
        Nref    = 1.0000e+16 ,  1.0000e+16      # [cm^(-3)]
        gamma   = 1 ,   1       # [1]
        Talpha  = -1.5000e+00 , -1.5000e+00     # [1]
        Tcoeff  = 2.55 ,        2.55    # [1]
        Etrap   = 0.0000e+00    # [eV]
}

Auger * coefficients:
{ * R_Auger = ( C_n n + C_p p ) ( n p - ni_eff^2)
  * with C_n,p = (A + B (T/T0) + C (T/T0)^2) (1 + H exp(-{n,p}/N0))
        A       = 1.0000e-30 ,  1.0000e-30      # [cm^6/s]
        B       = 0.0000e+00 ,  0.0000e+00      # [cm^6/s]
        C       = 0.0000e+00 ,  0.0000e+00      # [cm^6/s]
        H       = 0.0000e+00 ,  0.0000e+00      # [1]
        N0      = 1.0000e+18 ,  1.0000e+18      # [cm^(-3)]
}

# Taken from GaAs

BarrierTunneling
{ * Non Local Barrier Tunneling
  * G(r) = g*A*T/kB*F(r)*Pt(r)*ln[(1+exp((E(r)-Es)/kB/T))/(1+exp((E(r)-Em)/kB/T))]
  * where:
  *     Pt(r) is WKB approximation for the tunneling probability
  *     g = As/A, As is the Richardson constant for carriers in semiconductor
  *     A is the Richardson constant for free electrons
  *     F(r) is the electric field
  *     E(r) is carrier energy
  *     Es is carrier quasi fermi energy in semiconductor
  *     Em is carrier fermi energy in metal
        mt      = 0.05 ,        0.14    # [1]
}

}
```

**Listing E.14: Code to extract select parameters for the simulations**

```
# Plot light J-V and P-V curves and extract Photovoltaic parameters
# or Plot dark J-V characteristics

# #setdep @node|-2@

set N      @node@
set i      @node:index@

# proj_load  @plot@ PLT_JV($N)
proj_load  Light_IVn@previous@_des.plt PLT_JV($N)

#- Automatic alternating color assignment tied to node index
#-------------------------------------------------------------------#
set COLORS  [list orange green blue red violet brown orange magenta]
set NCOLORS [llength $COLORS]
set color   [lindex  $COLORS [expr $i%$NCOLORS]]


# Plot light J-V characteristics and extract PV parameters
cv_createDS J($N)  "PLT_JV($N) Bottom_contact OuterVoltage" "PLT_JV($N) Bottom_contact
    TotalCurrent"

cv_inv J($N) y

cv_create V($N)  "PLT_JV($N) Bottom_contact OuterVoltage" "PLT_JV($N) Bottom_contact OuterVoltage"

cv_createWithFormula P($N)  "<V($N)>*<J($N)>" A A
cv_display P($N) y2

cv_setCurveAttr J($N)  "light-JV" $color solid  2 circle 3 defcolor 1 defcolor
cv_setCurveAttr P($N)  "light-PV" $color dashed  2 none 3 defcolor 1 defcolor

gr_setAxisAttr X {Voltage (V)}  16 0 {} black 1 14 0 5 0
gr_setAxisAttr Y {Current Density (mA/cm^2)} 16 0 30  black 1 14 0 5 0
gr_setAxisAttr Y2 {Power (mW/cm^2)} 16 0 26  black 1 14 0 5 0

# Extract Photovoltaic parameters
# Extract short circuit current density, Jsc [mA/cm^2]
set Jsc($N) [cv_compute "vecvaly(<J($N)>,0)" A A A A]
ft_scalar Jsc [format %.2f $Jsc($N)]

# Extract open circuit voltage, Voc [V]
set Jmin [cv_compute "vecmin(<J($N)>)" A A A A]
if {$Jmin <= 0} {
        set Voc($N) [expr [cv_compute "veczero(<J($N)>)" A A A A]]
} elseif {$Jmin <= 1e-6} {
        set Voc($N) [expr [cv_compute "vecvalx(<J($N>,$Jmin)" A A A A]]
}
ft_scalar Voc [format %.4f $Voc($N)]

# Extract fill factor (FF), maximum power outpout (Pm [mW/cm2]) and efficiency (eff)
  set Ps 100 ;#Incident light power density for AM1.5g radiation in mW/cm^2

if {$Voc($N) > 0} {
        set Pm($N) [cv_compute "vecmax(<P($N)>)" A A A A]
        ## fillfactor in %
        set FF($N) [expr $Pm($N)/($Voc($N)*$Jsc($N))*100]
        ## efficiency in % (mW/cm^2/(100mW/cm^2)*100%)
        set Eff($N) [expr $Pm($N)/$Ps*100]
}
```

```
ft_scalar Pm [format %.4f $Pm($N)]
ft_scalar FF  [format %.4f $FF($N)]
ft_scalar Eff  [format %.4f $Eff($N)]
```

The final set of code stood in its own workbench and was used for the defect simulations:

**Listing E.15: Code to generate the structure**

```
;;#################################################################
;; Dan Turner-Evans                                               #
;; 05/24/12                                                       #
;; A 2D GaAsP on SiGe microwire to test the E&M package           #
;;#################################################################

(sde:clear)

;;--------------------
(display "init parameter")(newline)
;;geometry
(define height 40) ; um
(define diameter 2) ; um
(define pitch 4); um
(define spacing 4); um
(define bottom_emitter_t 0.1); um
(define masking_oxide_t 0.2); um
(define exposed_h 5); um
(define gap 0.1); um
(define defect_h 2); um
(define sq_h 2); um
(define top_emitter_t 0.1); um
(define window_t 0.02); um
(define MgF_t 0.1); um
(define TiOx_t 0.06); um
(define fname "n@node@_msh")
(define elGridFname "n@node@_el_msh"); mixed element grid file name for sdevice simulation
(define top_window_d 1e19)
(define top_emitter_d 1e19)
(define top_base_d 1e17)
(define defect_d 1e19)
(define bottom_emitter_d 6e19)
(define bottom_base_d 1e17)
(define WireLT @SiGe_SRHLifeTime@)
(define TopCellLT @GaAsP_SRHLifeTime@)
(define DefectLT @Defect_SRHLifeTime@)

;; ---------------------------------------
(display "create structure... \n")
;;--------------------
(sdegeo:set-default-boolean "ABA")
(display "   back reflector")(newline)
(sdegeo:create-rectangle (position (* pitch -0.5) 0 0) (position  (* pitch 0.5) -1 0) "Silver" "
    Back-Reflector")

;;--------------------
(display "fill with gas")(newline)
(sdegeo:create-rectangle (position (* pitch -0.5) 0 0) (position  (* pitch 0.5) (+ height spacing
    defect_h sq_h (- (* pitch 0.5) gap) window_t) 0) "Gas" "ambient")

;;--------------------
(display "  top ARC")(newline)
```

```
(sdegeo:create-circle (position 0 (+ height defect_h sq_h window_t TiOx_t MgF_t) 0) (- (* pitch
    0.5) gap) "MgF" "Top_ARC")

;;--------------------
(display "  bottom ARC")(newline)
(sdegeo:create-circle (position 0 (+ height defect_h sq_h window_t TiOx_t) 0) (- (* pitch 0.5) gap
    ) "TiOx" "Bottom_ARC")

;;--------------------
(display "  top window")(newline)
(sdegeo:create-circle (position 0 (+ height defect_h sq_h window_t) 0) (- (* pitch 0.5) gap) "
    GaInP" "Top_Window_Circle")

;;--------------------
(display "  top cell")(newline)
(sdegeo:create-circle (position 0 (+ height defect_h sq_h) 0) (- (* pitch 0.5) gap) "GaAsP" "
    Top_Cell_Emitter")
(sdegeo:create-circle (position 0 (+ height defect_h sq_h) 0) (- (* pitch 0.5) (+ gap
    top_emitter_t)) "GaAsP" "Top_Cell_Circ")
(sdegeo:create-rectangle (position (+ (* pitch -0.5) gap) (+ height defect_h) 0) (position (- (*
    pitch 0.5) gap) (+ height defect_h sq_h) 0) "GaAsP" "Top_Cell_Rect")

;;--------------------
(display "  defective region")(newline)
(sdegeo:create-rectangle (position (+ (* pitch -0.5) gap) (- height exposed_h) 0) (position (- (*
    pitch 0.5) gap) (+ height defect_h) 0) "GaAsP" "Defect_Region")

;--------------------
(display "  oxide")(newline)
(sdegeo:create-rectangle (position (- (* diameter -0.5) masking_oxide_t) 0 0) (position (+ (*
    diameter 0.5) masking_oxide_t) (- height exposed_h) 0) "Oxide" "Boot")

;;--------------------
(display "  wire")(newline)
# (sdegeo:create-rectangle (position (* diameter -0.5) 0 0) (position (* diameter 0.5) height 0) "
    SiliconGermanium" "Wire_Emitter")
(sdegeo:create-rectangle (position (* diameter -0.5) 0 0) (position (* diameter 0.5) height 0) "
    SiliconGermanium" "Wire_Base")

;;--------------------
(display "save boundary")(newline)
(sdeio:save-tdr-bnd "all" (string-append fname ".bnd"))

; ---------------------------------------
(display "place dopants, set lifetime ... \n")
;; constant window doping
(sdedr:define-constant-profile "WindowDop" "NDopantActiveConcentration" top_window_d)
(sdedr:define-constant-profile-region "WindowDop" "WindowDop" "Top_Window_Circle")

;; constant top cell emitter doping
(sdedr:define-constant-profile "TopCellEmitterDop" "NDopantActiveConcentration" top_emitter_d)
(sdedr:define-constant-profile-region "TopCellEmitterDop" "TopCellEmitterDop" "Top_Cell_Emitter")

;; constant top cell base doping
(sdedr:define-constant-profile "TopCellBaseDop" "PDopantActiveConcentration" top_base_d)
(sdedr:define-constant-profile-region "TopCellBaseCircDop" "TopCellBaseDop" "Top_Cell_Circ")
(sdedr:define-constant-profile-region "TopCellBaseRectDop" "TopCellBaseDop" "Top_Cell_Rect")

(sdedr:define-constant-profile "TopCellLTe" "eLifetime" TopCellLT)
(sdedr:define-constant-profile "TopCellLTh" "hLifetime" TopCellLT)
(sdedr:define-constant-profile-region "TopCellLTe1" "TopCellLTe" "Top_Window_Circle" 0 "Replace")
```

```
(sdedr:define-constant-profile-region "TopCellLTh1" "TopCellLTh" "Top_Window_Circle" 0 "Replace")
(sdedr:define-constant-profile-region "TopCellLTe2" "TopCellLTe" "Top_Cell_Emitter" 0 "Replace")
(sdedr:define-constant-profile-region "TopCellLTh2" "TopCellLTh" "Top_Cell_Emitter" 0 "Replace")
(sdedr:define-constant-profile-region "TopCellLTe3" "TopCellLTe" "Top_Cell_Circ" 0 "Replace")
(sdedr:define-constant-profile-region "TopCellLTh3" "TopCellLTh" "Top_Cell_Circ" 0 "Replace")
(sdedr:define-constant-profile-region "TopCellLTe4" "TopCellLTe" "Top_Cell_Rect" 0 "Replace")
(sdedr:define-constant-profile-region "TopCellLTh4" "TopCellLTh" "Top_Cell_Rect" 0 "Replace")

;; constant bottom cell base doping
(sdedr:define-constant-profile "WireDop" "PDopantActiveConcentration" bottom_base_d)
(sdedr:define-constant-profile-region "WireDop" "WireDop" "Wire_Base")

;; Gaussian bottom cell emitter doping
(sdedr:define-refinement-window "BottomCelEmitterDopTop" "Line"
        (position (* diameter -0.5) height 0)
        (position (* diameter 0.5) height 0))
(sdedr:define-refinement-window "BottomCelEmitterDopLeft" "Line"
        (position (* diameter -0.5) (- height (+ exposed_h 0.1)) 0)
        (position (* diameter -0.5) height 0))
(sdedr:define-refinement-window "BottomCelEmitterDopRight" "Line"
        (position (* diameter 0.5) (- height (+ exposed_h 0.1)) 0)
        (position (* diameter 0.5) height 0))
(sdedr:define-gaussian-profile "BottomCelEmitterDop" "NDopantActiveConcentration"
        "PeakPos" 0   "PeakVal" bottom_emitter_d "Length" 0.05 "Erf"  "Factor" 0.)
(sdedr:define-analytical-profile-placement "BottomCelEmitterDopTop" "BottomCelEmitterDop" "
    BottomCelEmitterDopTop" "Negative" "NoReplace" "Eval")
(sdedr:define-analytical-profile-placement "BottomCelEmitterDopRight" "BottomCelEmitterDop" "
    BottomCelEmitterDopRight" "Positive" "NoReplace" "Eval")
(sdedr:define-analytical-profile-placement "BottomCelEmitterDopLeft" "BottomCelEmitterDop" "
    BottomCelEmitterDopLeft" "Negative" "NoReplace" "Eval")

(sdedr:define-constant-profile "WireLTe" "eLifetime" WireLT)
(sdedr:define-constant-profile "WireLTh" "hLifetime" WireLT)
(sdedr:define-constant-profile-region "WireLTe" "WireLTe" "Wire_Base" 0 "Replace")
(sdedr:define-constant-profile-region "WireLTh" "WireLTh" "Wire_Base" 0 "Replace")

;; constant defect doping
(sdedr:define-constant-profile "DefectDop" "PDopantActiveConcentration" defect_d)
(sdedr:define-constant-profile-region "DefectDop" "DefectDop" "Defect_Region" 0 "Replace")

(sdedr:define-constant-profile "DefectLTe" "eLifetime" DefectLT)
(sdedr:define-constant-profile "DefectLTh" "hLifetime" DefectLT)
(sdedr:define-constant-profile-region "DefectLTe" "DefectLTe" "Defect_Region" 0 "Replace")
(sdedr:define-constant-profile-region "DefectLTh" "DefectLTh" "Defect_Region" 0 "Replace")

;; ---------------------------------------
(display "define contacts... \n")
(sdegeo:define-contact-set "BottomContact" 4  (color:rgb 1 0 0 ) "##" )
(sdegeo:define-contact-set "TopContact" 4  (color:rgb 0 0 1 ) "##" )
(sdegeo:define-2d-contact (find-edge-id (position 0 0 0)) "BottomContact")
(sdegeo:define-2d-contact (find-edge-id (position 0 (+ height defect_h sq_h window_t (- (* pitch
    0.5) gap)) 0)) "TopContact")
(sde:refresh)

;; ---------------------------------------
(display "add refinements ... \n")
;; global refinement
(sdedr:define-refinement-size "ref.global" 0.5 0.5 0 0.5 0.5 0 )
(sdedr:define-refinement-window "win.global" "Rectangle"
        (position (* pitch -0.5) 0 0)
```

```
        (position  (* pitch 0.5) (+ height spacing defect_h sq_h (- (* pitch 0.5) gap) window_t)
            0))
(sdedr:define-refinement-placement "ref.global" "ref.global" "win.global" )

;; on doping
# (sdedr:define-refinement-size "doping" 0.1 0.05 0 0.1 0.05 0 )
# (sdedr:define-refinement-function "doping" "DopingConcentration" "MaxTransDiff" 1)
# (sdedr:define-refinement-placement "doping" "doping" "win.global" )

;; bottom contact
(sdedr:define-refinement-window "BC" "Rectangle" (position (* diameter -0.5) 0 0 ) (position (*
    diameter 0.5) 0.2 0))
(sdedr:define-multibox-size "Size.BC" 0.1 0.1 0.1 0.01 1 1.5)
(sdedr:define-multibox-placement "Placement.BC" "Size.BC" "BC")

;; emitter
(sdedr:define-refinement-window "Emit_Top" "Rectangle" (position (* diameter -0.5) height 0 ) (
    position (* diameter 0.5) (- height 0.2) 0))
(sdedr:define-multibox-size "Size.Emit_Top" 0.1 0.1 0.1 0.01 1 -1.5)
(sdedr:define-multibox-placement "Placement.Emit_Top" "Size.Emit_Top" "Emit_Top")

(sdedr:define-refinement-window "Emit_Side_R" "Rectangle" (position (- (* diameter 0.5) 0.2) (-
    height exposed_h) 0 ) (position (* diameter 0.5) height 0))
(sdedr:define-multibox-size "Size.Emit_Side_R" 0.1 0.1 0.01 0.01 -1.5 -1.5)
(sdedr:define-multibox-placement "Placement.Emit_Side_R" "Size.Emit_Side_R" "Emit_Side_R")

(sdedr:define-refinement-window "Emit_Side_L" "Rectangle" (position (+ (* diameter -0.5) 0.2) (-
    height exposed_h) 0 ) (position (* diameter -0.5) height 0))
(sdedr:define-multibox-size "Size.Emit_Side_L" 0.1 0.1 0.01 0.01 1.5 1.5)
(sdedr:define-multibox-placement "Placement.Emit_Side_L" "Size.Emit_Side_L" "Emit_Side_L")

;; top cell
(sdedr:define-refinement-window "Top_Cell" "Rectangle" (position (* pitch -0.5) (+ height defect_h
     sq_h) 0 ) (position (* pitch 0.5) (+ height defect_h sq_h (* pitch 0.5) ) 0))
(sdedr:define-multibox-size "Size.Top_Cell_T" 0.1 0.1 0.1 0.01 1 -1.05)
(sdedr:define-multibox-placement "Placement.Top_Cell_T" "Size.Top_Cell_T" "Top_Cell")
(sdedr:define-multibox-size "Size.Top_Cell_L" 0.1 0.1 0.01 0.1 1.05 1)
(sdedr:define-multibox-placement "Placement.Top_Cell_L" "Size.Top_Cell_L" "Top_Cell")
(sdedr:define-multibox-size "Size.Top_Cell_R" 0.1 0.1 0.01 0.1 -1.05 1)
(sdedr:define-multibox-placement "Placement.Top_Cell_R" "Size.Top_Cell_R" "Top_Cell")

;; ---------------------------------------
(display "build mesh... \n")
(sde:build-mesh "snmesh" "-y 1e5" elGridFname ) ;;-y sets the max aspect ratio of the elements

(display "done.")(newline)
```

**Listing E.16: Code to create an FDTD grid**

```
############################################################
# Dan Turner-Evans                                         #
# 05/04/12                                                 #
# A Si microwire to test the E&M package                   #
############################################################

tensor {
#  MESH {
#     MinCellSize direction Y = 1
#  }
  EMW {
     parameter filename = "@parameter@"
```

```
    ComplexRefractiveIndex WavelengthDep  Real  Imag
    wavelength = @wl@
    NPWX = 5
    NPWY = 30
                Grading off
  }
}
```

**Listing E.17: Code to setup and run the simulation for a TM excitation source**

```
#define height 40
#define diameter 2
#define pitch 4
#define spacing 4
#define defect_h 2
#define sq_h 2
#define gap 0.1
#define window_t 0.02

Globals {
        GridFile         = "@tdr@"
        ParameterFile    = "@parameter@"
        InspectFile      = "@plot@"
        LogFile          = "@log@"
        TotalTimeSteps = 10000000
        NumberOfThreads = maximum
}

ComplexRefractiveIndex {
        WavelengthDep = {Real,Imag}
}

PECMedia {
        Region = {"Back_Reflector"}
}

Boundary {
        Type             = Periodic
        Sides            = {X}
}

Boundary {
        Type             = CPML
        Sides            = {Y}
}

PlaneWaveExcitation {
        BoxCorner1       = (@< pitch*-0.5>@, @< height + defect_h + sq_h + pitch*0.5 - gap +
            window_t + 0.5*spacing >@, 0)
        BoxCorner2       = (@< pitch*0.5>@, @< height + defect_h + sq_h + pitch*0.5 - gap +
            window_t + 0.5*spacing >@, 0)
        Theta            = 180
        Psi              = 0
        Wavelength       = @<1000.*wl>@
        Intensity        = 0.1
        Nrise            = 4
}



Plot {
```

```
        Name     = "n@node@_Eabs"
        Quantity = {AbsElectricField, AbsMagneticField}
        FinalPlot = yes
}

Extractor {
        Name             = "n@node@_a"
        Quantity         = {AbsorbedPhotonDensity}
}

Sensor {
        Name             = "total"
        Quantity         = PhotonFluxDensity
        BoxCorner1       = (@< pitch*-0.5>@, @< height + defect_h + sq_h + pitch*0.5 - gap +
            window_t + 0.25*spacing >@, 0)
        BoxCorner2       = (@< pitch*0.5>@, @< height + defect_h + sq_h + pitch*0.5 - gap +
            window_t + 0.25*spacing >@, 0)
        Mode             = {Integrate}
}

Sensor {
        Name             = "reflected"
        Quantity         = PhotonFluxDensity
        BoxCorner1       = (@< pitch*-0.5>@, @< height + defect_h + sq_h + pitch*0.5 - gap +
            window_t + 0.75*spacing >@, 0)
        BoxCorner2       = (@< pitch*0.5>@, @< height + defect_h + sq_h + pitch*0.5 - gap +
            window_t + 0.75*spacing >@, 0)
        Mode             = {Integrate}
}

Sensor {
        Name       = "absorbed_total"
        Quantity   = absorbedPhotonDensity
        BoxCorner1 = (@< pitch*-0.5>@, 0, 0)
        BoxCorner2 = (@< pitch*0.5>@, @< height + defect_h + sq_h + pitch*0.5 - gap + window_t >@,
             0)
        Mode       = {Integrate}
}

Sensor {
        Name       = "absorbed_Top_Cell"
        Quantity   = absorbedPhotonDensity
        Region     = {"Top_Cell_Emitter","Top_Cell_Circ","Top_Cell_Rect"}
        Mode       = {Integrate}
}

Sensor {
        Name       = "absorbed_Defect_Region"
        Quantity   = absorbedPhotonDensity
        Region     = {"Defect_Region"}
        Mode       = {Integrate}
}

Sensor {
        Name       = "absorbed_Bottom_Cell"
        Quantity   = absorbedPhotonDensity
        Region     = {"Wire_Base"}
        Mode       = {Integrate}
}

Detector {
```

```
        Tolerance       = 1e-4
}
```

**Listing E.18: Code to extract the reflection, transmission, and absorption of the structure for the TM excitation**

```
#-----------------------------------------
# $Id: //tcad/support/main/examples/getting-started/emw/simple3d/inspect_ins.cmd#3 $
# Author: Gergoe Letay
#setdep @node|emw@
load_library extend
# extract photon flux
set gc "[file tail [file rootname @plot@]]"
proj_load "$gc.plt"
set Ntot        [ds_getValue $gc "totalIntegr BoxYmin/PhotonFluxDensity"]
set Nr    [ds_getValue $gc "reflectedIntegr BoxYmax/PhotonFluxDensity"]
set Na    [ds_getValue $gc "absorbed_totalIntegr Box/AbsorbedPhotonDensity" ]
set Na_Top_Cell_Emitter [ds_getValue $gc "absorbed_Top_CellIntegr Top_Cell_Emitter/
    AbsorbedPhotonDensity" ]
set Na_Top_Cell_Circ [ds_getValue $gc "absorbed_Top_CellIntegr Top_Cell_Circ/AbsorbedPhotonDensity
    " ]
set Na_Top_Cell_Rect [ds_getValue $gc "absorbed_Top_CellIntegr Top_Cell_Rect/AbsorbedPhotonDensity
    " ]
set Na_Top_Cell [expr $Na_Top_Cell_Emitter+$Na_Top_Cell_Circ+$Na_Top_Cell_Rect]
set Na_Defect_Region [ds_getValue $gc "absorbed_Defect_RegionIntegr Defect_Region/
    AbsorbedPhotonDensity" ]
set Na_Bottom_Cell [ds_getValue $gc "absorbed_Bottom_CellIntegr Wire_Base/AbsorbedPhotonDensity" ]
set Ni [expr $Ntot+$Nr]

# calculate relative values
set R [expr 1.*$Nr/$Ni]
set A [expr 1.*$Na/$Ni]
set A_Top_Cell [expr 1.*$Na_Top_Cell/$Ni]
set A_Defect_Region [expr 1.*$Na_Defect_Region/$Ni]
set A_Bottom_Cell [expr 1.*$Na_Bottom_Cell/$Ni]
set RA [expr $R+$A]

# write it back to swb
ft_scalar R [format %.3g $R]
ft_scalar A [format %.3g $A]
ft_scalar A_Top_Cell [format %.3g $A_Top_Cell]
ft_scalar A_Defect_Region [format %.3g $A_Defect_Region]
ft_scalar A_Bottom_Cell [format %.3g $A_Bottom_Cell]
ft_scalar RA [format %.3g $RA]
```

**Listing E.19: Code to setup and run the simulation for a TE excitation source**

```
#define height 40
#define diameter 2
#define pitch 4
#define spacing 4
#define defect_h 2
#define sq_h 2
#define gap 0.1
#define window_t 0.02

Globals {
        GridFile        = "@tdr@"
        ParameterFile   = "@parameter@"
```

```
        InspectFile     = "@plot@"
        LogFile         = "@log@"
        TotalTimeSteps = 10000000
        NumberOfThreads = maximum
}

ComplexRefractiveIndex {
        WavelengthDep = {Real,Imag}
}

PECMedia {
        Region = {"Back_Reflector"}
}

Boundary {
        Type            = Periodic
        Sides           = {X}
}

Boundary {
        Type            = CPML
        Sides           = {Y}
}

PlaneWaveExcitation {
        BoxCorner1      = (@< pitch*-0.5>@, @< height + defect_h + sq_h + pitch*0.5 - gap +
            window_t + 0.5*spacing >@, 0)
        BoxCorner2      = (@< pitch*0.5>@, @< height + defect_h + sq_h + pitch*0.5 - gap +
            window_t + 0.5*spacing >@, 0)
        Theta           = 180
        Psi             = 90
        Wavelength      = @<1000.*wl>@
        Intensity       = 0.1
        Nrise           = 4
}



Plot {
        Name    = "n@node@_Eabs"
        Quantity = {AbsElectricField, AbsMagneticField}
        FinalPlot = yes
}

Extractor {
        Name            = "n@node@_a"
        Quantity        = {AbsorbedPhotonDensity}
}

Sensor {
        Name            = "total"
        Quantity        = PhotonFluxDensity
        BoxCorner1      = (@< pitch*-0.5>@, @< height + defect_h + sq_h + pitch*0.5 - gap +
            window_t + 0.25*spacing >@, 0)
        BoxCorner2      = (@< pitch*0.5>@, @< height + defect_h + sq_h + pitch*0.5 - gap +
            window_t + 0.25*spacing >@, 0)
        Mode            = {Integrate}
}

Sensor {
        Name            = "reflected"
```

```
        Quantity        = PhotonFluxDensity
        BoxCorner1      = (@< pitch*-0.5>@, @< height + defect_h + sq_h + pitch*0.5 - gap +
            window_t + 0.75*spacing >@, 0)
        BoxCorner2      = (@< pitch*0.5>@, @< height + defect_h + sq_h + pitch*0.5 - gap +
            window_t + 0.75*spacing >@, 0)
        Mode            = {Integrate}
}

Sensor {
        Name        = "absorbed_total"
        Quantity    = absorbedPhotonDensity
        BoxCorner1 = (@< pitch*-0.5>@, 0, 0)
        BoxCorner2 = (@< pitch*0.5>@, @< height + defect_h + sq_h + pitch*0.5 - gap + window_t >@,
            0)
        Mode        = {Integrate}
}

Sensor {
        Name        = "absorbed_Top_Cell"
        Quantity    = absorbedPhotonDensity
        Region      = {"Top_Cell_Emitter","Top_Cell_Circ","Top_Cell_Rect"}
        Mode        = {Integrate}
}

Sensor {
        Name        = "absorbed_Defect_Region"
        Quantity    = absorbedPhotonDensity
        Region      = {"Defect_Region"}
        Mode        = {Integrate}
}

Sensor {
        Name        = "absorbed_Bottom_Cell"
        Quantity    = absorbedPhotonDensity
        Region      = {"Wire_Base"}
        Mode        = {Integrate}
}

Detector {
        Tolerance       = 1e-4
}
```

**Listing E.20: Code to extract the reflection, transmission, and absorption of the structure for the TE excitation**

```
#-----------------------------------------
# $Id: //tcad/support/main/examples/getting-started/emw/simple3d/inspect_ins.cmd#3 $
# Author: Gergoe Letay
#setdep @node|emw1@
load_library extend
# extract photon flux
set gc "[file tail [file rootname @plot@]]"
proj_load "$gc.plt"
set Ntot        [ds_getValue $gc "totalIntegr BoxYmin/PhotonFluxDensity"]
set Nr    [ds_getValue $gc "reflectedIntegr BoxYmax/PhotonFluxDensity"]
set Na    [ds_getValue $gc "absorbed_totalIntegr Box/AbsorbedPhotonDensity" ]
set Na_Top_Cell_Emitter [ds_getValue $gc "absorbed_Top_CellIntegr Top_Cell_Emitter/
    AbsorbedPhotonDensity" ]
set Na_Top_Cell_Circ [ds_getValue $gc "absorbed_Top_CellIntegr Top_Cell_Circ/AbsorbedPhotonDensity
    " ]
```

```
set Na_Top_Cell_Rect [ds_getValue $gc "absorbed_Top_CellIntegr Top_Cell_Rect/AbsorbedPhotonDensity
    " ]
set Na_Top_Cell [expr $Na_Top_Cell_Emitter+$Na_Top_Cell_Circ+$Na_Top_Cell_Rect]
set Na_Defect_Region [ds_getValue $gc "absorbed_Defect_RegionIntegr Defect_Region/
    AbsorbedPhotonDensity" ]
set Na_Bottom_Cell [ds_getValue $gc "absorbed_Bottom_CellIntegr Wire_Base/AbsorbedPhotonDensity" ]
set Ni [expr $Ntot+$Nr]

# calculate relative values
set R [expr 1.*$Nr/$Ni]
set A [expr 1.*$Na/$Ni]
set A_Top_Cell [expr 1.*$Na_Top_Cell/$Ni]
set A_Defect_Region [expr 1.*$Na_Defect_Region/$Ni]
set A_Bottom_Cell [expr 1.*$Na_Bottom_Cell/$Ni]
set RA [expr $R+$A]

# write it back to swb
# ft_scalar R [format %.3g $R]
# ft_scalar A [format %.3g $A]
ft_scalar A_Top_Cell_TE [format %.3g $A_Top_Cell]
ft_scalar A_Defect_Region_TE [format %.3g $A_Defect_Region]
ft_scalar A_Bottom_Cell_TE [format %.3g $A_Bottom_Cell]
# ft_scalar RA [format %.3g $RA]
```

**Listing E.21: Code to map the FDTD grid onto the FEM mesh**

```
File{
*-Input
   Grid     = "n@node|sde@_el_msh.tdr"
   OpticalSolverInput = "*_a_eml.tdr"
   IlluminationSpectrum= "am15g_50nm_TE_TM_mod.txt"
   Parameters ="@parameter@"
*-Output
   Plot     = "@tdrdat@"
   Current = "@plot@"
   Output  = "@log@"
}

Physics {
    Optics(
        OpticalGeneration(
            ComputeFromSpectrum ()
        )
        OpticalSolver(
            FromFile(
                IdentifyingParameter = ("Wavelength" "Psi")
            )
        )
    )

}

Plot {
  OpticalGeneration
}


Math{
  RhsMin = 1E-12
  Extrapolate
```

```
  Derivatives
  RelErrControl
  Iterations=20
  ExtendedPrecision
  Digits=7
  Notdamped=100
  ErrRef(electron) = 1E0
  ErrRef(hole) = 1E0
  ExitOnFailure
  Number_of_Threads = maximum
  StackSize = 20000000  * 20MB; needed for NewRayTracer
  Method=Super
*   CNormPrint
}


Solve{
        Optics
}
```

**Listing E.22: Code to run the device physics**

```
File{
*-Input
   Grid     = "n@node|sde@_el_msh.tdr"
   LifeTime = "n@node|sde@_el_msh.tdr"
   Parameters ="@parameter@"
#if @GaAsP_SRHLifeTime@ == 1E-07 && @Defect_SRHLifeTime@ == 1E-12
   OpticalGenerationInput = "n117_des.tdr"
#else
   OpticalGenerationInput = "n@node|sdevice@_des.tdr"
#endif
*-Output
   Plot     = "@tdrdat@"
   Current = "@plot@"
   Output  = "@log@"
   NonLocalPlot = "n@node@_nl"
}


Electrode{
 { Name="TopContact"  Voltage=0 hRecVelocity = 100}
 { Name="BottomContact"  Voltage=0 eRecVelocity = 100}
}

Physics {
 AreaFactor = @< 1E11/4 >@ * to get current in mA/cm^2
 Fermi
 Recombination(
   SRH
  )
  Mobility(
   DopingDep
   HighFieldSat
  )

  ThermionicEmission

  eBarrierTunneling "TD_NLM" (
      Band2Band
```

```
      TwoBand
  )

  hBarrierTunneling "TD_NLM"(
      Band2Band
      TwoBand
  )

 Optics(
    OpticalGeneration(
        ReadFromFile(
#           Datasetname=AbsorbedPhotonDensity
            Scaling =0
            TimeDependence(
                WaveTime = (0.9, 10)
                Scaling = 1.0
            )
        )
     )
  )
}

# Physics (materialInterface="SiliconGermanium/GaInP") {
#   Recombination(surfaceSRH)
# }

Physics (materialInterface="Ambient/GaInP") {
  Recombination(surfaceSRH)
}

Physics (materialInterface="Ambient/GaAsP") {
  Recombination(surfaceSRH)
}

Physics (materialInterface="Oxide/SiliconGermanium") {
  Recombination(surfaceSRH)
}

Physics (materialInterface="Oxide/GaAsP") {
  Recombination(surfaceSRH)
}

Physics (material = "GaInP") {
  Recombination(
    Radiative
    Auger
  )
}

Physics (material = "GaAsP") {
  Recombination(
    Radiative
    Auger
  )
}


Plot {
  xMoleFraction Doping DonorConcentration AcceptorConcentration
  eEffectiveStateDensity hEffectiveStateDensity EffectiveIntrinsicDensity IntrinsicDensity
  eDensity hDensity SpaceCharge
```

```
  eQuasiFermiPotential hQuasiFermiPotential BandGap ConductionBandEnergy ValenceBandEnergy
      ElectronAffinity
  ElectricField ElectricField/vector ElectrostaticPotential
  eLifetime hLifetime SRH Auger TotalRecombination SurfaceRecombination RadiativeRecombination
  eCurrent/Vector hCurrent/Vector current/vector
  eMobility hMobility eVelocity hVelocity
  SRH Auger TotalRecombination SurfaceRecombination RadiativeRecombination
  BarrierTunneling
  eBarrierTunneling hBarrierTunneling
  NonLocal
  OpticalGeneration
}

NonLocalPlot ((0, 0)) {
  ConductionBand  ValenceBand
  hDensity  eDensity
  hQuasiFermi  eQuasiFermi
  NonLocal
}




Math{
  RhsMin = 1E-12
  Extrapolate
  Derivatives
  RelErrControl
  Iterations=20
  ExtendedPrecision
  Digits=7
  Notdamped=100
  ErrRef(electron) = 1E0
  ErrRef(hole) = 1E0
  ExitOnFailure
  Number_of_Threads = maximum
  StackSize = 20000000  * 20MB; needed for NewRayTracer
  Method=Super
  NonLocal "TD_NLM" (
    MaterialInterface = "SiliconGermanium/GaAsP"
    Length=15e-7          # [cm] distance to anchor point
    Permeation = 15e-7
  )
  DirectCurrent
#  Cylindrical(0.0)

  Transient=BE
  TransientDigits=7
  TransientErrRef(electron) = 1E0
  TransientErrRef(hole) = 1E0

*   CNormPrint
}


Solve{
                NewCurrentPrefix = "tmp_"

                Coupled  { poisson }
                Plot( FilePrefix = "n@node@_Banddgm")
#               Coupled  { poisson electron }
```

```
#               Coupled  { poisson hole }
#               Coupled  { poisson electron hole }

                Transient (
                  InitialStep=1e-20 MaxStep =0.2 MinStep = 1e-40 Increment=2
                  InitialTime=0 FinalTime=1
                ){ Coupled (Iterations=20) {Poisson Electron Hole  } }

                NewCurrentPrefix = "Light_IV"

                Quasistationary (
                  InitialStep=1e-4 MaxStep =1e-3 MinStep = 1e-30 Increment=1.7 DoZero
                  Goal{ voltage = 1.5 Name="BottomContact" }
                ){ Coupled {Poisson Electron Hole  }
                    Plot( FilePrefix = "n@node@_Banddgm_Jsc" Time = (0) )
                 }

                NewCurrentPrefix = "tmp_2"

                Quasistationary (
                  InitialStep=1e-2 MaxStep =0.1 MinStep = 1e-30 Increment=1.5 DoZero
                  Goal{ current = 0 Name="BottomContact" }
                ){ Coupled {Poisson Electron Hole  }
                 }
                   Plot( FilePrefix = "n@node@_Banddgm_Voc")

  System("rm -f tmp*") *remove the plot we dont need anymore.
  System("rm -f tmp2*") *remove the plot we dont need anymore.
}
```

**Listing E.23: Code to extract the current-voltage characteristics**

```
# Plot light J-V and P-V curves and extract Photovoltaic parameters
# or Plot dark J-V characteristics

# #setdep @node|sdevice1@

set N     @node@
set i     @node:index@

# proj_load  @plot@ PLT_JV($N)
proj_load  Light_IVn@previous@_des.plt PLT_JV($N)

#- Automatic alternating color assignment tied to node index
#-------------------------------------------------------------------#
set COLORS  [list orange green blue red violet brown orange magenta]
set NCOLORS [llength $COLORS]
set color   [lindex  $COLORS [expr $i%$NCOLORS]]


# Plot light J-V characteristics and extract PV parameters
cv_createDS J($N)  "PLT_JV($N) BottomContact OuterVoltage" "PLT_JV($N) BottomContact TotalCurrent"

cv_inv J($N) y

cv_create V($N)  "PLT_JV($N) BottomContact OuterVoltage" "PLT_JV($N) BottomContact OuterVoltage"

cv_createWithFormula P($N)  "<V($N)>*<J($N)>" A A
cv_display P($N) y2

cv_setCurveAttr J($N)  "light-JV" $color solid  2 circle 3 defcolor 1 defcolor
```

```
cv_setCurveAttr P($N)  "light-PV" $color dashed  2 none 3 defcolor 1 defcolor

gr_setAxisAttr X {Voltage (V)}  16 0 {} black 1 14 0 5 0
gr_setAxisAttr Y {Current Density (mA/cm^2)} 16 0 30  black 1 14 0 5 0
gr_setAxisAttr Y2 {Power (mW/cm^2)} 16 0 26  black 1 14 0 5 0

# Extract Photovoltaic parameters
# Extract short circuit current density, Jsc [mA/cm^2]
set Jsc($N) [cv_compute "vecvaly(<J($N)>,0)" A A A A]
ft_scalar Jsc [format %.2f $Jsc($N)]

# Extract open circuit voltage, Voc [V]
set Jmin [cv_compute "vecmin(<J($N)>)" A A A A]
if {$Jmin <= 0} {
        set Voc($N) [expr [cv_compute "veczero(<J($N)>)" A A A A]]
} elseif {$Jmin <= 1e-6} {
        set Voc($N) [expr [cv_compute "vecvalx(<J($N>,$Jmin)" A A A A]]
}
ft_scalar Voc [format %.4f $Voc($N)]

# Extract fill factor (FF), maximum power outpout (Pm [mW/cm2]) and efficiency (eff)
  set Ps 100 ;#Incident light power density for AM1.5g radiation in mW/cm^2

if {$Voc($N) > 0} {
        set Pm($N) [cv_compute "vecmax(<P($N)>)" A A A A]
        ## fillfactor in %
        set FF($N) [expr $Pm($N)/($Voc($N)*$Jsc($N))*100]
        ## efficiency in % (mW/cm^2/(100mW/cm^2)*100%)
        set Eff($N) [expr $Pm($N)/$Ps*100]
}
ft_scalar Pm [format %.4f $Pm($N)]
ft_scalar FF  [format %.4f $FF($N)]
ft_scalar Eff  [format %.4f $Eff($N)]
```

**Listing E.24: Code to plot optical generation cross sections for TM excitation**

```
#!MC 1120

$!VarSet |MFBD| = '/home/dt/STDB/Defects/01-2D'

## Load data in Tecplot using the SWB-Loader
$!READDATASET "n@node|emw@_a_eml.tdr" DATASETREADER = "SWB-Loader"

$!TWODAXIS YDETAIL{ISREVERSED = NO}

$!EXPORTSETUP IMAGEWIDTH = 439

$!EXPORTSETUP EXPORTFNAME = '/home/dt/STDB/Defects/01-2D/n@node|emw@_@<int(@wl@*1000)>@_nm_TM.tif'

$!EXPORT
  EXPORTREGION = CURRENTFRAME

$!RemoveVar |MFBD|

$!QUIT
```

**Listing E.25: Code to plot optical generation cross sections for TE excitation**

```
#!MC 1120
```

```
$!VarSet |MFBD| = '/home/dt/STDB/Defects/01-2D'

## Load data in Tecplot using the SWB-Loader
$!READDATASET "n@node|emw1@_a_eml.tdr" DATASETREADER = "SWB-Loader"

$!TWODAXIS YDETAIL{ISREVERSED = NO}

$!EXPORTSETUP IMAGEWIDTH = 439

$!EXPORTSETUP EXPORTFNAME = '/home/dt/STDB/Defects/01-2D/n@node|emw1@_@<int(@wl@*1000)>@_nm_TE.tif
    '

$!EXPORT
  EXPORTREGION = CURRENTFRAME

$!RemoveVar |MFBD|

$!QUIT
```

## E.2 Comparison between Lumerical and Sentaurus FDTD

The Atwater Group has typically used Lumerical for optical absorption simulations and Sentaurus for device physics modeling. Dr. Mike Kelzenberg successfully coupled the two to enable full optoelectronic modeling by using Matlab to interpolate the Lumerical FDTD grid onto the Sentaurus FEM mesh.(186) However, the interpolation process is slow and awkward. Sentaurus has a built in FDTD simulation, and, though its accuracy and limitations are not well understood, it has an efficient interpolation process. Thus, I explored the use of Sentaurus for full optoelectronic simulations.

Figure **E.2** displays a comparison between the Lumerical and Sentaurus simulations for a two dimensional "wire" profile. While there are some discrepancies between the two, especially at longer wavelengths for TE polarization, in general, they agree quite well.

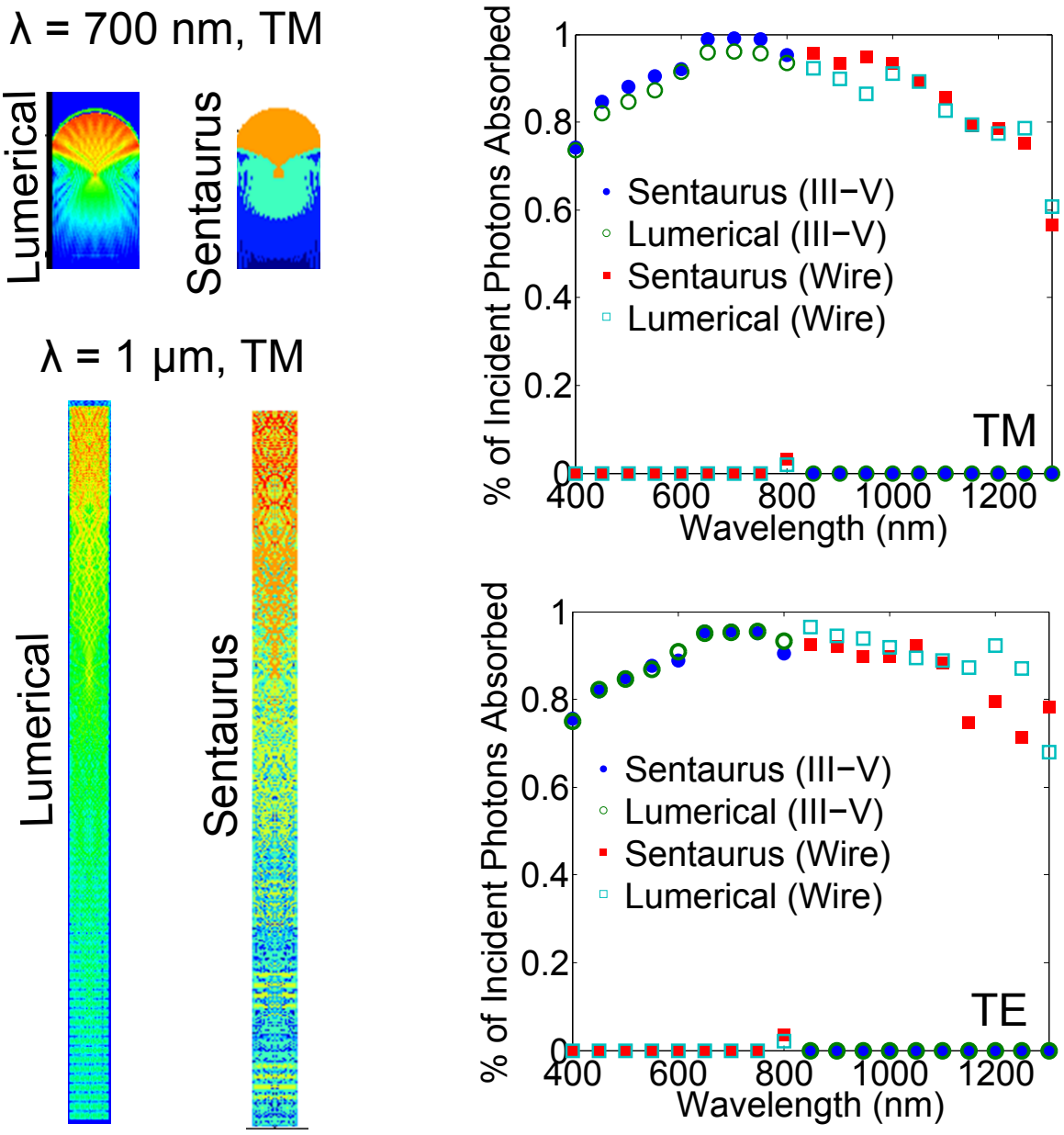


Figure E.2: Comparison of FDTD simulations from Sentaurus and Lumerical. (left) Absorption profiles from the two software programs at 700 nm and 1 $\mu$m. (right) % of Incident Photons Absorbed vs. Wavelength for both TM and TE polarizations.

# Bibliography


[1] International Energy Agency. Electricity/heat in world in 2009, 2013.

[2] U.S. Envionmental Protection Agency. Draft inventory of U.S. greenhouse gas emissions and sinks: 1990-2011, 2013.

[3] J. Rogelj, D. L. McCollum, A. Reisinger, M. Meinshausen, and K. Riahi. Probabilistic cost estimates for climate change mitigation. *Nature*, 493(7430):79–83, 2013.

[4] N. S. Lewis. Powering the planet, 2013.

[5] K. Aanesen, S. Heck, and D. Pinner. Solar power: Darkest before dawn. McKinsey & Company, 2012.

[6] U.S. Energy Information Administration. Levelized cost of new generation resources in the annual energy outlook 2013, 2013.

[7] G. Carr. Sunny uplands. *The Economist*, (June 2-8), 2012.

[8] E. Wesoff. Solar 2.0: The next business cycle in PV, 2013.

[9] Advanced Research Projects-Energy. $1/W photovoltaic systems. U.S. Department of Energy, 2010.

[10] K. Kato, A. Murata, and K. Sakuta. Energy pay-back time and life-cycle $CO_2$ emission of residential PV power system with silicon PV module. *Progress in Photovoltaics: Research and Applications*, 6(2):105–115, 1998.

[11] L. Kazmerski. Best research-cell efficiencies, 2013.

[12] K. E. Plass, M. A. Filler, J. M. Spurgeon, B. M. Kayes, S. Maldonado, B. S. Brunschwig, H. A. Atwater, and N. S. Lewis. Flexible polymer-embedded Si wire arrays. *Advanced Materials*, 21(3):325–328, 2009.

[13] J. M. Spurgeon, K. E. Plass, B. M. Kayes, B. S. Brunschwig, H. A. Atwater, and N. S. Lewis. Repeated epitaxial growth and transfer of arrays of patterned, vertically aligned, crystalline Si wires from a single Si(111) substrate. *Applied Physics Letters*, 93(3), 2008.

[14] N. Ashcroft and N. Mermin. *Solid State Physics*. Holt, Rinehart, and Winston, New York, NY, 1976.

[15] H. Ibach and H. Luth. *Solid-State Physics: An Introduction to Principles of Materials Science*. Springer-Verlag, New York, NY, 2009.

[16] C. Kittel. *Introction to Solid State Physics*. John Wiley & Sons, Inc., Hoboken, NJ, 2005.

[17] S.M. Sze and Kwok K. Ng. *Physics of Semiconductor Devices*. Wiley-Interscience, Hoboken, NJ, 2007.

[18] C. H. Henry. Limiting efficiencies of ideal single and multiple energy gap terrestrial solar cells. *Journal of Applied Physics*, 51(8):4494–4500, 1980.

[19] P. T. Landsberg and P. Baruch. The thermodynamics of the conversion of radiation energy for photovoltaics. *Journal of Physics A: Mathematical and General*, 22(11): 1911, 1989.

[20] I. Tobas and A. Luque. Ideal efficiency of monolithic, series-connected multijunction solar cells. *Progress in Photovoltaics: Research and Applications*, 10(5):323–329, 2002.

[21] W. Shockley and H. J. Queisser. Detailed balance limit of efficiency of p-n junction solar cells. *Journal of Applied Physics*, 32(3):510–519, 1961.

[22] M. A. Green. *Silicon Solar Cells: Advanced Principles and Practice*. Centre for Photovoltaic Devices and Systems, University of New South Wales, New South Wales, Australia, 1995.

[23] R. S. Wagner and W. C. Ellis. Vapor-liquid-solid mechanism of single crystal growth. *Applied Physics Letters*, 4(5):89–90, 1964.

[24] E. I. Givargizov. Periodic instability in whisker growth. *Journal of Crystal Growth*, 20(3):217, 1973.

[25] J. B. Hannon, S. Kodambaka, F. M. Ross, and R. M. Tromp. The influence of the surface migration of gold on the growth of silicon nanowires. *Nature*, 440(7080):69–71, 2006.

[26] C. M. Lieber and Z. L. Wang. Functional nanowires. *MRS Bulletin*, 32(2):99–108, 2007.

[27] B. M. Kayes, H. A. Atwater, and N. S. Lewis. Comparison of the device physics principles of planar and radial p-n junction nanorod solar cells. *Journal of Applied Physics*, 97(11):114302–11, 2005.

[28] S. W. Boettcher, J. M. Spurgeon, M. C. Putnam, E. L. Warren, D. B. Turner-Evans, M. D. Kelzenberg, J. R. Maiolo, H. A. Atwater, and N. S. Lewis. Energy-conversion properties of vapor-liquid-solid grown silicon wire-array photocathodes. *Science*, 327 (5962):185–187, 2010.

[29] S. W. Boettcher, E. L. Warren, M. C. Putnam, E. A. Santori, D. Turner-Evans, M. D. Kelzenberg, M. G. Walter, J. R. McKone, B. S. Brunschwig, H. A. Atwater, and N. S. Lewis. Photoelectrochemical hydrogen evolution using Si microwire arrays. *Journal of the American Chemical Society*, 133(5):1216–1219, 2011.

[30] M. D. Kelzenberg, D. B. Turner-Evans, B. M. Kayes, M. A. Filler, M. C. Putnam, N. S. Lewis, and H. A. Atwater. Photovoltaic measurements in single-nanowire silicon solar cells. *Nano Letters*, 8(2):710–714, 2008.

[31] M. D. Kelzenberg, S. W. Boettcher, J. A. Petykiewicz, D. B. Turner-Evans, M. C. Putnam, E. L. Warren, J. M. Spurgeon, R. M. Briggs, N. S. Lewis, and H. A. Atwater. Enhanced absorption and carrier collection in Si wire arrays for photovoltaic applications. *Nature Materials*, 9(3):239–244, 2010.

[32] M. D. Kelzenberg, D. B. Turner-Evans, M. C. Putnam, S. W. Boettcher, R. M. Briggs, J. Y. Baek, N. S. Lewis, and H. A. Atwater. High-performance Si microwire photovoltaics. *Energy & Environmental Science*, 4(3):866–871, 2011.

[33] M. C. Putnam, D. B. Turner-Evans, M. D. Kelzenberg, S. W. Boettcher, N. S. Lewis, and H. A. Atwater. 10 $\mu$m minority-carrier diffusion lengths in Si wires synthesized by Cu-catalyzed vapor-liquid-solid growth. *Applied Physics Letters*, 95(16):163116–3, 2009.

[34] M. C. Putnam, S. W. Boettcher, M. D. Kelzenberg, D. B. Turner-Evans, J. M. Spurgeon, E. L. Warren, R. M. Briggs, N. S. Lewis, and H. A. Atwater. Si microwire-array solar cells. *Energy & Environmental Science*, 3(8):1037–1041, 2010.

[35] J. M. Spurgeon, S. W. Boettcher, M. D. Kelzenberg, B. S. Brunschwig, H. A. Atwater, and N. S. Lewis. Flexible, polymer-supported, Si wire array photoelectrodes. *Advanced Materials*, 22(30):3277–3281, 2010.

[36] A. C. Tamboli, C. T. Chen, E. L. Warren, D. B. Turner-Evans, M. D. Kelzenberg, N. S. Lewis, and H. A. Atwater. Wafer-scale growth of silicon microwire arrays for photovoltaics and solar fuel generation. *Photovoltaics, IEEE Journal of*, 2(3):294–297, 2012.

[37] S. M. Eichfeld, H. Shen, C. M. Eichfeld, S. E. Mohney, E. C. Dickey, and J. M. Redwing. Gas phase equilibrium limitations on the vaporliquidsolid growth of epitaxial silicon nanowires using $SiCl_4$. *Journal of Materials Research*, 26(17):2207–2214, 2011.

[38] C. E. Kendrick, H. P. Yoon, Y. A. Yuwen, G. D. Barber, H. Shen, T. E. Mallouk, E. C. Dickey, T. S. Mayer, and J. M. Redwing. Radial junction silicon wire array solar cells fabricated by gold-catalyzed vapor-liquid-solid growth. *Applied Physics Letters*, 97(14):143108–3, 2010.

[39] L. Tsakalakos, J. Balch, J. Fronheiser, B. A. Korevaar, O. Sulima, and J. Rand. Silicon nanowire solar cells. *Applied Physics Letters*, 91(23):233117–3, 2007.

[40] E. Garnett and P. D. Yang. Light trapping in silicon nanowire solar cells. *Nano Letters*, 10(3):1082–1087, 2010.

[41] B. Tian, X. Zheng, T. J. Kempa, Y. Fang, N. Yu, G. Yu, J. Huang, and C. M. Lieber. Coaxial silicon nanowires as solar cells and nanoelectronic power sources. *Nature*, 449 (7164):885–889, 2007.

[42] F. Qian, Y. Li, S. Gradecak, H. Park, Y. Dong, Y. Ding, Z. L. Wang, and C. M. Lieber. Multi-quantum-well nanowire heterostructures for wavelength-controlled lasers. *Nat Mater*, 7(9):701–706, 2008.

[43] R. Yan, D. Gargas, and P. Yang. Nanowire photonics. *Nat Photon*, 3(10):569–576, 2009.

[44] R. Chen, T. D. Tran, K. W. Ng, W. S. Ko, L. C. Chuang, F. G. Sedgwick, and C. Chang-Hasnain. Nanolasers grown on silicon. *Nat Photon*, 5(3):170–175, 2011.

[45] M. Khajavikhan, A. Simic, M. Katz, J. H. Lee, B. Slutsky, A. Mizrahi, V. Lomakin, and Y. Fainman. Thresholdless nanoscale coaxial lasers. *Nature*, 482(7384):204–207, 2012.

[46] J. H. Choi, A. Zoulkarneev, S. I. Kim, C. W. Baik, M. H. Yang, S. S. Park, H. Suh, U. J. Kim, H. Bin Son, J. S. Lee, M. Kim, J. M. Kim, and K. Kim. Nearly single-crystalline GaN light-emitting diodes on amorphous glass substrates. *Nat Photon*, 5 (12):763–769, 2011.

[47] J. Kupec, R. L. Stoop, and B. Witzigmann. Light absorption and emission in nanowire array solar cells. *Opt. Express*, 18(26):27589–27605, 2010.

[48] G. Anjia, H. Yijie, H. Shu, T. Sarmiento, E. Pickett, L. Dong, L. Shuang, A. Lin, S. Thombare, Y. Zongfu, F. Shanhui, P. McIntyre, Y. Cui, and J. Harris. Design and growth of III-V nanowire solar cell arrays on low cost substrates. In *Photovoltaic Specialists Conference (PVSC), 2010 35th IEEE*, pages 002034–002037, 2010.

[49] C. Chang, C. Chi, M. Yao, N. Huang, C. Chen, J. Theiss, A. W. Bushmaker, S. LaLumondiere, T. Yeh, M. L. Povinelli, C. Zhou, P. D. Dapkus, and S. B. Cronin. Electrical and optical characterization of surface passivation in GaAs nanowires. *Nano Letters*, 2012.

[50] K. Cho, D. J. Ruebusch, M. H. Lee, J. H. Moon, A. C. Ford, R. Kapadia, K. Takei, O. Ergen, and A. Javey. Molecular monolayers for conformal, nanoscale doping of InP nanopillar photovoltaics. *Applied Physics Letters*, 98(20):203101–3, 2011.

[51] C. Colombo, M. Heibeta, M. Gratzel, and A. Fontcuberta i Morral. Gallium arsenide p-i-n radial structures for photovoltaic applications. *Applied Physics Letters*, 94(17): 173108–3, 2009.

[52] Y. Dong, B. Tian, T. J. Kempa, and C. M. Lieber. Coaxial group IIInitride nanowire photovoltaics. *Nano Letters*, 9(5):2183–2187, 2009.

[53] Z. Fan, H. Razavi, J. Do, A. Moriwaki, O. Ergen, Y. Chueh, P. W. Leu, J. C. Ho, T. Takahashi, L. A. Reichertz, S. Neale, K. Yu, M. Wu, J. W. Ager, and A. Javey. Three-dimensional nanopillar-array photovoltaics on low-cost and flexible substrates. *Nat Mater*, 8(8):648–653, 2009.

[54] G. Mariani, P. Wong, A. M. Katzenmeyer, F. Leonard, J. Shapiro, and D. L. Huffaker. Patterned radial GaAs nanopillar solar cells. *Nano Letters*, 11(6):2490–2494, 2011.

[55] G. Mariani, A. C. Scofield, C. Hung, and D. L. Huffaker. GaAs nanopillar-array solar cells employing in situ surface passivation. *Nat Commun*, 4:1497, 2013.

[56] G. Mariani, Z. Zhou, A. Scofield, and D. L. Huffaker. Direct-bandgap epitaxial coremultishell nanopillar photovoltaics featuring subwavelength optical concentrators. *Nano Letters*, 13(4):1632–1637, 2013.

[57] H. Goto, K. Nosaki, K. Tomioka, S. Hara, K. Hiruma, J. Motohisa, and T. Fukui. Growth of core-shell InP nanowires for photovoltaic application by selective-area metal organic vapor phase epitaxy. *Applied Physics Express*, 2(3), 2009.

[58] J. Wallentin, N. Anttu, D. Asoli, M. Huffman, I. berg, M. H. Magnusson, G. Siefer, P. Fuss-Kailuweit, F. Dimroth, B. Witzigmann, H. Q. Xu, L. Samuelson, K. Deppert, and M. T. Borgstrm. InP nanowire array solar cells achieving 13.8% efficiency by exceeding the ray optics limit. *Science*, 2013.

[59] J. Geisz, D. Friedman, J. Ward, A. Duda, W. Olavarria, and T. Moriarty. 40.8% efficient inverted triple-junction solar cell with two independently metamorphic junctions. *Applied Physics Letters*, 93(12):123505, 2008.

[60] R. R. King, D. C. Law, K. M. Edmondson, C. M. Fetzer, G. S. Kinsey, H. Yoon, R. A. Sherif, and N. H. Karam. 40% efficient metamorphic GaInP/GaInAs/Ge multijunction solar cells. *Applied Physics Letters*, 90(18):183516–3, 2007.

[61] C. V. Falub, H. von Känel, F. Isa, R. Bergamaschini, A. Marzegalli, D. Chrastina, G. Isella, E. Müller, P. Niedermann, and L. Miglio. Scaling hetero-epitaxy from layers to three-dimensional crystals. *Science*, 335(6074):1330–1334, 2012.

[62] P. Gibart. Metal organic vapour phase epitaxy of GaN and lateral overgrowth. *Reports on Progress in Physics*, 67(5):667, 2004.

[63] B. M. Kayes, M. A. Filler, M. C. Putnam, M. D. Kelzenberg, N. S. Lewis, and H. A. Atwater. Growth of vertically aligned Si wire arrays over large areas ($> 1$ cm$^2$) with Au and Cu catalysts. *Applied Physics Letters*, 91(10):103110–3, 2007.

[64] A. A. Istratov and E. R. Weber. Electrical properties and recombination activity of copper, nickel and cobalt in silicon. *Applied Physics A*, 66(2):123–136, 1998.

[65] A. A. Istratov and E. R. Weber. Physics of copper in silicon. *Journal of The Electrochemical Society*, 149(1):G21–G30, 2002.

[66] H. Okamoto. Cu-Si (copper-silicon). *Journal of Phase Equilibria*, 23(3):281–282, 2002.

[67] C. E. Kendrick and J. M. Redwing. The effect of pattern density and wire diameter on the growth rate of micron diameter silicon wires. *Journal of Crystal Growth*, 337 (1):1–6, 2011.

[68] N. Shin and M. A. Filler. Controlling silicon nanowire growth direction via surface chemistry. *Nano Letters*, 12(6):2865–2870, 2012.

[69] J. G. Swadener and S. T. Picraux. Strain distributions and electronic property modifications in Si/Ge axial nanowire heterostructures. *Journal of Applied Physics*, 105 (4):044310–9, 2009.

[70] Y. Cui, X. Duan, J. Hu, and C. M. Lieber. Doping and electrical transport in silicon nanowires. *The Journal of Physical Chemistry B*, 104(22):5213–5216, 2000.

[71] S. M. Eichfeld, T. Ho, C. E. Eichfeld, A. Cranmer, S. E. Mohney, T. S. Mayer, and J. M. Redwing. Resistivity measurements of intentionally and unintentionally template-grown doped silicon nanowire arrays. *Nanotechnology*, 18(31):315201, 2007.

[72] G. Imamura, T. Kawashima, M. Fujii, C. Nishimura, T. Saitoh, and S. Hayashi. Distribution of active impurities in single silicon nanowires. *Nano Letters*, 8(9):2620–2624, 2008.

[73] K. Lew, L. Pan, T. E. Bogart, S. M. Dilts, E. C. Dickey, J. M. Redwing, Y. Wang, M. Cabassi, T. S. Mayer, and S. W. Novak. Structural and electrical properties of trimethylboron-doped silicon nanowires. *Applied Physics Letters*, 85(15):3101–3103, 2004.

[74] L. Pan, K. Lew, J. M. Redwing, and E. C. Dickey. Effect of diborane on the microstructure of boron-doped silicon nanowires. *Journal of Crystal Growth*, 277(14): 428–436, 2005.

[75] T. Stelzner, M. Pietsch, G. Andrä, F. Falk, E. Ose, and S. Christiansen. Silicon nanowire-based solar cells. *Nanotechnology*, 19(29):295203, 2008.

[76] E. C Garnett, W. Liang, and P. Yang. Growth and electrical characteristics of platinum-nanoparticle-catalyzed silicon nanowires. *Advanced Materials*, 19(19):2946–2950, 2007.

[77] Solecon Laboratories. Silicon/germanium resistivity and carrier concentration calculators, 2008. `http://www.solecon.com/sra/rho2ccal.htm`.

[78] D. J. Hamilton and W. G Howard. *Basic Integrated Circuit Engineering*. McGraw-Hill, New York, 1975.

[79] S. M. Hu, P. Fahey, and R. W. Dutton. On models of phosphorus diffusion in silicon. *Journal of Applied Physics*, 54(12):6912–6922, 1983.

[80] R. R. King, R. A. Sinton, and R. M. Swanson. Studies of diffused phosphorus emitters: saturation current, surface recombination velocity, and quantum efficiency. *Electron Devices, IEEE Transactions on*, 37(2):365–371, 1990.

[81] B. Hartiti, A. Slaoui, J. C. Muller, R. Stuck, and P. Siffert. Phosphorus diffusion into silicon from a spin-on source using rapid thermal processing. *Journal of Applied Physics*, 71(11):5474–5478, 1992.

[82] M. Schaper, J. Schmidt, H. Plagwitz, and R. Brendel. 20.1%-efficient crystalline silicon solar cell with amorphous silicon rear-surface passivation. *Progress in Photovoltaics: Research and Applications*, 13(5):381–386, 2005.

[83] L. Cai, A. Rohatgi, S. Han, G. May, and M. Zou. Investigation of the properties of plasma-enhanced chemical vapor deposited silicon nitride and its effect on silicon surface passivation. *Journal of Applied Physics*, 83(11):5885–5889, 1998.

[84] M. J. Kerr and A. Cuevas. Recombination at the interface between silicon and stoichiometric plasma silicon nitride. *Semiconductor Science and Technology*, 17(2):166, 2002.

[85] P. Doshi, G. E. Jellison, and A. Rohatgi. Characterization and optimization of absorbing plasma-enhanced chemical vapor deposited antireflection coatings for silicon photovoltaics. *Appl. Opt.*, 36(30):7826–7837, 1997.

[86] J. E. Allen, E. R. Hemesath, D. E. Perea, J. L. Lensch-Falk, Z.Y Li, F. Yin, M. H. Gass, P. Wang, A. L. Bleloch, R. E. Palmer, and L. J. Lauhon. High-resolution detection of Au catalyst atoms in Si nanowires. *Nat Nano*, 3(3):168–173, 2008.

[87] T. J. Kempa, B. Tian, D. R. Kim, J. Hu, X. Zheng, and C. M. Lieber. Single and tandem axial p-i-n nanowire photovoltaic devices. *Nano Letters*, 8(10):3456–3460, 2008.

[88] J. S. Kang and D. K. Schroder. Gettering in silicon. *Journal of Applied Physics*, 65 (8):2974–2985, 1989.

[89] N. C. Strandwitz, D. B. Turner-Evans, A. C. Tamboli, C. T. Chen, H. A. Atwater, and N. S. Lewis. Photoelectrochemical behavior of planar and microwire-array Si—GaP electrodes. *Advanced Energy Materials*, 2(9):1109–1116, 2012.

[90] Z. Yu, L. Xiang, W. Xue, and H. Wang. The bending properties of flexible ITO films. In *Optical Fiber Communication and Optoelectronics Conference, 2007 Asia*, pages 148–150, 2007.

[91] L. Hu, H. S. Kim, J. Lee, P. Peumans, and Y. Cui. Scalable coating and properties of transparent, flexible, silver nanowire electrodes. *ACS Nano*, 4(5):2955–2963, 2010.

[92] P. Lee, J. Lee, H. Lee, J. Yeo, S. Hong, K. H. Nam, D. Lee, S. S. Lee, and S. H. Ko. Highly stretchable and highly conductive metal electrode by very long metal nanowire percolation network. *Advanced Materials*, 24(25):3326–3332, 2012.

[93] F. Xu and Y. Zhu. Highly conductive and stretchable silver nanowire conductors. *Advanced Materials*, 24(37):5117–5122, 2012.

[94] C. Chen, L. Dou, R. Zhu, C. Chung, T. Song, Y. B. Zheng, S. Hawks, G. Li, P. S. Weiss, and Y. Yang. Visibly transparent polymer solar cells produced by solution processing. *ACS Nano*, 6(8):7185–7190, 2012.

[95] C. Kim, S. Cha, S. C. Kim, M. Song, J. Lee, W. S. Shin, S. Moon, J. H. Bahng, N. A. Kotov, and S. Jin. Silver nanowire embedded in P3HT:PCBM for high-efficiency hybrid photovoltaic device applications. *ACS Nano*, 5(4):3319–3325, 2011.

[96] D. Leem, A. Edwards, M. Faist, J. Nelson, D. C. Bradley, and J. C. de Mello. Efficient organic solar cells with solution-processed silver nanowire electrodes. *Advanced Materials*, 23(38):4371–4375, 2011.

[97] Z. Yu, L. Li, Q. Zhang, W. Hu, and Q. Pei. Silver nanowire-polymer composite electrodes for efficient polymer solar cells. *Advanced Materials*, 23(38):4453–4457, 2011.

[98] C. Chung, T. Song, B. Bob, R. Zhu, H. Duan, and Y. Yang. Silver nanowire composite window layers for fully solution-deposited thin-film photovoltaic devices. *Advanced Materials*, 24(40):5499–5504, 2012.

[99] C. Yang, H. Gu, W. Lin, M. M. Yuen, C. P. Wong, M. Xiong, and B. Gao. Silver nanowires: From scalable synthesis to recyclable foldable electronics. *Advanced Materials*, 23(27):3052–3056, 2011.

[100] E. C. Garnett, W. Cai, J. J. Cha, F. Mahmood, S. T. Connor, G. M. Christoforo, Y. Cui, M. D. McGehee, and M. L. Brongersma. Self-limited plasmonic welding of silver nanowire junctions. *Nat Mater*, 11(3):241–249, 2012.

[101] J. Christofferson and A. Shakouri. Thermoreflectance based thermal microscope. *Review of Scientific Instruments*, 76(2):024903–024903–6, 2005.

[102] Z. Yan, J. Christofferson, A. Shakouri, D. Li, A. Majumdar, W. Yiying, R. Fan, and Y. Peidong. Characterization of heat transfer along a silicon nanowire using thermoreflectance technique. *Nanotechnology, IEEE Transactions on*, 5(1):67–74, 2006.

[103] J. R. Bolton, S. J. Strickler, and J. S. Connolly. Limiting and realizable efficiencies of solar photolysis of water. *Nature*, 316(6028):495–500, 1985.

[104] P. Denholm, E. Ela, B. Kirby, and M. Milligan. The role of energy storage with renewable electricity generation. National Renewable Energy Lab, January 2010.

[105] S. C. Roy, O. K. Varghese, M. Paulose, and C. A. Grimes. Toward solar fuels: Photocatalytic conversion of carbon dioxide to hydrocarbons. *ACS Nano*, 4(3):1259–1278, 2010.

[106] R. E. Algra, M. A. Verheijen, M. T. Borgstrom, L. Feiner, G. Immink, W. J. P. van Enckevort, E. Vlieg, and E. P. A. M. Bakkers. Twinning superlattices in indium phosphide nanowires. *Nature*, 456(7220):369–372, 2008.

[107] M. S. Gudiksen, L. J. Lauhon, J. Wang, D. C. Smith, and C. M. Lieber. Growth of nanowire superlattice structures for nanoscale photonics and electronics. *Nature*, 415 (6872):617–620, 2002.

[108] K. Hillerich, K. A. Dick, C. Wen, M. C. Reuter, S. Kodambaka, and F. M. Ross. Strategies to control morphology in hybrid group IIIV/group IV heterostructure nanowires. *Nano Letters*, 13(3):903–908, 2013.

[109] J. Hwang, Y, A. Boukai, and P. Yang. High density n-Si/n-$TiO_2$ core/shell nanowire arrays with enhanced photoactivity. *Nano Letters*, 9(1):410–415, 2008.

[110] J. Shi, Y. Hara, C. Sun, M. A. Anderson, and X. Wang. Three-dimensional high-density hierarchical nanowire architecture for high-performance photoelectrochemical electrodes. *Nano Letters*, 11(8):3413–3419, 2011.

[111] B. Aurian-Blajeni, M. Halmann, and J. Manassen. Electrochemical measurement on the photoelectrochemical reduction of aqueous carbon dioxide on p-gallium phosphide and p-gallium arsenide semiconductor electrodes. *Solar Energy Materials*, 8(4):425–440, 1983.

[112] E. E. Barton, D. M. Rampulla, and A. B. Bocarsly. Selective solar-driven reduction of $CO_2$ to methanol using a catalyzed p-GaP based photoelectrochemical cell. *Journal of the American Chemical Society*, 130(20):6342–6344, 2008.

[113] M. Tomkiewicz and J. M. Woodall. Photoassisted electrolysis of water by visible irradiation of a p-type gallium phosphide electrode. *Science*, 196(4293):990–991, 1977.

[114] R. A. Logan, H. G. White, and W. Wiegmann. Efficient green electroluminescent junctions in GaP. *Solid-State Electronics*, 14(1):55–70, 1971.

[115] A. D. Howard and G. B. Stringfellow. Effects of dimethylhydrazine on Zn, C, and H doping of GaP. *Journal of Crystal Growth*, 310(11):2702–2706, 2008.

[116] X. Wang, A. Wakahara, and A. Sasaki. Si and Zn doping of GaP grown by OMVPE using tertiarybutylphosphine. *Journal of Crystal Growth*, 158(12):49–52, 1996.

[117] J. P. André, J. Hallais, and C. Schiller. Heteroepitaxial growth of GaP on silicon. *Journal of Crystal Growth*, 31(0):147–157, 1975.

[118] K. J. Bachmann, U. Rossow, N. Sukidi, H. Castleberry, and N. Dietz. Heteroepitaxy of GaP on Si(100). *Journal of Vacuum Science & Technology B: Microelectronics and Nanometer Structures*, 14(4):3019–3029, 1996.

[119] V. K. Dixit, T. Ganguli, T. K. Sharma, R. Kumar, S. Porwal, V. Shukla, A. Ingale, P. Tiwari, and A. K. Nath. Studies on MOVPE growth of GaP epitaxial layer on Si(001) substrate and effects of annealing. *Journal of Crystal Growth*, 293(1):5–13, 2006.

[120] V. K. Dixit, Tapas Ganguli, T. K. Sharma, S. D. Singh, Ravi Kumar, S. Porwal, Pragya Tiwari, Alka Ingale, and S. M. Oak. Effect of two-step growth process on structural, optical and electrical properties of MOVPE-grown GaP/Si. *Journal of Crystal Growth*, 310(15):3428–3435, 2008.

[121] X. Liu, I. Kim, and D. Aspnes. Initial stages of GaP heteroepitaxy on nanoscopically roughened (001)Si. *Journal of Vacuum Science & Technology*, 25(4):1448–1452, 2007.

[122] J. M. Olson, M. M. Al-Jassim, A. Kibbler, and K. M. Jones. MOCVD growth and characterization of GaP on Si. *Journal of Crystal Growth*, 77(13):515–523, 1986.

[123] H. B. Pogge, B. M. Kemlage, and R. W. Broadie. The heteroepitaxial growth of GaP films on Si substrates. *Journal of Crystal Growth*, 37(1):13–22, 1977.

[124] L. Samuelson, P. Omling, and H. Grimmeiss. Electrical and optical-properties of GaP grown on Si by MOVPE. *Journal of Crystal Growth*, 68(1):340–344, 1984.

[125] T. Soga, T. Suzuki, M. Mori, T. Jimbo, and M. Umeno. The effects of the growth parameters on the initial stage of epitaxial growth of GaP on Si by metalorganic chemical vapor deposition. *Journal of Crystal Growth*, 132(12):134–140, 1993.

[126] T. Soga, T. Jimbo, and M. Umeno. Growth and characterization of two-dimensional GaP on Si by metalorganic chemical vapor deposition. *Journal of Crystal Growth*, 146(14):554–557, 1995.

[127] T. Suzuki, T. Soga, T. Jimbo, and M. Umeno. Growth mechanism of GaP on Si substrate by MOVPE. *Journal of Crystal Growth*, 115(14):158–163, 1991.

[128] D. E. Aspnes and A. A. Studna. Dielectric functions and optical parameters of Si, Ge, GaP, GaAs, GaSb, InP, InAs, and InSb from 1.5 to 6.0 eV. *Physical Review B*, 27(2):985–1009, 1983.

[129] C. F. Bohren and D. R. Huffman. *Absorption and Scattering of Light by Small Particles*. John Wiley & Sons, New York, 2004.

[130] M. L. Young and D. R. Wight. Concentration dependence of the minority carrier diffusion length and lifetime in GaP. *Journal of Physics D: Applied Physics*, 7(13): 1824, 1974.

[131] T. G. Deutsch, C. A. Koval, and J. A. Turner. IIIV nitride epilayers for photoelectrochemical water splitting: GaPN and GaAsPN. *The Journal of Physical Chemistry B*, 110(50):25297–25307, 2006.

[132] S. V. Dudiy, A. Zunger, M. Felici, A. Polimeni, M. Capizzi, H. P. Xin, and C. W. Tu. Nitrogen-induced perturbation of the valence band states in $GaP_{1-x}N_x$ alloys. *Physical Review B*, 74(15):155303, 2006.

[133] W. Shan, W. Walukiewicz, K. M. Yu, J. W. Ager Iii, E. E. Haller, J. F. Geisz, D. J. Friedman, J. M. Olson, S. R. Kurtz, H. P. Xin, and C. W. Tu. Band anticrossing in IIINV alloys. *Physica Status Solidi (b)*, 223(1):75–85, 2001.

[134] K. M. Yu, W. Walukiewicz, J. W. Ager, Iii, D. Bour, R. Farshchi, O. D. Dubon, S. X. Li, I. D. Sharp, and E. E. Haller. Multiband GaNAsP quaternary alloys. *Applied Physics Letters*, 88(9):092110–3, 2006.

[135] J. F. Geisz. III-N-V semiconductors for solar photovoltaic applications. *Semiconductor Science and Technology*, 17(8):769, 2002.

[136] J. F. Geisz, J. M. Olson, D. J. Friedman, K. M. Jones, R. C. Reedy, and M. J. Romero. Lattice-matched GaNPAs-on-silicon tandem solar cells. In *Photovoltaic Specialists Conference, 2005. Conference Record of the Thirty-first IEEE*, pages 695–698, 2005.

[137] J. V. Holm, H. I. Jørgensen, P. Krogstrup, J. Nygård, H. Liu, and M. Aagesen. Surface-passivated GaAsP single-nanowire solar cells exceeding 10% efficiency grown on silicon. *Nat Commun*, 4:1498, 2013.

[138] J. R. Waldrop, R. W. Grant, and E. A. Kraut. Measurement of AlP/GaP (001) heterojunction band offsets by x-ray photoemission spectroscopy. In *Proceedings of the 20th annual conference on the physics and chemistry of semiconductors interfaces*, volume 11, pages 1617–1620. AVS, 1993.

[139] B. Monemar. Determination of band gap and refractive index of aip from optical absorption. *Solid State Communications*, 8(16):1295–1298, 1970.

[140] H. M. Manasevit and W. I. Simpson. The use of metal-organics in the preparation of semiconductor materials: I. epitaxial gallium-V compounds. *Journal of The Electrochemical Society*, 116(12):1725–1732, 1969.

[141] A. C. Tamboli, M. Malhotra, G. M. Kimball, D. B. Turner-Evans, and H. A. Atwater. Conformal GaP layers on Si wire arrays for solar energy applications. *Applied Physics Letters*, 97(22):221914–3, 2010.

[142] V. Dixit, T. Ganguli, T. Sharma, S. Singh, R. Kumar, and S. Porwal. Effect of two-step growth process on structural, optical and electrical properties of MOVPE-grown GaP/Si. *Journal of Crystal Growth*, 310(15):3428–3435, 2008.

[143] R. Braunstein, A. R. Moore, and F. Herman. Intrinsic optical absorption in germanium-silicon alloys. *Physical Review*, 109(3):695–710, 1958.

[144] R. R. King, C. M. Fetzer, K. M. Edmondson, D. C. Law, P. C. Colter, H. L. Cotal, R. A. Sherif, H. Yoon, T. Isshiki, D. D. Krut, G. S. Kinsey, J. H. Ermer, Sarah Kurtz, T. Moriarty, J. Kiehl, K. Emery, W. K. Metzger, R. K. Ahrenkiel, and N. H. Karam. Metamorphic III-V materials, sublattice disorder, and multijunction solar cell approaches with over 37% efficiency. In *19th European Photovoltaic Solar Energy Conference and Exhibition*, 2004.

[145] I. Vurgaftman, J. R. Meyer, and L. R. Ram-Mohan. Band parameters for III-V compound semiconductors and their alloys. *Journal of Applied Physics*, 89(11):5815–5875, 2001.

[146] K. K. Lew, L. Pan, E. C. Dickey, and J. M. Redwing. Vapor-liquid-solid growth of silicon-germanium nanowires. *Advanced Materials*, 15(24):2073–2076, 2003.

[147] Edward D. Palik. *Handbook of Optical Constants of Solids*. Academic Press, 1991.

[148] G. D. Clark and N. Holonyak. Optical properties of gallium arsenide-phosphide. *Physical Review*, 156(3):913–924, 1967.

[149] The Ioffe Institute. New semiconductor materials. characteristics and properties, 2001. `http://www.ioffe.rssi.ru/SVA/NSM/Semicond/`.

[150] S. Chih-Tang, R. N. Noyce, and W. Shockley. Carrier generation and recombination in p-n junctions and p-n junction characteristics. *Proceedings of the IRE*, 45(9):1228–1243, 1957.

[151] M. T. Sheldon, C. N. Eisler, and H. A. Atwater. GaAs passivation with trioctylphosphine sulfide for enhanced solar cell efficiency and durability. *Advanced Energy Materials*, 2(3):339–344, 2012.

[152] V. E. Ferry, L. A. Sweatlock, D. Pacifici, and H. A. Atwater. Plasmonic nanostructure design for efficient light coupling into solar cells. *Nano Letters*, 8(12):4391–4397, 2008.

[153] http://www.synopsys.com. TCAD Sentaurus, 2012.

[154] H. W. Yu, E. Y. Chang, H. Q. Nguyen, J. T. Chang, C. C. Chung, C. I. Kuo, Y. Y. Wong, and W. C. Wang. Effect of substrate misorientation on the material properties of GaAs/$Al_{0.3}Ga_{0.7}As$ tunnel diodes. *Applied Physics Letters*, 97(23):231903–3, 2010.

[155] J. R. Jain, A. Hryciw, T. M. Baer, D. A. B. Miller, M. L. Brongersma, and R. T. Howe. A micromachining-based technology for enhancing germanium light emission via tensile strain. *Nat Photon*, 6(6):398–405, 2012.

[156] H. J. Song, S. M. Yoon, H. Shin, H. Lim, C. Park, and H. C. Choi. Growth of germanium nanowires using liquid $GeCl_4$ as a precursor: the critical role of Si impurities. *Chemical Communications*, (34):5124–5126, 2009.

[157] H. Okamoto. Reevaluation of thermodynamic models for phase diagram evaluation. *Journal of Phase Equilibria*, 12:623–643, 1991.

[158] R. W. Olesinski and G.J. Abbaschian. Cu-Ge (copper germanium). *Binary Alloy Phase Diagrams, II Ed.*, pages 1414–1416, 1990.

[159] P. Patnaik. *Handbook of Inorganic Chemicals*. McGraw-Hill, New York, NY, 2002.

[160] E. I. Givargizov. Mechanism underlying the epitaxial growth of germanium films from the gaseous phase. *Soviet Physics - Solid State*, 5(4):840–845, 1963.

[161] J. W. Dailey, J. Taraci, T. Clement, D. J. Smith, J. Drucker, and S. T. Picraux. Vapor-liquid-solid growth of germanium nanostructures on silicon. *Journal of Applied Physics*, 96(12):7556–7567, 2004.

[162] S. Hu, P. W. Leu, A. F. Marshall, and P. C. McIntyre. Single-crystal germanium layers grown on silicon by nanowire seeding. *Nat Nano*, 4(10):649–653, 2009.

[163] F. A. Trumbore. Solid solubilities of impurity elements in germanium and silicon. *Bell System Technical Journal*, 39(1):205–233, 1960.

[164] A. D. Gamalski, J. Tersoff, R. Sharma, C. Ducati, and S. Hofmann. Metastable crystalline AuGe catalysts formed during isothermal germanium nanowire growth. *Physical Review Letters*, 108(25):255702, 2012.

[165] M. Lindblom, J. Reinspach, O. von Hofsten, M. Bertilson, H. M. Hertz, and A. Holmberg. High-aspect-ratio germanium zone plates fabricated by reactive ion etching in chlorine. *Journal of Vacuum Science & Technology B: Microelectronics and Nanometer Structures*, 27(2):L1–L3, 2009.

[166] K. Mizuguchi, N. Hayafuji, S. Ochi, T. Murotani, and K. Fujikawa. MOCVD GaAs growth on Ge (100) and Si (100) substrates. *Journal of Crystal Growth*, 77(13): 509–514, 1986.

[167] J. M. Olson and W. E. McMahon. Structure of Ge(100) surfaces for high-efficiency photovoltaic applications, 6-10 July 1998.

[168] G. Brammertz, Y. Mols, S. Degroote, M. Leys, J. Van Steenbergen, G. Borghs, and M. Caymax. Selective epitaxial growth of GaAs on Ge by MOCVD. *Journal of Crystal Growth*, 297(1):204–210, 2006.

[169] Y. K. Ha, C. Lee, J. E. Kim, H. Y. Park, S. B. Kim, H. Lim, B. C. Kim, and H. C. Lee. Defect luminescence in heavily Si-doped n- and p-type GaAs. *Journal of the Korean Physical Society*, 36(1):42–48, 2000.

[170] C. J. Hwang. Doping dependence of hole lifetime in n-type GaAs. *Journal of Applied Physics*, 42(11):4408–4413, 1971.

[171] F. J. Lopez, E. R. Hemesath, and L. J. Lauhon. Ordered stacking fault arrays in silicon nanowires. *Nano Letters*, 9(7):2774–2779, 2009.

[172] E. L. Warren. *Silicon microwire arrays for photoelectrochemical and photovoltaic applications*. PhD thesis, California Institute of Technology, 2012.

[173] M. T. Borgström, J. Wallentin, M. Heurlin, S. Fält, P. Wickert, J. Leene, M. H. Magnusson, K. Deppert, and L. Samuelson. Nanowires with promise for photovoltaics. *Selected Topics in Quantum Electronics, IEEE Journal of*, 17(4):1050–1061, 2011.

[174] E. J. Schwalbach and P. W. Voorhees. Phase equilibrium and nucleation in VLS-grown nanowires. *Nano Letters*, 8(11):3739–3745, 2008.

[175] C. Y. Wen, J. Tersoff, K. Hillerich, M. C. Reuter, J. H. Park, S. Kodambaka, E. A. Stach, and F. M. Ross. Periodically changing morphology of the growth interface in Si, Ge, and GaP nanowires. *Physical Review Letters*, 107(2):025503, 2011.

[176] C. Gmachl, F. Capasso, E. E. Narimanov, J. U. Nöckel, A. D. Stone, J. Faist, D. L. Sivco, and A. Y. Cho. High-power directional emission from microlasers with chaotic resonators. *Science*, 280(5369):1556–1564, 1998.

[177] Y. Cui, Q. Q. Wei, H. K. Park, and C. M. Lieber. Nanowire nanosensors for highly sensitive and selective detection of biological and chemical species. *Science*, 293(5533): 1289–1292, 2001.

[178] K. Mathieson, J. Loudin, G. Goetz, P. Huie, L. Wang, T. I. Kamins, L. Galambos, R. Smith, J. S. Harris, A. Sher, and D. Palanker. Photovoltaic retinal prosthesis with high pixel density. *Nat Photon*, 6(6):391–397, 2012.

[179] J. T. Robinson, M. Jorgolli, A. K. Shalek, M. Yoon, R. S. Gertner, and H. Park. Vertical nanowire electrode arrays as a scalable platform for intracellular interfacing to neuronal circuits. *Nat Nano*, 7(3):180–184, 2012.

[180] A. Ikedo, T. Kawashima, T. Kawano, and M. Ishida. Vertically aligned silicon microwire arrays of various lengths by repeated selective vapor-liquid-solid growth of n-type silicon/n-type silicon. *Applied Physics Letters*, 95(3):033502–3, 2009.

[181] K. Tomioka, M. Yoshimura, and T. Fukui. A III-V nanowire channel on silicon for high-performance vertical transistors. *Nature*, 488(7410):189–192, 2012.

[182] T. S. Arthur, D. J. Bates, N. Cirigliano, D. C. Johnson, P. Malati, J. M. Mosby, E. Perre, M. T. Rawls, A. L. Prieto, and B. Dunn. Three-dimensional electrodes and battery architectures. *MRS Bulletin*, 36(07):523–531, 2011.

[183] M. Lv, S. Su, Y. He, Q. Huang, W. Hu, D. Li, C. Fan, and S. Lee. Long-term antimicrobial effect of silicon nanowires decorated with silver nanoparticles. *Advanced Materials*, 22:54635467, 2010.

[184] M. Cazzanelli, F. Bianco, E. Borga, G. Pucker, M. Ghulinyan, E. Degoli, E. Luppi, V. Vniard, S. Ossicini, D. Modotto, S. Wabnitz, R. Pierobon, and L. Pavesi. Second-harmonic generation in silicon waveguides strained by silicon nitride. *Nat Mater*, 11 (2):148–154, 2011.

[185] R. Sanatinia, M. Swillo, and S. Anand. Surface second-harmonic generation from vertical GaP nanopillars. *Nano Letters*, 12(2):820–826, 2012.

[186] M. D. Kelzenberg. *Silicon Microwire Photovoltaics*. PhD thesis, California Institute of Technology, 2010.